Magnetic Polymethylmethacrylate Cements for Hyperthermic Cancer Treatment

A thesis submitted to the Faculty of Science, Agriculture and Engineering for the Degree of Doctor of Philosophy

By

Fatma Ozdemir

School of Engineering

Newcastle upon Tyne

January 2020

To my dear family who supported me on this journey

Abstract

Polymethyl methacrylate (PMMA) bone cements have been used for stabilizing bone prostheses and filling cavities due to their suitable mechanical properties. PMMA bone cements, with and without addition of magnetic glass-ceramic (MGC), have been recently investigated for the treatment of bone cancer. The addition of MGC to PMMA bone cements allows for the treatment of cancer via magnetic induction hyperthermia.

This PhD thesis focused on the potential of MGC addition to commercial dental and orthopaedic PMMA cements for bone cancer treatment. MGC was prepared by melt-quenching technique at 1550°C. It contained a crystalline magnetic phase embedded in the glass matrix. MGC was mixed with dental and orthopaedic PMMA cements in amounts up to 40%. A method for production of magnetic PMMA cements (MPCs) with high reproducibility and dimensional accuracy was developed. The mechanical properties, in vitro bioactivity, cytotoxicity and heat generation of the resulted MPCs were evaluated.

Compressive strength and four-point bending tests on MPCs were performed using the ISO 5833:2002 standard. The magnetic cements containing up to 30% MGC met the ISO 5833:2002 standard requirements.

In vitro bioactivity was tested in a simulated body fluid (SBF). Apatite crystals started to form on the surface of MPCs after 2 weeks of immersion in SBF, showing the bioactive properties of these MPCs. Although cytotoxicity test results were found inconclusive, there was a decrease in the cell viability with addition of MGC in the bone cement.

Preliminary induction heating tests showed that all MPC samples could be heated to a similar temperature range in 5 minutes using magnetic fields compatible with operating rooms in hospitals.

The thermal, mechanical and biological properties of MPCs, analysed during this PhD thesis, showed that MPCs are promising biomaterials for the treatment of bone cancer using magnetic induction hyperthermia.

Keywords*: Bone cement, PMMA, bone tumour, hyperthermia, magnetic glass ceramics, magnetic bone cement*

Acknowledgments

Throughout this PhD study, I have been lucky to meet and work with wonderful people who contributed to this project in many ways. The following words are dedicated to those people.

I owe my deepest gratitude to my supervisors, Dr Oana Bretcanu and Dr Iain Evans, for their guidance, encouragement, support and patience. They have always believed in me and helped in the most difficult times. They were not only my supervisors but a family to me. It was an honour to work with them and learn how to be an independent researcher.

Besides my supervisors, I would like to express my appreciation to Dr Matthew German for providing Wintercryl Rapid Repair Powder & Liquid components and sharing his knowledge in PMMA cement. I would like to thank Dr Kenneth Rankin for his contributions to cytotoxicity experiments.

I would like to thank all people in Stephenson Building but more specifically Stephenson Moore, Frank Atkinson, Adam Richardson, Paul Harrison, Brian Stoker and Chris Brown, who always cheered me up, for helping me cutting, manufacturing, preparing and testing the materials.

Thanks to all my friends in all continents who have been there when I needed most. Grand hotel team, Barker House kitchen mates, Stephenson Building Chihuahua gang and Robinson Library team that I will always appreciate for their invaluable support and motivation.

Lastly, I am grateful to my all family for their moral support and encouragement to follow my ideas and dreams. My dear aunty, Nurcan, has been a friend, mum, and my mentor throughout my life. No words are adequate to express my heartfelt thanks for her.

Table of Contents

List of Tables

List of Figures

Nomenclature

Acontrol	Absorbance value of control
Asample	Absorbance value of sample
B	Bending strength
F	Force
Fcontrol	Fluorescence reading of control
Fsample	Fluorescence reading of sample
H	Magnetic intensity
s	Second
Tc	Crystallisation temperature peak
Tc1	First crystallisation temperature peak
Tc2	Second crystallisation temperature peak
Tg	glass transition temperature
Tm	Melting temperature
Tm1	First melting temperature
Tm2	Second melting temperature
T_{max}	Maximum temperature
T_{set}	Setting temperature
t_{set}	Setting time
A_0	Initial area
A_T	Area at a specific temperature, T
E	Elastic modulus (Young's modulus)
F	Force
t	Time
ε	Strain
σ	Stress
$\sigma_{2\%}$	Stress at 2% offset line
σ_{max}	Maximum stress

List of Abbreviations

AIA	American Institutes of Architects
ANOVA	Analysis of Variance
ASHREA	American Society of Heating, Refrigerating and Air-conditioning Engineers
ASTM	American Society for Testing and Materials
AW	Apatite-Wollastanite
BG	Bioglass
CHPP	Continuous Hyperthermic Intraperitoneal Perfusion
CP	Calcium Phosphate
CPC	Calcium Phosphate Cement
CPD	Critical Point Dryer
CT	Computer Tomography
DAPI	4',6-Diamidino-2-Phenylindole (double stranded DNA staining)
DMEM	Dulbecco's modified eagle medium
DTA	Differential Thermal Analysis
EDX	Energy Dispersive X-ray
EMF	Electromotive Force
FBS	Fetal Bovine Serum
FDA	Food and Drug Administration
GC	Glass Ceramics
HA	Hydroxyapatite
HCA	Hydroxy Carbonate Apatite
HIPEC	Hyperthermic Intraperitoneal Chemotherapy
HSM	Hot Stage Microscope
HSPs	Shock Proteins
IMRT	Intensity-Modulated Radiation Therapy
MGC	Magnetic Glass Ceramic
MMA	Methyl Methacrylate
MTT	3-(4,5-dimethylthiazol-2-yl)-2,5-diphenyl tetrazolium bromide
OBS	Osteoblast Cells

PBS	Phosphate Buffered Solution
P-MGC	MGC containing Palacos cement
PMMA	Poly(methyl methacrylate)
PTFE	Polytetrafluoroethylene
RPMI	Roswell Park Memorial Institute
SAR	Absorbance Rate
SBF	Simulated Body Fluid
SEM	Scanning Electron Microscope
U2OS	Osteosarcoma Cells
WBH	Whole Body Hyperthermia
WHO	World Health Organisatin
W-MGC	MGC containing Wintercryl cement
XRD	X-Ray Diffraction

1 Introduction

An ancient physician Hippocrates who is also known as the “father of medicine” said “***Those who cannot be cured by medicine can be cured by surgery. Those who cannot be cured by surgery can be cured by fire. Those who cannot be cured by fire, they are indeed incurable***”.

According to the American Cancer Society, there will be an estimated 1,762,450 new cancer cases and 606,880 cancer deaths in 2019. Approximately 3,500 people will be diagnosed with bone cancer and about 1,660 of people will die [1]. In the UK, an average of 550 new cases of bone cancer are diagnosed every year [2]. Bone cancer does not only form as primary cancer, it also occurs as secondary cancer which is more commonly happen. According to the National Cancer Institute, approximately 280,000 adults between 18-64 years old, were living with secondary bone cancer in 2018 in the US alone [3]. There are a variety of treatment techniques for bone cancer that have been developed. The most common treatment techniques are listed as surgery, chemotherapy and radiotherapy. Whilst medication is used in chemotherapy to destroy cancer cells, X-ray beam is applied in radiotherapy.

Hyperthermia (heat treatment) is one of the techniques, which increases the body temperature above 37°C to destroy cancer cells. Although it is an accepted cancer treatment technique by the National Cancer Institute and American Cancer Society, it is still under clinical trials and mostly applied as an experimental technique [1]. It is preferably used in conjunction with chemotherapy and radiotherapy treatments. Hyperthermia can be induced for the following cancer types: bladder, breast, liver, kidney, pancreas, thyroid and sarcomas (bone and soft tissue cancers). However, there are some limitations caused by not being able to reach deep-seated tumours to kill cells or prevent the proliferation. Hyperthermia treatment should be applied carefully because increasing the time or temperature to reach deep-seated tumor may cause severe burnings and kill healthy cells. To date, hyperthermia treatment techniques have not been sufficient for bone tissue cancers since they could not be heated to a suitable temperature.

To overcome the limitations of reaching the deep-seated tumour, different methods were developed. Designing a device capable of reaching a deep-seated tumour sites to heat up to 46°C without giving any harm to normal, healthy tissues is very challenging [4]. This problem was tackled using magnetic materials. When magnetic particles are subjected to a variable electromagnetic field, they generate heat due to their magnetic properties and start acting as thermoseeds [5]. This technique is known as **magnetic hyperthermia**. In this application, a magnetic material is implanted in the tumour and an external alternating magnetic field is applied. The temperature of tumour could increase to 41°C-43°C. The increment in the temperature is based on the amount of magnetic phase in the composition, properties of magnetic materials, intensity and frequency of the magnetic field and thermal properties of bone. Recently, considerable attention has been paid to magnetic hyperthermia technique in order to treat cancerous cells. It is expected that magnetic hyperthermia will play a crucial role in the treatment of deep-seated tumor cells [6, 7].

In the late 1950s, PMMA (polymethylmethacrylate) bone cements were introduced to medical applications for the first time for the fixation of orthopaedic prosthesis. Since then, they have been widely used in many medical applications such as orthopaedics, dental and vertebral applications. The main reason is due to mechanical properties of PMMA bone cement provide a sufficient support to bone and implant. The cement acts as a buffer between the prosthesis and bone, and it provides optimal stress and strain distribution. Since it creates mechanical bond between bone and prosthesis, it is necessary to have valuable mechanical properties. Therefore, it has been mostly preferred in hip and knee replacements. 85% of knee replacements and 34% of hip replacements are performed using PMMA cement [8]. PMMA cement is not only used in total joint replacements to stabilise the prosthesis but also used in fractures, tumour surgery and percutaneous vertebroplasty [9]. PMMA bone cement is applied as one of the treatment techniques for bone cancer to strengthen the destructive bone and ease pain. PMMA bone cement has shown good outcomes for pelvis, spine and other flat bones [10].

Bone tumours lead to critical size bone defects, which are approximately between 1cm to 3 cm [11]. However, cancerous tissues continue growing and spreading to other parts of the body, thus the size of defect may exceed 5 cm. Therefore, there are a wide variety of sizes and shapes for bone defects. The volume of defect that can be treated using PMMA bone cement is usually between 1 mm^3 to 20 mm^3 [12]. After removal of the bone tumour, the cavity is filled with PMMA bonce cement to strengthen the weaken bone. If the volume of bone defect is larger than 20 mm^3 a prosthesis is implanted after the excision of tumoral tissue to support the bone. Afterwards, PMMA cement is used to fill the gap between bone and implant as it is applied in hip replacement [13]. For these kinds of applications, it has been suggested that the layer of PMMA cement should not exceed 5 mm since the thickness affects the temperature rise [14].

PMMA cement goes through an exothermic polymerisation reaction during hardening. It was thought that its high exothermic polymerisation reaction could kill bone cancer. However, the heat generated by PMMA bone cement was not found to be high enough to kill the cancerous cells entirely. Sturup et al [15]., reported that even the high exothermic polymerisation rate of the PMMA has no or little necrosis effect on the tumour cells *in vivo*. Thus, combining PMMA cement with magnetic hyperthermia has attracted a lot of attention.

Although there are numerous studies on investigations of magnetic particles, little work is done for the assessment of magnetic PMMA cement. Considering the pivotal role of bone cement in strengthening fractured and weakened bone, and the effectiveness of magnetic materials to heat deep-seated tumour cells, the combination of PMMA bone cement with magnetic particles is an innovative technique to cure bone cancer [16]. However, it should be noted that the mechanical properties of PMMA cement may degrade with the addition of magnetic particles; therefore, the properties of magnetic particles and the amount mixed in the PMMA structure must be well evaluated. Moreover, ageing and moisture uptake may lead to implant failure over the years after the implantation. Wear particles surrounding the implant region can accelerate its deterioration. However, few studies investigated effects of ageing and moisture uptake of PMMA cement on the mechanical properties yet.

PMMA cement is a bioinert material, thus, chemical or biological bonding to the bone cannot be stimulated. Hypothetically, magnetic PMMA cement will provide significant advantages for treatment of bone cancer via magnetic hyperthermia. Firstly, after excision of the tumour cells, the weakened bone is reinforced by bone cement. Secondly, the bioactive properties of magnetic glass ceramic will induce bone regeneration creating a chemical interfacial bond to the bone [17, 18]. Lastly, when the magnetic cement is exposed to a magnetic field, magnetic particles act as thermoseeds and start generating heat, which then destroys deep-seated remnant tumor cells. Hence, the recurrence of these tumoral tissues will be prevented by this technique so that there will be no need for another surgery after this treatment. If one tumour cell is not removed or killed, it may proliferate again. Further approach is eliminating chemotherapy and radiotherapy techniques by a successful use of magnetic hyperthermia, which has the advantage of not killing healthy cells [19, 20].

This thesis investigated magnetic PMMA cements that can be used to treat bone cancer using magnetic heat generation. Orthopaedic and dental commercial PMMA cements were used in this study; Palacos® and Wintercryl® PMMA cements were mixed with magnetic glass-ceramic in different ratios to investigate their properties including mechanical properties, bioactivity, cytocompatibility and heat generation during magnetic field application. Ageing and storage condition effects on PMMA cements were also assessed.

It was important to prepare samples in a consistent way to obtain reliable test results and reduce any variations, which could occur due to inconsistent dimensions, sanding and polishing. New silicone moulds were designed and fabricated to easily place and remove samples. All samples made using silicone mould had consistent dimensions.

This study was important to provide further knowledge in improving magnetic PMMA cements to be efficiently used in bone cancer treatment.

1.1 Aims & Objectives

The main aim of this project is to develop **magnetic PMMA cement** using an optimal ratio of magnetic glass-ceramic (MGC) that meets criteria of ISO 5833:2002 for mechanical properties, demonstrates bioactive properties and can efficiently be heated to a targeted temperature to kill cancerous cells. In order to achieve the aims, this study focuses on answering the following research questions:

- What is the best MGC ratio in the cement that can meet the criteria of ISO 5833:2002 standard for mechanical properties and lead to essential properties of cement such as bioactivity, and effective heat generation?
- Is magnetic PMMA cement cytotoxic?
- What is the effect of ageing PMMA cement on its mechanical properties?
- Can magnetic PMMA cements generate heat under magnetic field? If yes, what is the current and frequency that can effectively heat the samples under safe conditions?

In order to achieve these aims and answer to the research questions, the main objectives are:

- Synthesis and characterisation of magnetic glass-ceramics
- Development of a new mould design in order to sustain consistent dimensions and surface finish
- Assessment of mechanical and in vitro heat generation properties of magnetic PMMA cements
- Assessment of *in vitro* bioactivity and cytocompatibility properties of MPCs

1.2 Thesis Structure

This thesis is divided into five chapters as described below:

Chapter 1 presents an introduction to magnetic PMMA cements, aims and main objectives of this thesis.

A comprehensive literature review is provided in **chapte**r **2.** The chapter includes a section on bone structure, followed by different types of bone cancer and current treatment techniques, their limitations and side effects sections. Chapter 2 also contains sections on magnetic hyperthermia, which is aimed to be performed for deep-seated bone cancer tissues, properties of magnetic glass-ceramics and magnetic cement along with their drawbacks and limitations. In the last part, the properties of plain and magnetic PMMA cements and their applications are described, including their mechanical and heat generation properties under the applied magnetic field.

Chapter 3 presents the materials and methods used in this study. Firstly, the preparation of magnetic glass-ceramic and its characterisation techniques are explained, followed by the design and fabrication of new moulds, made of silicone rubber. The preparation and characterisation techniques to determine handling properties, mechanical properties and morphology of two commercial PMMA cements are further explained. Finally, the last part of chapter 3 presents the preparation and characterisation techniques of magnetic PMMA cements, including mechanical properties, handling properties, biological properties and preliminary heating test.

Experimental findings of this study and discussions are divided in two chapters. **Chapter 4** presents the charaterisation of magnetic glass-ceramic. The experiences in fabrication of silicone rubber mould and the dimensions of prepared test samples using the test moulds are provided. Lastly, mechanical properties of aged commercial PMMA cements as well as their setting properties and morphologies are presented in the following part. In **Chapter 5,** setting properties**,** mechanical properties, in vitro bioactivity, cytotoxicity and heat generation of the resulted magnetic PMMA cements are evaluated. A summary of results and discussion are given at the end of each part.

In Chapter 6, the main results of this research are summarised and discussed. The overall conclusions, limitations and possible future studies are reported.

2 Literature Review

2.1 Bone and Bone Structure

Bone is defined as a rigid endoskeleton which gives shape and mechanically optimal support to soft tissues and muscles and also assists movement [21, 22]. It has an active growing mechanism which undergoes remodeling throughout life. It consists of organic and inorganic phases. The inorganic phase is mainly composed of hydroxyapatite [$(Ca_{10}(PO_4)_6(OH)_2$] that is a crystalline calcium phosphate salt [22-24]. By this way, it has a significant contribution to calcium/phosphate ratio in the body. Other inorganic minerals are carbonate, magnesium, sodium and potassium ions [21, 24]. The organic matrix consists of collagen and non-collagenous organic materials [21, 22].

There are five major types of bones; long bones (tibia and femur), short bones (tarsal bones of the hand and foot), flat bones (skull), irregularly shaped bones (scapula) and sesamoid bones (patella). Most of the bones are composed of cortical and trabecular bones. Cortical (compact) bone, is found in the outer shell of the diaphysis (middle section of a long bone), is strong and dense and it is composed of osteons, osteoblast and osteocyte cells. Cancellous (trabecular) bone is lighter and less dense than cortical bone, and it consists of osteoblast cells, red blood cells, white blood cells and platelets. The mechanical properties of cancellous and compact bones are required in order to design biomaterials that would give enough support to the bones, which are given in Table 2.1.

Table 2.1 Mechanical properties of human bone [16]

	Tensile Strength [MPa]	**Compression Strength [MPa]**	**Strain to Failure**	**Young Modulus [GPa]**
Cortical Bone	50-150	100-230	1-3	7-30
Cancellous Bone	10-20	2-12	5-7	0.05-0.5

The bone sections, diaphysis, bone marrow, epiphysis and metaphysis, can be shown in long bone structure easier than another type of bones, as can be seen in Figure 2.1. The diaphysis is the central region of the long bone, which is a thick cortex involving compact bone and medullary cavity.

This cavity is filled with bone marrow that can be hematopoietic (red) and fat (yellow) tissues. The end sections of the bone are called epiphysis and involve cancellous bones. The metaphysis is found between diaphysis and epiphysis, involves a growth plate that plays an important role in remodeling during adolescence. Bone tumours mostly originate in the metaphysis [21, 22, 25].

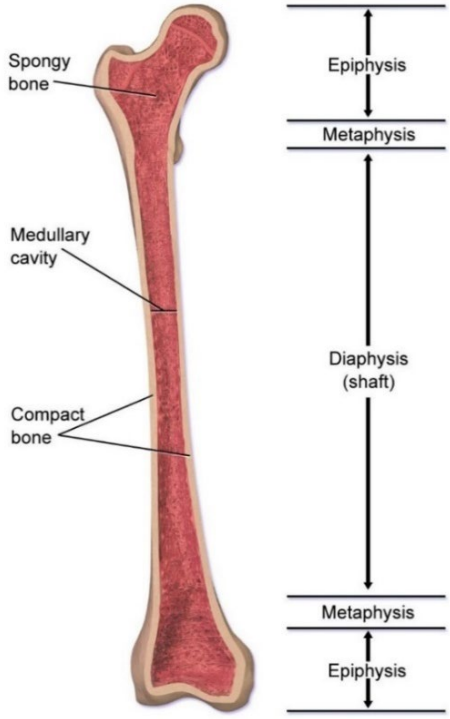

Figure 2.1 Schematic figure of the long bone [26]

Bone has a dynamic structure that regenerates itself. Osteoblast, osteocyte and osteoclast cells are crucial for bone regeneration [21, 22, 27]. Osteoblast cells are formed of mesenchymal stem cells. Thus, they are responsible for the formation of new bone. Eventually, they are trapped in the bone matrix. These entrapped cells then transform into osteocyte cells [21, 25], which are responsible for maintaining the mineral concentration of the body. Osteocytes are primary cells in the mature bone, and thus, they are the most common type of bone cells. However, these cells do not divide. The only type of cell that is capable of dividing is the osteogenic cell, which is transformed into osteoblast and osteoclast cells to maintain bone repairs and growth. Osteoclast cells are responsible for the breakdown of old bone. These cells are originated from hematopoietic stem cells, which are monocytes and macrophages [24, 25]. However, when the cells divide uncontrollably, they cause the growth of lump in the bone, which is called bone tumour, and it might be cancerous. Bone cancer and types will be explained in the next section.

2.2 Bone Cancer

Abnormal tissue growth, which is named as neoplasm, can be classified as benign or malignant [28]. Although a benign tumour is defined as abnormal cell growth, it does not spread to another part of the body, and when it is removed, it does not grow back. In contrast, a malignant tumour can spread and grow in another part of the body even after it is removed [28, 29]. Therefore, while benign tissues are considered as non-cancerous tissues, malignant tissues are defined as cancerous [30]. Primary bone tumours, which originate in the bone, are rare. According to the American Cancer Society, there were an estimated 1,762,450 new cancer cases in 2019 and 606,880 cancer deaths. For bone cancer, about 3,500 new cases will be diagnosed, and about 1,660 deaths from these cancers are expected. In the United States, in 2018, approximately 280,000 adults between the ages of 18-64 were living with metastatic bone cancer [1]. Every year, 580 new cases of primary bone cancer are diagnosed in the UK [2], yet it can be misleading as it is challenging to differentiate tissue lesions from cancerous cells. Conversely, the actual number of bone cancer cases are higher than these numbers as cancer does not always originate in the bone, but spreads to the bone from another part of the body. This is known as secondary or metastatic cancer.

Metastases more commonly occurs in the bone than primary bone cancer (see Figure 2.2) [29]. Metastatic cancers can be aggressive and may develop rapidly, as it can quickly proliferate even after they are removed. The most common types of primary cancer that spread to the bone are prostate, breast, lung, kidney and thyroid cancers [29, 31]. Welch-McCaffrey et al [32] ., have stated that, in 70-80% of patients who have bone cancer, it has originated in the breast, prostate or lung. Also 20% of the cancer is originates in the kidney, thyroid, liver, bowel, cervix, uterus or pancreas. According to Needham and Hoskin et al, diagnosed tumours in breast, lung and prostate regions, are directly related to metastatic bone cancer [29, 31].

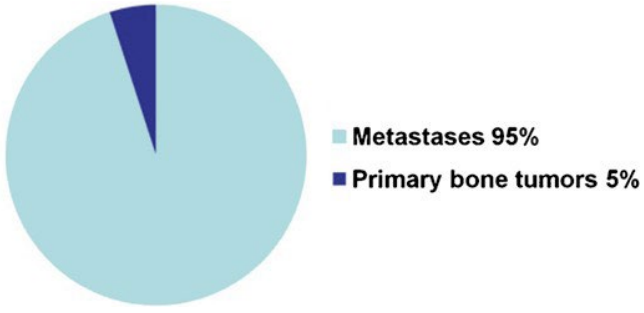

Figure 2.2 Comparison of metastatic cancer and primary bone tumours [29]

2.2.1 Diagnosis of Bone Tumor

Symptoms of the tumour are usually pain, fractures and swellings. The age of the patient and location of the lesion in the body as well as the gender are crucial to determine the type of cancer [33]. Blood test, imaging and biopsy techniques are performed to understand whether there is a tumour, lymph nodes (small structures, which filters bacteria, viruses etc.) or cancer. A blood test is the first analysis, when imaging procedures are applied in order to determine the precise location and the size of the tumour [34]. Imaging yields valuable information regarding the diagnosis stage, the volume of cancerous tissue, observing the stage of healing and recurrence of the tissue. An imagining technique is chosen depending on the age of the patient and sensitivity to the radiation [29, 34].

Different imaging techniques used for diagnosis are;

- **A radiograph** is an initial technique applied using x-ray and this technique is especially performed for children. It has a low radiation dose, low cost and easy to obtain [29, 34].
- **Bone Scan** involves radionuclide agent to visualize evaluation of the bone tumour. The abnormal tissues tend to absorb radioactive reagents. By this way, any region in the bone that has abnormality is detected as “hot spots”. Bone scan can be used to determine osseous metastases in the body as well [29].
- **Ultrasound** can be used as guidance for biopsy purposes due to its limited efficiency to detect the lesions [29].
- **Computed Tomography (CT or CAT) Scan** provides multiplanar imaging while exposing the patient to high ionizing radiation using x-ray [33-35]. The radiation dose of CT has been reduced in recent years maintaining the quality of imaging, due to adverse side effects of radiation, especially in children [34]. It is usually preferred for characterisation of bone tumour [29].
- **Magnetic Resonance Imagining (MRI)** can detect and differentiate healthy and cancerous tissues better than computed tomography [33, 35]. It applies a magnetic field to create an image of the lesion rather than radiation [29, 34]. It is most suitable for soft tissue lesion detections [29].

- **Positron Emission Tomography (PET) Scan** includes injection of a radiotracer within the body. The radiotracer contains glucose which is absorbed by high metabolic lesions. PET scan is eligible for the whole-body scan, soft tissues and skeleton. It can be combined with CT (PET/CT) or MRI (PET/MRI) to improve the detection and localization of the lesion as well as the stage of cancer [29, 33-35].

A biopsy is a further step to the diagnosis of the lesion which is an initial surgical procedure. A part of the lesion is removed for histological and pathological examination. Biopsy should be applied carefully as there is a high risk of spreading cancer to healthy tissues and also to prevent future complications during limb salvage surgery [28, 33, 36].

2.3 Primary malignant and benign bone tumours

The World Health Organization (WHO) has classified bone tumours regarding the histologic tissue and their differentiation pattern. A complete diagnosis may not be possible in some cases, thereby, evaluation of bone lesion can be done with the help of some characteristic information such as patient's age and a major site of the lesion. Gender of the patient can also narrow down the possibilities and help eliminations. The WHO classification of the primary bone tumours provided and other characteristic information are provided in Table 2.2.

Table 2.2 Tumor sites, types, age, gender prevalence and major sites in the body [29, 37] (M=male, F= female)

Tumour	**Tumour Type**	**Benign/Malignant**	**Main Age**	**Gender**	**Major Site**
Osteosarcoma	Osteogenic tumour	Malignant	10-25	M>F	Metaphysis of long bone
Chondrosarcoma	Cartilage tumor	Malignant	40-70	M>F	Pelvis, rib, femur, humerus
Ewing's Sarcoma	Ewing tumour	Malignant	5-20	M=F	Long bones, pelvis
Chordoma	Notochordal tumors	Malignant	40-70	M=F	Sacrum, skull base, spine
Malignant Fibrous	Fibrohistioctic tumour	Malignant	Adults	M>F	Metaphysis of long bones
Osteochondroma	Cartilage tumour	Benign	10-20	M=F	Medullary cavity, femur, tibia
Enchondroma	Cartilage tumour	Benign	Children& Adults	M=F	Proximal humerus, distal femur, hands and feet
Giant Tumor Cells	Giant cell tumour	Benign	20-45	F>M	Epiphysis of long bones
Osteoid Osteoma	Osteogenic tumour	Benign	7-25	M>F	Femur, tibia, spine
Fibrous Dysplasia	Miscellaneous lesion	Benign	5-30	M=F	Intramedullary, femur, tibia and skull

The most common primary malignant bone tumours are osteosarcoma (35%), chondrosarcoma (25%), Ewing sarcoma (16%), chordoma (8%) and malignant fibrous histiocytoma (5%) (Figure 2.3) [29].

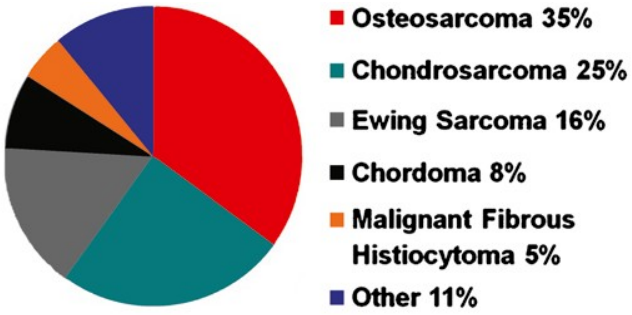

Figure 2.3 The percentage of malignant bone cancer types [29]

The most common primary malignant bone tumour seen in children and adolescents is **osteosarcoma (osteogenic sarcoma)** [34]. It can be mostly seen during the bone formation phase. Hypothetically, malignant transformation is derived from mesenchymal cells [34, 38, 39]. Osteosarcoma can originate anywhere in the skeleton, mostly seen in the centre of the long bones but rarely can be seen in soft tissues. The most common parts in the body that osteosarcoma can occur are arms and legs as well as around knee and shoulder [34, 38]. In the UK, approximately 30 children are diagnosed with osteosarcoma [40].

Chondrosarcoma usually occurs in cartilage in the bone, which is mostly seen in adults between the age of 30 and 80 years old [29]. However, there are some incidences that can be seen in children as well [41]. It can be mostly observed in pelvis, femur, humerus, scapula and ribs [29].

Ewing sarcoma is mostly seen in children and adolescents between the age of 10 and 20 years old. The origin tissue of the Ewing sarcoma is still unknown but mostly occurs in pelvis, femur and tibia [29].

Chordoma is a rarely seen slow-growing type of bone tumour. The origin of the tumour mostly is primitive spine, thus, this type of tumour can be seen in the spinal cord and in the skull base [28, 29].

A malignant fibrous histiocytoma is mostly seen in adults who are between the age of 30 and 70 years old. It originates in fibroblast, histiocytes and pleomorphic cells. Similar to osteosarcoma, it can originate in the centre of a long bone in femur and humerus [29].

The most common primary benign bone tumours are osteochondroma (35%), enchondroma (20%), giant cell tumour (15%), osteoid osteoma (10%) and fibrous dysplasia (5%) (Figure 2.4) [29]. Benign bone tumours are not cancerogenic. However, they can be destructive and might need the same treatment techniques as malignant bone tumours.

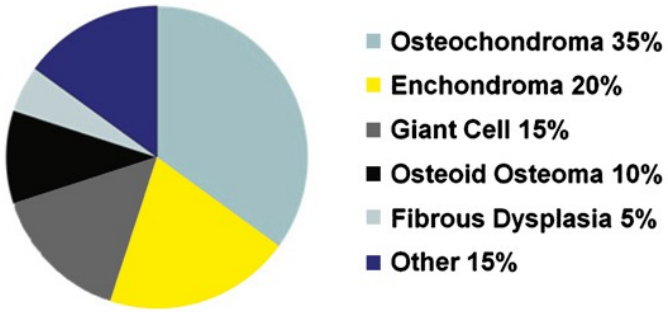

Figure 2.4 The percentage of primary benign tumour types [29]

Osteochondroma is a common type of benign tumour in the age range of 10 and 20 years and mostly seen in the metaphysis of the long bones [37, 38].

Enchondroma has a wide range of possibilities that can be seen in anyone [37]. It mostly occurs in the diaphysis of the long bones and medullary cavity in the hands and feet [38].

Giant cell tumour is mostly seen in adults who are in the age between 20 to 45 years [37]. This type of benign tumour can be seen in the epiphysis of long bones [37], as well as in knee and sacrum [38]. Even though it is a benign tumour, it can still be aggressive and regrow after curettage possibly at a rate of 20% to 50% [37, 42]. Some clinical studies showed that the transformation of giant cell tumour to the malignant tumour is possible [42, 43].

Osteoid osteoma is mostly seen children and young adults between 10 and 30 years of age [37]. It mostly arises in long bones and rarely in the spine [38].

Fibrous Dysplasia is a rare type of primary benign bone tumour and that can be seen in children and adults between the age of 5 and 30 years old [37]. The reason for the formation of this tumour is due to the failure of bone forming cells. It is mostly seen in long bones, pelvis, ribs and skull [37, 38].

2.3.1 Treatment Techniques for Bone Cancer

After diagnosing the tumour, based on type, size, stage of the tumour and location, an appropriate treatment technique is applied. Patient's age and general health can also play an essential factor in that decision. The most common treatment techniques are:

- Surgery
- Chemotherapy
- Radiation therapy
- Targeted therapy

Surgery is a primary treatment technique for a bone tumour by removing the entire cancerous tissue [36, 44]. It is essential to not leave any cancer cells behind as it can grow and proliferate again. Therefore, the outer shell (margin) of the removed tissue is pathologically tested. If there are residual cancer cells around the edge, it is called a positive margin. On the contrary, negative margin means there are no cancer cells left in the region. In order to be sure that the removed region has negative margins, the surgeon removes some healthy tissue along with the tumour tissue. This technique is called **wide-excision**. In some cases, the whole limb might be removed, and this is called **amputation**. This type of surgery has been gradually reduced in the past 20 years [44, 45]. However, it can still be the safest option to prevent recurrence of cancer [44]. Another surgery type is **limb-salvage,** which includes wide-excision. The limb can still function, but it will need a bone graft or prosthesis for support [36, 45].

If the tumour is in pelvic bone, jaw, skull or spine, the wide-excision technique cannot be performed. Therefore, the suggested techniques are curettage, cryosurgery and bone cement. **Curettage** is removing the tumour tissue using a curette by scraping. It is not only a treatment technique but also can be used as a diagnosing technique [28, 29, 45]. In **cryosurgery** treatment, after removing the tumour tissue within the bone, the cavity is filled with liquid nitrogen. The drastic drop in the temperature freezes and kills the cancer cells. **Bone cement** is used to fill the cavity after the removal of tumour tissue, and as well as filling the gap between the prosthesis and the bone [45]. More information about bone cement are given in Section 2.7.

Chemotherapy and **radiotherapy** treatment techniques can be applied solely or together, depending on the tumour type and size. These therapy techniques can also be applied after the surgery to prevent the reoccurrence of cancer.

Chemotherapy uses drugs that are circulated along the bloodstream to reach and kill tumour cells. It is mostly performed for osteosarcoma and Ewing sarcoma bone tumours [36]. The most common drugs are Doxorubicin (Adriamycin®), Cisplatin, Etoposide (VP-16), Ifosfamide (Ifex®), Cyclophosphamide (Cytoxan®), Methotrexate and Vincristine (Oncovin®) [36, 45]. The side effects of the chemotherapy are hair loss, mouth soreness, nausea and loss of appetite. However, in the long term, it can damage healthy cells, which are mostly blood cells [45].

In radiotherapy, X-ray beams are applied to shrink and kill cancer cells [36, 46]. In order to perform an effective treatment, high doses are applied. However, it can be harmful to healthy tissues. Therefore, it is usually applied in conjunction with another treatment [36, 46]. There are two types of radiation therapies; external-beam therapies and internal radiation therapy. Intensity-modulated radiation therapy (IMRT) and proton beam radiation therapy are two examples of external beam therapies and in these therapies, radiation is delivered from an outsource machine to the body. IMRT is a technique that aims to deliver maximised radiation dose to the tumoral tissue without damaging normal tissue. Determination and planning of the dose is done by conformal radiation and the beam can be directly sent to targeted area [47]. Proton beam therapy uses high energy protons to destroy cancer cells. However, it is only been successful in specific cancer types; brain, neck, head and sarcomas [48]. Internal radiation therapy, also called brachytherapy, uses permanent or temporary radioactive materials inserted into the cancerous tissue. These materials can be seeds, balloons, wires or tubes [49]. The side effects of the therapy are fatigue, loss of appetite, redness in the skin, hair loss, low blood counts, nausea and vomiting [45].

In **targeted therapy**, new generation drugs are specifically designed to detect mutations in genes. These mutations cause changes in protein structures of the cells, hence, the drugs can recognise and inhibit the proteins[45, 50, 51]. The targeted drugs, then, can block the cancerous growth cells and kills them by delivering toxic materials into the cells. This type of therapy can be more effective than chemotherapy, especially for chordomas. Denosumab (Xgeva® or prolia®), a monoclonal antibody-based drug, has been used in targeted therapy for bone cancer [45, 51].

According to WHO, cancer treatment techniques can also induce deaths due to their side effects. Although the surveillance rate of cancer has been increasing every year, there are new treatment techniques emerging to decrease the effects and increase the efficiency of the treatments [52]. Regardless of the side effects in the body such as nausea and hair loss, there is also an undeniable traumatic psychological effect on cancer patients.

2.3.2 Hyperthermia

In the last two decades, hyperthermia has been seen as a promising technique that aims to destroy cancer cells by increasing the body temperature to a high 'fever' using an external source [7, 53, 54]. However, hyperthermia has been known since 300 BC [19, 20, 55]. Hippocrates and Parmenides emphasised the importance of heat to cure any diseases which are not curable by surgery or medicine. The terminology itself comes from the Greek word; '*hyper*' means raise and '*thermia*' means temperature. It attracted attention in the 1970s for the treatment of cancer and since then it has been investigated as a low risk treatment with very encouraging and promising potential [20].

Hyperthermia aims to destroy cancerous cells by raising the temperature to 41-45°C while preserving healthy tissues (Figure 2.5). The effectiveness of the therapy depends on the exposure time and temperature [19]. This technique can be either performed on its own or in conjunction with established therapy techniques such as chemotherapy and radiotherapy [19, 56]. According to the studies reported by Issels et al. [57] and Kampinga et al. [58] the use of hyperthermia increases the sensitivity of the cells to the uptake of chemical drugs and radiation doses since it increases blood flow.

Exposure to high temperature affects cancerous cells more than healthy cells due to physiological and biological changes [19, 20]. The protein damage in cancer cells starts at 39°C and that can be irreversible. At 41-42°C cancer cells can be inactivated and beyond that, the threshold temperature leading to necrotizing is 45°C. It has been clinically indicated that an applied temperature between 41-43°C, enhances the efficiency of radiotherapy and chemotherapy. The side effects of radiotherapy and chemotherapy may persist even with the adjunctive use of hyperthermia therapy; however, these can be minimized by reducing the dosage of chemotherapeutical drugs and radiation [20, 55].

Cancer cells have poor blood circulation which causes accumulation of lactic acid with a high level of glucose, resulting in low pH [7, 20]. Due to these reasons, cancer cells become more sensitive to high temperature, however, the overexpression of a type of proteins called heat shock proteins (HSPs) in cancer cells creates thermotolerance due to high heat exposure. Exposing the tissue to high temperature (40-44°C) still leads the cells to apoptosis due to disorder in the cell cycle, inadequate nutrients and low pH [20, 53].

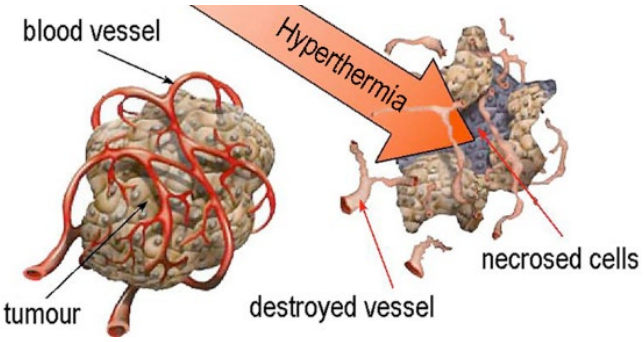

Figure 2.5 Effect of hyperthermia on cancerous cells [59]

2.3.2.1 Hyperthermia Techniques

There are three main application techniques of hyperthermia depending on the location, size and stage of cancer. These techniques are whole-body, regional and local hyperthermia. The external sources of delivering heat to cancerous tissue are microwaves, ultrasound, infrared radiators, radiofrequency energy and other sources as implants, hot water and magnetic materials which will be described in the next sections below [19, 20, 53, 55]. In order to reach a targeted temperature in the tumour site, the specific absorption rate (SAR), a measure of absorption rate by the human body, should be considered to define the exposure time and applied energy by the external sources [19].

Whole Body Hyperthermia (WBH) is the most efficient technique for metastatic cancer that has spread throughout the whole body [53, 56]. It aims to stabilise the temperature in the whole body between 41- 42°C by using different techniques such as radiant WBH and extracorporeal WBH [19, 20]. It is important to monitor the temperature that reaches the target temperature but does not exceed it. Therefore, the temperature of the cancerous tissue site, skin and air are monitored [20]. The heat is provided by thermal conduction techniques using hot water baths, hot water blankets, thermal chambers and radiant heat. In radiant WBH, microwaves radiation, infrared radiation and radiant heat are used.

In extracorporeal WBH, heated blood is circulated throughout the bloodstream in the body. The process can take 3-4 hours depending on the technique. Reaching the target temperature might take 1- 2 hours and that temperature would be maintained for one hour, then it will be cooled down for another hour [20, 53]. WBH has been very promising in making the cancerous cells sensitive to chemotherapy and radiation [19, 20, 53, 56].

Local Hyperthermia is commonly used for superficial, intracavitary, intraluminal and intracranial tumours such as breast cancer, malignant gliomas, head and neck cancers, locally advanced cancers and soft tissue sarcomas [53]. The heat is delivered with microwaves, radiofrequency and ultrasound using superficial applicators or probes such as spiral, waveguide, current sheet, horn or compact applicators [19, 53, 56]. The penetration depth of local hyperthermia is not deeper than 3-4cm and the temperature reaches 42°C - 43°C. There are three techniques to deliver heat depending on the region of cancerous tissue. **The external or superficial** technique is performed for the tumour below the skin using external applicators with high-frequency energy waves. This is a convenient technique for breast cancer and cervical lymph node metastases from head and neck cancer. **Endocavitary or intraluminal** technique is performed by inserting radiative probes into the organs which have natural openings such as vagina, rectum, cervix and urethra. **Interstitial** is similar to endocavitary technique but anaesthesia is applied in order to place the probe into a deeply seated tumour site. This technique can be performed for brain tumours as well [19, 20, 56].

Regional (part-body) Hyperthermia is preferred for deep-seated and locally advanced cancers (not eligible for surgery) such as bladder, cervical, rectal, prostate, soft tissue and ovarian cancers [19, 20, 53]. Depending on the size and location of the cancerous tissue, there are three different techniques to apply regional hyperthermia using external applicators, thermal perfusion and continuous hyperthermic intraperitoneal perfusion (CHPP). The **external applicators** can be named as radiofrequency and microwave which is used to distribute heat to deeply seated cancers [19, 20, 53]. However, it is hard to deliver and sustain the thermal conditions without over-heating the normal surrounding tissue [19]. The limbs and some organs can be heated to the target temperature using **thermal perfusion** technique which is circulating heated blood. CHPP is an alternative technique for curing stomach and peritoneal mesothelioma cancers.

This technique can be applied with chemotherapeutic drugs as well which is then called hyperthermic intraperitoneal chemotherapy (HIPEC). CHPP or HIPEC is performed during the surgery circulating warmed fluid (with or without anticancer drug) through the peritoneal layers increasing the temperature within the region to 41-42°C [19, 20, 53].

2.3.2.2 Side Effects and Limitations of Hyperthermia Treatments

Although the applied temperature is maintained between 41-43°C, the deposition of heat can cause blisters, pain and burnings. Maintaining a homogenous temperature within and around the targeted area stands out as the main limitation of hyperthermia treatment. The distribution of heat to the targeted area is challenging since the heat can harm healthy tissue. Secondly, heat shock proteins (HSPs) can hamper the effectiveness of applied heat to the cancer cells [20, 55].

2.3.3 Magnetic Hyperthermia

Magnetic hyperthermia or magnetic field hyperthermia technique has been a promising solution to address the limitations and side effects of the aforementioned therapy techniques. Considerable attention has been paid to this treatment technique when using magnetic materials [16] such as magnetite [60] and magnetic glass-ceramics [54, 61, 62]. These studies will be described in Section in 2.6.2 and 2.8 respectively. When magnetic materials are subjected to a variable electromagnetic field they generate heat and start acting as thermoseeds depending on their magnetic properties [5].

Using magnetic materials results in more localized heat distribution to the deep-seated cancerous bone tissues while preserving the healthy cells, so that higher temperature (46-48°C) can be applied [19, 20, 55]. The heat generation can be achieved by hysteresis loss and eddy current, which are explained below [55].

Hysteresis loss (Figure 2.6) is achieved by placing the magnetic material inside a conductive coil. It is known that a current flowing through a conductive coil induces a magnetic field. This magnetic field (H, A/m) can be strengthened by increasing the voltage, which in turn increases the magnetic intensity as well as the flux density (B**,** Tesla) of the magnetic material to a maximum saturation point. When the solenoid current is removed, flux density reduces to a point higher than the initial flux of the magnetic material. From this point on, restarting the solenoid current in the opposite direction, repeats the process in the opposite polarity and a loop is formed called the hysteresis loop.

The hysteresis loss is the area of the enclosed loop as seen in Figure 2.6, which is in the form of heat energy. For instance, if the area of the loop is small then the hysteresis loss is small [55].

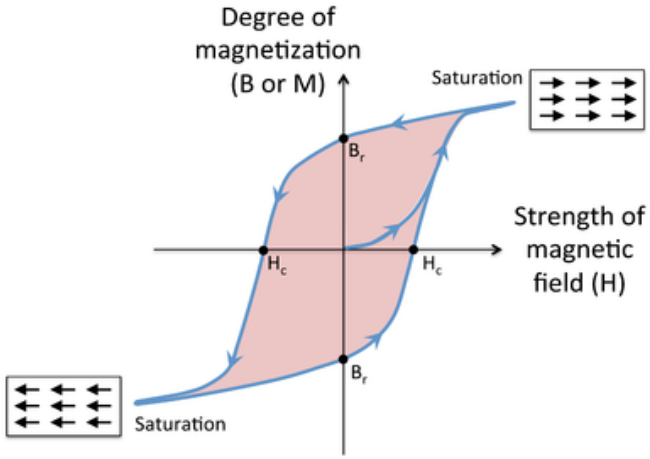

Figure 2.6 shows a standard B-H curve [63]

When a conductive coil is connected to an alternating current, according to Faraday's law, an electromotive force (EMF) is induced inside the material. This interacts with the magnetic flux (B) of the coil and forms eddy currents. The eddy currents cause power loss in the form of heat, which is called eddy current loss [55].The magnetic glass-ceramics have attracted attention due to their heat generation abilities under magnetic field that can kill the cancerous cells. In addition to that some glass-ceramics can enhance bone regeneration after surgery. The properties of glass-ceramics and magnetic glass-ceramics are described in next sections 2.6 and 2.6.2 .

2.4 Glass and Glass-Ceramic

Ceramics are crystalline inorganic materials composed of at least two chemical elements [64, 65]. Glasses are non-crystalline, amorphous structures prepared by the rapid cooling of the melt. Because they do not go through crystallisation, they maintain their amorphous structure [66]. However, glass-ceramics are polycrystalline materials that consist of a mixture of glass and ceramic phases, hence they show both amorphous and crystalline phases. Therefore, glass-ceramics show better mechanical strength compared to the glasses [67]. The difference between glass structure and crystalline structure can be seen in Figure 2.7. While crystals have long range and organised atoms, glasses have the short atomic range and disorganised atoms.

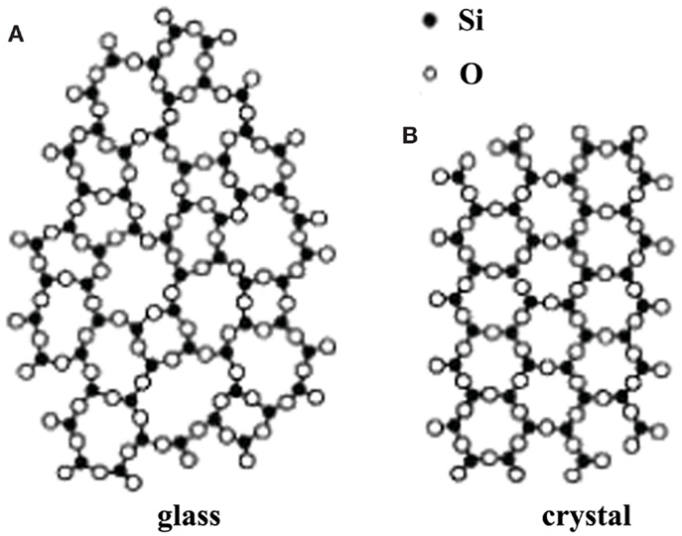

Figure 2.7 Difference between A) amorphous and B) crystalline structure of SiO2 [61]

The specific volume-temperature diagram (Figure 2.8) explains the behaviour of crystalline and amorphous materials during the change in the temperature. Cooling a liquid from high temperature will either form a crystal or supercooled liquid. For crystalline materials during cooling from point A to point B, specific volume decreases dramatically. Decreasing the temperature below the melting temperature (Tm) leads to crystallisation and it causes a sharp decrease in the volume. From point B to point C, the specific volume continues decreasing slowly and the melt solidifies becoming a crystalline material. If the material can be cooled rapidly below the melting point without going through the crystallisation and there are no discontinuous changes in the structure during the cooling, then it becomes a supercooled liquid. During supercooled liquid phase, the change in the specific volume is not sudden as it occurs with crystalline materials. The decrease in the temperature will increase the viscosity gradually and lead to atom movements and rearrangements in the structure.

At further decreases in the temperature, the viscosity is so high that the supercooled liquid will become a solid (Point D). Glass transition range, where on the curve connection between supercooled liquid and glassy state, is defined as transition temperature (Tg). The glass can be characterised by Tg value and it is a very important indicator that shows the temperature where the glass starts showing viscoelastic behaviour [64, 68, 69].

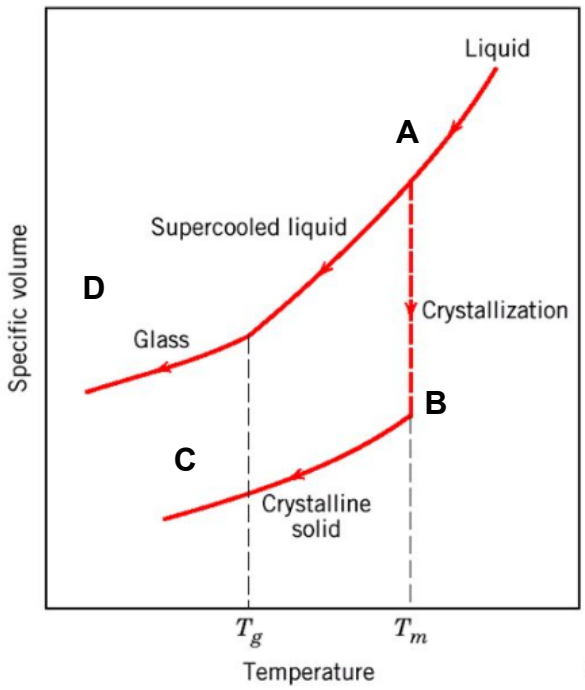

Figure 2.8 Diagram of specific volume-temperature variation for amorphous and crystalline materials [70]

2.5 Formation of Glass-ceramics from Glass

The production of glass-ceramics starts with the production of glass. A scheduled controlled heat treatment process allows the formation of glass-ceramics from a base glass and that allows the glass-ceramics to have different properties over the glass.

The formation of glass-ceramics involves nucleation and crystallisation steps resulting in the crystallisation of the glass. During the nucleation phase, a sufficient number of nuclei is formed when the material is further heated up to crystallisation temperature, the nuclei will grow into crystals within the glass structure [71]. It is crucial to perform a careful and controlled heat treatment to form a sufficient number of small crystals. The number, growth rate and size of crystals can be controlled by the time and temperature of heat treatment and this can alter the properties of the GC [66].

2.6 Bioactive Glasses and Glass-Ceramics

Bioceramic materials have been developed for use in medical and dental applications. Their high biocompatibility features make them primary materials for supporting and/or replacing the hard tissues such as bone and tooth. Bioceramic materials are divided into three groups: bioinert, resorbable and bioactive materials. Whilst bioinert materials (zirconia and alumina) cannot form any chemical bond between the tissue and the implant, bioactive materials (bioactive glasses and glass-ceramics) can provide chemical interactions between the living tissue and the implant, forming an interfacial bonding to the bone that enhances the bone regeneration. Resorbable materials (calcium phosphates) are degradable materials that can be simultaneously replaced by the tissue in a period of time [72].

Bioactivity of a material can vary based on the composition and type of the material and it can have an impact on the formation of interfacial bonding between the implant and host tissue. To evaluate the bioactivity level of the material, the bioactivity index (IB) is used.

$$I_B = 100/t_{0.5bb},$$

In the formula, $t_{0.5bb}$ is the time needed for 50% of the implant surface to form a chemical bond with the bone [73-75]. According to its bioactivity level, the bioactive materials are classified into two groups, class A and class B.

If IB value is greater than 8 the material is defined as osteoproductive. These materials do not only bond to the bone and induce new growth but also help the formation of soft tissues. These type of materials are involved in Class A materials [75].

If IB value is lower than 8 but greater than 0 then the material is defined as osteoconductive. These materials bond to the bone and enhance the bone growth but do not stimulate soft tissue formation [75].

Bioactive glass-ceramics have attracted attention in the medical field since they trigger the chemical reaction that forms a strong interfacial bond to connective tissue and enhances the regeneration and ingrowth of bone [18]. This makes them appropriate and very useful biomaterials not only to replicate natural bone but also to replace the bone tissue while triggering the stem cell growth.

The formation of bonding to the bone is created by hydroxycarbonate apatite layer (HCA) formation on the surface of the bioactive material and as stated in Section 2.1, apatite is found in the mineral phase of the bone. Such similarity creates a strong interfacial bonding. In vitro, a simulated body fluid (SBF) that mimics human blood plasma, is used to test the bioactivity of the materials. After immersion in the SBF solution, the ion exchange and chemical reaction between the fluid and materials induce the formation of HCA layer [72, 75]. Figure 2.9 represents SEM images of the HCA formation on the surface of a bioactive glass-ceramic. The formation and growth of globular apatite crystals can clearly be seen throughout the 28-day immersion in SBF [76]. Such strong bounding between HCA and the glass *in vitro* mimics the interfacial bonding that takes place in the body [72]. Buhner and Lemaitre et al. [77] reported that *in vitro* bioactivity test, which uses SBF, is not convenient to predict interfacial bonding of the material *in vivo*. It is known that, SBF solution only mimics the inorganic part of human blood plasma, therefore, it does not maintain and provide physiological conditions in the human body. Moreover, the solution is lack of proteins and the carbonate content is not controlled. Due to these facts, SBF should be combined with cell experiments for a better evaluation [29].

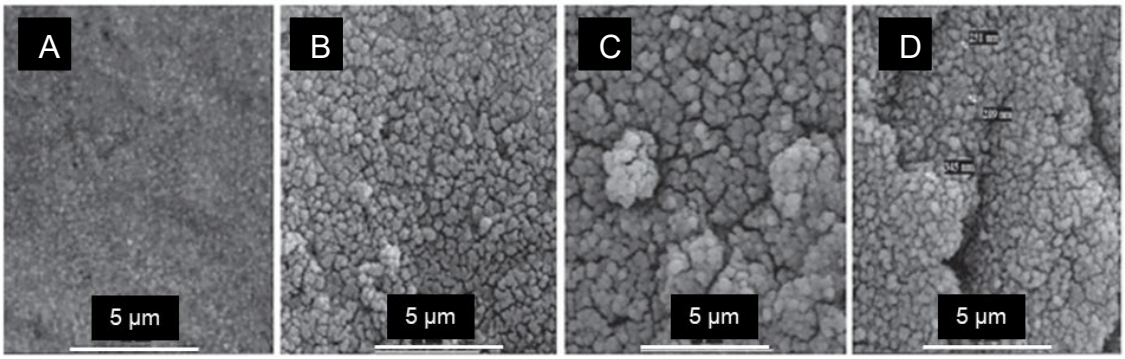

Figure 2.9 SEM images of HCA layer on a bioactive glass-ceramic A) 1-day B) 3-day C) 7-day D) 28-day [76]

In the early 1970s, Larry L. Hench and his colleagues have tried different glass compositions which would bind to the bone [73]. Then, in 1971, Hench et al., published a paper which mentioned the first bioactive glass, Bioglass® (45S5), having a composition of 45% SiO_2, 24.5% CaO, 24.5%Na_2O and 6%P_2O_5 (wt%). The glass is named 45S5 because the composition has 45% SiO_2 and Ca/P ratio is 5:1 in molar ratio and 45S5 Bioglass® is approved by the FDA to be used as a bone graft [66, 72-74]. Examples of other bioglass compositions explored by Hench and his colleagues will be provided in Section 2.6.1.

The main conditions of achieving bioactive glass were determined as having less than 60 mol % SiO_2, high content of CaO and Na_2O and high CaO/P_2O_5 ratio. The phase diagram of Na_2O-CaO-SiO_2 (Figure 2.10) at constant 6 wt % P_2O_5, created by Hench, shows the change in the bioactivity of glass and glass-ceramics depending on the change in the composition [71, 78, 79].

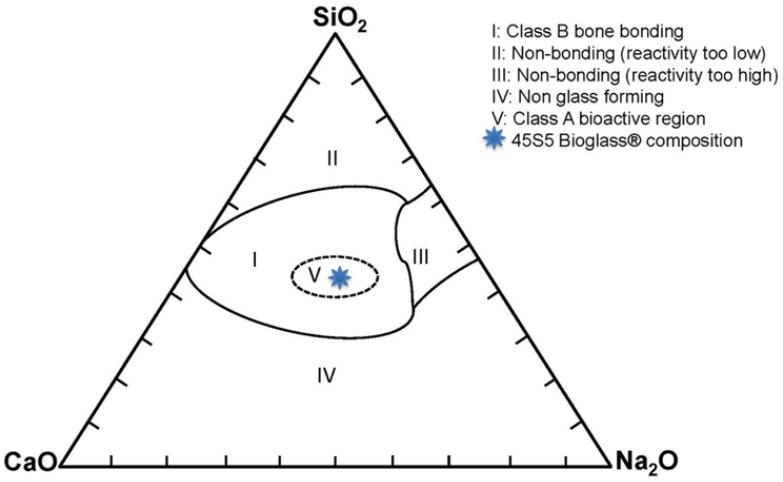

Figure 2.10 Na_2O-CaO-SiO_2 diagram for bioactivity at a constant 6% P_2O_5 (wt %) [79]

According to the diagram, region I represents class B glasses, having compositions between 52 and 60 mol% SiO_2; they show lower bioactivity rate between I_B=2 and I_B=8. Hydroxyapatite is one of the main examples of class B bioactive ceramics. Class A glasses belong to region V which shows the highest bioactivity as I_B=8 and I_B=10. These bioactive glasses are 45S5 Bioglass® and 55S4.3 Bioglass® (see Table 2.3 for the composition). An example of class A glass-ceramic is Cervital®. The composition of some common bioactive glass and glass-ceramics is given in Table 2.3. The bioactive materials in this class not only enhance the osteoconductivity (enhancing bone formation) but also promote osteoinductivity (enhancing transformation of undifferentiated cells to osteoblast cells). Region II represents bioinert materials since increasing the content of SiO_2 decreases the reactivity of the glass. Region III represents resorbable bioactive materials and they degrade within a few days. Region IV type biomaterials are not forming glass structure [71, 75, 78, 79].

2.6.1 Commercial Bioactive Ceramics

Bioactive glasses have low strength to be used in load-bearing applications. This issue leads to producing glass-ceramics (GC). The bioactive glass-ceramics have been widely used in orthopaedic load-bearing applications due to their high mechanical strength. The composition of the bioactive glasses and glass-ceramics can be tailored or modified for required uses. The compositions of the most common bioactive glasses and glass-ceramics are given in Table 2.3. Bioceramics such as Ceravital® (glass-ceramics), Dicor® (glass-ceramics), Bioverit® (glass-ceramics) and Cerabone® A-W (glass-ceramics) and bioglasses such as 45S5, 45S5,4F and 55S4.3 have been in the market since 1985 [80-83].

Table 2.3 Composition of the most common commercial bioactive glass and glass-ceramics (in wt %) [78, 82, 84, 85]

Composition(wt%)	45S5	45S5.4F	55S4.3	Ceravital®	Dicor®	Bioverit®	A/W®
SiO_2	45	45	55	46.2	61.9	38.7	34
CaO	24.5	14.7	19.5	20.2	3.92	-	44.7
Na_2O	24.5	24.5	19.5	4.8	-	10.4	-
P_2O_5	6	6	6	-	-	8.2	16.2
CaF_2	-	9.8	-	-	-	-	0.5
$Ca(PO_3)_2$	-	-	-	25.5	-	-	-
MgO	-	-	-	2.9	15.5	27.7	4.6
K_2O	-	-	-	0.4	15.4	6.8	-
Al_2O_3	-	-	-	-	0.6	1.4	-
MgF	-	-	-	-	-	4.9	-
TiO_2	-	-	-	-	-	1.9	-

The mechanical properties of Bioglass®, Cerabone A-W®, Bioverit® and Ceravital® are provided in Table 2.4 along with the properties of bone. The table shows that bending strength, fracture toughness and Vickers hardness of commercial Bioglass® is lower than cortical bone, whilst glass-ceramics are either above or within the range. Therefore, Bioglass® is mostly used in non-load bearing applications. Bioglass has good biological properties such as biocompatibility and bioactivity but its poor mechanical properties lead to development of composite materials to provide better mechanical properties that can be used in load-bearing applications. These biomaterials are commonly used for dental implants, eye lenses, cranial repairs and orthopaedic applications [86]. Moreover, they also can be used in drug delivery systems, cell separations, coatings on the prostheses, compositions of scaffolds and magnetic hyperthermia treatment of cancer [87-89].

Table 2.4 Comparison between mechanical properties of bone, commercial bioactive glass and glass-ceramics (adapted from [90-92])

Materials	**Vickers Hardness (MPa)**	**Bending Strength (MPa)**	**Fracture toughness (MPa)**	**Young's Modulus (GPa)**
Cortical Bone	60-75	50-150	2-12	7-30
Concellous Bone	40-60	10-20	0.1	0.05-0.5
Bioglass® 45S5	4.58±9.4	40-42	0.6	35
Cerabone® A/W	680	215	2.0	118
Bioverit®	500	100-160	0.5-1.0	70-88
Ceravital®	294	100-130	4.6	100-159

2.6.2 Bioactive magnetic glass-ceramics

Magnetic glass ceramics (MGCs) provide two major advantages for hyperthermia treatment of bone cancer. Firstly, they are bioactive thus, they create a strong bond to the bone by forming an apatite-like layer on the surface and promote bone growth. Secondly, when they are subjected to a variable electromagnetic field they generate heat due to their magnetic properties and start acting as thermoseeds [5]. It is expected that these features will provide better results in the treatment of bone cancer via magnetic hyperthermia technique. The effect of high temperature on cancer cells and magnetic hyperthermia technique was discussed in Section 2.3.2 and 2.3.3. Different compositions of magnetic glass-ceramics and their magnetic properties have been reported in the literature.

The first bioactive magnetic glass ceramic, $40Fe_2O_3$-$29CaO$-$31SiO_2$-$3B_2O_3$-$3P_2O_5$ (wt%), was synthesised by Kokubo et al. [93] to treat musculoskeletal tumours. This magnetic glass ceramic (MGC), containing 36 wt% magnetite, had 32 $A.m^2/kg$ of saturation magnetisation and 10 kA/m of coercive force. Moreover, in vivo study showed that outer cortex of a rabbit's tibia was heated to 43°C in 5 minutes under a magnetic field of 24 kA/m and 100 kHz frequency. The result of the study showed that the thermoseed behaviour of the magnetic glass ceramic was efficient for the hyperthermic treatment of cancer [93].

Bretcanu et al. [61] synthesised a magnetic glass-ceramic, $24.7SiO_2$-$13.5Na_2O$-$13.5CaO$-$3.3P_2O_5$-$14FeO$-$31Fe_2O_3$ (wt%), which provided a unique crystalline phase. The composition had 45 wt% magnetite, thereby, it was named S45. The generated saturation magnetization was 34 $A.m^2/kg$ and coercive force was 6.8 kA/m. Bioactivity tests showed apatite-like layer formation on the surface after soaking for 2 weeks in a simulated body fluid (SBF).

In order to evaluate the effect on magnetic properties depending upon the crystallographic structure and microstructure of the system SiO_2-Na_2O-CaO-P_2O_5-FeO-Fe_2O_3. Bretcanu et al. [6] prepared a different composition of MGCs having 35% of magnetite (wt%), that was named S35. The effect of magnetite amount on the magnetic properties was analysed using two MGCs, S35 and S45. Characterisation tests showed that S35 had a smaller amount of iron oxides and smaller crystal sizes than S45. However, S45 had a higher amount of crystallized magnetite resulting in higher saturation magnetisation. S35 had 65W/g and S45 had 25W/g power loss under 40kA/m magnetic field and 440 kHz frequency. The quantity of iron ions had a significant impact on the structure and the characteristics of the hysteresis cycle [6].

Table 2.5 Compositions of S35 and S45 magnetic glass ceramics [6]

Composition (wt%)						
Glass	**SiO_2**	**Na_2O**	**CaO**	**P_2O_5**	**FeO**	**Fe_2O_3**
S35	29.3	15.9	15.9	3.9	10.9	24.1
S45	24.7	13.5	13.5	3.3	14.0	31.0

Ebisawa et al. [62] synthesised a magnetic glass ceramic in the system of 40Fe_2O_3-32CaO-31SiO_2-3P_20_5 (wt%) containing 36wt% magnetite, which was named CSFe+P. However, the bioactivity test results demonstrated that there wasn't any apatite-like layer formation. Therefore, 3B_2O_3 (wt%) was included in the composition and named CSFe+BP. According to the in vivo and in vitro bioactivity tests this CSFe+BP showed high bioactivity properties forming an apatite-like layer and bonding to the bone. Furthermore, when the MGC was exposed to a magnetic field, the saturation magnetisation was 32 $A.m^2/kg$ and the coercive force was 10 kA/m.

Table 2.6 Compositions of CS+FeP and CS+FeBP MGCs [62]

	Composition (wt%)				
Glass	**CaO**	**SiO_2**	**Fe_2O_3**	**B_2O_3**	**P_2O_5**
CSFe + P	32.0	31.0	40	0.0	3.0
CSFe + BP	29.0	31.0	40	3.0	3.0

Synthesis of $35SiO_2$-$25CaO$-$5P_2O_5$-$9MnO$-$10Li_2O$-$16Fe_2O_3$ (wt%) magnetic glass-ceramic, which was named as 10LFS, was performed and characterized by Wang et al. Regarding the results of magnetic field application at 80 kA/m, the glass-ceramic showed 0.01 $A.m^2/kg$ saturation magnetism with 4 kA/m coercive force [94].

Recently, a composition of $45CaO$-$33SiO_2$–$16P_2O_5$-$4.5MgO$-$0.5CaF_2$ (wt%) containing 25% graphite-modified Fe_3O_4 magnetic glass ceramic (BFC) was synthesised by Zhao et al. The composition showed 10.6 Am^2/kg saturation magnetism when it was exposed to 1600 kA/m magnetic field. In order to analyse the temperature rise in the sample, an alternating magnetic field of 1.9 kA/m and 252 kHz was applied. The temperature increase was 20°C after 20 seconds of magnetic field exposure. Power loss was determined as 8.4 W/g. According to in vitro bioactivity test, formation of apatite layer was observed after 5 days of immersion in SBF [95].

Table 2.7 Compositions of the synthesised magnetic glass-ceramics

	Composition (wt%)											
Material	**CaO**	**SiO_2**	**FeO**	**Na_2O**	**P_2O_5**	**Fe_2O_3**	**B_2O_3**	**MgO**	**CaF_2**	**Li_2O**	**MnO_2**	**References**
MGC by Kokubo	29.0	31.0	-	-	3.0	40.0	3.0	-	-	-	-	[93]
10LFS	25.0	35.2	-	-	5.0	16.0	-	-	-	10.0	9.0	[94]
CSFe+P	32.0	31.0	-	-	3.0	40.0	-	-	-	-	-	[62]
CSFe+BP	29.0	31.0	-	-	3.0	40.0	3.0	-	-	-	-	
S35	15.9	29.3	10.9	15.9	3.9	24.1	-	-	-	-	-	[61]
S45	13.5	24.7	14.0	13.5	3.3	31.0	-	-	-	-	-	
BFC	45.0	33.0	-	-	16.0	-	-	4.5	0.5	-	-	[95]

According to the aforementioned studies, magnetic glass-ceramics can be sufficiently used to treat bone cancer and to reinforce apatite-like layer growth. These glass-ceramics can be added into bone cements as fillers. This can be advantageous since the bone cements are widely used for orthopaedic applications. The acrylic bone cement, polymethyl methacrylate (PMMA), is the most used cement for the orthopaedic surgeries, however, this cement does not show any tendency to create an attachment to the bone tissue. Therefore, the magnetic glass-ceramic containing PMMA bone cements can have the ability to enhance bone formation supporting prosthesis and filling the cavities in the bone and to generate heat under magnetic field. PMMA bone cement and magnetic glass-ceramic containing PMMA bone cement will be extensively explained in the following sections 2.7 and 2.8.

2.7 Polymethyl Methacrylate Bone Cement

A standard definition of cement is “a binding element or agent such as a substance to make objects adhere to each other” [96]. Cement is not only used in civil engineering but also used in modern medicine, whilst sharing a common purpose and elements.

Bone cement has been used in medical applications for more than 50 years. There are two common types of bone cement used in medical applications, calcium phosphate cement (CPC) and polymethyl methacrylate (PMMA) cements. CPCs are mixtures of one or more calcium phosphate (CPs) powders with water or aqueous solutions that can set at room or body temperature. CPCs can easily be moulded or injected into irregular cavities of the bone tissue, restoring the structure and functions of the bone, and stimulating new bone formation. Due to their similarity with biological hydroxyapatite (HA), the mineral phase of natural bones and teeth, CPCs have been found in several applications as fillers for bone fractures or bone defects, craniomaxillofacial, dental and orthopaedic applications. However, CPCs are brittle and due to that reason their inferior low mechanical properties limit their use in load-bearing applications [97]. Maintaining suitable mechanical properties to support the bone is essential for orthopaedic applications and this reason leads to the use of PMMA bone cement widely. PMMA bone cement is a crucial material for orthopaedic and dental surgeries due to its valuable mechanical properties and biocompatibility. PMMA cements are described as self-curing acrylic bone cements that undergo an exothermic reaction when the powder and liquid components are mixed. It has been successfully utilised for stabilising and anchoring prostheses (see Figure 2.11) and as well as filling voids and vertebral fractures [98].

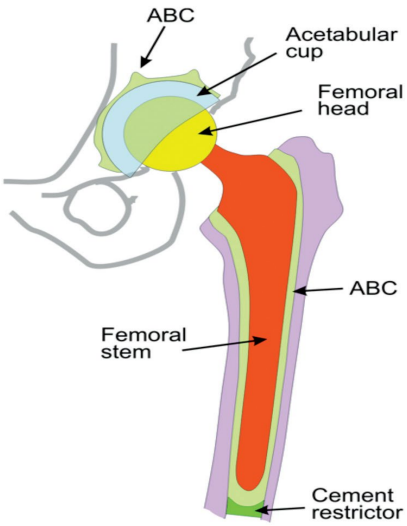

Figure 2.11 Schematic image of cemented femoral stem implantation in hip arthroplasty (ABC=acrylic bone cement, [98])

PMMA cement does not adhere to the bone when it is used with prostheses but it acts as a grout that fills the space between the prosthesis and the bone (Figure 2.11). It creates an interlock between the bone and the prostheses that helps to distribute optimal stress and provide a buffer effect for the excessive force to the bone [99]. Consequently, it protects the bone against high local stresses and transfers load evenly from the prostheses to the bone. For such load-bearing applications, the mechanical properties of the cement have become significant. In addition to the many valuable properties of the cement, it is mouldable and can be readily formed into specific shapes [100].

Although PMMA bone cement is the most widely used type of cement, its biological and mechanical properties have a significant influence on long-term orthopaedic applications [101]. The medical applications that the cement is widely used are vertebral, orthopaedic and dental applications and also drug delivery. [102] Moreover, there are on-going studies to treat bone tumour using PMMA bone cement containing magnetic particles. It has been found that magnetic bone cement can kill the cancer cells via applied electromagnetic fields [60]. The magnetic PMMA bone cement studies will be explained in Section 2.8.

PMMA bone cement is prepared by mixing the liquid and the powder components which are shown in Table 2.8 [18, 100]. The ratio between the powder and liquid is mostly 2:1 (g/ml). The powder component contains a polymer, PMMA, and an initiator which is benzoyl peroxide (BPO) [14].

A radiopacifier, which can be either barium sulphate ($BaSO_4$) or zirconium dioxide (ZrO_2) is included into the powder component as a contrast agent in order to make the cement radiopaque, so it becomes visible under X-Ray [14]. $BaSO_4$ usually tends to cluster in the mass of cement, which might cause the mechanical properties of the cement to weaken. Studies showed that ZrO_2 does not cause clustering in the cement and provides better contrast under X-ray [103]. The liquid component contains a monomer, methyl methacrylate (MMA) and an activator, N, N-dimethyl-p-toluidine (DMPT) to accelerate the speed of the reaction. Additionally, to prevent the self-curing (auto-polymerisation) of the composition when it is exposed to light or high temperatures during the storage, a stabiliser, hydroquinone is included in the liquid component [18, 104]. Through the mixing procedure hydroquinone is inhibited, and the reaction can start [103, 105, 106].

Table 2.8 Components of PMMA Bone Cement [100]

Powder	Liquid
Polymer – polymethyl methacrylate, PMMA	**Monomer**–methyl metharyclic, MMA
Radiaopacifier-barium sulphate or zirconium dioxide ($BaSO_4$ or ZrO_2)	**Activator** - N,N-dimethyl-p-toulidine (DMPT)
Initiator- benzoyl peroxide (BPO)	**Stabilizer**-hydroquinone
Antibiotics[a]**-** **(**e.g. gentamycine)	**Antibiotics**[a]**-** **(**e.g. gentamycine)
Colorant[b] (e.g. chlorophyll)	**Colorant**[b] (e.g. chlorophyll)

[a] Antibiotics can be either added in powder component or in liquid.

[b] Colorant can either be in powder or in the liquid component

A colourant can be added into the liquid and/or powder component to make the cement more visible and differentiate it from the bone. Chlorophyll is one of the examples of the colourants which gives a green colour to the cement [107]. Additionally, antibiotics can be added either into the powder or liquid components or can be found in both components. This helps to treat bacterial infections that might occur around the implant. The composition of some of the commercial PMMA bone cements is provided in Table 2.9.

Table 2.9 The commercially available PMMA bone cements

	Simplex P [105] [108]	**Palacos R** [105, 109] [108]	**Palacos MV** [110]	**Palacos LV** [111]	**CMW1** [105]	**Cemex XL** [108]	**Cemex RX** [108]
Powder Component	**40.00**	**40.00**	**40.0**	**40.00**	**39.99**	**50.00**	**40.00**
PMMA (wt%)	88.50	84.5	86.00	84.00	88.84	85.00	88.27
BPO (wt%)	1.50	0.75	0.9	1.00	2.05	3.00	2.73
BaSO4 (wt%)	10.00	-	-	-	9.10	12.00	9.00
ZrO2 (wt%)	-	15.00	12.00	15.00	-	-	-
Liquid Component	**20 .00**	**20.00**	**20**	**20.00**	**18.37**	**18.33**	**13.30**
MMA (wt%)	97.50	92.00	92.00	92.00	99.18	98.20	99.10
DMPT (wt%)	2.50	2.00	2.00	2.00	0.82	1.80	0.90
Hydroquinone (ppm)	80.00	60.00	60.00	60.00	25.00	75.00	75.00
Viscosity	Medium	High	Medium	Low	High	Low	Medium

*Viscosity will be extensively explained in Section 2.7.2.1

2.7.1 Polymerisation of PMMA bone cement

PMMA bone cement is formed by a polymerisation reaction (addition polymerisation) between powder and liquid components. The chemical structures of MMA and PMMA are given in Figure 2.12.

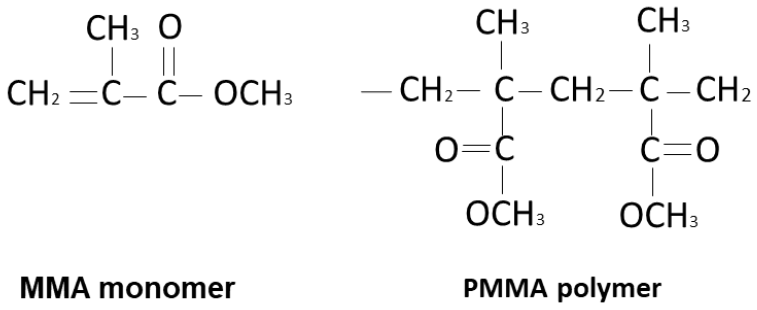

Figure 2.12: Chemical structure of MMA and PMMA [112]

There are three stages in the polymerisation process; initiation, propagation and termination stages. **Initiation stage** starts with the formation of a free radical group as a consequence of the reduction and oxidation reaction between BPO and DMPT. By this reaction, BPO is decomposed by DMPT into a benzoyl radical group. This radical group then reacts with MMA monomer (Figure 2.13), which is then called initiation stage [18, 100, 107, 112]. **Propagation stage** is typically the growth of the chain. Newly formed free radical groups attach to the carbon double bonds (C=C) of another monomer and create long chains, shown in Figure 2.14. The addition of each new chain releases energy which is approximately 57kJ/mol of MMA. Therefore, the polymerisation reaction is an exothermic reaction, which typically reaches 86-100°C in air (dry environment) [18, 100, 107, 112]. It has been reported that polymerisation reaction of PMMA cement reached 40°C when the cement was in saline solution (wet environment) at room temperature. In addition to that, polymerisation reaction was delayed for 5 minutes when the cement was in the solution [113].The exothermic reaction and temperature of PMMA cement is not only affected by the environment but also surface to volume ratio of the cement has an influence. The exothermic reaction temperature increases with the increase in thickness of PMMA cement. Therefore, the layer of cement was limited as 3-5 mm depending on the interdigitating of cancellous bone [99], although defect size may vary. **Termination stage** (Figure 2.15) is described as when the reaction stops since the free radical groups attach to the last monomers and there is no unpaired electron left, hence a new free radical group cannot be formed [18, 107].

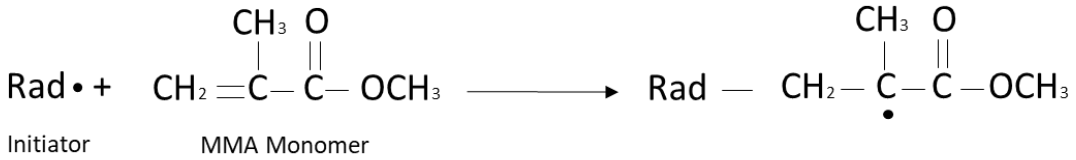

Figure 2.13 Initiation stage of polymerisation reaction [99, 114]

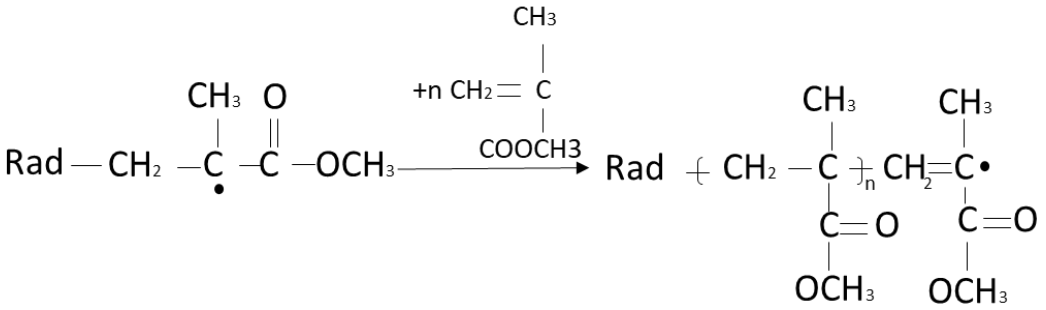

Figure 2.14 Propagation stage of polymerisation reaction [99, 114]

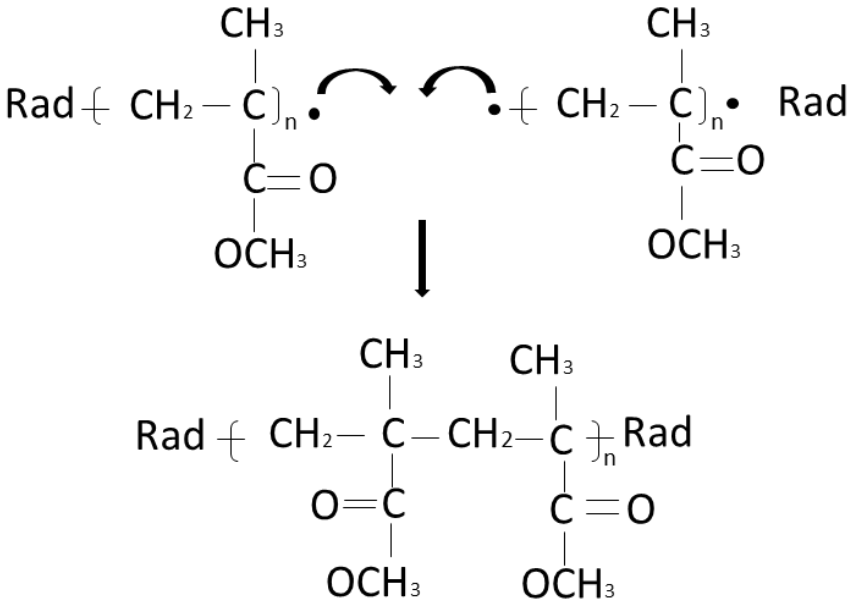

Figure 2.15 Termination stage polymerisation reaction [99, 114]

The rapid chain growth continues with the free radical attaching MMA monomers until reaching 100,000 to 1,000,000 molecular weights of PMMA polymer. In this stage heat generation and viscosity increase but mobility of MMA monomer decreases. When the last radical groups attached to the last monomers and electrons are paired the reaction terminates [99]. However, BPO content in PMMA powder has an impact on termination rate. Increasing the initiator (BPO) content level in PMMA decreases the polymerisation time and termination rate, which results in lower the molecular weight. It should be noted that molecular weight influences properties of polymers, therefore, measuring molecular weight of PMMA is important. It can be determine using gel permeation chromatography technique.

Molecular weight of the polymerised cement highly depends on the molecular weight of PMMA beads and MMA, concentration of initiator, sterilisation technique and presence of stabiliser. It has an influence on properties of the cement such as swelling of PMMA powders, viscosity of dough, waiting time and mechanical properties of cured cement [100, 115]. It was reported that lower molecular weight PMMA cement had lower mechanical properties compared to high molecular weight PMMA cement [116].

2.7.2 Properties of Bone Cement

PMMA bone cement is a bioinert material and therefore, it does not form any chemical interaction with the bone. In contrast, its mechanical properties attracted attention and thus, it is the most widely used bone cement in the medical applications. However, there are some factors that can alter their mechanical and biological properties. The properties of the cement and the factors will be described in this section.

2.7.2.1 The Setting Mechanism

The cold-curing (auto-polymerisation) process is divided into four groups; Mixing, waiting (dough), working and hardening (setting) time (Figure 2.16). The definition and the properties of each phase are explained below.

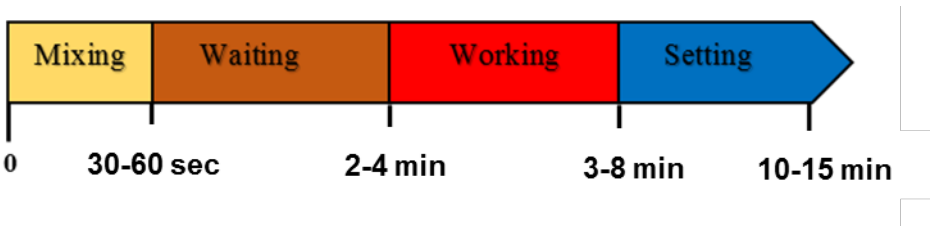

Figure 2.16 Time scale of the curing phases of typical PMMA cements

Mixing time is defined as the integration of powder and liquid until a homogenous mixture is obtained. MMA starts to dissolve the powder and releases BPO which initiates the reaction. In this stage, powder and liquid should not be mixed aggressively as this increases porosity and this affects the mechanical properties of the cement. Mixing time varies between 30 seconds and one minute [14, 117].

Waiting time/ dough time starts from the beginning of the mixing phase and terminates when the paste can be touched by a gloved finger without sticking. The time of this phase lasts for 2-4 minutes at ambient temperature (18-22°C) and relative humidity between 40 and 60%. The viscosity of the cement and as well as room temperature and humidity can shorten or lengthen the waiting time. If the cement is intended to be injected, it should be poured into a syringe or injection gun at the end of the mixing phase, before the start of the waiting phase [14, 117].

Working time is the period that cement can be injected/placed into the cavity of the bone. This phase lasts approximately 3-8 minutes depending on the viscosity, ambient temperature and humidity. It is important that the implantation of the cement is completed before the working period ends [14, 117].

Setting time is the phase when cement hardens and become a solid structure. During this phase, volumetric and thermal shrinkage takes place in the cement (Shrinkage will be explained in Section 2.7.2.2). Setting time usually takes 10-15 minutes [14, 117]. The time scale should be carefully followed as a few minutes could affect the workability of cement. Any delay in waiting and working time will make the cement stiff and hardened, hence, the surgeon will not be able to inject or place the cement into the body [14, 117].

According to ISO 5833:2002 [118], the setting time (tset) starts from the beginning of the mixing phase until the cement reaches the setting temperature (Tset) and the Tset is calculated through Equation 2-1,

$$Tset = \frac{Tmax+Tamb}{2} \qquad \text{Equation (2-1)}$$

where Tmax is the maximum temperature that the reaction reaches and Tamb is the ambient temperature. Tset defines the setting temperature [118]. The curve below (Figure 2.17) shows the exothermic polymerisation reaction of the cement where Tmax and Tset can be determined.

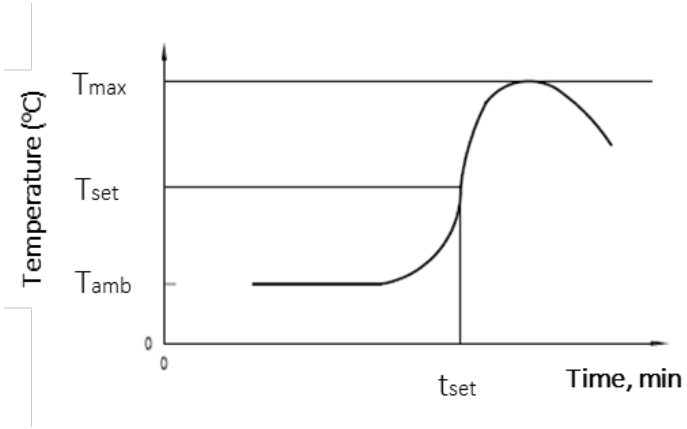

Figure 2.17 Shows determination of maximum temperature and setting time according to ISO 5833-2002 [118]

The length of each phase has an important effect on handling and placing/injecting the cement into the patient's bone. If the waiting time is too long, then the surgeon will have to wait until it gets workable, but this is usually undesirable as the conditions during the surgery can get severe while the wound is open. In contrast, dough stage (working time) should be long enough to be able to handle the cement and place into the wound in time.

All commercial bone cement companies are required to provide the time scale of the phases depending on the ambient temperature in surgery rooms. This information must be strictly followed by the surgeon and/or practitioner since any delay during the operation or exceeding the time phases can cause complications in the body, as the cement will become stiff and hardened. Due to this reason, the cement will not be workable anymore as it affects the handling process and the surgeon will not be able to inject or place the cement into the body. A few minutes or even seconds is important during the handling process. Therefore, practise and knowledge by the user, who is mostly a surgeon and/or a practitioner, is highly recommended before using it during surgery. It is recommended to have two cement kits in case of any complication during the mixing or handling the cement.

The factors that affect the setting mechanism are explained below;

Mixing speed: Rapid and aggressive mixing can lengthen the dough time, resulting in increased porosity and poor mechanical strength [99].

Room Temperature: Dough and setting times decrease with increasing room temperature, whereas in low temperatures both the dough and setting time are longer [119, 120]. The effect of temperature on the time profile of cement can be seen in Figure 2.18.

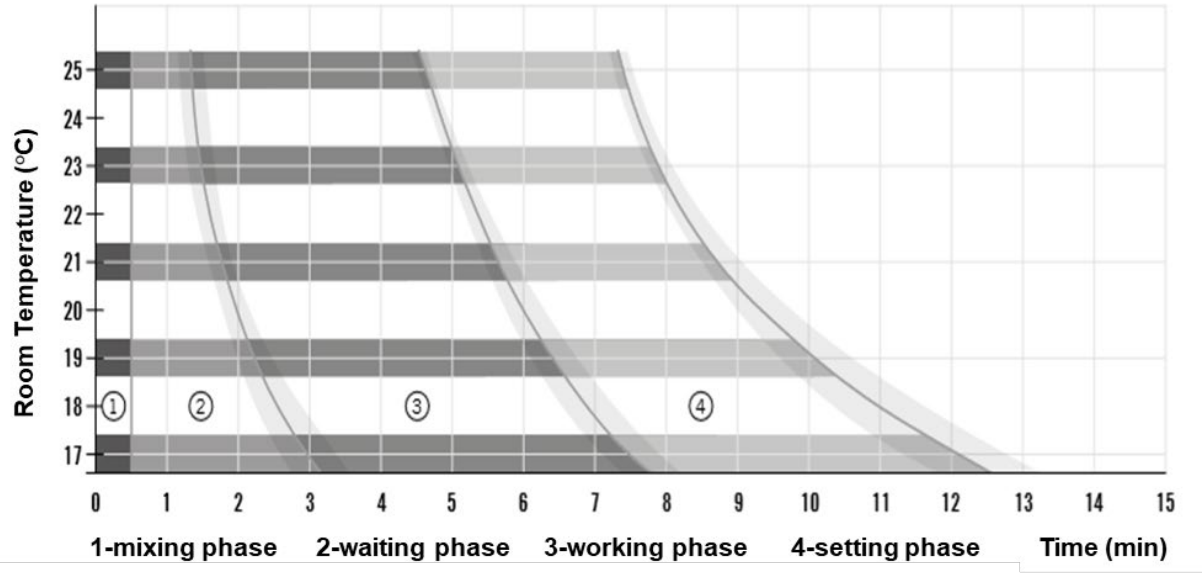

Figure 2.18 Effect of room temperature on the phases of Palacos® MV (medium viscosity) bone cement [110]

Humidity: Setting time increases proportionally to humidity. In order to reduce the variations in setting time, humidity should be controlled at 50±10% [119].

Viscosity: There are three types of cement viscosities defined as low, medium and high. The liquid to powder ratio (LPR) determines the viscosity of the cement. As the ratio goes from low to high, the waiting and setting time get shorter [14, 121]. Low viscosity cements have longer waiting time, shorter working time since it sustains the sticky phase longer than medium and high viscosity cements. Medium viscosity bone cements have properties of both low and high viscosity cements. Curing starts in a low viscosity condition during the mixing phase and the viscosity gradually increases during the waiting time [9, 100]. High viscosity bone cements have a very short waiting and setting time. The cement will be doughy immediately and ready to be applied. It is crucial to determine the end of the working time before it becomes unworkable.

This is advantageous to the surgeon as it identifies longer working times [100, 122]. Working time for high viscosity cement needs to be closely monitored; it is not always easy to determine the end of the working time when it gets too rigid to interdigitate with the bone. The influence of viscosity of PMMA bone cement (i.e. Palacos® bone cement) on mixing, waiting, working and setting time is shown in Table 2.10. The viscosity of the cement is important to provide a longer time to allow injecting the cement into cavities. It should also have a shorter setting time to prevent any inclusion of blood into the cement, which decreases the durability of the cement [14, 121].

Table 2.10 Setting properties of Palacos® LV (low viscosity), MV (medium viscosity) and R (high viscosity, HV) bone cements at 22°C (The data presents approximated times)

Viscosity	Mixing Time	Waiting Time	Working Time	Setting Time
Palacos® LV	30 s	5 min	7 min	10 min
Palacos® MV	30 s	1.5 min	5.5 min	8 min
Palacos® R (HV)	30 s	50 s	4.5 min	7.5 min

2.7.2.2 Shrinkage

Shrinkage is described as a reduction in the volume of material. During the polymerisation reaction, volumetric shrinkage occurs in the cement and at the end of the curing, volumetric shrinkage is accompanied by thermal shrinkage when the cement has gained its mechanical properties. The volumetric shrinkage can vary between ranges of 2% - 7% [123, 124]. Volumetric shrinkage is presented as a change of volume in converting monomer to the polymer during the formation process [125]. It is reported that shrinkage is mostly related to the residual monomer level after curing. It is reported that mixing time, the ratio between BPO and DmpT and powder to liquid ratio have a major effect on shrinkage [126]. Thermal shrinkage occurs due to the exothermic reaction at the end of the curing phase when the cement has gained its mechanical properties [126, 127].

PMMA bone cement is injected or placed between bone and prosthesis and the exothermic reaction takes place in the body. Consequential drop in temperature due to the temperature differences between metal, bone and cement leads to the shrinkage that will result in loosening in the interface of cement and prosthesis [128, 129].

Polymerisation shrinkage can also develop porosity due to the solidification process from liquid to solid. Contribution to porosity and shrinkage decreases mechanical properties, bending strength and fatigue life. Residual stress in the bone is an induced consequence of shrinkage in the cement, which can cause microcracks in the cement resulting in failure of the prosthesis [126]. In order to achieve good clinical outcomes, the characteristics and dimensional stability of the cement should be considered. Minimizing potential shrinkage in the structure is an important factor to maintain the desired mechanical properties of the cement.

2.7.2.3 Porosity

Porosity can be described as a fraction of empty spaces within the solid mass/volume. One of the complications in the bone cement is porosity due to mixing technique, mixing speed, trapped air and shrinkage [130]. Air interaction while mixing the cement and transferring the cement into the gun can increase the porosity in the cement structure [131]. Thus, vacuum mixing reduces the porosity by 40% since it prevents air interaction. On the contrary, hand mixing has the highest possibility of leading to a more porous structure. Lewis et al [132]., reported that the average porosity of manually mixed Simplex® P was between 9.4% and 12.5%. However, when it was mixed with vacuum mixing technique the average porosity was between 0.5% and 6.5%.

High porosity in the structure reduces mechanical strength and fatigue life. In addition to this, excessive porosity in the structure can also induce shrinkage and initiation of microcracks. This results in decreasing fracture toughness. Reducing the porosity may prevent the risk of revision in joint replacement surgery [123, 131, 133].

2.7.3 Mechanical Properties

Mechanical properties of bone cements are important in load-bearing applications over the lifetime of the patient [60]. It is expected that the cement transfers the load evenly from the implant to the bone. As was previously mentioned, the composition of bone cement, mixing technique and additives may influence mechanical properties of PMMA bone cement [107]. Therefore, mechanical properties of bone cements must be tested under established test requirements of ISO and ASTM standards which are also requested by the FDA [107, 134]. ISO 5833-2002 standard [118] and ASTM F451-16 (Standard Specifications for Acrylic Bone Cement) [135] should be followed to ensure that mechanical properties of PMMA bone cement are eligible to be used in human body for a long term treatment.

The standards define the requirements of compressive strength, bending strength and bending modulus for PMMA bone cements and the tests are performed 24±2 hours after the mixing starts. According to the report provided by the FDA, compressive strength can be determined using either ISO 5833:2002 or ASTM 451-16 since both standards specify the same conditions. The minimum requirement of compressive strength of PMMA bone cement is 70 MPa and the test sample dimensions are determined as 6±0.1 mm in diameter and 12±0.1 mm height. Regarding ISO 5833:2002 specifications, the test machine should be at least 4 kN with a crosshead speed between 19,8 mm/min and 25,6mm/min; however, ASTM 451-16 do not specify minimum load cell. The requirement of a deformation crosshead speed is between 20 mm/min and 25,4mm/min. Schematic diagram of compression test is provided in *Figure 2.19*.

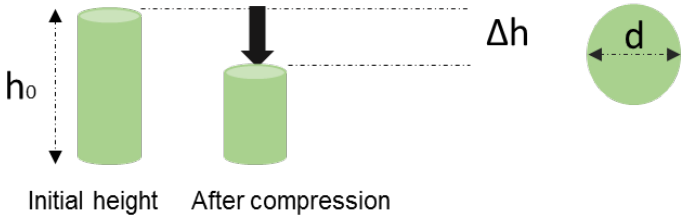

Figure 2.19 Schematic diagram of compression test (h0 refers to initial height, F is the applied force, d is diameter, ∆h is the difference between initial height and the height after compression)

The standards provide a typical load-displacement curve of PMMA bone cement sample (Figure 2.20) and the test is stopped when the sample fractures or ultimate load has been passed.

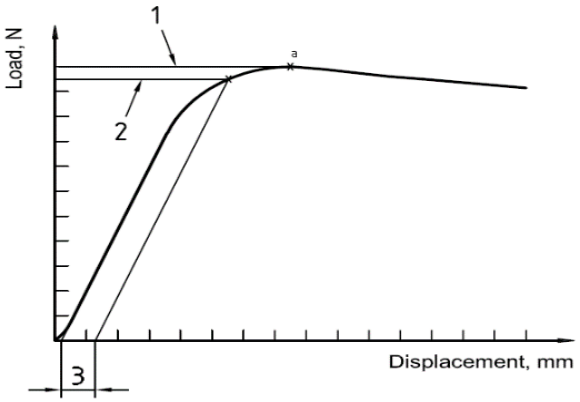

Figure 2.20 Typical load-displacement curve, 1- ultimate load, 2- yield load, 3- 2% offset line and a defines upper yield point (standard ISO 5833:2002)

Compressive strength is calculated for each sample by dividing applied force to cross-sectional area (mm^2), as shown in Equation 2-2. The force should be recorded at the point of fracture, upper yield point or 2% offset line, whichever occurs first.

$$\sigma = \frac{F}{A_0} \qquad \textit{Equation 2-2}$$

Where σ is stress, F is applied force, A_0 is the initial cross-sectional area of the sample.

Determination of bending strength and modulus is specified in IS0 5833:2002 standard, which requires four-point bending test. The standard indicates that samples should be 75±0.1 x 10±0.1 x 3.3±0.1 mm. PMMA bone cement should have a minimum bending strength of 50MPa and a minimum bending modulus of 1800 MPa using a 5mm/min crosshead speed. A schematic diagram of four-point bending test set-up is shown in Figure 2.21. Bending modulus and bending strength are calculated as described in Equation 2-3 and Equation 2-4

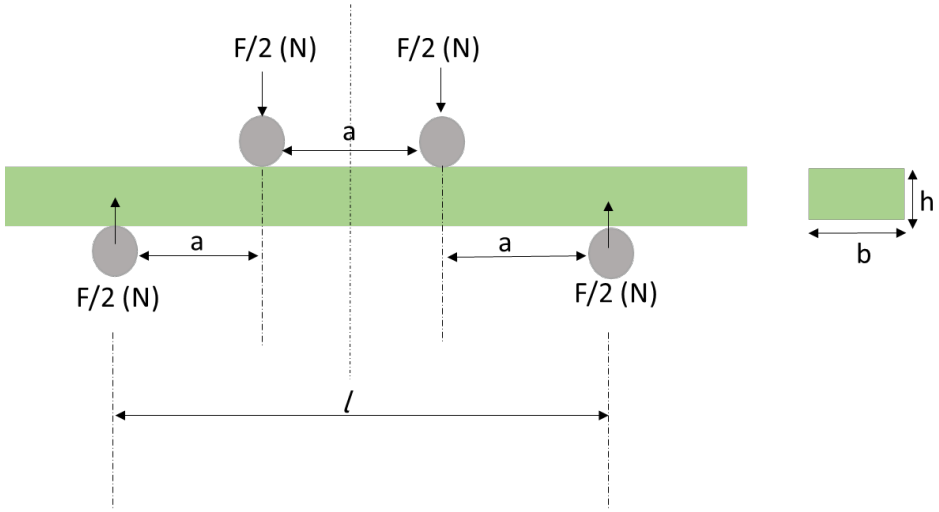

Figure 2.21 Schematic diagram of the four-point bending test set-up of ISO 5833-2002

$$E = \frac{\triangle F a}{4 f b h^3} * (3l^2 - 4a^2) \qquad \text{Equation 2-3}$$

$$B = \frac{3Fa}{bh^2} \qquad \textit{Equation 2-4}$$

Where, E (MPa) is bending modulus and B (MPa) is bending strength,

$\triangle F$ is the load range (50 N – 15 N = 35 N);

a is the distance between the inner and outer loading points (20 mm);

l is the distance between the outer loading points (60 mm);

f is the difference between the deflections at 15 and 50N (mm);

b is the average measured width of the specimen, (mm);

h is the average measured thickness of the specimen, (mm);

F is the force at fracture (N)

The commercial bone cements containing antibiotics, COPAL® G+C, COPAL® G+V, Palacos® R+G, CMW® 1G, SmartSet® GHV and Refobactin® Bone Cement R, were tested using ISO 5833 standard requirements for compressive strength, bending strength and bending modulus. As can be seen in Figure 2.22**,** all the bone cements passed the threshold values. The comparison between the commercial cements showed that whilst SmarSet® GHV had the lowest compressive strength, bending strength and bending modulus values, CMW® 1G had the highest results among the other commercial bone cements [136]. It should be considered that the addition of antibiotics might weaken the bending strength of the cement.

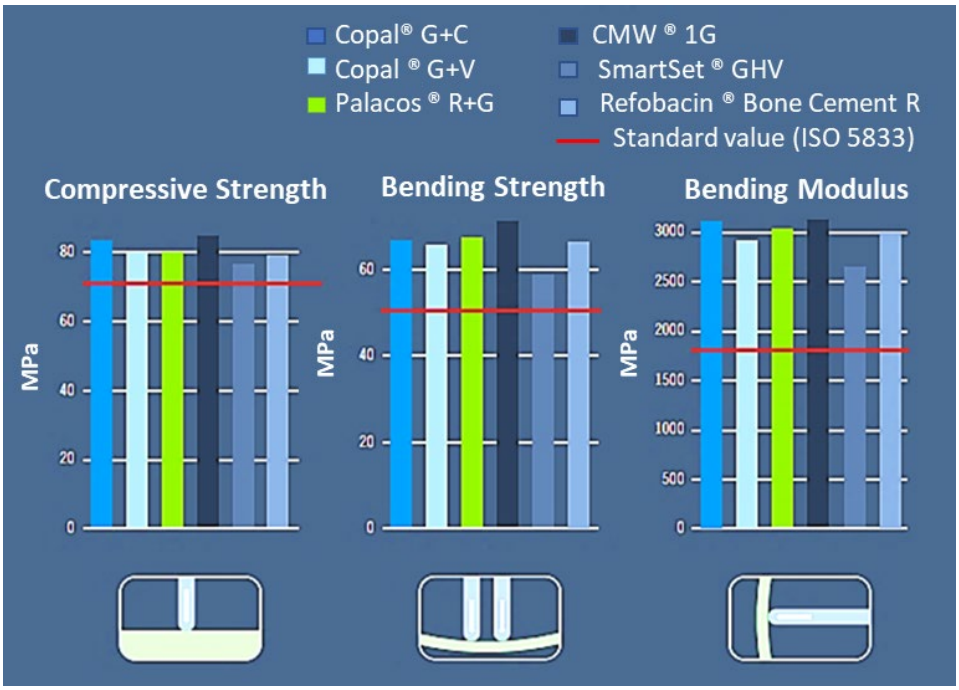

Figure 2.22 Comparison of mechanical tests results between commercial bone cement [136]

The typical flexural strength versus compressive strength properties of femur cortical bone, dentine and PMMA bone cement are illustrated using Edu Pack 2018 in Figure 2.23. The database does not contain PMMA bone cement but PMMA itself. Despite the cement having valuable mechanical properties, femur cortical bone has higher flexural and compressive strength than PMMA whilst dentine has similar flexural strength with PMMA. In the figure, PMMA shows flexural strength between 72.3-131 MPa and compressive strength between 72.4 and 124 MPa.

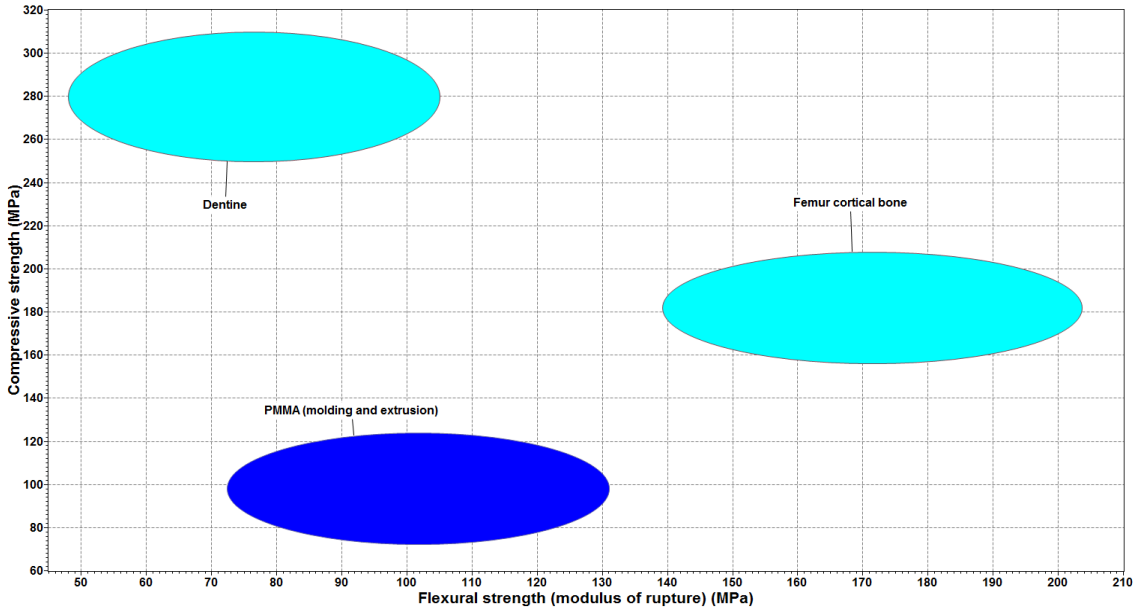

Figure 2.23 Compressive strength vs Flexural strength (EduPack 2018)

2.7.4 Drawbacks of PMMA bone cement

Even though PMMA bone cement has been successfully used in many applications, it has some complications and drawbacks. In the United Kingdom, 80.000 hip prostheses were performed in 2012 and approximately 8.600 prostheses had undergone through revision surgeries [137]. According to the National Joint Registry's annual report published in 2018 (covering from 2003-2017 and excluding insufficient reports) a total of 2,308,950 joint replacements were performed and 992,090 of them were hip replacements. 27,650 of these replacements had undergone through revisions. Moreover, it was reported that 34% of the primary hip replacements were performed using bone cement [8]. NHS has reported that approximately 1 in 10 people go through revision surgery every year [138]. One of the most significant reasons of prosthetic implants is aseptic loosening [139]. This may occur due to wear debris from the surface of prosthetic implants and ineffective application techniques of bone cement [140].

PMMA is an inert biomaterial, therefore, chemical or biological bonding to the bone cannot be formed and it may cause a failure of the implant by the formation of a fibrous layer. Hence, wear particles surround the implant and accelerate the deterioration [18]. The toxicity of MMA and the high exothermic polymerization reaction can cause chemical and thermal necrosis of healthy bone cells and the function of the immune system might be destroyed [141]. In addition to that, leakage of the residual monomer may also go into the blood supply which causes toxicity in the cells.

Even if PMMA has good mechanical strength under static conditions, it might break under much lower stresses than the expected ultimate strength values [142]. One of the reasons of that is adding radiopacifiers such as zirconium or barium sulphate reduces the mechanical properties of the bone cement due to agglomeration in the mass of cement and this might cause loosening of the implant [101]. However, the performance of the cement might also be affected by their chemical composition, mixing methods, viscosity, porosity and other additives (i.e antibiotics) as well as sterilisation methods [100].

The increase of failure rates (~10%) 5-10 years post-surgery is a further complication to the use of PMMA. The reason for these failures, besides aseptic loosening reasons which were mentioned above, is ageing and moisture uptake rate of the PMMA cement. However, these reasons are not widely investigated. Some studies showed that mechanical properties start decreasing over time [143, 144].

2.8 Magnetic Bone Cement

Malignant bone tumours reduce the quality of bone and can cause fractures. Therefore, bone cement implantation is applied not only to reinforce the bone but may also treat the bone tumour. Due to the high exothermic polymerization reaction of PMMA, it has been thought that the malignant tumour cells can be killed by the released heat from the cement [145]. Sturup et al., reported that even the high exothermic polymerization rate of the PMMA has no or little necrosis effect on the tumour cells *in vivo* [4, 15].

Among all the cancer treatment techniques, magnetic hyperthermia is expected to play a key role in the treatment of deep-seated tumour cells. To date, hyperthermia treatment techniques have not been effective for bone tissue cancer since the bone tissue could not be heated up to a suitable temperature. Studies showed that magnetic bone cements show promising results for this field of research [16].

Preparation for hyperthermia treatment starts with excision of the cancerous bone tissue and is followed by filling the cavity with magnetic based PMMA bone cement [146]. The affected volume is then exposed to an alternating magnetic field to increase the temperature of the cement and margins up to 46°C to kill any remnant cancer cells and to help prevent any reoccurrence [61].

The composite PMMA bone cement containing the magnetic glass ceramic prepared by Bretcanu et al., reported in Section 2.6.2, was characterised performing calorimetric and heating induction tests. In order to analyse the thermal effects of MGC amount in the cement, MGC was mixed into the composition of bone cement in different percentages (10, 15 and 20% (wt %)). The resulted composites named P10, P15 and P20, respectively. Powder to liquid ratio was kept at 2:1 (g/ml). In order to analyse the mechanical properties of the composite samples, the mechanical tests were performed according to the standard of ISO 5833:2002. The test results are shown in Figure 2.24. While the compressive strength test results showed higher values than the required value, 70 MPa, the bending strength test results showed a gradual decrease increasing the MGC content. P20 had a lower value than the required value, 50MPa [147].

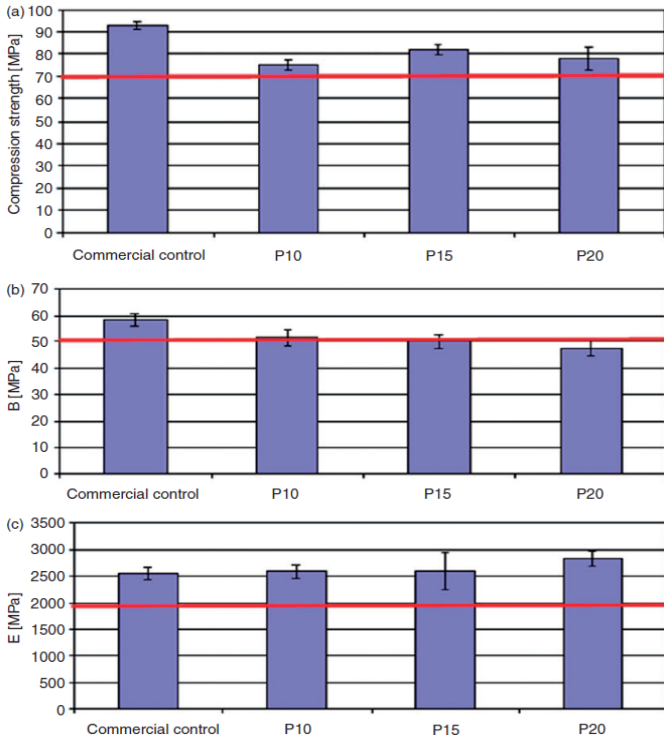

Figure 2.24 shows the mechanical test results of control (PMMA bone cement without MGC), P10, P15 and P20 bone cements a) compressive strength b) bending strength c) bending modulus (The red line refers to the minimum requirement values of ISO 5833:2002) [147]

In vitro magnetic induction test results showed that the saturation magnetisation was 1.6, 2.5 and 4.2 Am^2/kg for P10, P15 and respectively P20. Coercitive force showed a similar trend for all the samples (approximately 9.7 kA/m). It has been observed that thermal power losses increased with the increase of amount (wt%) of the magnetic glass ceramic. In order to analyse the effect of applied magnetic fields on the heating properties of the samples, different magnetic fields, 18, 25.6 and 31.2 kA/m were performed for 10 minutes (Figure 2.25). It can be stated that increasing the magnetic field, the temperature of the magnetic bone cement samples increases. The MG63 tumour cells were seeded on P10 sample in order to analyse the effect of magnetic hyperthermia on the cancer cells in the magnetic field of 18 kA/m. The cellular death was observed after 30 minutes at 43°C [148].

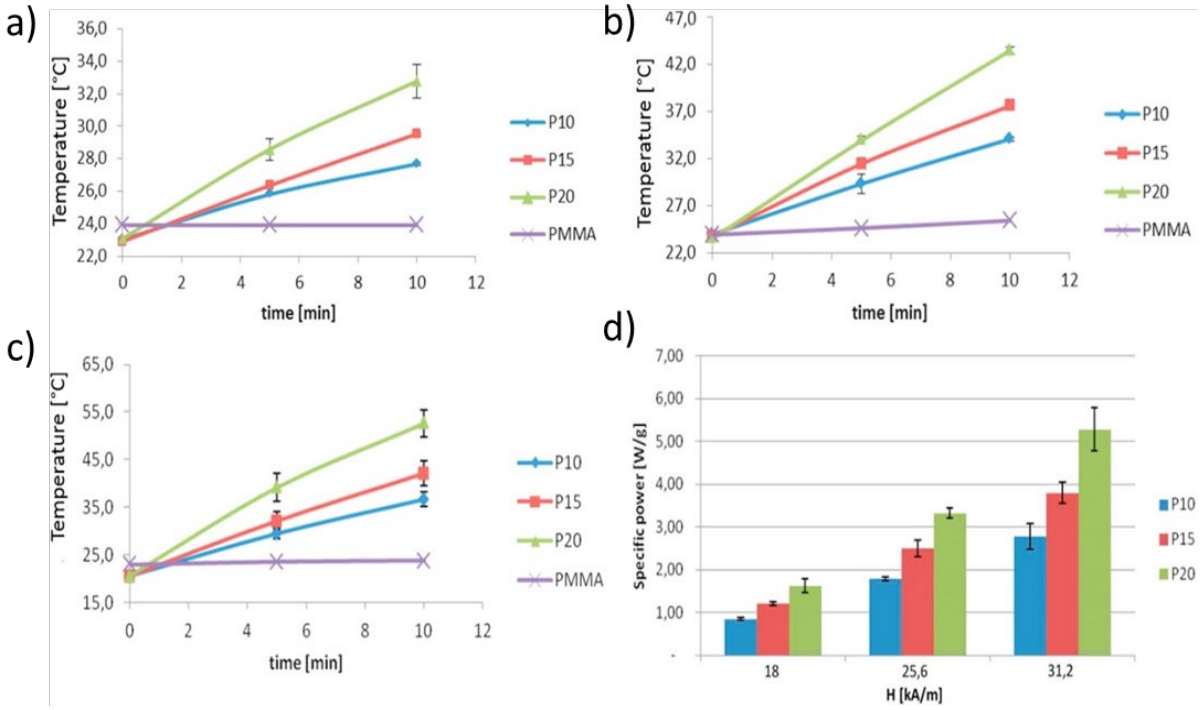

Figure 2.25 Temperature- time profiles of P10, P15 and P20 and PMMA (control sample without MGC) a) at 18 kA/m b) at 25.6 kA/m c) at 31.2 kA/m d) specific power loss of the samples at each magnetic field [148]

Kawashita et al [60]., developed a new PMMA bone cement (PMMAc), using a PMMA powder to MMA liquid weight ratio of 2:3. The bone cement was combined with magnetite in ratios of 40%, 50% and 60% (wt%) and named as M-40c, M-50c, and M-60c, respectively. PMMAc was used as a control group. Weight ratios of compositions are shown below in Table 2.11.

Table 2.11 Composition of PMMA containing magnetite in wt% [60]

	Powder (wt%)		Liquid (wt%)	Ratio (wt%)
Sample	**Fe_3O_4**	**PMMA**	**MMA**	**PMMA/MMA**
M-40c	40	24	36	2:3
M-50c	50	20	30	2:3
M-60c	60	16	24	2:3
PMMAc	0	40	60	2:3

The authors showed that increasing the amount of magnetite in the composition the setting time increased due to inhibition of polymerisation of MMA [60]. SEM results demonstrated that magnetite particles were uniformly dispersed in PMMA bone cement, except for M-60c which had a high viscosity. Therefore, the sample M-60c was not analysed in further tests. During the polymerisation of the samples, the temperatures were recorded to analyse the effect of magnetite particles on the peak temperature. The temperature vs time graph of PMMAc, M-40c and M-50c can be seen in Figure 2.26. The PMMAc had the highest exothermic peak at 95°C after 10 min. M-40c had an exothermic peak at 85°C after approximately 13 min and M-50c had the lowest peak at 75°C after 14.5 min. It was clear that increasing the weight of the magnetite in the cement composition lowered the peak temperature during the polymerisation reaction [60].

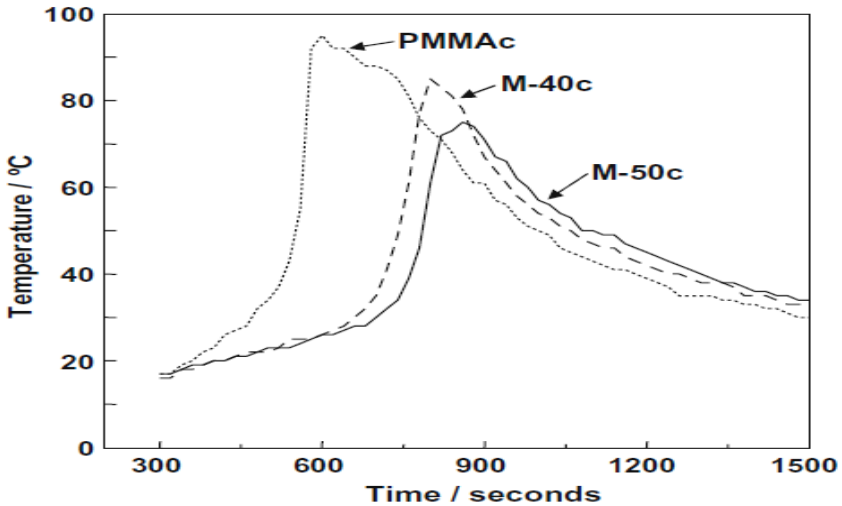

Figure 2.26 Temperature-time variation during polymerisation of magnetite bone cement, PMMA-c, M-40c and M-50c [60]

As agglomeration of radiopacifiers leads to a decrease in the mechanical properties, it was thought that the addition of magnetite particles might behave in the same way as well. Therefore, the compressive strength test was performed to understand the behaviour of the samples. The compressive strength of the cement decreased with the increase of the magnetite content in the cement from 40 to 50 wt%. However, the addition of magnetite slightly increased the compressive strength compared to plain PMMA sample. The test results are shown in Table 2.12.

Table 2.12 Compressive strength (MPa) of M-40c, M-50c and PMMAc [60]

Sample	Number of tested samples	Compressive strength (MPa)
M-40c	15	91.4± 6.1
M-50c	15	89.2± 6.5
PMMAc	14	85.3± 6.9

The magnetic induction test was performed exposing the samples to 300 Oe (~24 kA/m) alternating magnetic field for 10 minutes in order to observe the heating rate of the samples. As expected, the control sample PMMAc did not show any change in temperature under 300 Oe magnetic field for 10 minutes (see Figure 2.27). However, M-40c and M-50c reached temperatures of 70°C within 30 seconds of exposure to 300 Oe magnetic field. Therefore, the applied magnetic field was reduced to 120 Oe (~10 kA/m) and the temperature of M-40c slightly increased up to 40°C, whereas M-50c reached around 48°C in 10 minutes [60].

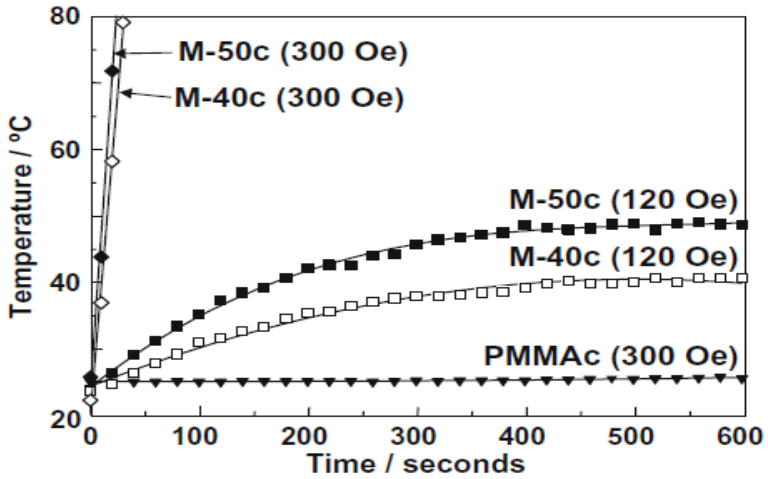

Figure 2.27 Heat generation under 120 Oe and 300 Oe magnetic fields during 10 min exposure time for PMMAc (plain PMMA), M40c and M50c [60]

2.9 Summary of Literature Review

Surgery stands as a main technique for treatment of bone cancer tissue. After excision of cancerous tissues, PMMA bone cement is used to support the weakened bone. Chemotherapy and radiotherapy techniques are still necessary in order to kill remnant cancerous cells that reoccurrence can be prevented. However, it is well-known that chemotherapy and radiotherapy can damage healthy cells and cause potential side effects in the body. Moreover, hyperthermia has been seen a promising technique to destroy cancer cells by increasing the temperature up to 45°C. Whilst hyperthermia showed positive results for superficial tumour tissues, it was not effective for deep seated tissues. Increasing the temperature or application time caused deposition of heat and burnings. Moreover, the applied temperature could not be applied homogenously within and around the targeted area. Due to these limitations, considerable attention has been paid to magnetic hyperthermia.

Magnetic material selection is crucial not only for heat generation abilities but also for creating interfacial bonding to bone. However, most of the magnetic glass-ceramics (MGC) proposed by several authors did not show bioactive properties, except the MGCs developed by Bretcanu et al. [61] and Kokubo et al [93]. Since PMMA bone cement has already been used in bone cancer surgery, the addition of MGC in the cement has been recently investigated for the treatment of bone cancer. However, it should be noted that magnetic PMMA cement can only be used for bone cancer treatment and not applicable for soft tissue cancers. From the fundamental theory and previous works in this area, the following conclusions can be drawn that increasing MGC content slightly decreased mechanical properties of cement but increased the heat generation. In the literature, the magnetic PMMA cement reported by Kawashati et al. [60] was lack of bioactive properties and therefore, the cement would not enhance stimulation of osteoconductivity.

In this study, it was important to produce magnetic PMMA cement that meets the criteria of standard ISO 5833:2002 for mechanical properties, exhibits bioactive and cytocompatibility properties and can be heated to a targeted temperature to kill the cancerous cells.

In the next chapter, preparation and characterisation methods of MGC, plain PMMA cement and magnetic PMMA cement are presented.

3 Methodology

In this chapter, the materials and methods used in this study are presented. Firstly, the production of magnetic glass-ceramics and their characterisation techniques are explained. Next, silicone rubber mould design and design justifications are described. Finally, preparation and characterisation techniques of plain and magnetic PMMA cements are presented.

3.1 Production of Magnetic Glass Ceramics

Magnetic glass-ceramic in the system of $24.7SiO_2$-$13.5Na_2O$-$13.5CaO$-$3.3P_2O_5$-$14FeO$-$31Fe_2O_3$ (wt%), which was developed by Bretcanu et al. [61] was produced by the melting and quenching technique. The raw reagents used for the MGCs are given in Table 3.1. They were weighed and mixed in a plastic bottle using a roller mixer for an hour. After that, the mixture was transferred into a Pt-Rh crucible.

Table 3.1 Raw reagents for producing MGC

Raw Reagents (Sigma Aldrich, UK)	**Purity**
Na_2CO_3	≥99.5%
$CaCO_3$	≥98.5-100.5%
SiO_2	≥98%
Fe_2O_3	≥99%
$Ca_3(PO4)_2$	≥96.0%
$FeC_2O_{4.2}H_2O$	≥99%

The heat treatment was performed in two stages. Firstly, the raw reagents were decomposed in a furnace (Carbolite, CWF-B 1200, UK) at 900°C using a 10°C/min heating rate and 1 hour holding time. The crucible containing the raw reagents was weighed before and after decomposition stage to calculate the mass loss (wt%) during decomposition. The crucible was subsequently transferred into a melting furnace (Carbolite, HTF 1800, UK) and the decomposed reagents were melted at 1550°C using a 10°C/min heating rate and 25 minutes holding time. The decomposition and melting processes of the MGC are shown in Figure 3.1

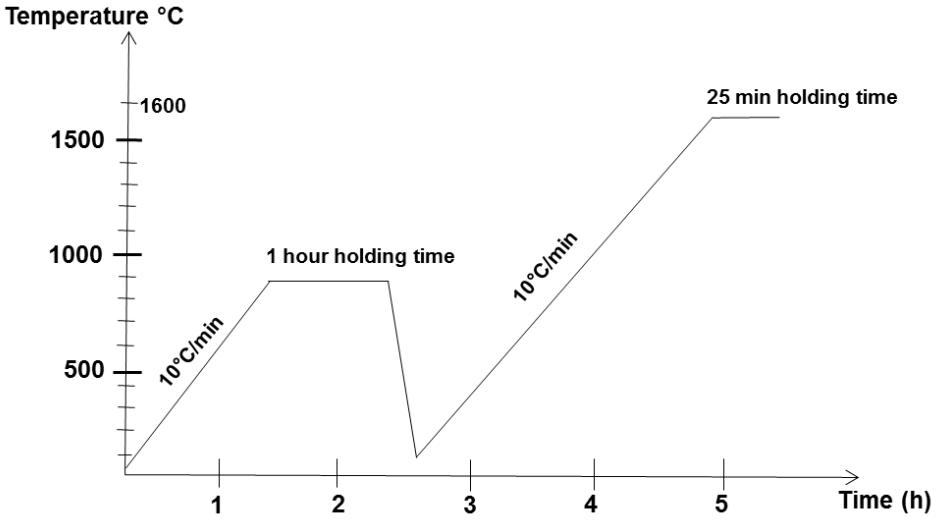

Figure 3.1. Decomposition and melting processes of the reagents

The melt was quenched in cold water and glass-ceramic frits were immediately drained and left to dry overnight (Figure 3.2). The crucible after quenching the melt and the MGC frits were weighed to calculate the yield (wt%).

As reported by Bretcanu et al. [61], the magnetite phase formed during quenching and there was no need for another heat treatment. In addition to that, secondary heat treatment would affect the properties of magnetic phase since the crystal sizes should be small for an efficient heat generation.

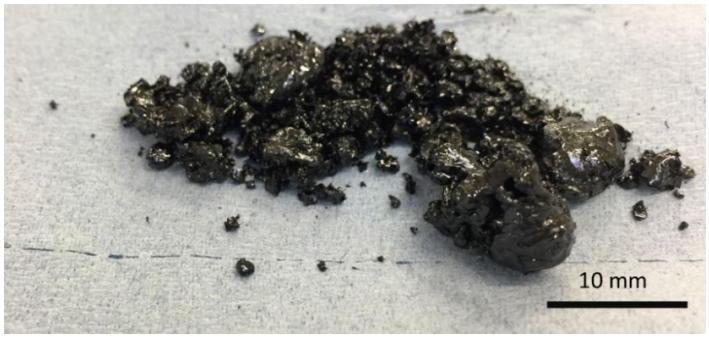

Figure 3.2. Magnetic glass-ceramic frits after quenching in cold water

Magnetic glass ceramic frits were ground using a single zirconia grinding bowl milling machine (Planetary Mono Mill Pulverisette 6, Fritsch GmbH, Germany) at a rotational speed of 420 rpm for four 3 minutes cycles. In order to obtain ≤53μm of particle sizes, the collected powder was sieved using an automatic sieve shaker (Impact Test Equipment Ltd, UK). Characterisation of Magnetic Glass Ceramics

3.2 Characterisation of Magnetic Glass Ceramics

In order to identify the crystalline phase, characteristic temperatures and morphological structure of glass ceramics, X-ray diffraction (XRD), differential thermal analyses (DTA), hot-stage microscope (HSM) and scanning electron microscope (SEM) was performed.

3.2.1 X-Ray Diffraction Analysis

X-ray powder diffraction (XRD) was performed to identify the presence of magnetite crystalline phase in the magnetic glass ceramics using a Philips PW3040/60 X-ray generator. This technique provides unique fingerprints of the amorphous and crystalline phases the materials. When X-Ray beams are passed through amorphous materials do not exhibit sharp peaks but crystalline materials can produce sharp diffraction peaks. It is due to periodically arranged atoms in a crystal. The diffraction peaks give information on unit cell matrix of a crystalline material, crystal size, phase identification and superlattice structure. The diffraction occurs when the Bragg's law is satisfied and the equation is given below.

$n\lambda = 2d \sin\theta$

where λ is the wavelength of the incident X-rays, n is an integer, d is the interplanar spacing of the crystal and θ is the angle of incidence.

MGC powder, iron oxide and pure magnetite were analysed operating the XRD at 40kV and 30mA using a Cu-Kα X-ray radiation source with a characteristic wavelength (λ) of 1.5418Å. The detector was set to scan over a range of 2θ angles from 10 º to 70 º, at a step size of 0.02º, 2s per step. The results were analysed using X'Pert High Score software. MGC powder peaks were compared to reference materials, iron oxide and pure magnetite, for magnetite phase identification. While iron oxide would only have hematite phase, pure magnetite would have only magnetite phase.

3.2.2 Differential Thermal Analysis

In order to investigate the glass transition (Tg) temperature and crystallization temperature (Tc) of the novel magnetic glass-ceramic sample, the differential thermal analysis (DTA) was performed using Setaram Labsys instrument. This technique identifies the difference in temperature between the sample and the reference under similar conditions when the samples are exposed to heat. Exothermic and endothermic peaks show the changes in crystallinity, dehydration, physical changes and chemical reactions in the sample.

Alumina, an inert material, was used as the reference sample. DTA was performed in air, up to a maximum temperature of 1550 ºC with a 20 ºC/min heating rate. A mass of ~50mg was used for both the MGC sample and alumina reference. DTA was performed three times for each batch. The results were recorded and analysed using Calisto software.

3.2.3 Hot-Stage Microscope

A heating microscope (Misura, Expert System Solutions, Italy) was used to observe the sintering behaviour of the MGC sample. The test was carried out in the air, up to 1550 ºC using a heating rate of 5 ºC/min. The powder was pressed in a small cylindrical die (2 mm diameter x 3 mm height) and placed on a holder. The changes in silhouettes of the material at different temperatures were analysed and recorded by a video-camera. The shrinkage in the area of the sample was calculated at different temperatures based on the change in the area of the sample using Equation 3-1.

$$\textit{Shrinkage (\%)} = 1 - \frac{A_T}{A_0} \times 100 \qquad \text{Equation 3-1}$$

where in A_0 (mm^2) is the initial area of the material and A_T (mm^2) is the area of the material at temperature T.

3.2.4 Scanning Electron Microscope

Hitachi TM3030 scanning electron microscope, was used at 15kV to analyse the morphology of magnetic glass-ceramics powdered sample. Elemental composition of the samples was observed using energy dispersive X-ray (EDX) analysis.

3.3 Mould Design and Design Justifications

Consistency in the dimensions and finish of samples is very important in order to obtain reliable and accurate results from mechanical tests. To accommodate various standards and future tests, the moulding system should be able to adapt to different shapes and sizes. It should also allow repeated use and be sufficiently flexible to facilitate removal of samples.

Test sample moulds are typically made from machined blocks of polytetrafluoroethylene (PTFE) that are the same size as the test samples. Whilst PTFE is a suitable material due to its relatively high stiffness and resistance to adhesion, removing the samples from such rigid PTFE moulds can result in rough edges on the samples. The standards anticipate and even allow for this, suggesting that sanding the edges is an appropriate method to remove rough edges of each sample. However, sanding or abrasive removal of PMMA cement could result in undesirable changes in mechanical and chemical properties and may introduce surface defects. Thus, the results of flexural and compression tests may not provide representative values of the cement obtained from PTFE moulds. Additionally, sanding each sample causes dimensional inconsistencies within the sample batch and is a time-consuming operation.

The key features of a good mould design may be summarised as:

- easy to manufacture
- low cost of materials and labour
- reusable design
- ease of forming and removing samples
- durable
- provide reproducible samples with consistent dimensions

By setting these objectives, the samples should be usable directly from the mould with no further requirements for post-processing such as sanding to control the size or surface finishing. Silicone rubber allows the aforementioned features through its beneficial properties such as low cost, easily modifiable and dimensional accuracy.

3.3.1 General Mould Fabrication Technique

Prior to fabrication of silicone rubber mould, the acrylic box and patterns of the samples were designed and drawn in Autodesk Inventor with the required dimensions (Figure 3.3). A laser cutter was used to cut separate components (walls, base and sample patterns) on acrylic sheets. The components were designed with mortices and tenons (*Figure 3.4*) which helped to assemble the final mould with ease.

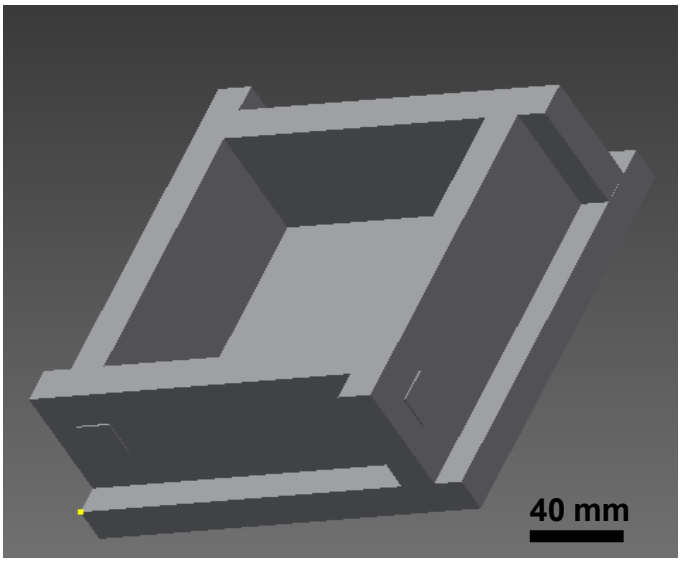

Figure 3.3 Assembly design of the acrylic box drawn using Autodesk Inventor

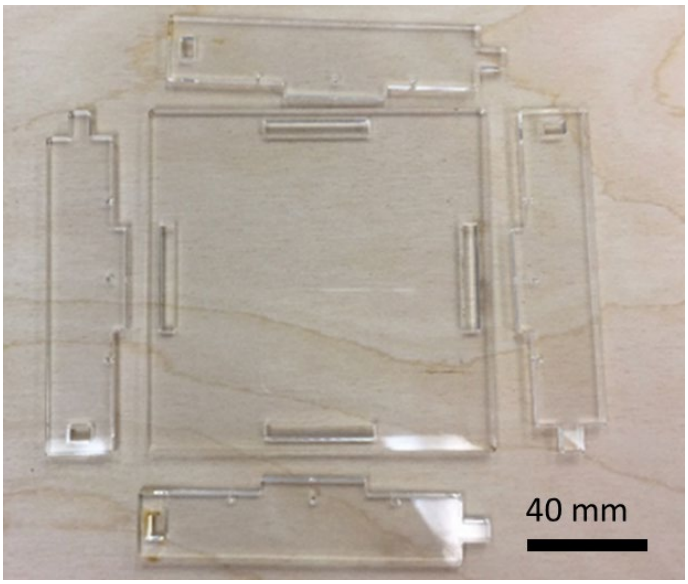

Figure 3.4 Acrylic components used for a box design

After assembling the box, a silicone mould release agent was applied on its inner surfaces in order to support removal of the silicone rubber easily after curing. The moulds were made of silicone rubber using Xiameter® silicone rubber base and catalyst (RTV-3120 base and RTV-3000 F catalyst).

In order to have a rigid solid silicone rubber mould, the ratio of base to catalyst was 10 to 1 (wt %) [149]. The volume of each mould was calculated and converted into weight. The calculated amounts of the silicone base and catalyst were mixed into a plastic container using a wooden stick for 1-2 minutes to obtain a homogenous mixture. Afterwards, the plastic container was placed in a vacuum chamber and degassed to speed up the removal of the internal air bubbles produced during mixing. After approximately 1 minute, when the air bubbles at the surface decrease, the container was removed from the vacuum chamber. The mixture was poured into the acrylic box from 20 cm distance to reduce the formation of air bubbles. The acrylic moulding box was returned into the vacuum chamber for 1 minute to release any trapped bubbles in the structure and it was kept at room temperature overnight to fully cure.

3.3.2 Fabrication of Four-Point Bending Test Sample Mould

The dimensions of the sample patterns were drawn in Autodesk Inventor with dimensions of 75±0,1 x 10±0,1 x 3,3±0,1 mm as indicated in standard BS ISO 5833-2002 (Implants for surgery — Acrylic resin cements) for performing 4-point bending tests. The box cavity was designed to fit three sample patterns, as seen in Figure 3.5-A. The patterns were designed to have features at the ends of the samples as sacrificial overflow spaces to accommodate any excess cement during the forming process; this allowed for more rapid mould filling and a location for temperature probes. The surfaces of sample patterns were refined using a 300-grit carbide paper, to have smooth surfaces of the cement samples. Narrow holes were provided for the mould's sacrificial cavity using metal wires (~2mm diameter) as shown in Figure 3.5-B.

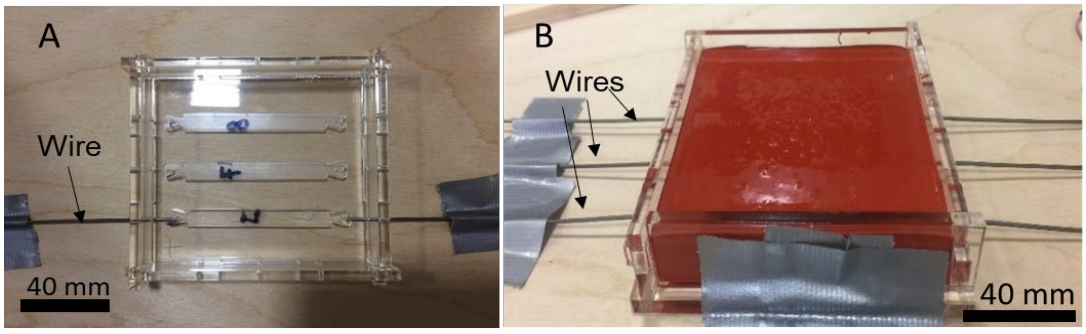

Figure 3.5 A) Acrylic box with the wires B) Silicone mould in the acrylic box during curing

3.3.3 Fabrication of Compressive Test Sample Mould

Standard ISO 5833-2002 suggests that samples should have 6±0.1mm diameter and 12±0.1mm height to perform compressive strength test. Therefore, cylinder sample patterns made of precision ground steel bars were cut in the required dimensions. An additional sample size with 12±0.1mm in diameter and 24±0.1mm in height was made, using steel cylinders, in order to understand the effect of sample dimensions on compressive strength. The rationale for double dimension sample preparation was to understand the effect of thickness on compressive test results since the polymerisation temperature, porosity and defects in the samples would be different relative to the dimensions. This was investigated since the defect sizes in the bone may vary. The reason for using steel bars instead of acrylic was that the laser-cutting machine melted the edges of the samples, which reduced the dimensions by approximately 1 mm. Ten cylindrical patterns for each mould were cut with required dimensions and the most dimensionally consistent three patterns were used. The compression strength test sample mould box can be seen in Figure 3.6.

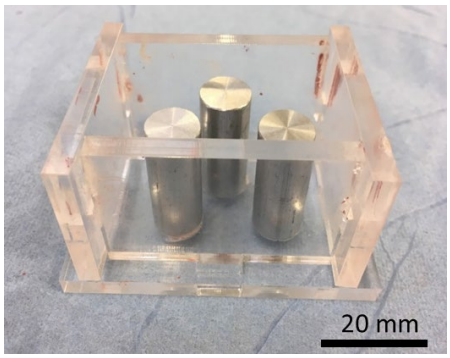

Figure 3.6 Compression test sample box with steel patterns

3.3.4 Fabrication of Cytocompatibility Test Sample Mould

The acrylic box was designed having four-disc patterns so that the PMMA cement samples would be placed into 12-well cell culture plates to perform cell viability assay. Considering the dimensions of the wells in the cell culture plate, the acrylic discs were cut with dimensions of 20 mm diameter and 5 mm height using a laser-cut machine. The acrylic box and the four patterns are shown in Figure 3.7.

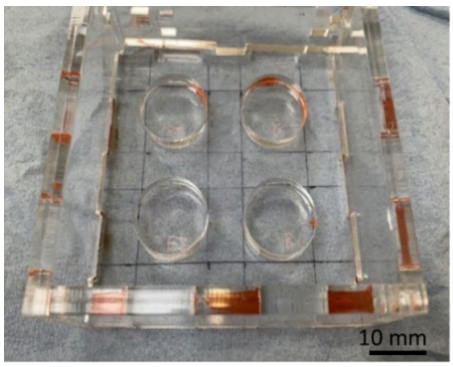

Figure 3.7 Cell viability assay sample box with disc patterns

3.3.5 Fabrication of Induction Heating Test Sample Mould

The acrylic box was designed having four cubic patterns. Eight 10x10x10 mm^3 cubes were laser-cut, measured by a calliper, out of which four were chosen and fitted into the acrylic box as seen in Figure 3.8. To discard any unwanted variables caused by weight inconsistency during the induction heating tests, special care was taken to achieve dimensional accuracy throughout the samples.

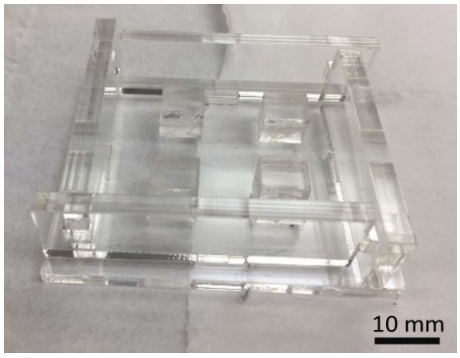

Figure 3.8 Induction heating test sample box with cubic patterns

3.4 PMMA Cement

As previously discussed in section 2.7, polymethylmethacrylate (PMMA) bone cement involves two components: poly (methyl methacrylate) (PMMA) powder and methyl methacrylate (MMA) liquid. They form a solid rigid cement after the mixture of two components undergo free radical polymerisation reaction. In this study, two commercially available cement kit, Palacos® MV powder and liquid (Heraeus Kulzer, UK) bone cement and Wintercryl rapid repair powder and liquid (John Winter & Co, UK) dental cement were used throughout the study. As discussed in section 2.7.4, ageing and moisture uptake can affect the properties. In order to evaluate the effect of ageing on the mechanical properties both plain cement, Palacos® MV (P0) and Wintercryl (W0) were assessed at different time points (1, 2, 3, 7, 14, 21, 28, 60 and 180 days).

P0 samples were always stored in closed air. In addition to the effect of ageing, W0 samples were stored in open and closed air. For closed air storage sealed plastic bags were used. Although gas diffusion was still possible from the plastic bags, the influence of humidity on the PMMA cement samples could be analysed. Therefore, the aim was to understand the effect of storage condition over time on further release of residual MMA monomer. For each time point and conditions, six samples were prepared and four-point bending test, compressive test and hardness test were carried out.

3.4.1 Humidity and Ambient Temperature Data

According to the requirements in standard ISO 5833:2002, humidity and ambient temperature were recorded during the whole experimental procedure for cement preparation, since the beginning of the mixing period and until the hardening of the cement samples. For this reason, El-sub 2 data logger (Lascar,UK) was used to record both ambient temperature and humidity.

3.4.2 Preparation of PMMA Cement

The samples were prepared following the manufacturer's instructions and standard ISO 5833:2002). Palacos® MV cement was provided in a kit, which contained one ampoule of MMA liquid (20mL) and one pack of PMMA powder (40g). Wintercyl cement kit had PMMA powder (3kg) and MMA component (1L). The composition of PMMA cements were provided by the safety data sheets (SDS) are given in Table 3.2.

Table 3.2 Composition of Palacos®MV and Wintercryl Cement

	Composition (wt%)	**Palacos ® MV**	**Wintercryl Cement**
Powder	poly(methyl acrylate, methyl methacrylate)	86%	>98%
	dibenzoyl peroxide	0.9%	-
	zirconium dioxide	12%	-
	colourant	Colorant E141	N/A
Liquid	methyl metacrylate	92.6%	> 90%
	N,N-dimethyl-p-toluidine	2%	< 1.0%
	ethylene glycol dimethacrylate	-	2.5-10%
	colourant	E141	-
	hydroquinone	60 ppm	N/A

*N/A, the information is not provided on the SDS of the product

The cement components and silicone sample mould were stored at room temperature (18-22°C) for two hours prior to mixing. The preparation technique, mixing time and powder to liquid ratio was strictly kept identical for both types of cements, Palacos® MV and Wintercyrl. The mixing ratio between the powder and liquid components was kept at 2:1 (g/ml). The liquid component was measured and poured into a ceramic mixing bowl firstly and after that, powder component, which was already weighed, was added into the liquid. Two components were mixed by hand using a spatula, for approximately 30s until a homogenous mixture was obtained.

The ceramic bowl was closed with a lid during the waiting time to prevent evaporation of MMA liquid [14]. The waiting time was typically between 2-5 minutes, however, this varied depending on the ambient temperature. Therefore, the mixture was checked regularly with a gloved finger until it didn't stick on the glove. The working time was between 1.5-2 minutes. During the working time phase, a consistent kneading procedure was performed to break up any remaining pockets of the powder component so that the powder would be homogenously distributed in the paste. The dough was then placed into the required mould for hardening phase. Mixing, waiting, working and hardening times were constantly recorded for every sample regardless of the type of test. Prior to each sample preparations, the moulds were marked to identify the orientation and position. For every sample preparation, the same position was used. The samples were then marked and coded after the removal from the mould.

3.4.2.1 Four-point Bending Test Sample Preparation

The fabrication of four-point bending test mould is described in Section 3.2.2. For the preparation of the test samples, cement dough was divided into two pieces and formed into two rolls (approximately 50mm long and 4-6 mm diameter) having equal weights (Figure 3.9). These rolls were then placed into the moulds. Thermocouples were positioned into the sides of the mould, protruding into the sacrificial end spaces to record the temperature-time profile of the cement.

Since ISO standard 5833:2002 required to use 25 gram of PMMA cement for monitoring temperature, the standard could not be followed due to limited Palacos cement kit. Therefore, silicone mould was designed to accommodate thermocouples through the sacrificial edges. By this way, the temperature profiles of cement samples could still be recorded and comparisons within and between the sample batches could be made.

However, it was acknowledged that the recorded temperature would not reflect the actual polymerisation temperature of PMMA cement because the polymerisation starts at the centre of the samples. Since the samples would be used for four-point bending test, the thermocouples could not be placed in the centre. Aluminium (~1.5 mm thickness) and wooden plates were placed on the top of the mould. Two weights, 5 kg each, were placed on the wooden plate to apply an even pressure on the cement samples.

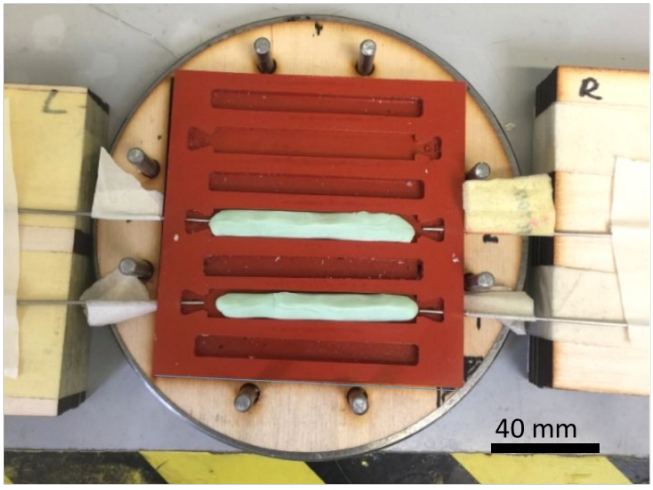

Figure 3.9 Rolls of Palacos® cement samples in the four-point bending mould

3.4.2.2 Compressive Test Sample Preparation

The fabrication of compressive test sample mould is described in 3.2.3. The test samples were prepared in a similar way as four-point bending test samples. As previously mentioned, the compression test samples were prepared in two different sizes; 6 x 12 mm and 12 x 24 mm. The reason of different sizes was to understand the influence of dimensions and application since polymerisation temperatures, porosities and defect sizes would be different between two sizes. The representative image of Wintercryl cement samples placed into the moulds can be seen in Figure 3.10. As the mould cavities for this test were cylindrical, it is pertinent to note that forcing the cement into the cavities may have resulted in trapped air. Therefore, the cement, in the dough stage, were rolled thin and compressed after being placed into the cavities.

This ensured that the cement took the shape of the mould fully and pushed excess air out. Aluminium (~1.5 mm thickness) plate was placed on the top of the mould. A 3 kg weight was used for these samples.

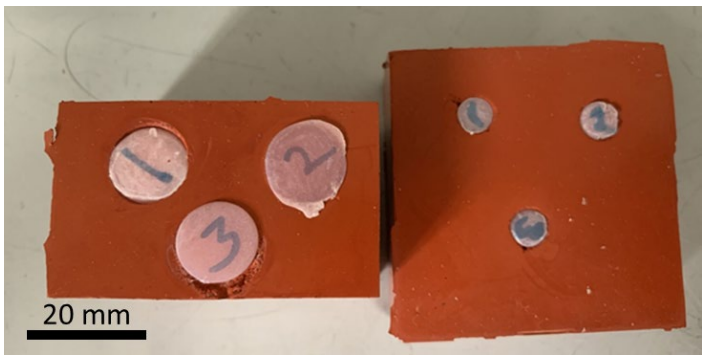

Figure 3.10 Wintercryl cement samples in two different sizes for the compression tests

3.5 Characterisation of PMMA Cement Samples

3.5.1 The Setting Temperature

Polymerisation temperature of each cement was recorded using T-type wire thermocouples connected to the TC-08 thermocouple data logger (Pico Technology, UK) and data was continuously gathered using Picolog software. Prior to placing the thermocouples through the sacrificial ends, the travel distance of the thermocouples was measured and labelled. The thermocouple tips were then sprayed with silicone mould release and inserted through the mould. After mixing the cement, when it reached the working time it was placed in the mould in two rolls. Four thermocouples recorded the temperature of the cements from each side of the bars, and one thermocouple recorded the ambient temperature, as shown in Figure 3.11. For each batch of cement prepared for four-point bending test, the time and temperature were recorded from the beginning of the mixing period.

The temperature-time curves were plotted to determine the maximum temperature in order to identify the setting temperature and time, as shown in Figure 2.17, Section 2.7.2.1. Setting temperature and time were calculated using Equation 2-1. Also, a stopwatch was used to record mixing, waiting and working time of each cement. It should be noted that method of setting time evaluation suggested by ISO 5833:2002 could not be followed due to not having enough amount of cement material. The mould design only allows to understand the behavior of cement during setting time and effects of ambient temperature on setting time of the material. However, this design does not allow to exhibit materials accurate setting time and temperature properties.

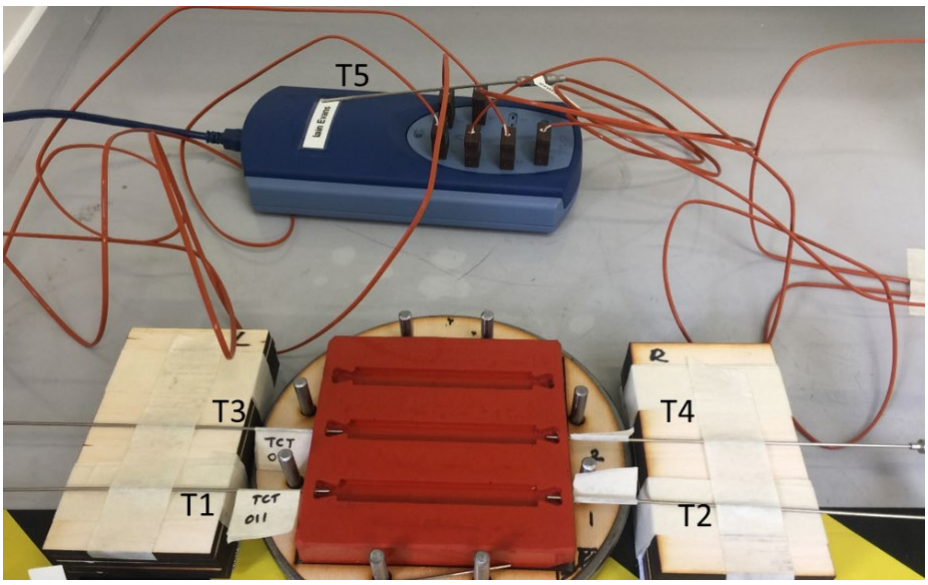

Figure 3.11 Silicone mould with five thermocouples, T1, T2, T3, T4 and T5

3.5.2 Bending Strength and Modulus

Mechanical properties of the cement are important for load-bearing applications. According to standard ISO 5833-2002, PMMA bone cement should have a minimum bending strength of 50MPa and a minimum bending modulus of 1800 MPa. Therefore, a four-point bending test was performed to assess the bending modulus and strength of the samples using a standard calibrated test machine AGS-X (Shimadzu, Japan) with a load cell of 1kN and a cross-head speed rate of 5mm/min, as specified in the ISO 5833:2002 standard. Test samples with dimensions of 75±0,1 mm length, 10±0,1 mm width and 3,3±0,1 mm thickness were prepared according to this standard. In order to achieve reliable test data of the cement, dimensional measurements were taken ten times along the thickness and width and four times for the length using a digital calliper.

The four-point bending rig was set with a distance between the outer loading points of 60 mm and a distance between inner loading points of 20 mm, as shown in Figure 3.12. In order to align the samples in the centre of the bed, the distance was measured and marked based on the dimensions of the sample. Each sample was carefully placed in the centre of the rig. In order to measure the deflection of the samples, an LVDT sensor was installed which was integrated into the manufacturer's data-logging system.

The sensor measures the mid-span deflection of the sample and the crosshead measures the stroke. The force and stroke were zeroed and calibrated before each testing session. The deflection of the specimen against applied force was recorded using TrapeziumX software supplied by the manufacturer. The applied stroke and resultant force were continuously increased until failure of the specimen or until the mid-span deflection of the sample reached a 12 mm safety limit.

The aged test samples of Wintercryl cement, W0, (kept in open air and in closed air storage) and Palacos® cement, P0, (kept in closed air storage) were tested 1, 2, 3, 7, 14, 21, 28, 60 and 180 days after setting. Bending modulus and bending strength were calculated using Equation 2-3 and Equation 2-4. Although ISO 5833:2002 suggests performing the tests on five samples to calculate the average of each test group, all tests were completed using six samples (n=6, providing 162 samples in total).

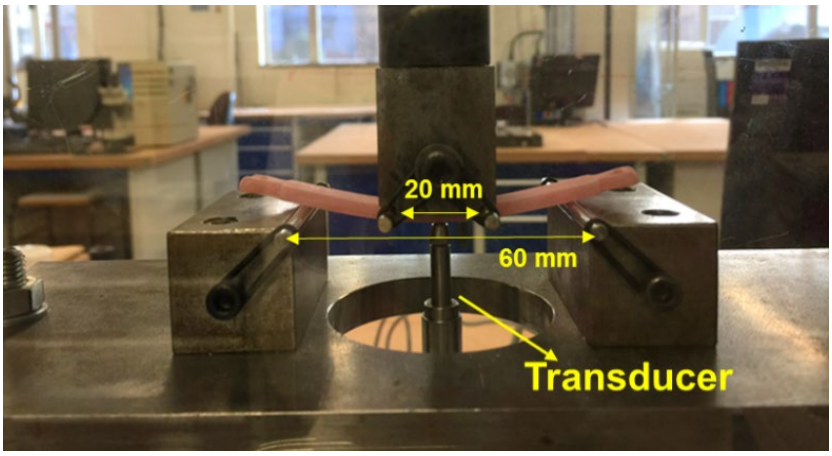

Figure 3.12 Four-point bend test setting

3.5.3 Compressive Strength

Compressive strength was tested in line with the standard BS ISO 5833:2002 and the requirement for the compressive strength value is minimum 70MPa. Palacos® and Wintercryl cements (kept in open air and closed air storage) with 6±0.1mm diameter and 12±0.1mm height and double dimension Wintercryl cement samples (kept in closed air storage) with 12±0.1mm diameter and 24±0.1mm height were tested. Each sample was measured five times along the height and across the diameter using a calibrated digital calliper. The aged test samples of W0 (kept in open air and closed air storage) and P0 (kept in closed air storage) were tested 1, 2, 3, 7, 14, 21, 28, 60 and 180 days after setting. Each batch had six samples and the average and standard deviation were calculated (n=6, providing 216 samples in total).

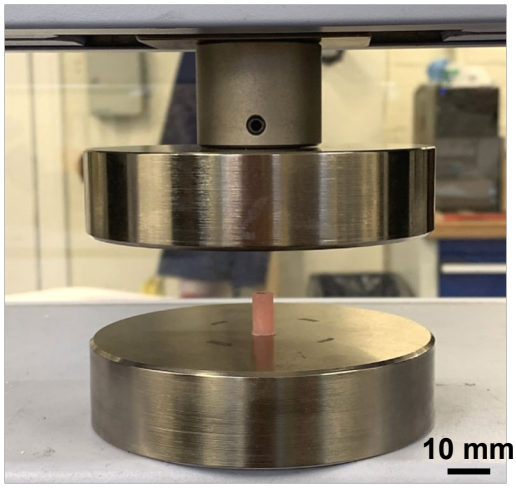

Figure 3.13 Compressive strength test

Prior to the test, the force and stroke were zeroed and calibrated according to manufacturer's instructions. The centre of the plate, where the sample would be placed, was marked. Each sample was then tested using AGS-X (Shimadzu, Japan) with a load cell of 10kN, at a constant cross-head speed of 20mm/min and a 50N pre-load, as shown in Figure 3.13. During the test, load against displacement was continuously recorded and the test was stopped when the ultimate load point been reached, or fracture occurred. Load-displacement data was converted to a stress-strain curve. A 2% offset line was taken for each individual sample for the calculation of compressive strength. Stress was calculated by dividing the force by the initial cross- sectional area, as described in Equation 2-2.

The percentage strain (Ɛ%) of the sample was calculated, as shown in Equation 3-2.

$$\varepsilon\% = \left(\frac{\Delta h}{h_0}\right) x100 \qquad \text{Equation 3-2}$$

Where Δh represents the difference between initial height and the height after compression, h_0 is the initial height of the sample.

3.5.4 Vickers Hardness Test

In order to investigate the resistance of samples to indentation, a micro-hardness test was carried out using HV-100 (Mitutoyo, UK) hardness machine. The broken samples from the four-point bending test were used for the hardness test on the same day after the bending test. The aged test samples of W0 (kept in open and closed air storage) and P0 were tested 1, 2, 3, 7, 14, 21, 28, 60 and 180 days after setting. Each batch containing 6 samples were tested 3 times (n=6, providing 162 samples, 486 reading in total).

The surface of the samples was refined with a 600-grit carbide paper to flatten the surface. The load was set to 2.5kg and held for 10 seconds for each test (Figure 3.14). The microscope attached to the machine was used to measure the two diagonal lengths, d_1 and d_2, after the load was removed, as shown in Figure 3.15. The automated calculation of the HV value was given by the test machine on the display.

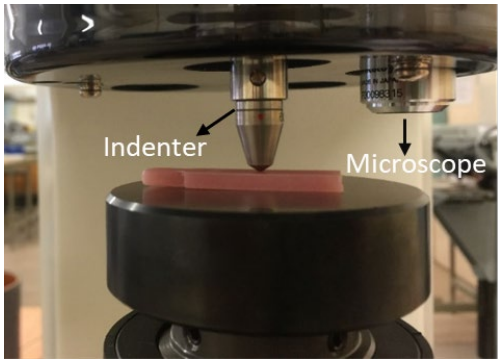

Figure 3.14 Representative image of Vickers hardness test

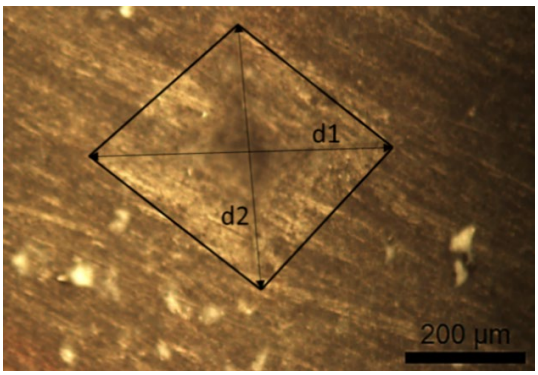

Figure 3.15 Representative image of indentation

3.5.5 Scanning Electron Microscope

Hitachi TM3030 scanning electron microscope (SEM) was used at 15kV to analyse the microstructure of the samples and elemental composition of the samples was observed using energy dispersive X-ray (EDX) analysis. In addition to this, the samples were gold coated (15nm) for better visualisation and observed under Tescan Vega 3 SEM at 8kV. The sample side in contact with silicone mould was examined under SEM for all samples.

3.6 Magnetic Glass-Ceramic Containing PMMA Cement

Two cement brands, Palacos® MV and Wintercryl rapid repair, were used to produce magnetic glass ceramic (MGC) cement samples. The MGC powder was mixed separately with Palacos® MV and Wintercryl cements in different wt% ratios; 10, 20, 30 and 40%.

The tests samples were named P10, P20, P30 and P40 for Palacos® MV and W10, W20, W30 and W40 for Wintercryl cements regarding the weight percentage of the MGC in the samples. MGC containing Wintercryl cement samples were called W-MGC and similarly, MGC containing Palacos® cement samples were called P-MGC for all MGC ratios (10, 20, 30 and 40 wt%).

3.6.1 Humidity and Ambient Temperature Data

The humidity and ambient temperature were measured in line with ISO 5833:2002 as described in Section 3.3.1.

3.6.2 Preparation of Magnetic Cement

Powder to liquid ratio (MGC+PMMA: MMA) was kept as 2:1 g/ml to have a medium viscosity cement. Appropriate amounts of PMMA and MGC powders were mixed manually in a glass beaker using a spatula to evenly blend both powder components. The powder mixture was then added to the liquid component. MGC cement samples were prepared following the same procedure described in Section 3.3.2. Mixing, waiting, working, and hardening times were recorded for each batch of the specimens.

3.6.2.1 Four-Point Bending Strength and Modulus Test Sample Preparation

Four-point bending flexural strength and modulus test samples were prepared as described in Section 3.3.2.1. P0 and W0, plain cements, were used as control samples (n=6). For each batch of W-MGC and P-MGC, six samples were prepared (n=6, providing 48 samples in total).

3.6.2.2 Compressive Strength Test Sample Preparation

The test samples were prepared, as described in Section 3.3.2.2. P0 and W0, plain cements, were used as control samples (n=6). For each batch of P-MGC and W-MGC, six samples were prepared (n=6, providing 48 samples in total).

3.6.2.3 Cytocompatibility Test Sample Preparation

The mould fabrication is described in Section 3.2.4. When the cement was in the dough stage, it was weighed and divided into four pieces. Each piece was rounded as a ball-like shape and placed into the mould. The ball-like shapes were gently compressed to ensure the cement would fill the disc shapes. A 3 kg weight was placed on the top of the mould. A representative image of the magnetic cement placed into the mould can be seen in Figure 3.16.

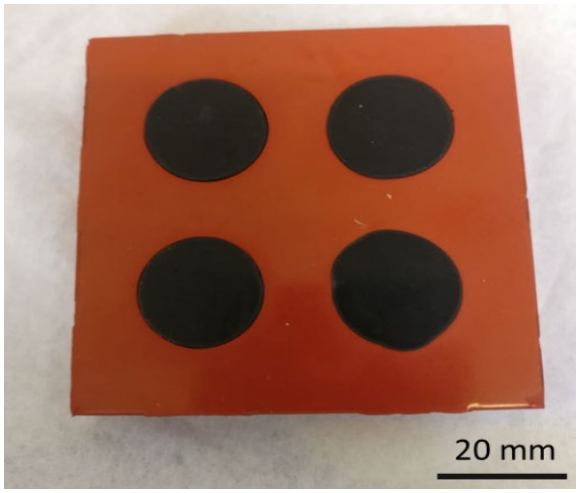

Figure 3.16 Magnetic cement test samples placed in cell viability test mould

3.6.2.4 Induction Heating Test Sample Preparation

The mould fabrication is described in Section 3.2.5. Since the test would be performed in non-contact conditions, cubic shape was preferred to minimise the contact between the acrylic holder and test sample. For the preparation of induction heating test samples, the cement in dough stage was weighed and divided into four pieces. Each piece was rounded like a ball and placed into the moulds. In order to have sharp shapes of cubic structure, the cement was carefully placed and pushed into the mould. A representative image of magnetic cement samples placed into the mould can be seen in Figure 3.17. A 3 kg weight was placed on the top of the mould.

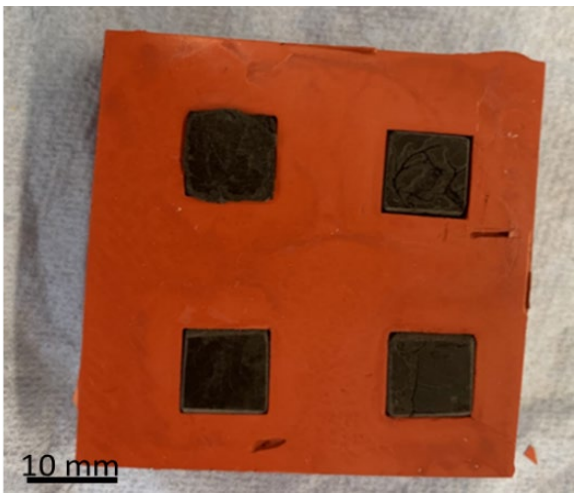

Figure 3.17 Magnetic cement samples placed in induction heating test mould

3.7 Characterisation of Magnetic Cement Samples

3.7.1 The Setting Temperature

Polymerisation temperature and time were recorded as described in Section 3.4.1. Setting time and temperatures of the samples were calculated through Equation 2-1.

3.7.2 Four-Point Bending Strength and Modulus Test

The test was set up and performed, as described in Section 3.4.2. The control (W0 and P0) and magnetic cement samples (P10, P20, P30, P40 and W10, W20, W30, W40) were tested 24±2 hours after the cement samples were polymerised. Bending strength and modulus was calculated using Equation 2-3 and Equation 2-4. The average and standard deviations of each test group were calculated (n=6, 48 samples)

3.7.3 Compressive Strength Test

The compressive strength test was set up and performed as described in Section 3.4.3. Both control and MGC cement samples were tested 24±2 hours after the cement samples were polymerised. Stress (σ) and strain (ε%) were calculated through Equation 2-2 and Equation 3-2 in order to evaluate 2% offset line as described in Section 3.4.3. The average and standard deviations of each test group were calculated (n=6, 48 samples).

3.7.4 Vickers Hardness Test

The broken samples from the four-point bending test were used for the hardness test on the same day after the bending test. The test was performed as described in Section 3.4.4. Each batch had six samples. For each test group, the average values and standard deviations were calculated (n=6, 48 samples in total, 162 readings).

3.7.5 Analysis of Water Absorption

The Archimedes method was followed to calculate the water absorption of the composite cement samples. Three samples from each group were used to calculate the average water absorption (%) and standard deviations. A density determination kit that was set up in Kern analytical balance (ABT 220-5DM). After taking the dry weight of samples, they were submerged in water and weighed in water. Finally, they were taken out of the water and weighed again to record the wet weight. Water on the surface was gently removed using a tissue before mass determination. The water absorption was determined using Equation 3-3,

$$\%\text{water absorption} = \frac{(m_1 - m_0)}{(m_1 - m_2)} \times 100 \qquad \text{Equation 3-3}$$

where m_1 is wet mass, m_0 is dry mass, and m_2 is submerged mass.

3.7.6 Scanning Electron Microscope

A Hitachi TM3030 scanning electron microscope was used at 15kV to analyse the microstructure of magnetic PMMA cements. Elemental composition of the samples was observed using energy dispersive X-ray (EDX) analysis.

3.7.7 In vitro Bioactivity Characterisation

In vitro bioactivity of the composite samples was assessed using simulated body fluid (SBF) solution proposed by Kokubo et al [150]. The ion concentrations in the solution mimics human blood plasma to enhance the formation of an apatite-layer on the surface of the bioactive samples.

SBF solution was prepared following the instructions in Kokubo's procedure using a 1-litre plastic bottle. The reagents from 1 to 8, given Table 3.3, were chronologically added into 700 mL deionized water at 20 minutes intervals. It was essential to dissolve the reagents entirely before adding the next reagent. The pH values and temperature were measured continuously using a portable pH meter FiveGo™ F2 (Mettler Toledo, Switzerland). Before adding reagent 9 (Tris buffer), deionized water was added until the solution was 1L.

Table 3.3 Reagents used for the preparation of SBF (pH 7.4, 1L)

Order	Reagent	Amount	Purity %
1	NaCl	8.035 g	99.5
2	$NaHCO_3$	0.355 g	99.5
3	KCl	0.225 g	99.5
4	K_2HPO_4 $3H_2O$	0.231 g	99.0
5	$MgCl_2 \cdot 6H_2O$	0.311 g	98.0
6	1M-HCl	35 mL	-
7	$CaCl_2$	0.292 g	95.0
8	Na_2SO_4	0.072 g	99.0
9	Tris Buffer	6.118 g	99.0
10	1M-HCl	0-10 mL	-

Tris buffer was added in small amounts until the solution reached 7.45 pH value and then HCl and the rest of the Tris buffer were alternately added to keep pH values between 7.42-7.45. After dissolving the entire amount of Tris buffer the pH value and temperature were stabilised with HCL at 7.40 at 36.5°C. Kokubo's protocol stated that the solution could be kept in the fridge for only one month. Therefore, the new SBF solution was prepared every month during the bioactivity test.

The test samples, W0, W10, W20, W30 and W40, were cut by laser cutting machine approximately 5 mm wide and 3 mm thick. In vitro bioactivity test was carried out for 1, 2, 3, 4, 8, 12, and 24 weeks and three samples were used for each time point. The samples were placed in plastic bottles, and 5 mL SBF solution was added. During the test, the samples were kept at 37°C in the incubator, and the solution was refreshed twice a week. This was done with extra care so that all samples were placed in the containers in the same position.

After each time-point, samples were removed from the bottle using tweezers and washed gently with deionised water to remove any unattached apatite particles. Next, the samples were left to dry at ambient temperature for 1 day. The scanning electron microscope was used to analyse the apatite layer on the surface of the samples. The characterisation and morphology of the samples were observed using SEM and EDX, as mentioned in Section 3.6.6.

3.7.8 Cytocompatibility Tests

In vitro biological behaviour of MGC cements was assessed using two different assays; MTT (3-[4,5-dimethylthiazol-2-yl]-2,5-diphenyltetrazolium bromide)] and Alamar Blue™. These assays measured cell adhesion, cell viability and proliferation. The cytocompatibility tests were performed at Northern Institute of Cancer Research, Newcastle University, with the collaboration of Dr Kenny Rankin. The MTT assay experiment was carried out with the MRes student, Nick Inmann. All tests were performed using the side of the sample that was in contact with silicone mould.

3.7.8.1 Tissue cell culture for MTT assay

Osteosarcoma, U2OS, cancer cells were cultured using Dulbecco's Modified Eagle Medium, DMEM, (Sigma, UK) supplemented with 1% L-glutamine, 10% fetal bovine serum (FBS), 1% penicillin/streptomycin in T125 flasks. The flasks were kept in an incubator at 37°C (5% CO_2 and 95% air in a humidified atmosphere). The cell media was refreshed every 2 days.

When the cells reached 70-80% confluency, the media in the flask was aspirated, and 10 mL of PBS were added to wash the cells. The flask was gently shaken to rinse the entire surface, and then PBS was aspirated. 3 mL of trypsin/EDTA (Gibco®) was added to detach the cells, and the flask was returned to the incubator and left for 5 minutes. The flask was checked again under an optical microscope, to look for undetached cell; to detach these cells, the flask was gently tapped. To wash the walls of the flask 7mL of fresh media were added in the flask and resuspended several times to collect the detached cells in a 50mL falcon tube. These cells were centrifuged at 500 rpm for 5 minutes, and then the trypsinised media was decanted. 10mL of fresh media was then added to neutralise any residual trypsin. The cells were resuspended several times to break apart any clumps to achieve homogeneity. Cells were counted using a Hemacytometer (Sigma-Aldrich) in order to calculate the number of cells in 1mL cell suspension. The total number was divided by 4 and multiplied by $1x10^4$ since each square (total four squares) of Hemacytometer had a value of 0.1 µL.

3.7.8.2 MTT Assay

MTT colourimetric assay was performed using Thiazolyl Tetrazolium Bromide (MTT, Sigma, UK) to evaluate cell viability and cell attachment of samples. In this assay, the viable cells would change the colour of MTT from yellowish to deep purple. This is due to the mitochondrial dehydrogenase of living cells that reduces the MTT dye to insoluble formazan, which has a deep purple colour. Then the formazan crystals are dissolved in a solvent reagent such as acidified isopropanol.

MTT assay was performed only on W0, W10, W20, W30 and W40 samples using U2OS cell lines since Palacos® MV cement kit could not be obtained for this assay. The test was performed for 1, 3 and 7 days as triplicate. Three samples for each test group and time point were prepared (n=3, 54 samples) as described in Section 3.5.2.3. It should be noted that six W0 samples were used. These samples were divided into two plates as W0-1 (plate-1) and W0-2 (plate-2). Three wells of each plate were used for positive controls (C+), media with U2OS cells. The disc-shaped samples were placed as shown in Figure 3.18. The samples were kept in 70% ethanol for 1 hour for sterilisation and then washed with PBS to neutralize the ethanol.

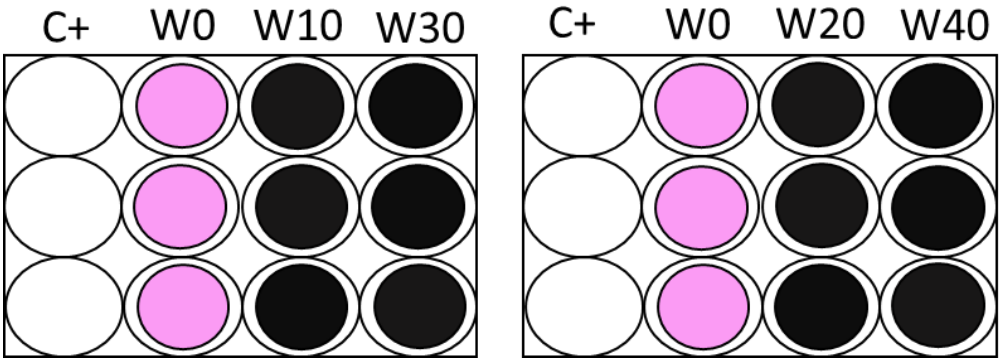

Figure 3.18 Schematic diagram of 12-well plates for MTT assay set up

At 0 time point, the sterilised samples were placed in a new 12-well plate. $5x10^5$ cells in 200 µL were seeded on the top surface of each sample and in the empty positive control wells. The plates were returned into the incubator to allow cell attachment and kept for 30 minutes. After that, 1.5mL of media was added into each well. The schematic diagram of the procedure is shown in Figure 3.19.

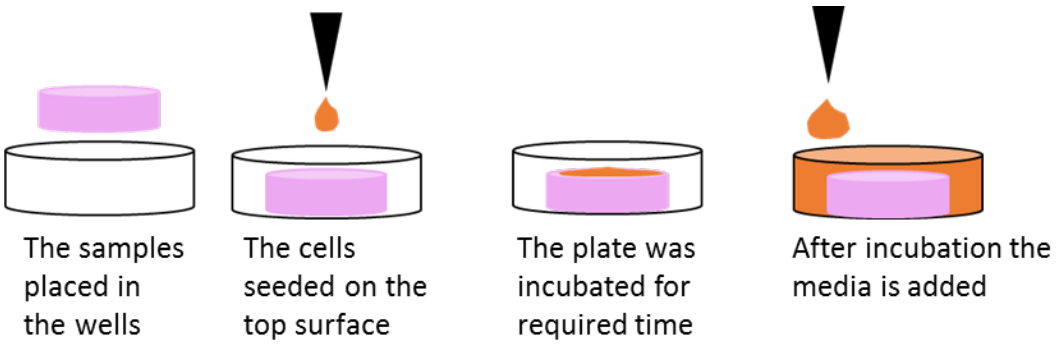

Figure 3.19 Schematic diagram of seeding the cells on the top surface of the samples

At each time point (1, 3 and 7 days), The MTT powder was weighed out in an amount to be diluted with media in 5mg/mL ratio. Sterilised 50 mL falcon tube was covered with Al foil to avoid light penetration. The MTT solution was mixed using a Vortex mixer until it dissolved in media. The solution was transferred to a new 50mL falcon tube using a 0.2µm pore size filter and a 20mL syringe. The disc-shaped samples were transferred to new 12 well-plates so that the MTT solution would only react with cells which were adhered on the surface of the samples. The old 12 well-plates were kept in order to analyse the positive control wells. Afterwards, 1.5mL of MTT solution was added to each well, and the plates were wrapped with Al foil. After 4 hours of incubation, MTT solution was aspirated, and 1.5mL of 100% isopropanol was added to each well. The plates were wrapped with foil again and placed on a plate rocker for 60 min at room temperature.

500 µL solubilized cells were removed from each well and placed in Eppendorf tubes and centrifuged at 12000 rpm for 1 minute to separate the cement debris that would affect the results. 200µL of the centrifuged solution was transferred into a 96 well-plate. 100% isopropanol solution was used as a negative control. 200 µL of 100% isopropanol was added in an empty well of 96-well plate. The spectrophotometer absorbance readings were taken at 570nm using a plate reader (680- Bio-Rad, UK).

The percentage of cell viability was expressed using Equation 3-4,

$$\text{Cell Viability } \% = \frac{\text{Asample}}{\text{Acontrol}} \times 100 \qquad \text{Equation 3-4}$$

where *Asample* refers to the absorbance value of the samples and *Acontro*l refers to the absorbance value of the positive control.

3.7.8.3 Tissue Cell Culture for Alamar Blue Assay

The Alamar Blue assay was performed using two cell lines, human osteoblast (OBS) and U2OS cells. Both cell lines were cultured in RPMI (Roswell Park Memorial Institute) 1640 media (Sigma, UK) supplemented with 1% L-glutamine, 10% fetal bovine serum (FBS),1% penicillin/streptomycin in T125 flasks. The flasks were kept in an incubator at 37°C (5% CO_2 and 95% air in a humidified atmosphere). The cell media was refreshed every 2 days. The cells were split and counted as described in 3.6.8.1.

3.7.8.4 Alamar Blue Assay

Cell proliferation on the surface of Palacos® MV and Wintercryl magnetic cements were assessed using Alamar Blue™ assay for 1, 3, 7, 10 and 14 days. In this assay, oxidation-reduction (REDOX) activity takes place which indicates the metabolic activity of cells. Due to the REDOX reaction, the AlamarBlue®, REDOX indicator, changes its colour from oxidized blue, non-fluorescent, to reduced pink, highly fluorescent.

The disc-shaped W0, P0, W-MGC and P-MGC samples, were prepared as described in 3.5.2.3, were laser-cut in quarters. Five samples for each W-MGC and P-MGC groups were prepared (n=5, 200 samples in total). However, W0 and P0 groups had six samples and these samples were divided in two groups. The samples in plate-1 were called W0-1 or P0-1 and the samples in plate-2 were called W0-2 or P0-2 (n=10, 100 samples in total). Throughout the assay, the total number of samples was 300 and 1200 readings were taken.

Five wells of each plate were used for positive controls (C+), media with cells. The disc-shaped samples were placed in 24 well-plates, as shown in Figure 3.20. The samples were soaked in 1mL of 70% ethanol for one hour for sterilisation. The ethanol was then aspirated and neutralised by adding 1mL of RPMI to each well. The 24 well-plates were incubated at 37 °C in 5% CO_2 for 24 hours. The plates were then taken from the incubator, and the samples were transferred into new 24-well plates.

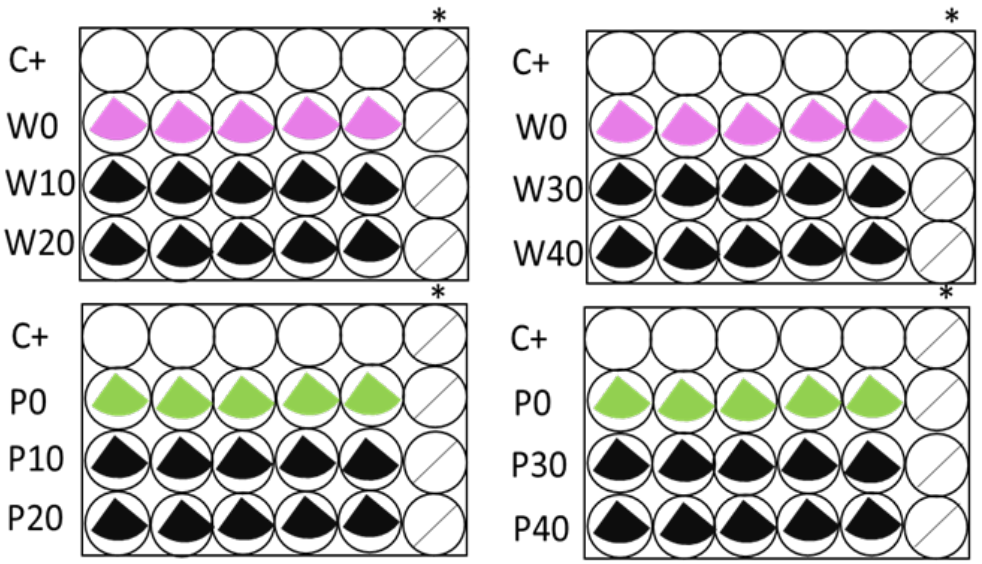

Figure 3.20 Schematic diagram of 24-well plates for Alamar Blue assay set up (indicates that the column was not used)*

At 0 time point, the two cell lines, OBS and U2OS, were counted and collected in different falcon tubes in the same way as described in Section 3.6.8.1. $1x10^4$ cells in 20µL of culture medium (RPMI) were seeded directly onto the top surface of each sample, and the plates were returned into the incubator. After 2 hours, 1mL of RPMI media was added to each well and returned to the incubator. The procedure was performed, as shown in Figure 3.19.

At 1, 3, 7, 10 and 14-day time-points, the samples were transferred to a new 24-well plate. The day 1 time-point 24 well-plate were kept due to containing positive control (cells+media) wells. In the new 24 well plates, the five wells were used for negative control (only media). The media in each well was refreshed adding 1mL of fresh RPMI media, and in order to perform the assay, 100 µL (10% v/v) of AlamarBlue™ was added. The plates were wrapped with Al foil and placed in an incubator at 37 °C in 5% CO_2 for 4 hours.

After the incubation, 4 aliquots of 150µL media from each well were transferred into 96 well plates (Costar) for fluorescence reading at 540nm and 580nm using FLUOstar® Omega plate reader (BMG Labtech). Remaining Alamar blue in the wells was aspirated, and 1mL of fresh RPMI was added into each well before the incubation period for the next time-point assay.

The cell viability was calculated as suggested in the manufacturer's protocol through,

$$Cell\ Viability\ \% = \frac{FSample}{FControl} \times 100$$ Equation 3-5

Where *Fsample* is fluorescence readings of the samples (W-MGC, P-MGC and their controls) and *Fcontrol* is fluorescence readings of control cells.

3.7.9 Fluorescence Imaging

The OBS and U2OS cell attachment was observed on the surfaces of the W0, W-MGC and also P0, P-MGC samples. The cells were seeded, as described in Section 3.6.8.3. In order to observe the cell attachment Vectashield® Hardset™ Antifade Mounting medium with DAPI (H-1500, Vector Laboratories, UK) stain was used. This technique allows staining the nucleus and DNA of the cell. According to the manufacturer's protocol, the samples were mounted on the microscope slides by applying a drop of dye (approximately 25 µL) to the surface of the sample. A coverslip was carefully placed on the top without causing any air bubbles, which could hinder the image. The samples were cured at room temperature for approximately 15-20 minutes. As the dye was sensitive to any lights, the samples were wrapped with Al foil and kept in the fridge (4°C).

Leica DM6 fluorescence microscope integrated with LAS X software was used to observe and record the stained cells images. DAPI was set in the software which excites at 360nm and emits at 460nm.

3.7.10 SEM Microscope Imagining for cell attachment

Tescan Vega3 (Tescan, UK) SEM was used to detect cell attachment for both cell lines (U20S and OBS) on P0 and P-MGC for 1 and 3-day time-points. Additionally, control samples, absent from cells, were observed under SEM to determine the effects of chemicals and treatments used through the cell fixation process, which are explained below.

For cell fixation, the samples were kept in 2% glutaraldehyde Sorenson's buffer solution (GA) overnight. After this step, the dehydration steps were applied. The samples were washed with PBS for 15 minutes twice, and then they were soaked in 25%, 50% and 75% ethanol solutions respectively, for 30 minutes each. In the end, the samples were kept in 100% ethanol for two hours, aspirating and refreshing the ethanol after the first hour. The samples were critical point dried (Bal-tec, UK) to remove the residual water in their structure. The dried samples were gold coated (15nm) and placed in a vacuum chamber of SEM. The images were taken at 200x and 1000x magnification at 8kV.

3.7.11 Induction Heating Test

It is essential to analyse the magnetic heating characterisation of the MGC containing bone cement samples to predict the behaviour of the materials when exposed to hyperthermia treatment in the body. As previously mentioned in Section 2.3.2, the temperature above 42^{o}C kill cancerous cells. This experiment was designed to increase temperatures to between 50-55˚C and to hold the temperature between these ranges. Although this ~5˚C higher than the minimum 42˚C, the increased temperature allows for heat losses in vivo.

The test samples were prepared, as described in Section 3.5.2.4. They were weighed in order to assess any weight loss during induction heating. The dimensions of the samples were measured using a digital calliper. Both MGC containing Palacos® and Wintercryl cements and control samples were tested (n=5, in total 50 samples).

The experiment was carried out at room temperature. The system was set up as in Figure 3.21. The cubic samples were placed in an acrylic holder, which was suspended in the middle of an induction coil, in a non-contact position. The infrared thermal camera, FLIR C2 (FLIR Systems, USA), was set at the point of the edge of the sample as indicated in the image.

In this way, the heat generated in the sample could be measured by a single camera measuring the three edges to provide more homogenous heat distribution throughout the sample rather than measuring only one face of the sample. The coil, acrylic sample holder and ambient temperature were also recorded by a thermal camera. Thus, the effect of radiation and convection from the surrounding material could be observed.

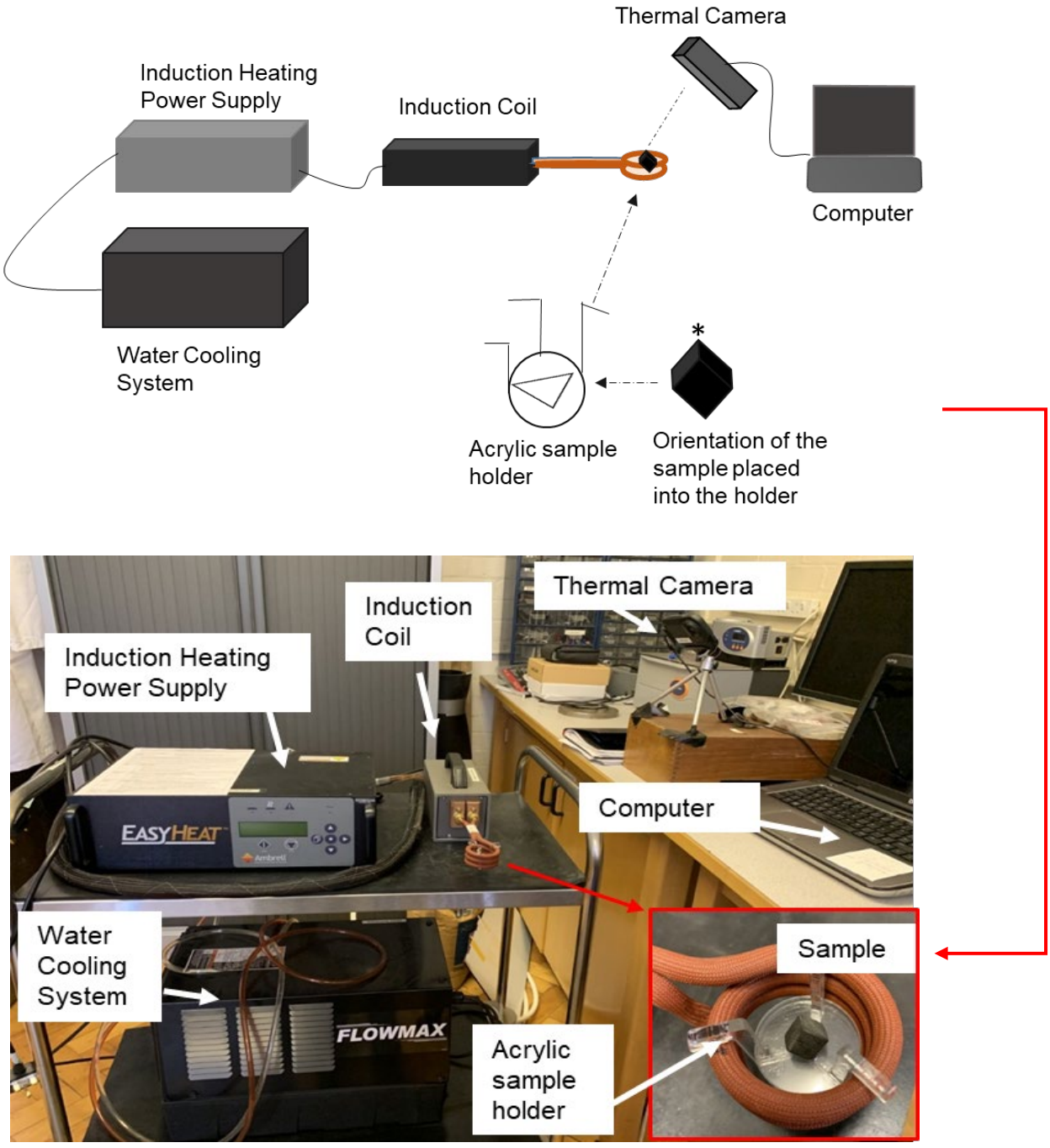

*Figure 3.21 Schematic diagram of induction heating test set-up (*indicates the temperature measuring point on the sample)*

The induction current was chosen so that the corresponding MGC samples would be heated to above 50°C within a similar range in 5 minutes. It was aimed to apply the lowest current possible to reach and maintain the targeted temperature for every sample group. Therefore, small gradients of current have been tested and optimal current for 10% MGC containing cement was found as 310A to reach temperature between 50-55 ̊C. The same procedure was applied to determine the holding current in order to maintain the temperature for five minutes. The induction current was manually reduced with the increase of MGC content from 10% to 40%. This reduce was approximately 25%, however, further increases or decreases were applied based on trial and error method. As a result of this, the magnetic samples were heated using currents between 200A and 310A depending on the MGC content at 290 kHz for 5 minutes using an induction heating system (Easy Heat 0224, Ambrell, USA). Once within the temperature range, the applied current was reduced to set the current value to keep the sample within the temperature range for another 5 minutes. This current value was called holding current. Table 3.4 shows the heating and holding currents based on the MGC content in the cement. The temperature changes on the surface of the sample, acrylic holder and coil were recorded in every 1 second by ResearchIR software and manually noted every 60 seconds.

Table 3.4 Induction heating of the samples

	Heating Current (A)	**Holding Current (A)**
0%MGC	310	270
10%MGC	310	270
20%MGC	240	210
30%MGC	220	187
40%MGC	200	170

3.8 Statistical Analysis

Statistical analysis of all quantitative data was analysed using Sigma Plot 13. The Shapiro-Wilk test was used to evaluate the normal distribution of the data. If the data was normally distributed ($p>0.05$) the results were statistically analysed performing one-way and two-way Analysis of Variance (ANOVA) followed by Tukey's *post hoc* tests to compare the means of samples. One-way Anova was performed for the data involved one factor (magnetic cement samples), in order to determine the statistical differences between sample groups. Two-way Anova was performed for the data involved two factors (time points and PMMA cement samples) in order to determine statistical differences between and within the sample groups. If the data was not normally distributed ($p<0,05$), Mann-Whitney non-parametric test was performed to determine statistical differences between and within the sample groups. The statistically significance value was set as $p<0.05$.

Box and whiskers were plotted to present the distribution of data, which shows maximum, upper quartile (Q3), median (Q2), lower quartile (Q1) and minimum. In this study, Minitab 18 was carried out to plot the data. A schematic diagram of box and whisker is shown in Figure 3.22. Calculations of Q1 and Q3 are given in equation 3-6 and equation 3-7. Interquartile range (IQR) is the difference between Q3 and Q1 (see equation 3-8), which presents 50% of data. Outliers are calculated using equation 3-9 and equation 3-10 below;

$$Q1 = (1/4)\,(n+1) \qquad \text{Equation 3-6}$$

$$Q3 = (3/4)\,(n+1) \qquad \text{Equation 3-7}$$

$$IQR = Q3 - Q1 \qquad \text{Equation 3-8}$$

$$\text{Outlier } 1 = Q1 - 1.5(IQR) \qquad \text{Equation 3-9}$$

$$\text{Outlier } 2 = Q3 + 1.5(IQR) \qquad \text{Equation 3-10}$$

Where n is sample number.

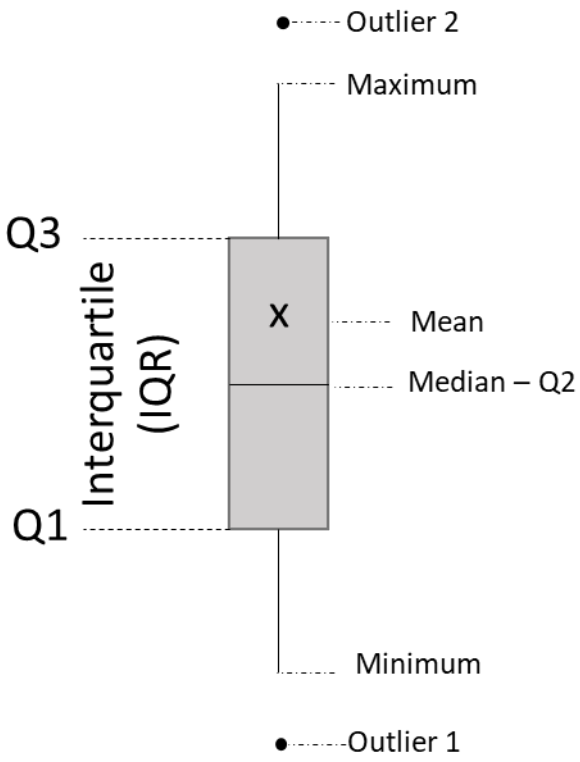

Figure 3.22 Schematic diagram of box and whisker plot

4 Results and Discussion: Production and Characterisation of Magnetic Glass Ceramic and PMMA Cement

This chapter presents the results of the production and characterisation of MGC. Silicone rubber mould design and the dimensions of prepared samples are demonstrated. Next, setting properties and morphologies of plain PMMA cement samples and the influence of ageing and storage conditions on mechanical properties of these cements are evaluated.

4.1 Production of Magnetic Glass-Ceramic

Glass-ceramic composition, preparation technique and melting temperature may alter their bioactivity, crystalline phases, mechanical properties and magnetism [151]. In this study, MGC in the system Na_2O-CaO- SiO_2-P_2O_5 - Fe_2O_3-FeO was produced by melting at 1550°C and quenching in water as described in Section 3.1. The frits (*Figure 4.1*-A) were ground and sieved (*Figure 4.1*-B) to obtain powder particles smaller than 53 µm (*Figure 4.1*-C). Each batch was produced, ground and sieved individually. The batches were then mixed into a larger batch in order to prevent variations in particle size distribution between the batches. The larger batch was used for producing test samples to obtain accurate results since the variations in particle sizes distribution can affect the results.

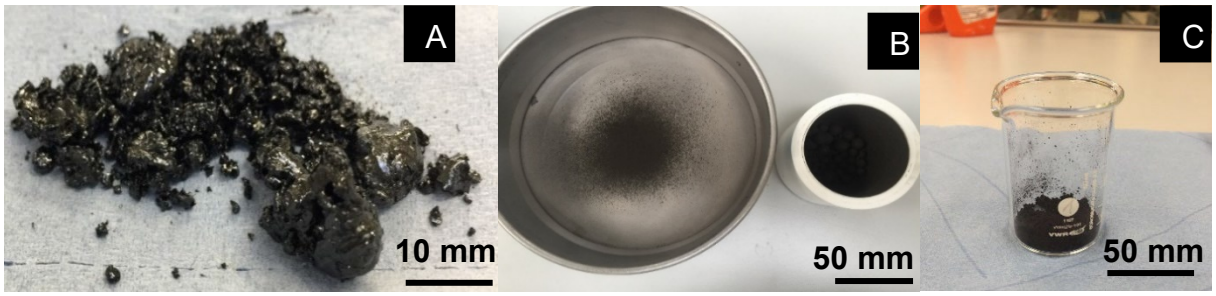

Figure 4.1 A) MGC frits B) Grinding and sieving C) MGC powder

In order to assess the yield percent of obtained MGC frits and MGC powder, the following equation is used

$$\text{Yield percent} = \frac{Actual\ mass}{Theoretical\ mass}\ x100 \qquad \text{Equation 4-1}$$

Table *4.1* presents the theoretical mass of MGC and the actual mass of three batches of MGC frits and obtained powders. The theoretical mass of MGC was 10 grams. However, only 7.40 ±0.3 g of frits was obtained, as part of the material remained on the crucible walls. Thus, yield was 74±3%. After grinding and sieving procedures, the obtained powder was 6.50±0.4 g, hence, the yield decreased to 65±4%.

Table 4.1 Theoretical and actual mass of the MGC obtained after quenching, grinding and sieving (The data presents mean value ± standard deviation (μ ±σ), n=3)

Material	Theoretical mass of MGC	Actual mass of MGC Frits	Obtained MGC Powder
Mass (g)	10	7.40±0.3	6.50±0.4

Approximately 12% of the material was lost during grinding and sieving. The crucible (Figure 4.2-A) with and without the reagents, after decomposition of the MGCs (Figure 4.2-B) and after quenching the melt (Figure 4.2-C) was weighed out.

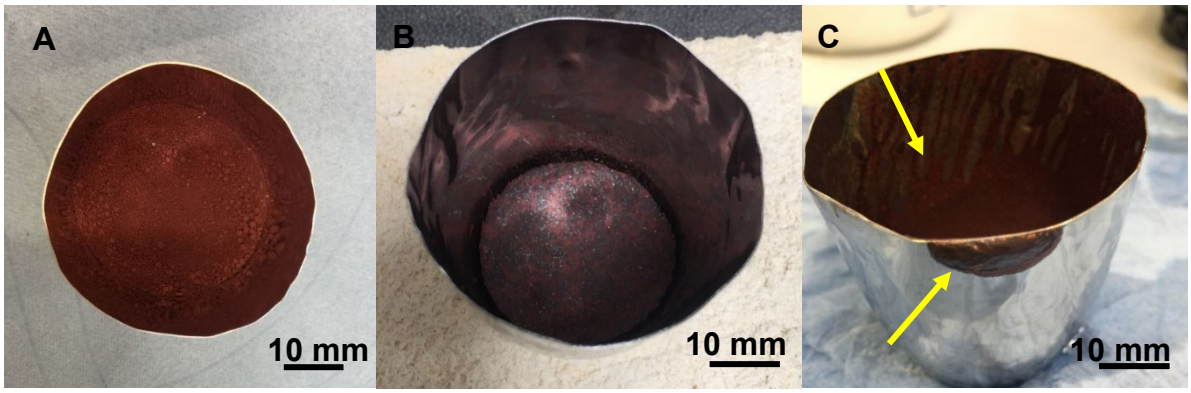

Figure 4.2 A) Raw reagents in Pt crucible B) Decomposed reagents in Pt crucible C) Residual MGC melt inside and around the Pt crucible after quenching (yellow arrows indicate the MGC residuals)

Table *4.2* provides the mass measurements of the materials and crucibles throughout the MGC production. The main reason for the difference between actual and theoretical mass was detected when the crucible was weighed after quenching the MGC. It showed that approximately 26% of the material could not be quenched and was left inside and around the crucible as noted in Figure 4.2-C. As it can be seen from Table 4.2, there was approximately 27.4% mass loss during the decomposition phase. This is due to the decomposition of Na_2CO_3, $CaCO_3$ and $FeC_2O_4.2H_2O$ reagents, which was reported by several studies [152-157].

Table 4.2 Mass measurements of the reagents and crucible throughout the melting and quenching procedure (The data presents mean value ± standard deviation (μ ±σ), n=3)

Material	Pt Crucible	Pt Crucible+Raw reagents	Pt Crucible+Decomposed Reagents	Pt crucible after quenching
Mass(g)	52.32	66.2±0.2	62.4±0.2	54.9±0.1

4.2 Characterisation of Magnetic Glass-Ceramic (MGC)

4.2.1 X-Ray Diffraction (XRD)

The XRD patterns obtained from MGC powder and the reference materials, magnetite and hematite powders, are presented in Figure 4.3. XRD patterns of eight batches of MGC powder and the reference materials are presented in Appendix A.1. A crystalline magnetite phase embedded in the amorphous glass phase can be clearly seen for MGC pattern. Magnetite crystal peaks were detected at 2θ value around 18.1°, 30.25°, 35.74°, 43.25°, 53.74, 57.2° and 62.8°. A small amorphous halo could be observed at 2θ between 26° and 38° which is in accordance with the other studies [61, 158]. As the plot shows, the MGC had only magnetite phase and the lack of non-magnetic hematite phase proved that the applied melting temperature was optimal to allow transformation of hematite (raw material) into crystalline magnetite. The influence of melting temperature on formation of crystalline magnetite was reported by Bretcanu et al [159]. It was found that increasing the melting temperature from 1400°C to 1550°C increased the crystalline magnetite and reduced hematite phase in the composition.

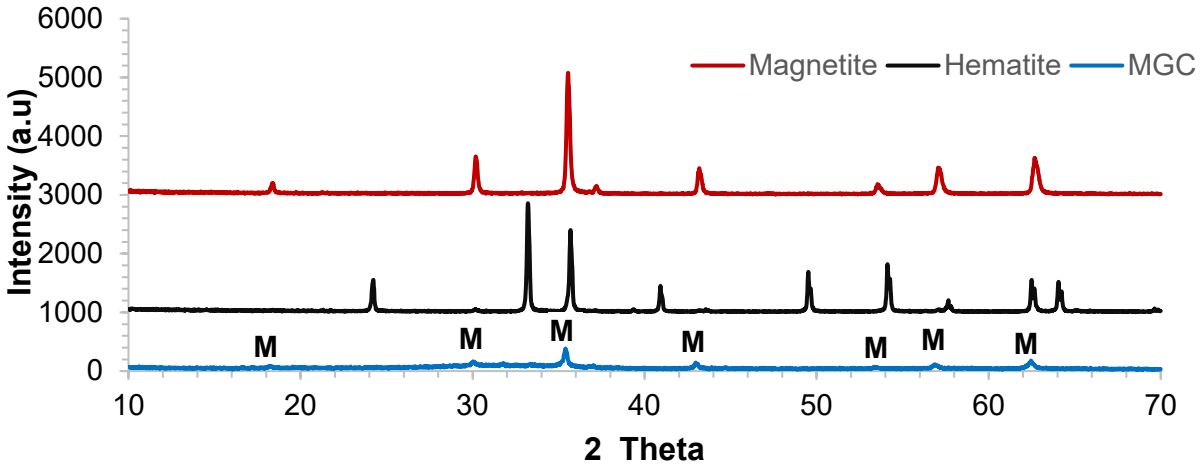

Figure 4.3 The XRD pattern of MGC, magnetite and hematite powders (M=magnetite crystals)

4.2.2 Differential Thermal Analysis (DTA)

DTA curve of MGC powder, using a heating rate of 20°C/min up to 1550°C is shown in Figure 4.4. DTA curves of six batches of MGC powder are presented in Appendix A.2. The curve exhibits characteristic temperature of glass-ceramics such as glass transition temperature (Tg), crystallisation temperature (Tc) and melting temperature (Tm). Tg was detected at 516°C, which is similar to Tg values for iron-rich glass-ceramic compositions [160]. This also proved that there was an amorphous phase in the glass-ceramics structure. Two exothermal peaks were observed at 624°C (Tc1) and 754°C (Tc2) related to the crystallisation temperatures. Two endothermal peaks were observed at 1068°C (Tm1) and 1294°C (Tm2) related to the melting temperatures. The two crystallisation and melting temperature peaks showed that two different crystalline phases formed during heating to 1550°C. Bretcanu et al. [6] reported the crystallisation of hematite and iron silicate for magnetic glass-ceramics in the system of Na_2O-CaO- SiO_2-P_2O_5 - Fe_2O_3-FeO during heating to 1550°C.

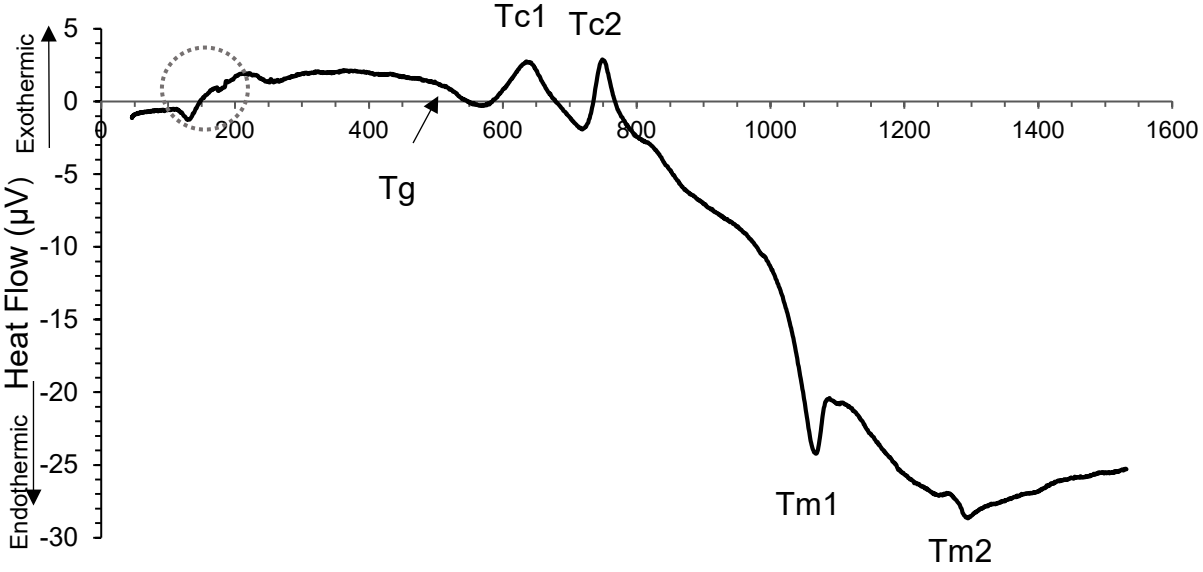

Figure 4.4 DTA curve obtained for MGC at 20°C/min (The circled area is an error of the DTA thermocouple at low temperature and can be ignored)

4.2.3 Hot Stage Microscope (HSM)

HSM was carried out in air up to 1050°C using a heating rate of 5°C/min in order to determine the shrinkage of the material. The silhouettes of the cylindrical samples were recorded and analysed by the software. Figure 4.5 shows characteristic silhouettes of the cylindrical sample during heating.

At room temperature (T_{AT}), the sample had sharp edges. It can be clearly seen that increasing the temperature to 998°C, reduced the size of the silhouette and slightly rounded the edges. From 998°C to 1045°C, the sample became smaller and more rounded and at 1048°C, the sample had a sphere-like shape and started to melt.

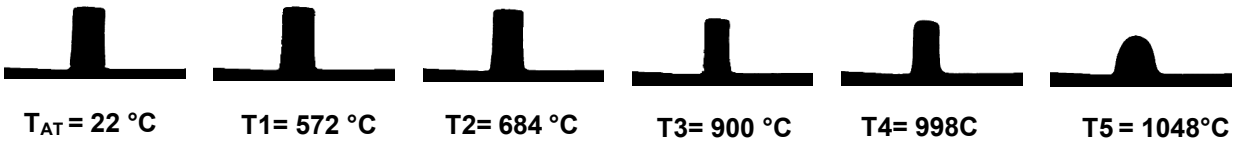

Figure 4.5 HSM silhouettes of typical MGC recorded at different temperatures

Figure 4.6 shows the shrinkage (%) of the sample throughout the heating process. Sintering and softening steps can be identified from the graph. Sintering started at T1 (572°C) and ended at T2 (684°C). The sample started to soften at T3 (~900°C) and ended at T4 (~998°C). The sample had a sphere-like shape at T5 (1048°C) and started to melt. The shrinkage of the sample before melting was ~18%. The sintering temperature range can be determined as 650-900°C. Tg (glass transition temperature) is related to viscosity of material. Therefore, Initial sintering temperature takes place after Tg [161, 162]. Although the heating rates were different, comparisons between DTA and HSM showed Tg and T1 took place at similar temperatures (Table 4.3). Moreover, Tc1 is similar to T2 and Tm1 is similar to T5.

Table 4.3 Comparison between characteristic temperatures obtained from DTA and HSM

DTA	**Tg**	**Tc1**	**Tc2**	**Tm1**	**Tm2**
T°C	516	624	754	1068	1294
HSM	**T1**	**T2**	**T3**	**T4**	**T5**
T°C	572	684	900	998	1048

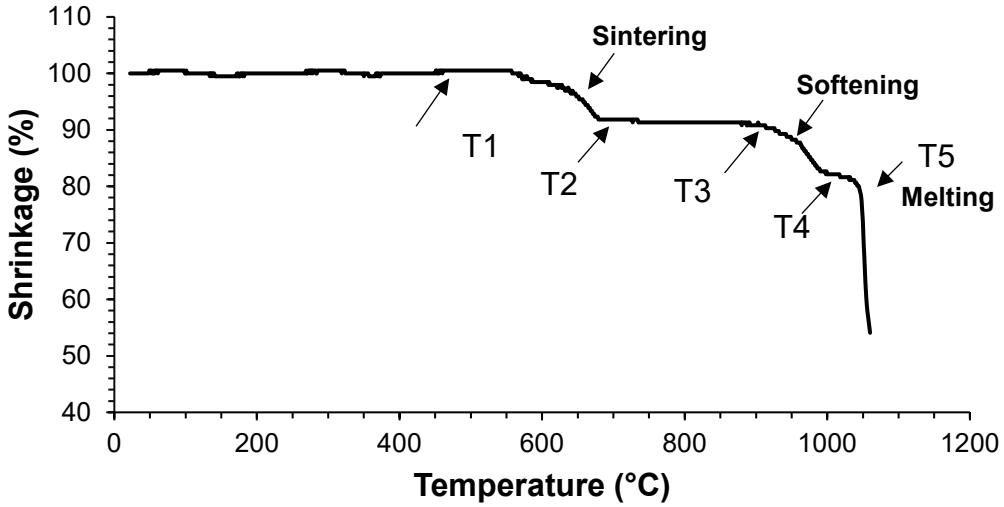

Figure 4.6 Shrinkage of typical MGC (corresponding to Figure 4.5) during heating

4.2.4 SEM Analysis

In order to analyse the morphology of the MGC powder, SEM analysis was performed. Figure 4.7 shows that sieved MGC powder had particles size less than 53 μm, irregular shapes and sharp edges. The majority of particles were smaller than 20μm and these fine particles tended to form clusters around the big particles, which were in the range of 30-50μm. In Figure 4.7-B and C, columnar octahedral shapes (indicated with red arrow) were observed, which represent the magnetite crystals embedded in the amorphous residual phase, in accordance with the literature [61, 163, 164]. Magnetite crystals were formed during quenching and were uniformly spread in the glass matrix. There was no need to perform any chemical etching to observe the magnetite phase since it was visible on the SEM as produced after grinding and sieving.

Electron diffraction X-ray (EDX) was performed on the glass-ceramics in order to assess the elemental composition, which consists of Fe, Na, P, Si and Ca. Figure 4.7 shows the EDX images and spectra of the MGC performed on the marked areas, magnetite crystalline phase (red circle) and glass-ceramic itself (yellow circle). The EDX spectrum of a “crystalline phase” showed a higher peak for Fe, when compared to “amorphous phase” spectrum. The intensity of Na, Si, P and Ca peak was lower in the “crystalline phase spectrum”.

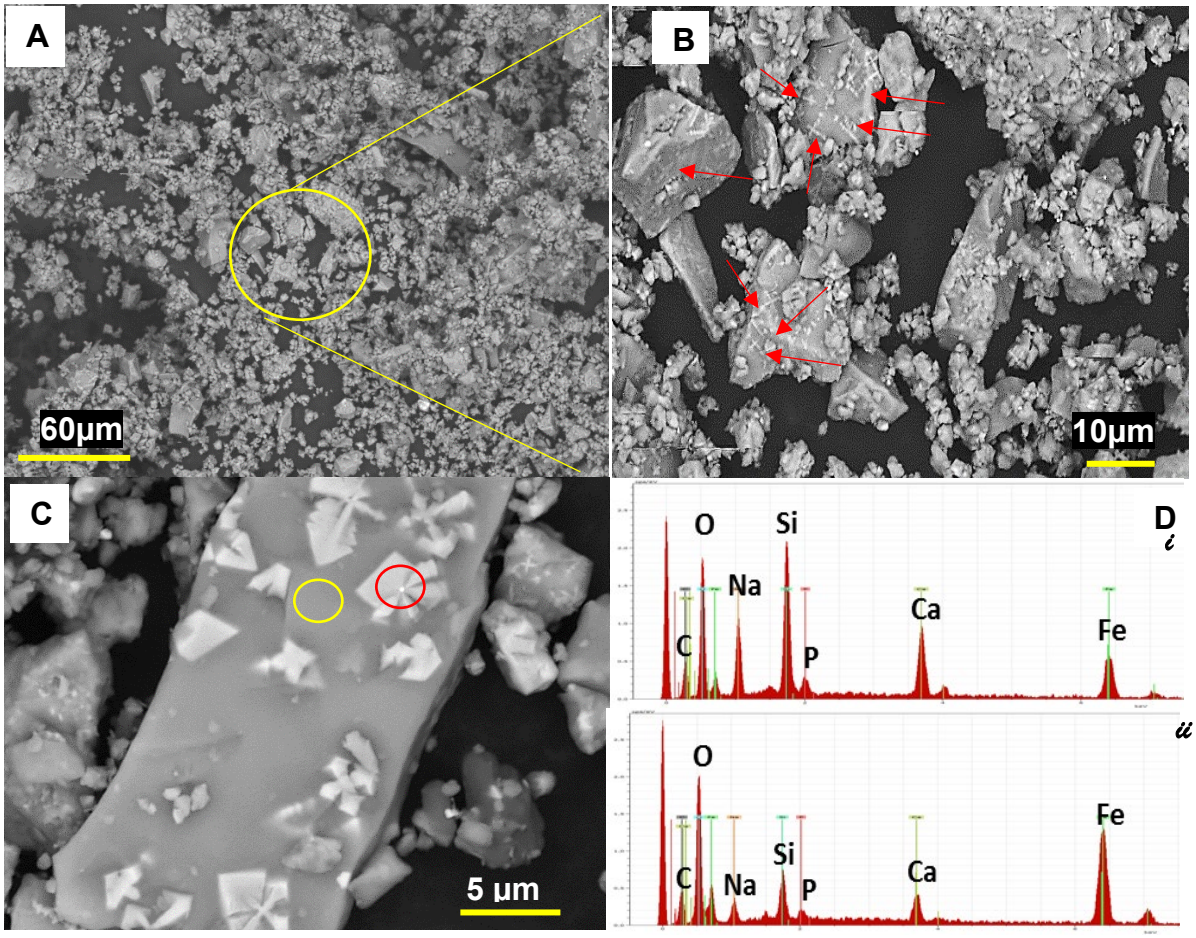

Figure 4.7 SEM image of MGC particles a) 500x magnification b) 2000x magnification c) 6000x magnification and EDS spectra (same scale) of MGC D-i) yellow circle ("amorphous phase") D-ii) red circle ("crystalline phase")

4.2.5 Summary of Results and Discussions

In this section, yield percent of the produced MGC and its properties obtained from XRD, DTA, HSM and SEM were presented. In order to determine crystalline phases of the MGC, XRD was carried out and the results were compared to XRD patterns of hematite and pure magnetite. It was found that MGCs only showed magnetite crystalline phase and a broad amorphous phase was observed between 26° and 38°.

Endothermic and exothermic peaks of MGC were investigated using DTA. These peaks referred to crystallisation and melting temperatures of this glass-ceramic. Two exothermic peaks and two endothermic peaks were observed during crystallisation and melting processes, which showed that there were two crystalline phases. The MGC crystallised at 624°C (Tc1) and 754°C (Tc2) and melted at 1068°C (Tm1) and 1294°C (Tm2). The Tg of MGC was detected at 516°C, which was consistent with a study

performed by Karamanov et al [160]. According to Bretcanu et al. [6] the two crystalline phases were hematite and silicate iron.

The behaviour of MGC during sintering and softening processes was evaluated by a heating microscope at a heating rate of 5°C/min at 1050°C. During the heating process, shrinkage (%) in area and corresponding silhouettes of MGC at specific temperatures were determined. The shrinkage of the sample before melting was ~18%. MGC started to sinter at 572°C, the softening phase started at 900°C and the beginning of melting phase was at 1048°C.

According to the SEM images, ground and sieved particles of MGC were smaller than ≤53μm with sharp edges. Interestingly, magnetite crystals could be observed on the surface of MGC samples without etching. SEM images indicated that a crystalline magnetite phase was homogenously embedded in a glassy matrix. This showed a successful formation and growth of magnetite crystals in the glass structure by the traditional melting and quenching technique. The presence of crystalline magnetite phase was confirmed using XRD and SEM. The crystalline phase embedded into an amorphous phase will not only act as thermoseeds under the applied alternating current, but it will also increase the strength of glass. Several studies showed that magnetite base glass-ceramics show promising results in hyperthermia applications and bone regeneration [6, 17, 54, 61, 94, 163, 164]. The bioactivity properties of the obtained MGC after mixing with PMMA cement will be explained in Section 5.1.7.

In the next section, the design and fabrication of silicone rubber moulds will be presented.

4.3 Fabrication of PMMA Cement Samples Using Silicone Rubber Mould

ISO 5833:2002 and ASTM F451-16 standards indicate that test sample moulds should be made from machined blocks of PTFE. It has high stiffness and resistivity to adhesion, but it may cause rough edges and surface defects on the samples, as well as undesired dimensions. Sanding or abrasive removal of PMMA cement could result in undesirable changes in mechanical and chemical properties and may have introduced surface defects and micro cracks. Thus, the results of flexural and compression tests may have not provided representative values of the cement. Additionally, sanding each sample would increase dimensional inconsistencies within the sample batch and was a time-consuming operation. Several studies reported that PMMA samples moulded in PTFE moulds required dry sanding to correct the dimensions and polishing to smoothen the rough edges and surfaces [144, 165-168].

The fabrication process of the silicone rubber mould for desired shapes and dimensions was quick, reliable and required only limited equipment. The dimensions of the test samples were consistent and did not require any further post-processing such as sanding to size or finishing. Since more than 650 samples were prepared during this study, this was a helpful method to reduce inconsistency in test results and save time. All dimensions of the test samples were measured after the samples were removed from silicone rubber moulds.

4.3.1 Four-point Bending Test Samples

In order to achieve reliable data of the sample dimensions, measurements were taken ten times for the thickness and width and four times for the length using a digital calliper. Table 4.4 presents the average values and standard deviations of 210 samples (both types of cement, with and without MGC) using the same mould. The required dimensions, as identified in the standards, were obtained within the specified tolerances. However, the dimension of the length could be largely ignored as the span length was used to perform the flexural strength test. Similarly, the sacrificial end spaces were also ignored as some were filled whilst others were only partially filled. Figure 4.8 shows Palacos® cement samples after they were removed from the mould.

Table 4.4 Dimensions of four-point bending samples

Length (mm)	Width (mm)	Thickness (mm)
74.16 ± 0.57	9.97±0.06	3.32±0.05

Figure 4.8 Palacos® cement four-point bending test samples after removal from the mould (Arrow indicates the sacrificial ends)

4.3.2 Compressive Test Samples

As previously stated, test samples were prepared to the dimensional requirements of ISO 5833:2002 standard (h=12mm, ø=6mm). Moreover, in order to assess the influence of dimensions on compressive strength, Wintercryl cement samples were also prepared in double dimensions (h=24mm, ø=12mm), which was called W-DD/Bag. All sample measurements were taken five times along the length and across the diameter using a digital calliper. Table 4.5 shows the average values and standard deviations of 210 samples prepared in line with standard ISO 5833:2002 and 54 samples prepared in double dimensions using the same moulds. Figure 4.9 shows Wintercryl cement samples prepared in double dimensions after they were removed from the mould to perform compressive strength test.

Table 4.5 Dimensions of compressive strength test samples

Samples	Length (mm)	Diameter (mm)
Standard Dimensions	12.01 ± 0.08	5.97±0.06
Double Dimensions	23.99 ± 0.10	11.93±0.09

Figure 4.9 Wintercryl cement compressive strength test samples (double dimension)

4.3.3 Cytocompatibility Test Samples

In order to place and remove the samples with ease from the 12-well cell culture plate, they were designed in disc shapes with 20 mm diameter and 5 mm thickness, considering the dimensions of the cell culture plates which were approximately 22 mm diameter and 6.9 mm height. The thickness and diameter of the samples were measured four times along the thickness and across the diameter. The average of the measurements and standard deviations of total 203 samples prepared for the test using the same mould were calculated and are presented in Table 4.6.

Table 4.6 Dimensions of cytocompatibility test samples

Diameter (mm)	Thickness (mm)
19.19 ± 0.27	5.03±0.32

As previously reported, using a laser-cutter reduced the dimensions of disc-shape acrylic patterns approximately 1 mm due to melting of the edges. This reduction in diameter can be largely ignored since the discs could fit into the wells and it would not have any significant effect on the test results. Figure 4.10 shows Wintercryl cement samples after they were removed from the mould.

Figure 4.10 Wintercryl cement cytocompatibility test samples

4.3.4 Induction Heating Test Samples

The test samples were designed and fabricated in cubic shapes to be placed in the acrylic holder, which was suspended in the middle of an induction coil. It is important to note that although there were no dimensional requirements for this test, special care was taken to avoid any significant inconsistency, which would cause a mass difference within and between the sample groups. All the measurements were repeated five times for reliability. Figure 4.11.

Table 4.7 shows the average values and standard deviations of 50 samples. All samples were prepared using the same mould. A representative image of 20% MGC containing Palacos® cement (P20) is shown in Figure 4.11.

Table 4.7 Dimensions of induction heating test samples

Length (mm)	Width (mm)	Height (mm)
10.13 ± 0.18	9.64±0.09	10.07±0.08

Figure 4.11 Palacos® cement containing 20% MGC samples (P20) used for induction test

4.3.5 Summary of Results and Discussions

In this section, the design and fabrication of silicone moulds and the dimensions of test samples were presented. The fabrication of silicone rubber mould was cheap and quick. It facilitated placing and removing the samples without any difficulties and all samples had consistent dimensions.

Special care was taken for the fabrication of mechanical test sample moulds. The dimensions of the samples using requirements of standard ISO 5833:2002 were 75±0,1 x 10±0,1 x 3,3±0,1 mm for four-point bending test samples and 6±0.1mm diameter and 12±0.1mm height to perform compressive strength test. The additional compressive strength test samples were aimed to have double dimensions of standard test samples: 12±0.1mm in diameter and 24±0.1mm in height. This was done to evaluate the influence of dimensions, which could lead to different setting time and temperature as well as defects and porosities in the cement structure. The measurements taken using a calliper after removing the samples from the mould indicated that the required dimensions of ISO 5833:2002 standard were fulfilled.

Cytocompatibility test samples were approximately 20 mm in diameter and 5 mm height. The measurements taken using a digital caliper showed that the dimensions of disc-shape acrylic patterns were reduced approximately by 1 mm due to laser-cut machine that melted the edges. Heating test samples were approximately 10x10x10 mm^3.

The next section presents handling properties, polymerisation temperature and microstructure and mechanical properties of the two commercial PMMA cements.

4.4 Characterisation of PMMA Cement

Commercial dental and orthopedic cements, Wintercryl (W) and Palacos® (P), respectively, were used in this study to evaluate their setting properties, microstructure, and mechanical properties. Although IS0 5833:2002 standard does not require an investigation of ageing effects on long-term mechanical properties of the cement, most of the failures in implants may strongly be related to this since the polymers can highly be affected by temperature and moisture in the environment. Therefore, the cement samples were aged up to 6 months to analyse the influence on mechanical properties of the samples.

Wintercryl (W) and Palacos® (P) cement samples were prepared as described in 3.3.2. Figure 4.12 demonstrates representative temperature (Figure 4.12-a) and humidity (Figure 4.12-b) recordings in different days. Test 1, test 2 and test 3 indicate different days that the samples were prepared in the same laboratory. The range of ambient temperature was between 20 and 25 ºC. The relative humidity was in a range of 40-57%, which is consistent with standard ISO 5833:2002. Relative humidity between 30-60% is suggested for operating rooms in hospitals by AIA (American Institutes of Architects) and ASHREA (American Society of Heating, Refrigerating and Air-conditioning Engineers). However, HTM (Health technical Memorandum) 2025 suggests that relative humidity should be kept between 40-60% [169]. It is important to note that ambient temperature and relative humidity play important roles in setting properties of PMMA bone cement, as reported in Chapter 2. The relative humidity lower than 40% and higher than 60% can influence the working time for 1-3 minutes [170].

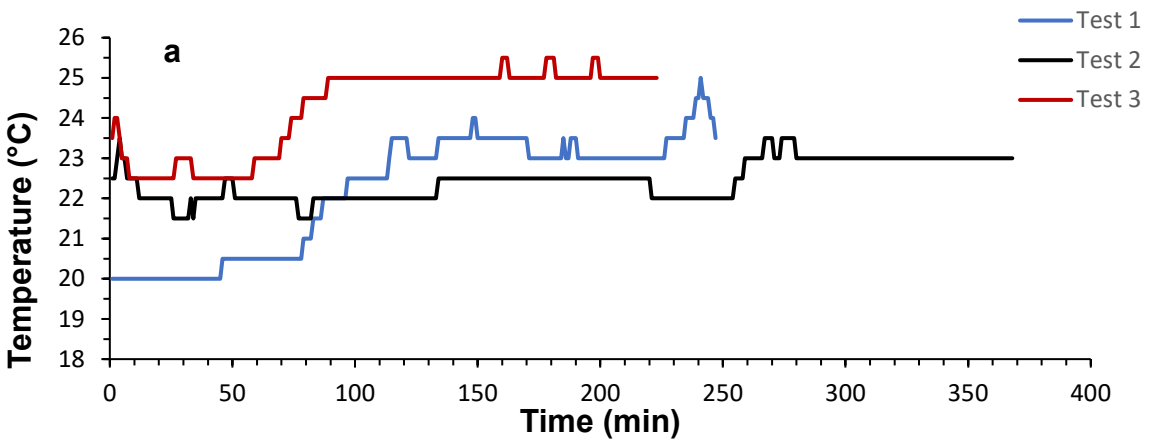

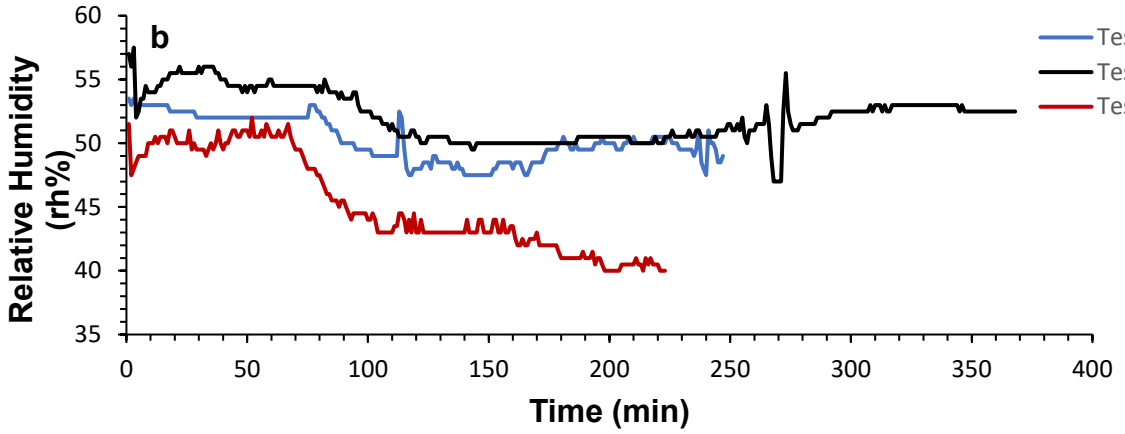

Figure 4.12 a) Relative humidity and b) corresponding temperature profiles during preparation of PMMA cement

4.4.1 Setting Properties and Polymerisation Temperature of Cement

The setting properties of the cements were evaluated mixing approximately 6 grams of powder with 3 ml of liquid (2:1g/ml). When the powder was in contact with the liquid, the temperature and time recordings were started. Mixing, working and waiting times were also manually recorded. The mixing time was approximately 30-40 seconds for every cement preparation, while the working time was kept to approximately 1.5-2 minutes. During the working time, the cement was divided into two parts and placed in the mould. Mixing, waiting and working times, of Palacos® (P) and Wintercryl (W) cement samples are summarised in Table 4.8. It was found that Palacos cement® had a shorter waiting time than Wintercryl cement at 23 ±1°C. While total time was approximately between 6-7.8 minutes for Wintercryl, it was approximately between 4-5.2 minutes for Palacos®.

Table 4.8 Setting properties of Palacos® (P) and Wintercryl (W) cement samples at 23°C ±1 (The data presents mean value ± standard deviation (μ ±σ) for waiting time, $5 \leq n \leq 3$)

Material	**Ambient Temperature**	**Mixing Time** (ΔT1)	**Waiting Time Interval** (ΔT2)	**Working Time Interval** (ΔT3)	**Total Time** (ΔT1+ΔT2+ΔT3)
W	23 ±1°C	~30-40 s	4.3±0.8 min	~1.5-2 min	~6-7.8 min
P	23 ±1°C	~30-40 s	2.1±0.4 min	~1.5-2 min	~4-5.2 min

It was expected that the setting properties of the cement samples would change at different ambient temperatures in accordance with the literature [14, 120]. Since the laboratory was not temperature controlled, the samples could not be prepared at a constant temperature. Therefore, the waiting times of the prepared samples were always recorded and assessed to understand how the ambient temperature influenced the setting properties of the cement. Table 4.9 provides waiting times of the cement at different ambient temperatures when the mixing and working times were kept constant. As expected, the increase of the ambient temperature from 19°C to 25°C, accelerated the waiting times for both P and W cements.

Table 4.9 Waiting times of Wintercryl (W) and Palacos® (P) cement samples at different ambient temperatures (The data presents mean value ± standard deviation (μ ±σ) for waiting time interval, $5 \leq n \leq 3$)

	Waiting Time Interval (ΔT2) (min)	
Ambient Temperature	**W**	**P**
25.5 ±0.5°C	3.2±0.2	1.5±0.3
20.5 ±0.5°C	5.9±0.3	2.9±0.4
19 ±0.5°C	6.7±0.5	4.1±0.2

The polymerisation reaction temperature profiles of Palacos® and Wintercryl cements were recorded as described in 3.4.1. Typical exothermic reaction temperatures during the polymerisation of selected Wintercryl and Palacos® cement samples at 23.7±0.1°C are shown in Figure 4.13. As previously reported, the waiting time of Palacos® cement was shorter than Wintercryl cement. The temperature recordings of the cement samples also confirmed that Palacos® cement samples reached the maximum polymerisation temperature in a shorter time than Wintercryl cement samples. The maximum temperature reached by P and W samples were 30.5°C and 32°C respectively (when the ambient temperature was 23.7±0.1°C). Since the temperatures were measured from sacrificial ends, these measurements do not reflect actual polymerisation temperatures. However, according to the graph and presented waiting times, it can be assumed that setting time of Palacos® cement may be shorter than Wintercryl cement.

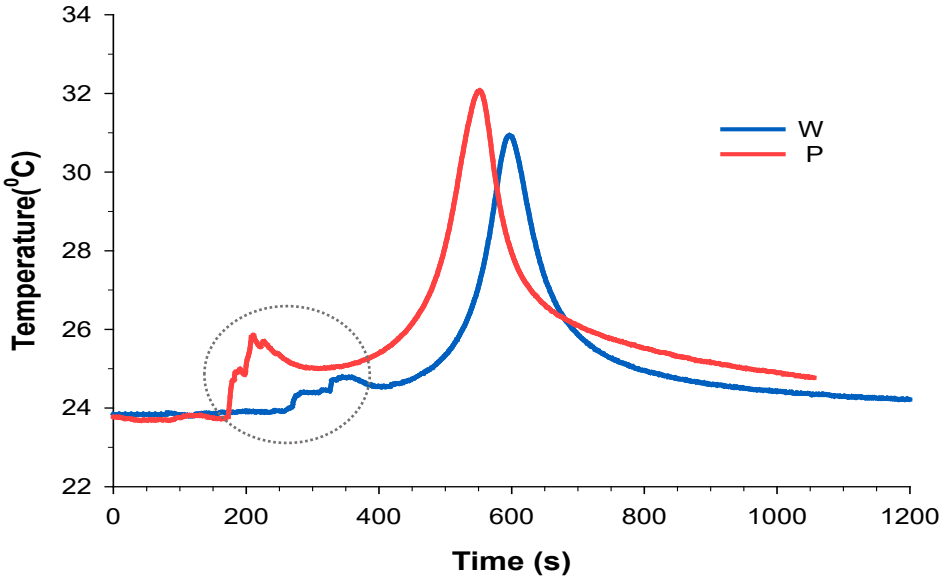

Figure 4.13 Polymerisation reaction temperature during the setting process of Palacos® (P) and Wintercryl (W) cement samples at 23.7°C (The temperature fluctuations in the circled area are due to touching the thermocouples while placing the samples in the mould)

It is worth noting that powder to liquid ratio, compositions of liquid and powder components and the amount of DMPT (N,N-dimethyl-p-toulidine) and BPO (benzoyl peroxide) have an impact on maximum polymerisation temperatures. It was reported that the size and size distribution of PMMA powder may also influence the temperature [171].

The temperature readings were taken from two cement bars at a time using four thermocouples; T1, T2, T3 and T4, see Figure 4.14. The pairs of cement bars prepared from each batch are coded A1-A2 (batch A), B1-B2 (batch B) and C1-C2 (batch C). Temperature recordings of three batches (6 samples) Wintercryl cement samples at 23.9±0.1°C are shown in Figure 4.15 (see Appendix B.1 for Palacos® cement). As the temperature measurements taken from both sides of the samples showed variations, the sample pairs and groups varied as well. These variations were due to not fully filling the sacrificial ends. Smaller volume of sacrificial ends led to lower temperature readings. Polymerisation temperature varied between approximately 29°C and 32°C.

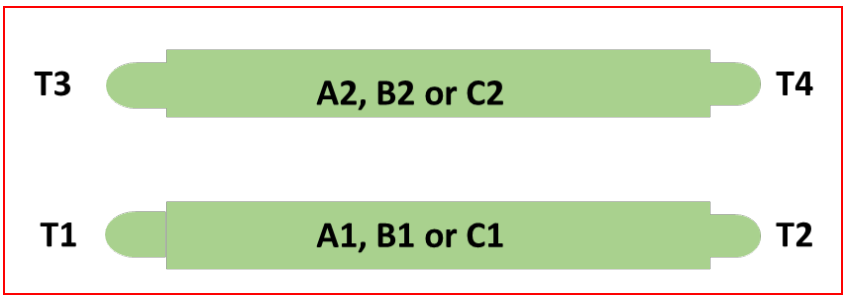

Figure 4.14 Schematic diagram of sample and thermocouple positions

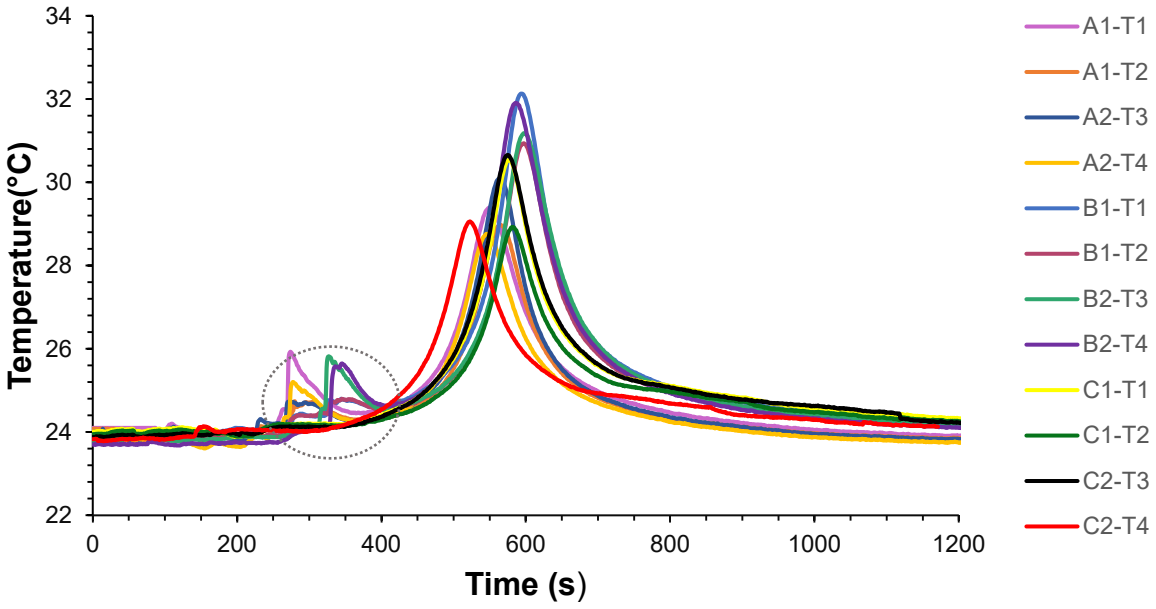

Figure 4.15 Temperature-time profiles of groups A, B and C of Wintercryl cement samples. (The temperature fluctuations in the circled area are due to touching the thermocouples while placing the samples in the mould)

The aim of recording the time and temperature of cement samples was to estimate the setting time and temperature. Since the sacrificial ends showed variations, this could not be done accurately. However, an example of how to determine the setting time for W cement, using B1-T1 pair is presented in Figure 4.16. Setting time of the cement was 9.2 minutes and setting temperature was 28°C. The temperature readings were not taken from the centre point of the samples to not create any surface defects since they would be used for the four-point bending test.

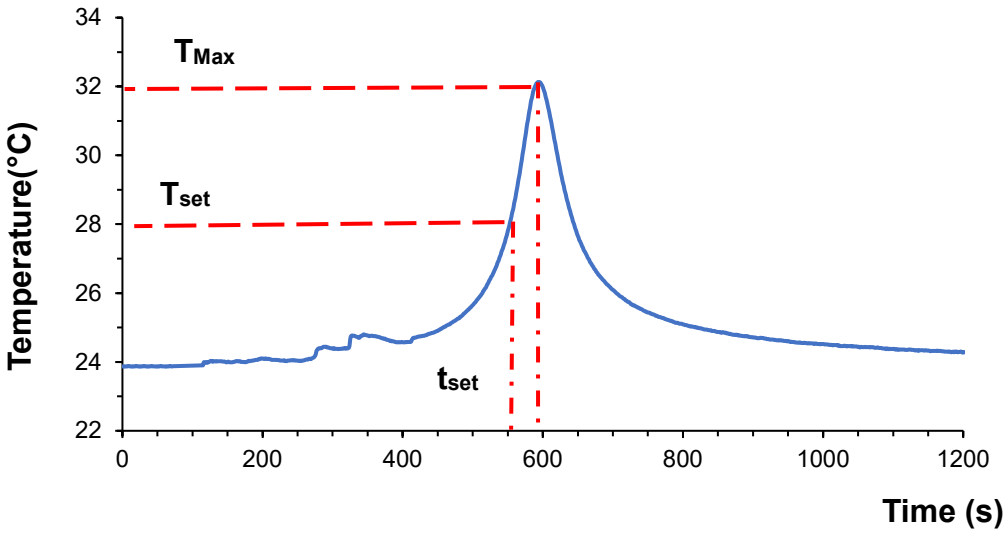

Figure 4.16 Temperature-time profile of Wintercryl cement sample (B1-T1). T_{max} refers to maximum temperature, T_{set} refers to the setting temperature and t_{set} is the setting time

4.4.2 Scanning Electron Microscope Imaging

The SEM analysis on the powder components of Wintercryl and Palacos® cements are provided in Figure 4.17a and Figure 4.17b respectively. The powder particle sizes of Winercryl were in the range of 10 to 100 µm. The majority of particles was smaller than 50 µm (Figure 4.17a). The powder particle sizes of Palacos® cement were mostly in the range of 10 to 60 µm with the majority of powder particles smaller than 50µm. Furthermore, Palacos® cement powder component contains radiopacifier, zirconium oxide (ZrO_2), which are the white particles dispersed between PMMA beads in Figure 4.17b. The particles size of ZrO_2 is less than 5 µm.

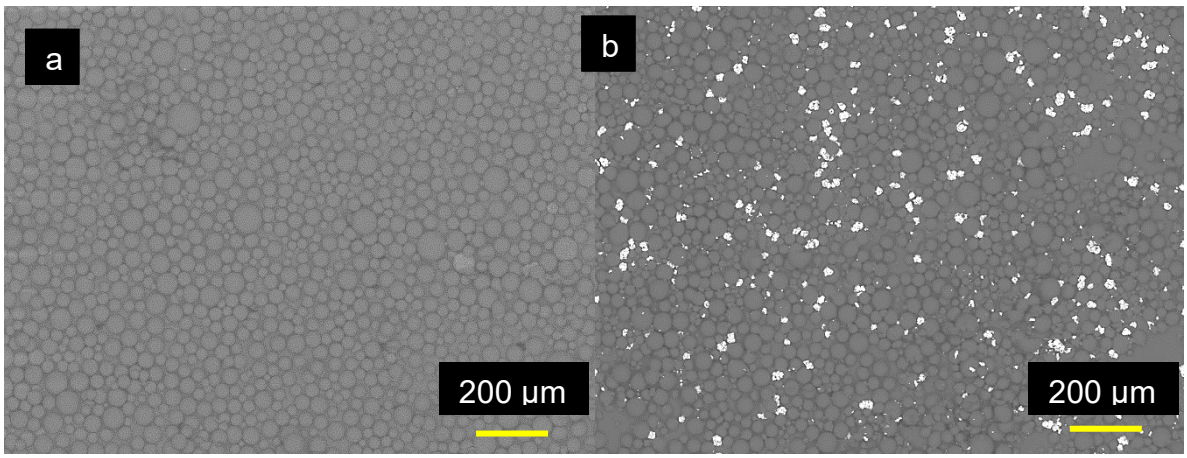

Figure 4.17 SEM images (100x magnification, backscattered electron imaging) of a) Wintercryl powder particles and b) Palacos® powder particles

Figure 4.18 presents the SEM images and corresponding EDS spectra of Wintercryl (Figure 4.18-a) and Palacos® (Figure 4.18-b) cements (after polymerisation). The elemental composition of the cement samples confirmed that Wintercryl cement sample only had carbon (C) and oxygen (O) elements, whilst Palacos cement had C, O and zirconium (Zr) elements. The radiaopacifier reagent, zirconia, could still be observed on the surface of the cement. The size of ZrO_2 particles were less than 10 µm and the particles formed small clusters (10-40 µm size).

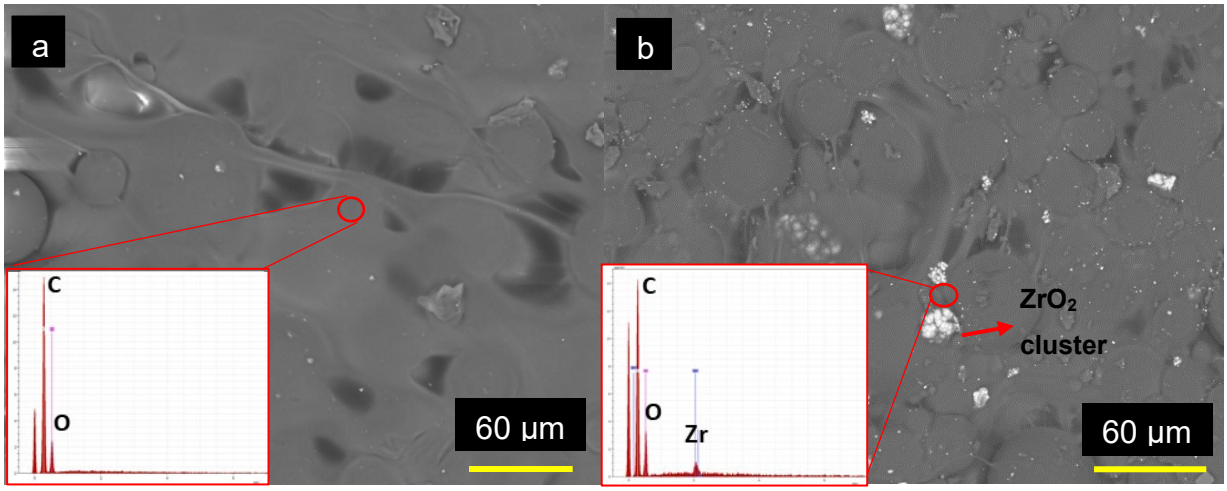

Figure 4.18 Morphology (500x magnification, backscattered electron imaging) and EDS spectra (same scale) of the cements a) Wintercryl cement b) Palacos® cement

For a deeper investigation on the surface morphology of Wintercryl and Palacos® cements, the samples were gold coated and analysed under Tescan SEM at 8kV. Figure 4.19-A shows the morphology of Wintercryl cement sample. PMMA beads of Wintercryl cement were in spherical forms in the range of 5 to 55 µm sizes. As can be seen, polymerisation of MMA created connections between PMMA beads; however, the beads could still be distinguished on the surface of the cement, maintaining their spherical shapes. The polymerisation of MMA monomer created some porosity. The length of the pores varied between 25 and 125 µm. The SEM image of Palacos® cement is shown in Figure 4.19-B. Similar to Wintercryl, spherical PMMA granules <50 µm were observed. Zirconia particles are less than 5 µm (see yellow arrows); however, they formed clusters with sizes between 10-40 µm. Pores created during polymerisation have sizes between 25-100 µm.

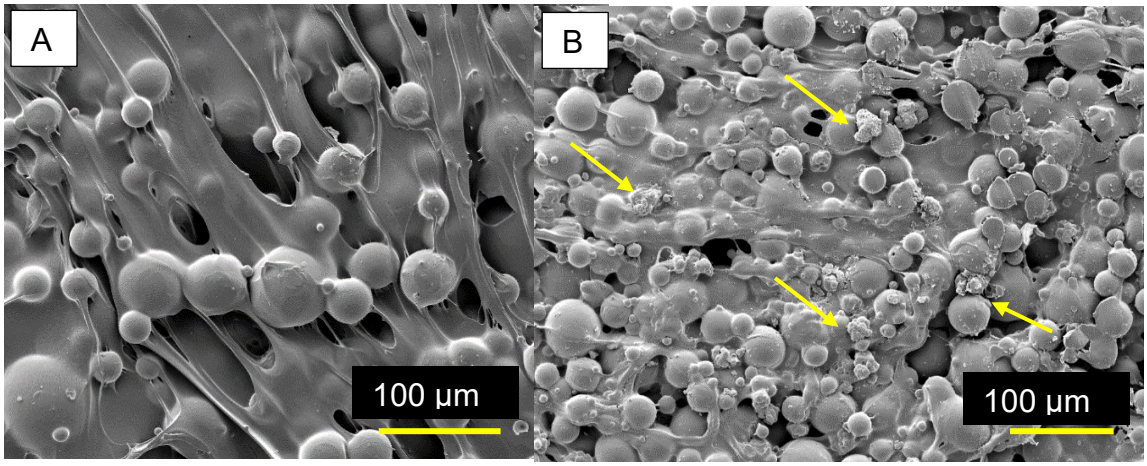

Figure 4.19 Morphology of plain a) Wintercryl and b) Palacos® cement samples at 500x magnification using secondary electron imaging, (yellow arrows represent zirconia particles)

Figure 4.20 shows the two surfaces of PMMA cement that were in contact with aluminium sheet (Figure 4.20-A) and silicone rubber (Figure 4.20-B). The surface that was contact with aluminium sheet was different than the surface was contact with silicone rubber. Whilst PMMA beads could be distinguished in Figure 4.20-B, the PMMA beads were covered with a layer of converted MMA in Figure 4.20-A. This may indicate that silicone rubber mould had hydrophobic properties, which caused low amount of converted monomer on the surface since PMMA beads could be distinguished on the surface of the cement. However, it could be seen that the side was in contact with aluminium sheet had higher amount of converted MMA monomer compared to the other side.

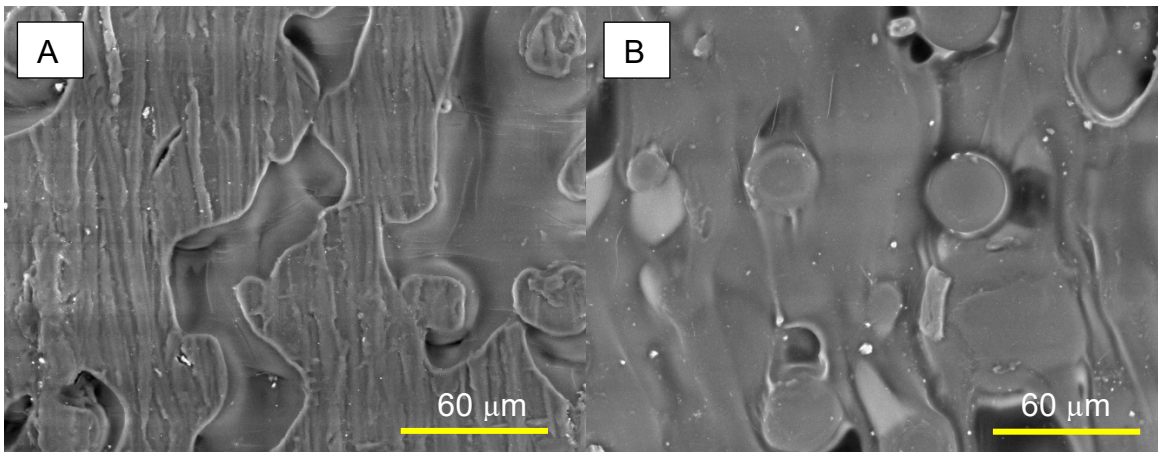

Figure 4.20 Morphology (500x magnification, backscattered electron imaging) of A) Aluminium sheet contacted side B) Silicone rubber contacted side of plain Wintercryl PMMA cement sample

4.4.3 Four-Point Bending Test

Bending strength and bending modulus properties of aged W-Air (Wintercryl cement kept in open air storage), W-bag (Wintercryl cement kept in closed air storage) and P-bag cement (Palacos cement kept in closed air storage) samples were assessed using four-point bending tests. Wintercryl cement samples were kept in open and closed air storage for 6 months whereas Palacos samples were always kept in a closed air storage. A representative image of fractured W-bag samples is provided in Figure 4.21. The fractures mostly occurred between the inner and outer loading points (See Figure 3.12, Chapter 3) rather than in the area of highest stress concentration, which is between the inner loading points, in the middle of the sample.

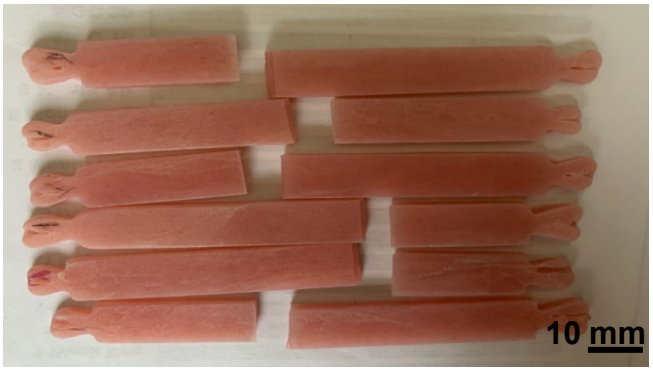

Figure 4.21 Representative images of W-bag four-point bending test samples

The time points were 1, 2, 3, 7, 14, 21, 28, 60, 180 days. Six samples were tested for each time point (162 samples in total). For the first three time points, not all samples fractured. On day 1, while five samples of W-air fractured and only three samples of W-bag and four samples of P-Bag fractured. On day 2, four samples of W-air, five samples of W-bag and two samples of P-bag fractured.

On day 3, three samples of W-air, two samples of W-bag and P-bag fractured. Moreover, one out of six test samples of W-air on day 2, 60 and 180, one sample of W-bag on day 21 and one sample of P-bag on day 60 fractured unpredictably (non-standard fracture). These samples were not included in data. These anomalies were due to the human error during the initial setting of the test rig and inner loading points. 20% of mean values of bending strength and modulus were analysed and these sample that have non-standard fractures were found below the limit. A representative image of a Wintercryl cement sample (W-air) tested on day 60 is shown in Figure 4.22.

Figure 4.22 Representative image of W-air sample on day 60 with non-standard fracture

As mentioned above, anomalies were excluded from the analysis. Table 4.10 provides the sample sizes of W-bag, W-air and P-bag sample groups at each time point, for bending strength (B) and bending modulus (E). The reason of different sample sizes of B and E for the same time point was due the samples, which did not fracture under the applied forces. For those samples, bending strength could not be calculated since it required the force at the fracture; however, bending modulus could be still calculated using load range between 50 N and 15 N.

Table 4.10 provides the sample sizes (n) of W-air, W-bag and P-bag samples at each time point for bending strength (B) and bending modulus (E) results.

Time Points		**Day 1**	**Day 2**	**Day 3**	**Day 7**	**Day 14**	**Day 21**	**Day 28**	**Day 60**	**Day 180**
W-Bag	*B*	n=3	n=5	n=2	n=6	n=6	n=5	n=6	n=6	n=6
	E	n=6	n=6	n=6	n=6	n=6	n=5	n=6	n=6	n=6
W-Air	*B*	n=5	n=3	n=3	n=6	n=6	n=6	n=6	n=5	n=5
	E	n=6	n=6	n=6	n=6	n=6	n=6	n=6	n=5	n=5
P-Bag	*B*	n=4	n=2	n=2	n=6	n=6	n=6	n=6	n=5	n=6
	E	n=5	n=5	n=6	n=6	n=6	n=6	n=6	n=5	n=6

Figure 4.23 and Figure 4.24 present bending strength results of the W-bag, W-air and P-bag samples for each time-point. The results show that all the samples had higher bending strength than the minimum requirements of ISO 5833:2002 standard (50 MPa). Over time, from day-1 to day-180, bending strength increased. Although, the growth was not linear and varied during the 6 months, it was probably due to the inhomogeneity of the material. Range of values for all samples were between 51.8 and 77.4 MPa (see Figure 4.23). The minimum value occurred on day-3 time point for W-air sample and the maximum value occurred on day-60 time point for P-bag sample. For day-3 time point, there were only two samples for W-bag and P-Bag cement groups so the graph (Figure 4.23) shows only the mean, minimum and maximum values. Regarding the mean values, the range of variation of bending strength was between 55.8 and 73.6 MPa (see Figure 4.24). Similarly, P-bag sample had only two samples on day-2 time point. Moreover, two-way ANOVA followed by Tukey *post hoc* analyses showed that there was no significant difference between W-bag, W-air and P-bag samples ($p>0.05$). However, each sample group (W-Bag, W-Air and P-Bag) showed significant differences ($p<0.05$) over the 6-month time period.

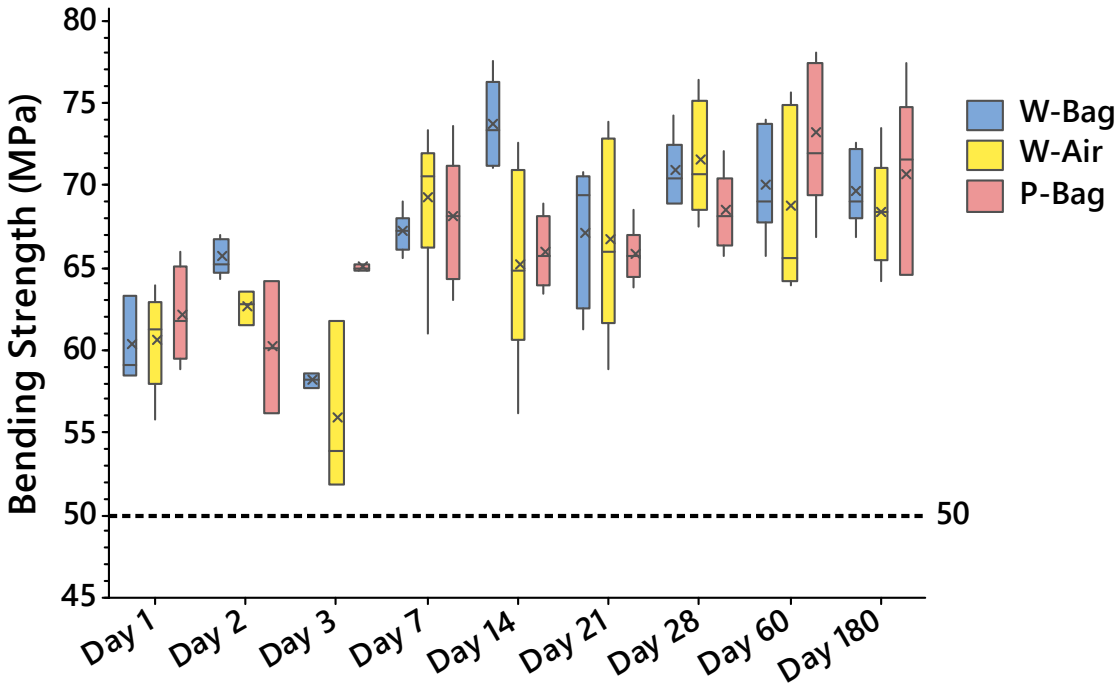

Figure 4.23 Data range of bending strength results of W-Bag, W-Air and P-Bag for each time point. The mean values of the samples are expressed with the X, and horizontal lines represent the median values.

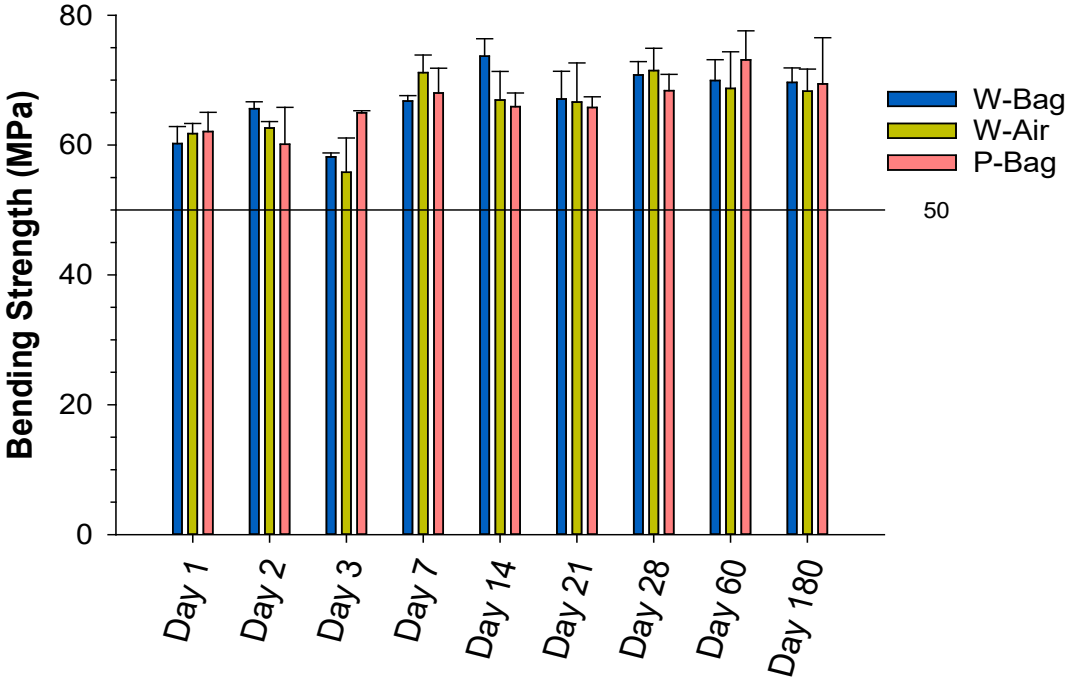

Figure 4.24 Bending strength results of W-Air, W-Bag and P-bag samples at different time points. The data presents mean value ± standard deviation (μ ±σ). The line is the minimum requirement of IS05833:2002 standard, 50MPa.

Figure 4.25 and Figure 4.26 display bending modulus results for W-Bag, W-air and P-Bag samples at each time point. The results show that all the samples had a higher bending modulus than the minimum requirement of ISO 5833:2002 (1800 MPa). Similar to bending strength results, bending modulus of the samples showed an increase comparing day-1 and day-180 despite the variations throughout the ageing process. Range of values for all samples were between 2.1 GPa and 3.7 GPa (see Figure 4.25). The minimum value occurred on day-2 time point for P-bag sample and the maximum value occurred on day-180 time point for P-bag sample. Regarding the mean values, the range of variation of bending modulus was between 2.4 GPa and 3.6 GPa (see Figure 4.26). Two-way ANOVA followed by Tukey *post hoc* analyses showed that there was no significant difference ($p>0.05$) between W-bag, W-air and P-bag but there were significant differences within the sample groups ($p<0.05$). Whilst W-bag samples showed significant differences ($p<0.05$) after day-7 time point, P-bag samples had significant differences ($p<0.05$) after day-21 time point compared to day-1 samples. However, W-air samples showed significant differences ($p<0.05$) only on day-60 and day-180 compared to day-1 samples.

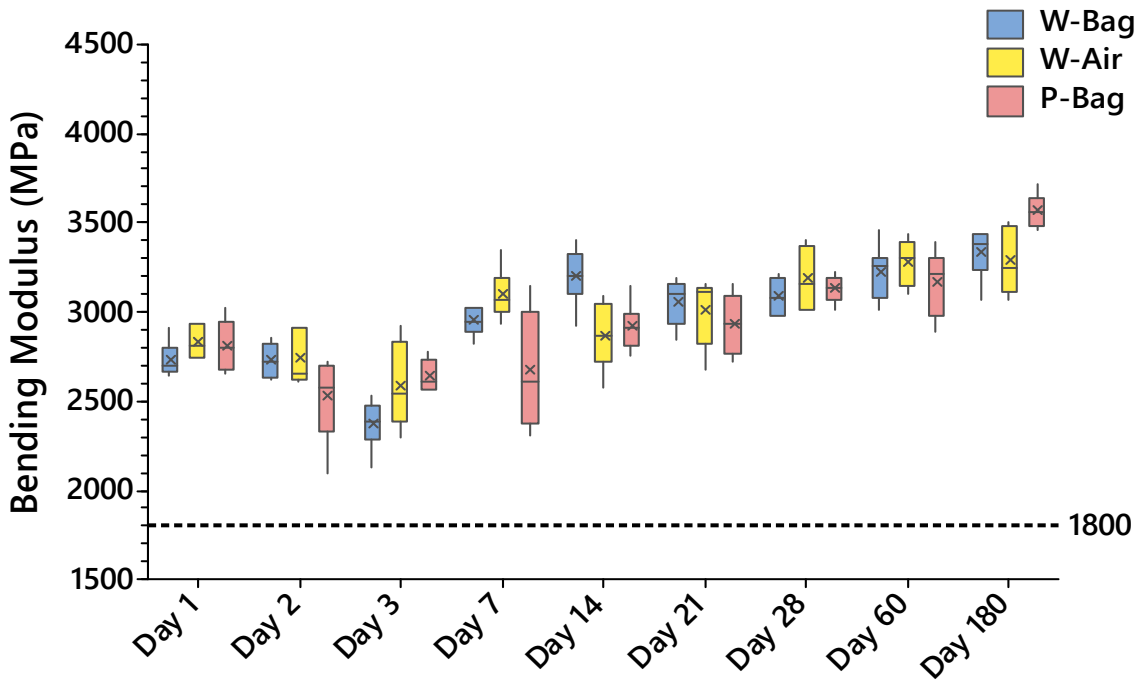

Figure 4.25 Data range of bending modulus results of W-Bag, W-Air and P-Bag for each time point. The mean values of the samples are expressed with the X, and horizontal lines represent the median values.

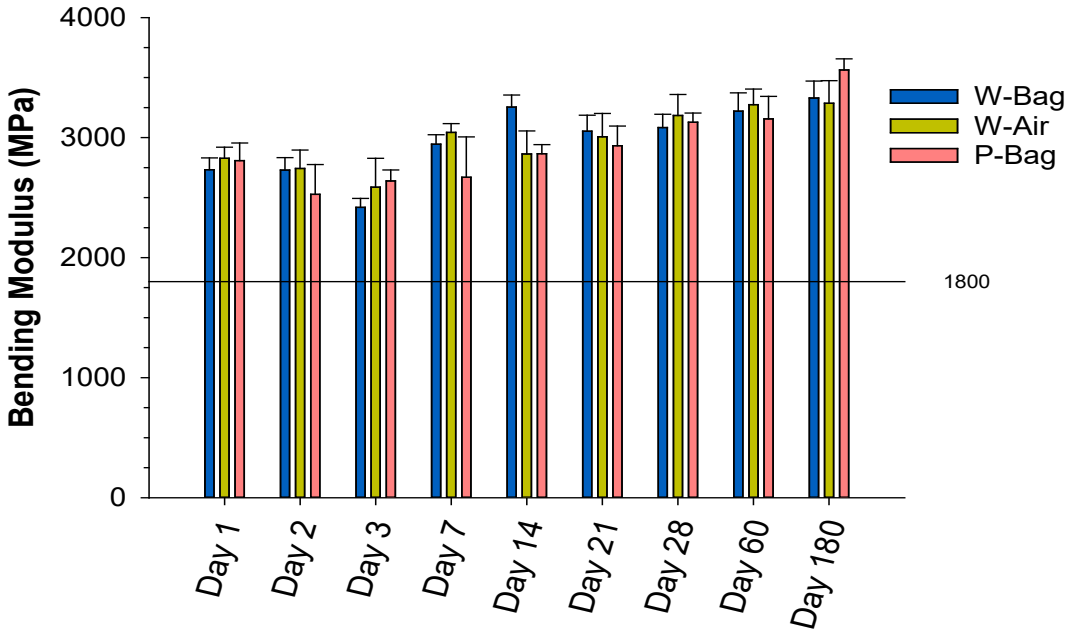

Figure 4.26 Bending modulus results of W-Air, W-Bag and P-bag samples at different time points. The data presents mean value ± standard deviation (μ ±σ). The line is the minimum requirement of IS05833:2002 standard, 1800MPa.

Typical stress-strain curves of the samples tested at each time point were analysed to understand their behavior under the applied force. The stress-strain curves of W-air, W-bag and P-bag are shown in Figure 4.27. The stress values at the fracture points were in a range of 54 MPa and 72 MPa. The minimum value was obtained for W-air and the maximum value was obtained for W-bag. The maximum strain (%) values decreased continuously throughout the ageing process. All samples were relatively ductile on days 1 to 3; thereafter, they all gradually transitioned into a more brittle state.

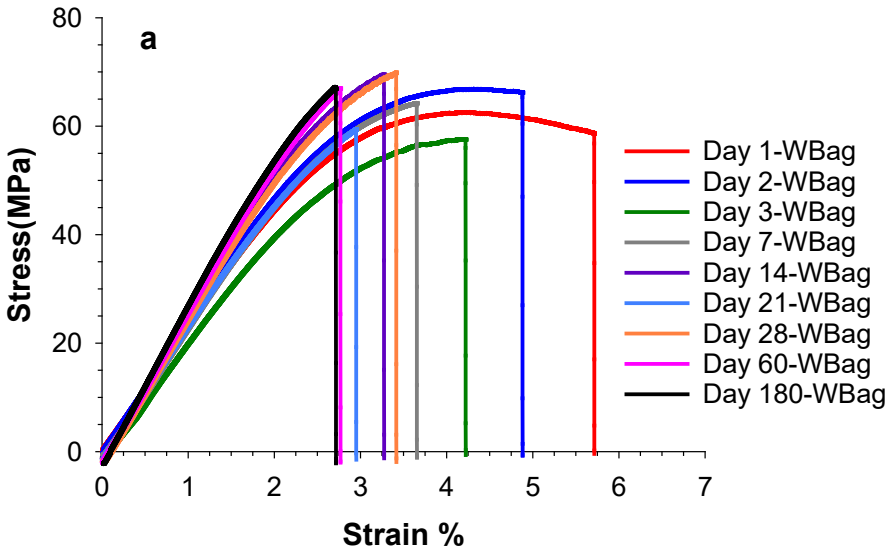

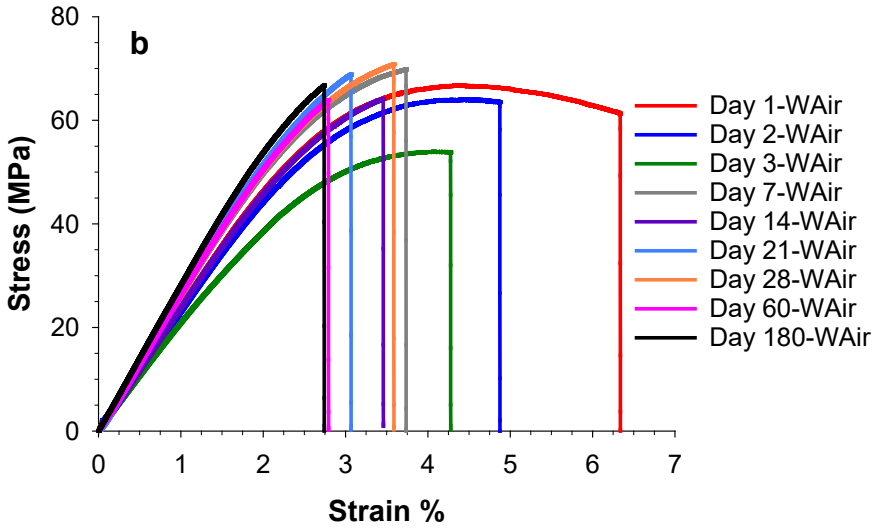

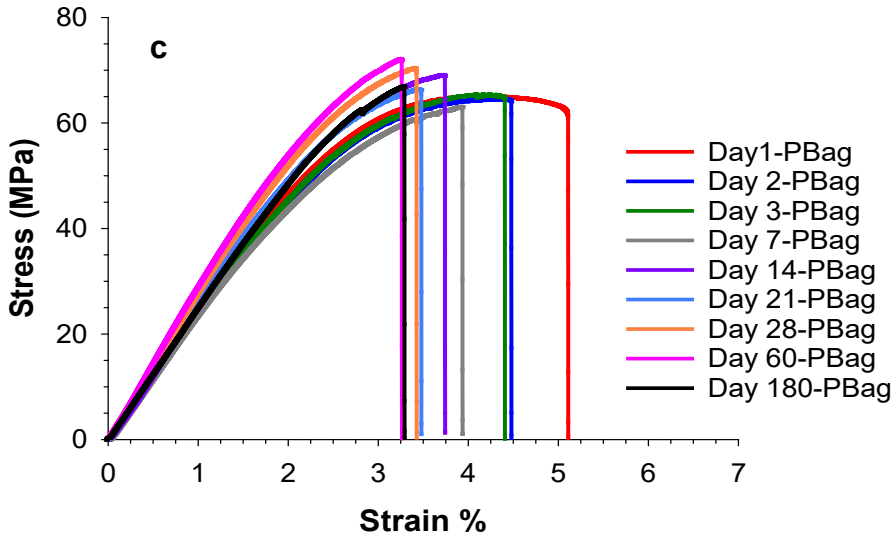

Figure 4.27 Stress-strain curves obtained during four-point bending test at each time point for typical a) W-Bag, b) W-Air and c) P-Bag samples

In the literature, investigation of ageing effects on mechanical properties of PMMA cement is limited. According to the tests performed in dry conditions, the polymerisation of PMMA cement may continue more than 5 years. Throughout the ageing process, bending strength and bending modulus increased [98, 144, 172] and this was attributed to further polymerisation and evaluation of interpenetrating network [98].

In this study, the bending strength and bending modulus of W-air, W-bag and P-bag increased from day-1 to day-180 even though this increase was non-linear. However, it was clearly seen that they exhibited variations throughout ageing, which is consistent with the study performed by Ayre et al [144]. Although the variations are strongly related to the inhomogeneity of the material, it may also be affected by the test conditions [173] and storage conditions [172]. The test environment and storage environment were not temperature controlled. The temperature and humidity recordings of test environment is presented in Appendix B.2. There was no significant change in the test environment during four-point bending test. Moreover, W-air and W-bag samples were always tested on the same day and variations between the groups can be seen at different time points. Comparing W-air and W-bag, the storage conditions (bag and air) may have had more influence on mechanical properties regarding the moisture uptake and ambient temperature [98, 144].

4.4.4 Compressive Strength Test

Wintercryl and Palacos® cement samples were aged to analyse the time influence on compressive strength properties. As previously stated, Wintercryl cement samples were kept in a bag and in air to understand the effect of storage condition (moisture uptake). In addition, the cement samples were prepared with two different dimensions, ø6x12h (mm) and ø12x24h (mm) to analyse the impact of dimensions on compressive strength properties since the samples had different polymerisation temperatures, porosities and defects. Figure 4.28 shows a representative image of Wintercryl cement samples after the compressive strength test; the height of the samples was reduced, and they were compressed into barrel-like shapes.

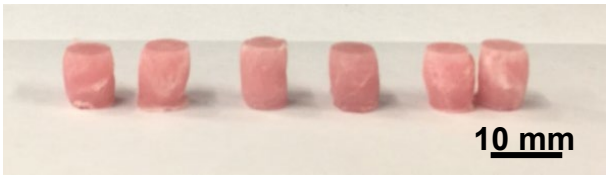

Figure 4.28 Wintercryl cement (W-air on day-1 time point) samples after compressive strength test (Initial dimensions ø6x12h mm)

One out of six samples of W-air on day-3 and P-bag samples on day-1 and day-2 time points unexpectedly fractured. Similarly, one out of six samples of W-DD/Bag (double dimension kept in closed air storage) also unexpectedly fractured on day 28, shown in Figure 4.29. These samples were considered anomalous and excluded from the data. 20% of mean values of compressive strength were analysed and these sample that had unexpected fractures were found below the limit. The reason of the anomalies can be linked to uneven surfaces and non-homogenous internal structure. Table 4.11 provides the number of samples of W-air, W-bag, W-DD/Bag and P-Bag samples included in data for compressive strength calculations.

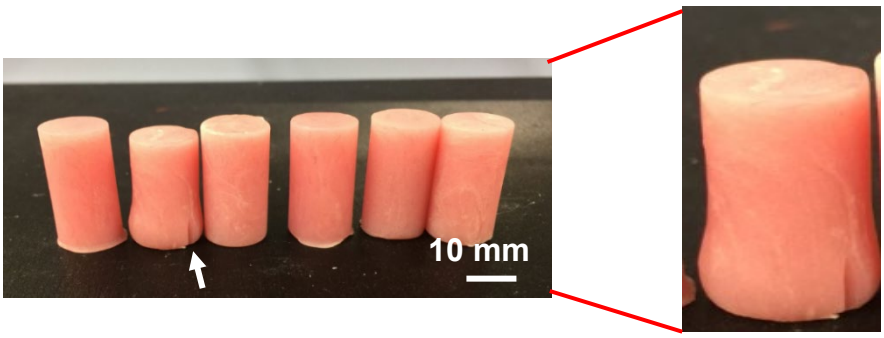

Figure 4.29 W-DD/Bag samples on day-28 after compressive test. The arrow indicates the second sample in the group, which was fractured. (Initial dimensions ø12x24h mm)

Table 4.11 Sample size (n) of W-air, W-bag, W-DD/Bag and P-bag sample groups at each time point for compressive strength test results

Time Points	Day 1	Day 2	Day 3	Day 7	Day 14	Day 21	Day 28	Day 60	Day 180
W-Bag	$n=6$	$n=6$	$n=6$	$n=6$	$n=6$	$n=6$	$n=6$	$n=6$	$n=6$
W-Air	$n=6$	$n=6$	$n=5$	$n=6$	$n=6$	$n=6$	$n=6$	$n=6$	$n=6$
P-Bag	$n=5$	$n=5$	$n=6$	$n=6$	$n=6$	$n=6$	$n=6$	$n=6$	$n=6$
W-DD/Bag	$n=6$	$n=6$	$n=6$	$n=6$	$n=6$	$n=6$	$n=5$	$n=6$	$n=6$

In order to calculate the compressive strength ($\sigma_{2\%}$) of W-air, W-bag and P-bag samples, 2% offset was taken on the elastic region of the stress-strain curves (Figure 4.30). The maximum compressive strength (σ_{max}) was detected and marked on the curve.

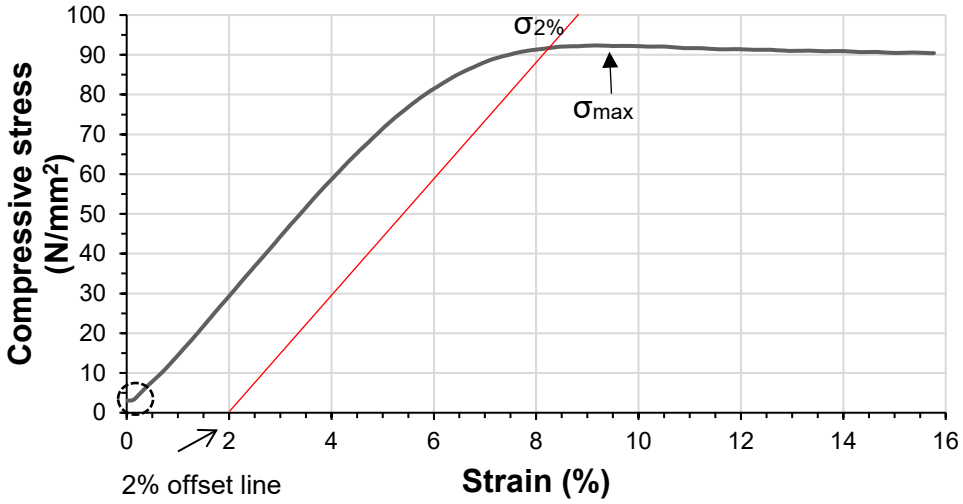

Figure 4.30 Stress-Strain curve of a selected sample to demonstrate the calculation of yield and compressive strength. Red line indicates 2% offset line. The dashed circle refers to 50N pre-load applied for 3 seconds.

The 2% offset line could not be calculated for all the W-DD/Bag samples. The maximum load cell was 10kN and some samples required forces higher than the 10kN to pass the 2% offset line or to break, whichever occurred first. Therefore, the force-displacement curves were incomplete. In order to standardise the compressive strength ($\sigma_{2\%}$) results, the gradients of the force vs displacement curves were analysed.

Since the gradients of the samples were similar, 10% below the maximum force values were taken in order to calculate the stress and strain values. Figure 4.31 shows force-displacement curves of three W-DD/Bag samples at day-1 time point, which did not pass 2% offset line due to the machine load cell limitations.

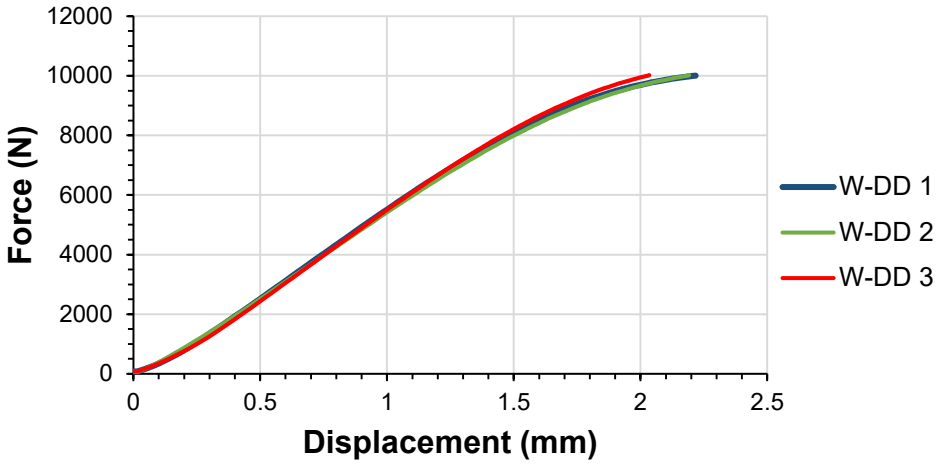

Figure 4.31 Three samples of W-DD/Bag at day-1 time point

Compressive strength test results of W-bag, W-air and P-bag are presented in Figure 4.32 and Figure 4.33. The graphs show compressive strength ($\sigma_{2\%}$) of the samples, which was calculated using 2% offset as shown in Figure 4.30. All samples met the minimum requirement of ISO 5833:2002 standard (70 MPa) and displayed a nonlinear pattern over the total period of 180 days. The range of values for all samples was between 60 and 118 MPa (see Figure 4.32). The minimum strength value occurred for W-Air sample on day-2 time point and the maximum strength value occurred for P-bag sample on day-60 time point. Regarding the mean values of all samples, the strength of all samples varied between 74.6 and 110.4 MPa (Figure 4.33). The mean values of W-Air samples showed the lowest compressive strength on day-2 and day-3 time points; however, these samples gradually increased over time. The highest values of compressive strength were obtained for P-bag samples. Two-way ANOVA analyses followed by Tukey *post-hoc* test showed that there were significant differences between W-Bag, W-Air and P-Bag sample groups ($p<0.05$). While there were no significant differences ($p>0.05$) within sample groups of W-Bag and W-Air compared to day-1 time point, P-Bag samples showed significant differences ($p<0.05$) from day-14 time point compared to day-1 time point.

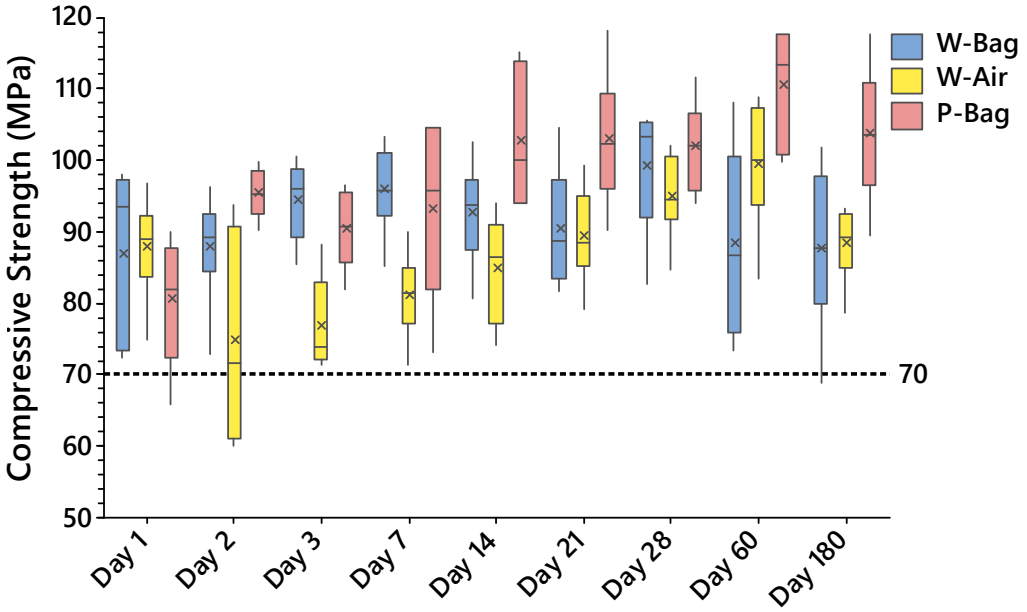

Figure 4.32 Data range of compressive strength test results of W-Bag, W-Air and P-Bag samples for each time point. The mean values of the samples are expressed with the X, and horizontal lines represent the median values. (Initial dimensions are ø6x12h mm)

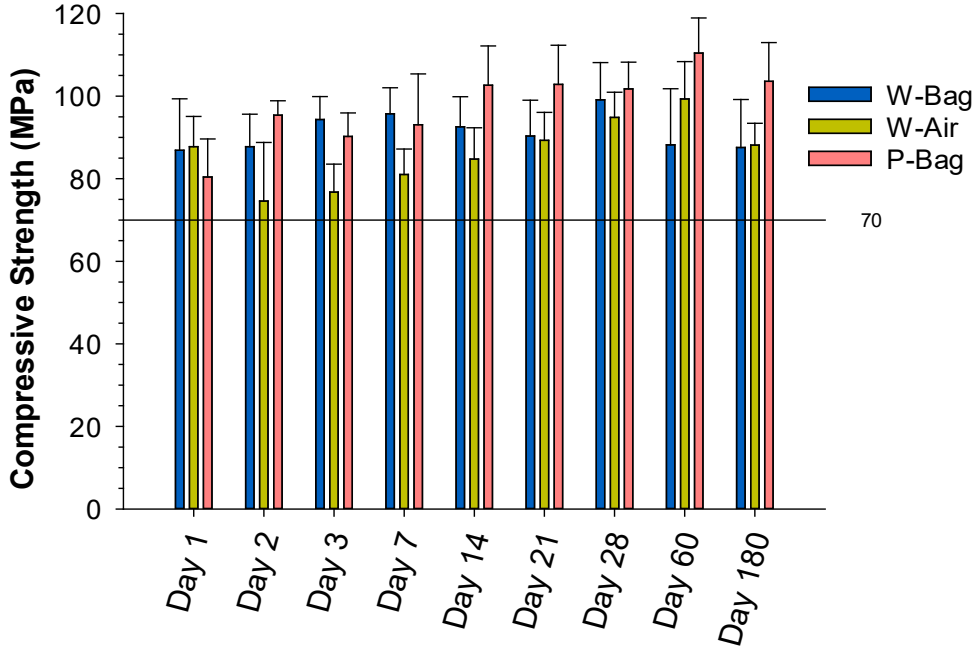

Figure 4.33 Compressive strength results of W-Bag, W-Air and P-Bag for each time-points. The data presents mean value ± standard deviation (μ ±σ). The line is minimum requirement of IS05833:2002 standard, 70MPa. (Initial dimensions are ø6x12h mm)

Compressive strength test results of W-DD/Bag samples for each time point are presented along with results of W-bag samples in Figure 4.34 and Figure 4.35. W-DD/Bag samples were prepared to understand how the dimensions would affect the compressive strength since increasing the thickness would have an influence on polymerisation temperature, porosities and possible defects in the samples. Moreover, the defect sizes in the bone vary as reported previously, therefore, thickness of applied PMMA cement varies as well due to this reason it was important to investigate the effect of thickness. Compressive strength ($\sigma_{2\%}$) of W-DD/Bag samples were calculated using 2% offset as shown in Figure 4.30 and the samples that did not pass 2% offset line were included in the data as described above (Figure 4.31). All W-DD/Bag samples met the requirement of standard ISO-5833:2002 (70 MPa) even though the dimensions were different. An outlier was detected on day-14 time point for W-DD/Bag sample (64 MPa), which is shown in Figure 4.34. This outlier was not included in calculation of mean values and standard deviation, which is presented in Figure 4.35. The range of values for all samples were between 68.8 and 108 MPa. Regarding the mean values of W-DD, the compressive strength ($\sigma_{2\%}$) values varied between 78.2 and 86.3 MPa (Figure 4.35). W-DD/Bag samples did not show a significant variation during ageing process ($p>0.05$). Compared to W-Bag samples, W-DD/ Bag samples had more reliable results due to reduced defect sizes since the sample preparation was easier than W-bag samples. Moreover, surface of the W-DD/Bag samples were flatter and even than surface of W-Bag samples. However, W-bag and W-DD/Bag samples were significantly different ($p<0.001$) regarding two-way ANOVA followed by Tukey post-hoc analyses.

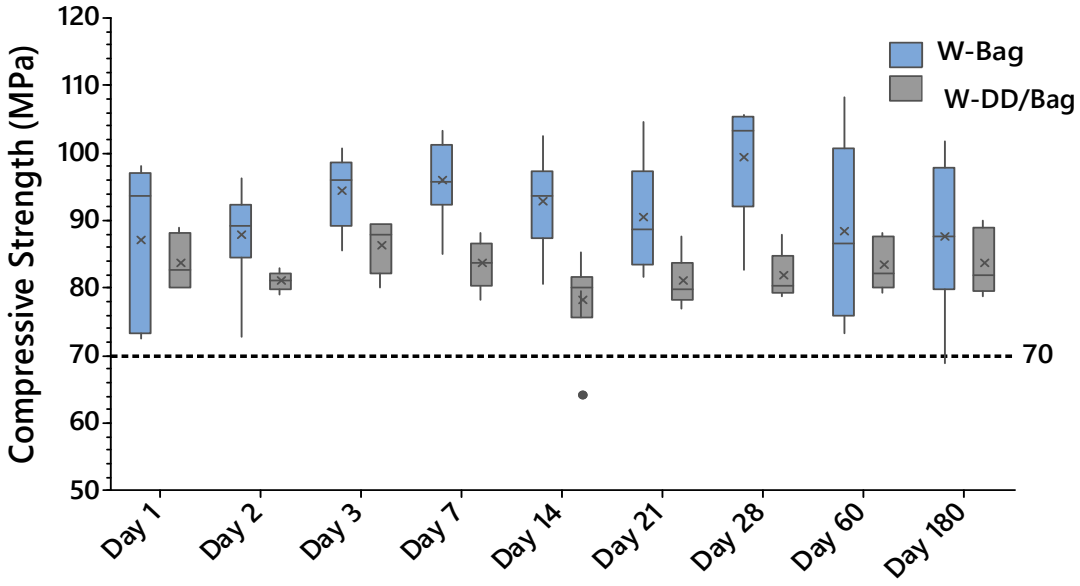

Figure 4.34 Data range of compressive strength test results of W-Bag and W-DD/Bag for each time point. The mean values of the samples are expressed with the X, and horizontal lines represent the median values. (Initial dimensions are ø6x12h mm for W-bag and ø12x24h mm for W-DD/bag)

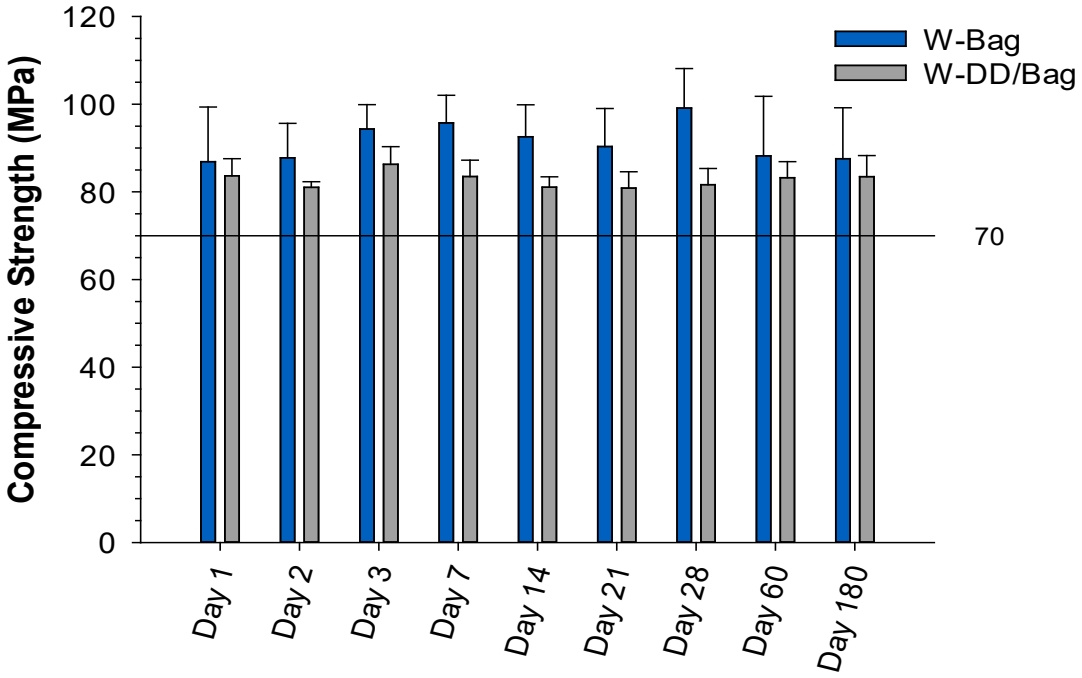

Figure 4.35 Compressive strength results of W-Bag and W-DD/Bag for each time point. The data presents mean value ± standard deviation (μ ±σ). The line is minimum requirement of IS05833:2002 standard, 70MPa. Outlier is not included. (Initial dimensions are ø6x12h mm for W-bag and ø12x24h mm for W-DD/Bag)

The typical stress-strain curves of W-bag (Figure 4.36-a), W-air (Figure 4.36-b), P-bag (Figure 4.36-c) and W-DD/Bag (Figure 4.36-d) samples at each time point are presented in Figure 4.36. The highest stress values of typical W-Bag, W-Air, P-Bag and W-DD/Bag throughout the ageing process were 102 MPa, 99 MPa, 118 MPa and 90MPa, respectively.

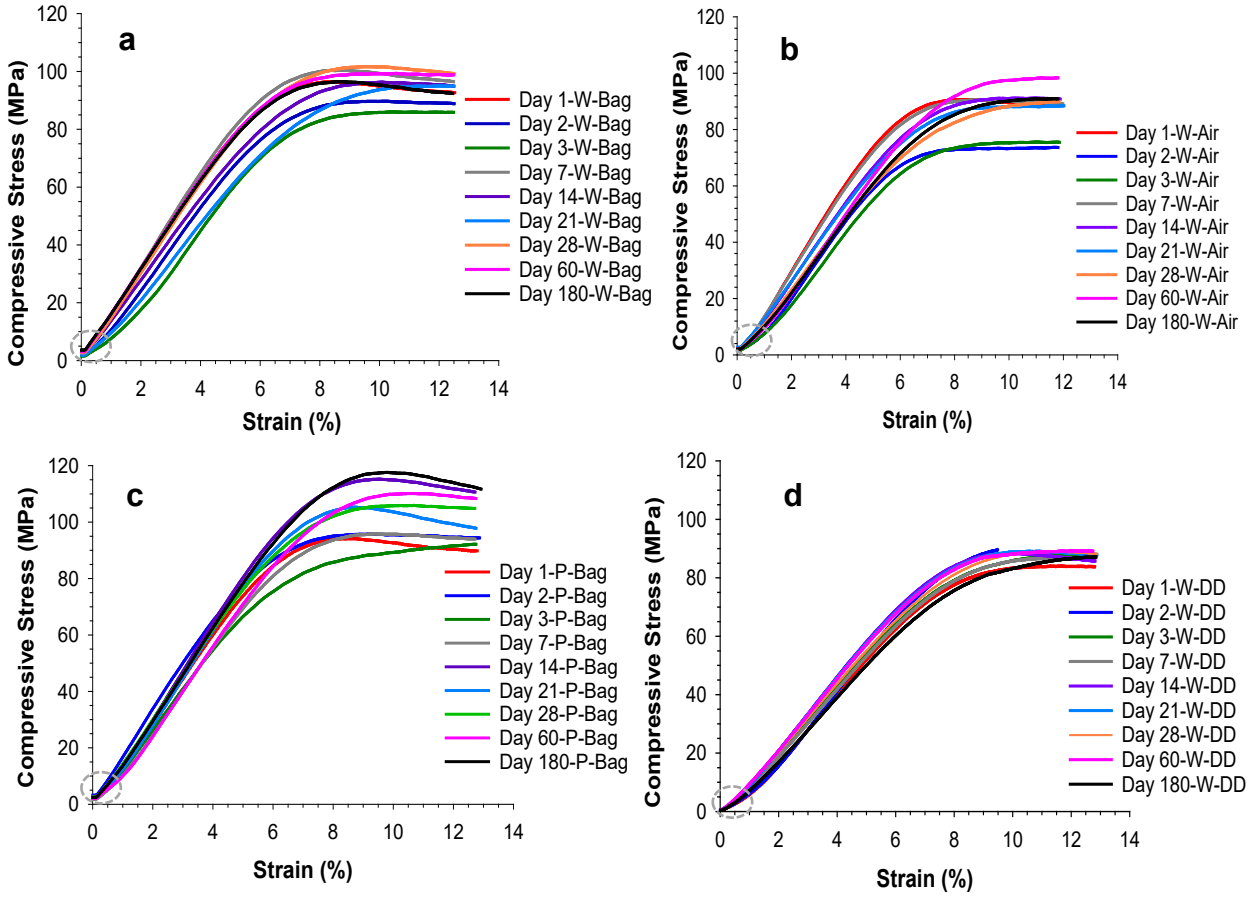

Figure 4.36 Stress-Strain curves of selected samples from a) W-Bag, b) W-Air, c) P-Bag and d) W-DD/Bag for each time point. The dashed circle refers the 50N pre-load applied for 3 seconds.

The average values and standard deviations of maximum compressive strength (σ_{max}) values of W-Bag, W-Air, W-DD/Bag and P-Bag samples for each time point are shown in Table 4.12. The highest values of compressive strength were obtained for P-bag samples (112 MPa).

Table 4.12 Maximum strength values of compressive test results of W-Bag, W-Air, W-DD-BAGand P-Bag samples. The data presents mean value ± standard deviation (μ ±σ).

	Compressive Strength (σ_{max}, MPa)			
Time Points/ Samples	**W-Bag**	**W-Air**	**W-DD/Bag**	**P-Bag**
Day 1	86.2 ± 11.0	88.0±7.4	88.6±2.5	83.1±7.9
Day 2	88.2±7.5	81.3±11.5	90.2±1.3	95.9±3.1
Day 3	95.3±5.5	83.3±8.5	90.2±1.3	94.2±7.3
Day 7	100.9±6.6	82.6±6.9	88.3±1.8	98.1±7.1
Day 14	94.2±5.7	87.2±7.0	89.6±1.3	103.5±9.2
Day 21	92.7±7.8	90.8±5.6	86.3±4.0	103.4±9.6
Day 28	88.2±9.3	81.3±4.4	90.2±13.6	95.4±7.1
Day 60	93.9±10.3	100.6±8.9	88.3±2.4	112.3±6.9
Day 180	92±7.5	90.3±4.7	88.0±1.7	105.1±7.5

Similar to bending strength and modulus results, compressive strength results of W-air, W-bag and P-bag also showed variations, which is in line with the results reported by Ayre et al [144]. These variations are also strongly related to the inhomogeneity of the material. It should be noted that W-air, W-bag, P-bag and W-DD/Bag for each time point were tested at the same conditions. P-bag samples showed higher compressive strength than W-bag samples, which confirmed the effect of pre-mixed ZrO_2 particles. Salih et al. [174] reported the influence of radiopacifier zirconium oxide on mechanical properties of PMMA cements due to having higher compressive strength than the polymer itself. The studies performed on ageing PMMA cement in air and an isotonic fluid showed different outcomes. Whilst the samples aged in air followed an increasing trend in flexural and compressive strength, the samples aged in the fluid showed reductions in the mechanical properties [98, 144, 172]. This highlights the importance of ageing conditions on mechanical properties.

4.4.5 Vickers Hardness Test

Vickers hardness was measured after the four-point bending test, using the half samples obtained. The influence of ageing on the hardness properties was tested on W-air, W-bag and P-bag cements at each time point as described in Section 3.4.4. Figure 4.37 and Figure 4.38 show the results of Vickers hardness test for 18 measurements ($n=6$, repeated three times) on W-Bag, W-Air and P-Bag cements for each time point. The hardness of the cements increased over the time period with a similar trend and the results are in accordance with a study performed by Ayre et al [144]. The hardness of P-bag samples was significantly higher than W-air and W-bag samples. The range of values for all samples were between 13.8 MPa and 25.8 MPa (see Figure 4.37). The minimum hardness value occurred for W-air sample on day-7 time point and the maximum value occurred for P-bag sample on day-180 time point. The mean values of all samples varied between 14.9 and 24.8 MPa (see Figure 4.38). The presence of ZrO_2 in the Palacos cement composition may be the reason for the higher hardness, which is in a good agreement with several studies [144, 174, 175]. According to two-way ANOVA with Tukey *post-hoc* analyses, there was no significant difference between W-bag and W-air ($p>0.05$) regarding the time-points; however, comparisons between P-bag and W-bag showed that the samples were significantly different at each time point. There were significant differences within the sample groups. W-Air, W-bag and P-bag samples, which aged more than two days, were found significantly different compared to day 1 samples ($p<0.001$).

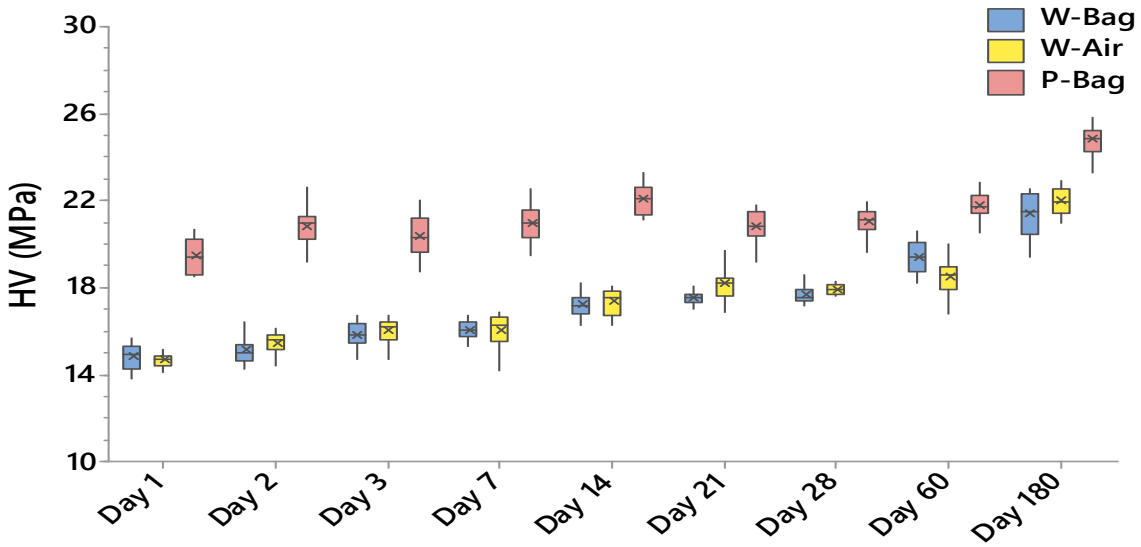

Figure 4.37 Data range of Vickers hardness test results for W-Bag, W-Air and P-Bag samples tested at each time points. The mean values of the samples are expressed with the X, and horizontal lines represent the median values. ($n=6, r=3$)

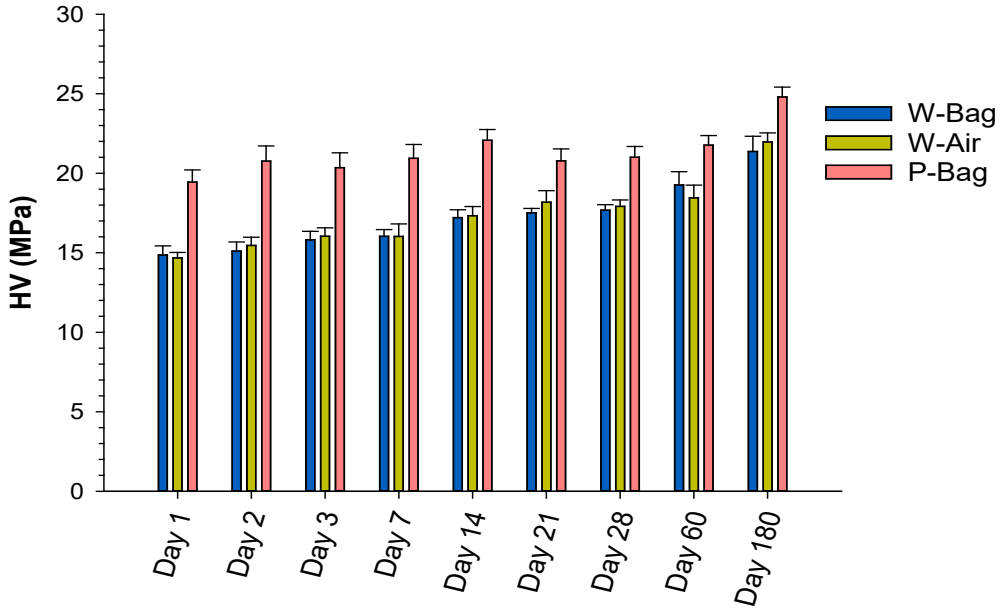

Figure 4.38 Vickers Hardness test results of W-bag, W-air and P-bag samples for each time point. The data presents mean value ± standard deviation (μ ±σ), (n=6, r=3).

4.4.6 Summary of Results and Discussions

In this section, setting and microstructure properties of Palacos and Wintercryl cement samples were provided. Moreover, the influence of ageing process on mechanical properties of the PMMA cements were presented.

Time recordings throughout the preparation stage of the PMMA cements showed that Palacos cement had a shorter waiting time than Wintercryl cement. Whilst the interval waiting time of Palacos was 2.1±0.4 min, it was 4.3±0.8 min for Wintercryl cement. It was speculated that Palacos cement may also have a shorter setting time based on temperature profiles demonstrated in Figure 4.13. This difference in handling properties of the two cement was attributed to the variation of the composition and particle size of PMMA cements.

SEM images demonstrated that PMMA beads of Wintercryl powder component varied in a range of 10-100 μm. PMMA beads of Palacos cement varied in a range of 10 to 60 μm. It was also shown that PMMA beads could be distinguished on the surface of polymerised structure and this showed incomplete polymerisation between polymer and monomer. It should be noted that PMMA dissolves in MMA [176].

Mechanical properties of aged samples were evaluated using four-point bending, compressive strength and Vickers hardness tests. All samples met the requirement of ISO 5833:2002 for bending strength (50 MPa), bending modulus (1.8 GPa) and compressive strength (70 MPa).

The range of average bending strength for all samples was between 55.8 and 73.6 MPa and bending modulus was between 2.4 and 3.6 GPa. Similarly, compressive strength test results demonstrated that all samples had higher compressive strength than the 70 MPa requirement of this standard. The range of average compressive strength for all samples was between 74.6 and 110.4 MPa. Although bending and compressive strength of the samples exhibited a non-linear increase with ageing time. This was attributed to non-homogenous structure of the cement due to incomplete polymerisation within the polymer matrix and variations in pore sizes. Moreover, stress-strain curves (Figure 4.27) obtained from the four-point bending test demonstrated the slight transition from ductility to brittleness. In addition to this, Vickers hardness of the samples gradually increased throughout the ageing period. The average Vickers hardness for all samples was in a range of 14.9 and 24.8 MPa.

Comparing Palacos cement and Wintercryl cements throughout their ageing processes, there were no significant differences on bending strength and bending modulus of the cement samples. However, all sample groups were significantly different to each other for compression tests. Palacos cement samples showed higher compressive strength results (mean values between 80 and 110 MPa), which were related to the pre-mixed ZrO_2 ceramics in the composition of the cement. Interestingly, it was observed that W-DD/Bag exhibited lower compressive strength (mean values between 78 and 86 MPa) than W-bag samples. This could be due to the limitations of performing the test using 10kN load cell test machine. Since the compressive force-displacement curves were not completed, a method was used to estimate the 2% offset compressive strength ($\sigma_{2\%}$) of these samples. Therefore, 10% below the maximum force was considered and converted to stress ($\sigma_{max\text{-}10\%}$). However, this was a prediction since the actual maximum force could not be detected. Moreover, W-DD/Bag did not show any trend regarding the ageing process.

Overall, this part of the study was important to establish a baseline and help to practise and improve the methodology before adding magnetic glass ceramics. All test samples were prepared using silicone mould design in order to have reliable and accurate test data. In that way, the test samples did not need any sanding or polishing to correct the

dimensions. This part of the study required preparation of more than 600 samples. Practising the application many times led to understand the behaviour of PMMA cement and optimisation of cement moulding into silicone rubber mould. In several studies PTFE mould was used since it was required in standard ISO 5833:2002. The authors reported that the prepared samples needed further processes such as sizing and polishing. However, silicone rubber mould was not only used to obtain accurate dimensions but to monitor the sample temperature. The setting time and temperature measurements of PMMA cement were performed using four-point bending silicone mould design rather than following standard ISO 5833:2002 due to limited material. Moreover, it was necessary to understand the influences of ageing and different dimension on mechanical properties of PMMA cement samples. Before the addition of magnetic glass ceramic in PMMA cement, it was essential to gain accuracy and consistency in sample preparation and testing.

In the next chapter, effects of MGC addition, from 10% to 40% (wt%), in Palacos and Wintercryl cement samples in handling properties, polymerisation reaction temperature, morphology of cements, mechanical properties, cytocompatibility and bioactivity properties as well as heat generation properties will be presented.

5 Results and Discussion: Characterisation of Magnetic PMMA Cement

In this chapter, results of characterisation of magnetic PMMA cements are presented. Characterisation techniques involved setting, microstructure, mechanical, and cytotoxicity, bioactive and heating properties of magnetic PMMA cement.

Magnetic glass ceramic (MGC) containing Wintercryl cement samples were called W-MGC and similarly, MGC containing Palacos® cement samples were called P-MGC for all MGC ratios (10, 20, 30 and 40 wt%). Wintercryl cement samples with 10, 20, 30 and 40% MGC powder were called W10, W20, W30 and W40 and similarly, Palacos cement samples were called P10, P20, P30 and P40. Plain Wintercryl and Palacos® cement samples, which did not have any MGC powder were called W0 (0% MGC) and P0 (0 % MGC) respectively. These samples were used as controls.

5.1 Characterisation of Magnetic Cement

MGC containing Palacos® (P-MGC) and Wintercryl (W-MGC) samples were prepared as described in 3.5.2. The ambient temperature and humidity of the fume cupboard were recorded during magnetic PMMA cement preparations. Figure 5.1 demonstrates representative temperature (Figure 5.1-a) and humidity (Figure 5.1-b) recordings in different days. Test 1 and test 2 indicate different days that the samples were prepared in the same laboratory. Whilst the range of temperature recordings were between 20 and 25 ºC, the relative humidity was in a range of 47 and 60% (rh%). The relative humidity was higher than 40%, which was in accordance with standard ISO 5833:2002. As previously reported (see Section 4.4), relative humidity can play an important role in viscosity of PMMA cement, which leads to variations in waiting and setting time of the cement.

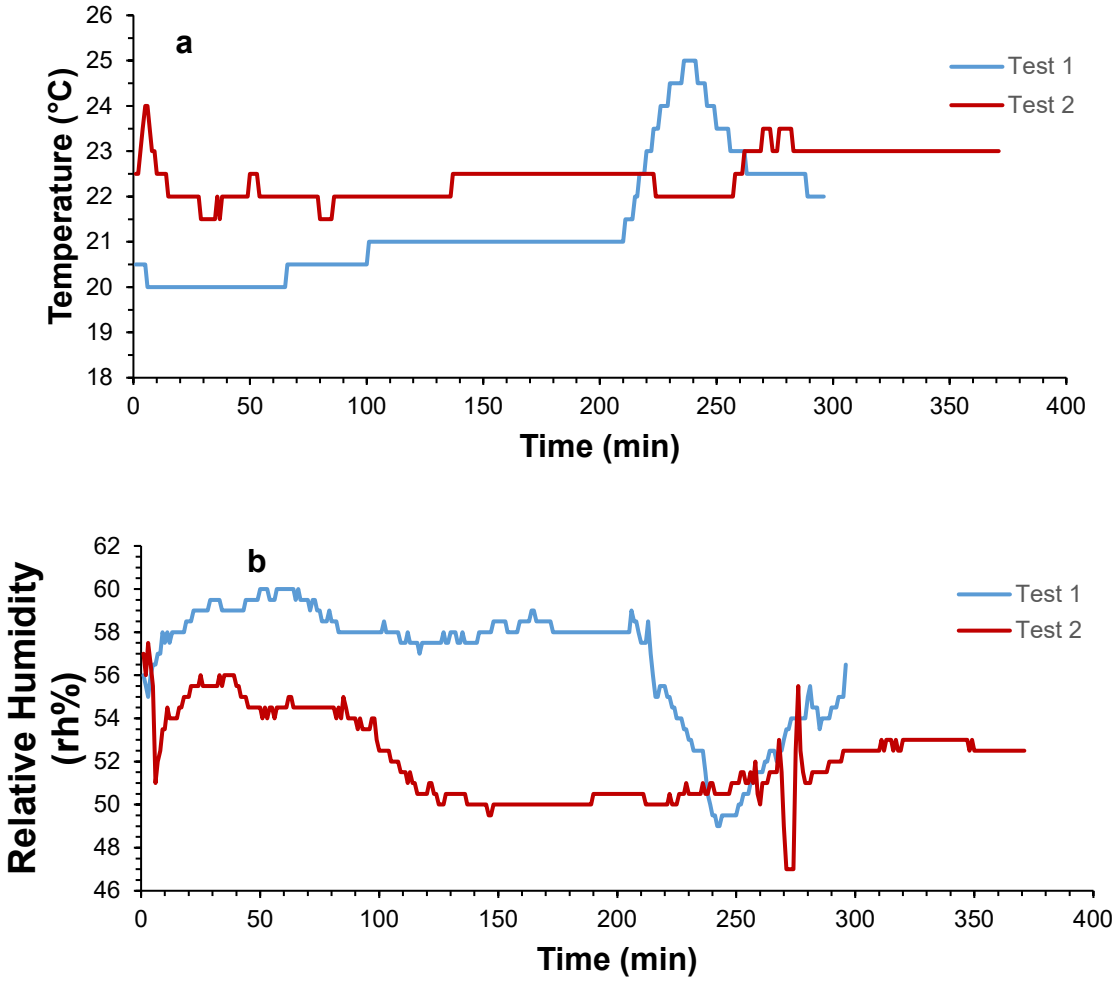

Figure 5.1 a) Temperature and b) corresponding relative humidity (%) profiles during preparation of magnetic PMMA cement samples in different days

5.1.1 Setting Properties of MGC Cements

The setting properties of the cements were evaluated for approximately 6 grams of powder mixed with 3 ml of liquid (2:1g/ml). When the powder (PMMA+MGC) was in contact with the liquid, the temperature and time recordings were started. In addition, the mixing, working and waiting times were also manually recorded. The mixing time was maintained to approximately 30-40 seconds for every cement preparation and the working time was kept approximately 1.5-2 minutes. Each mould allow the preparation of two cement samples. Therefore, during the working time, the cement was divided into two parts and placed in the mould. Table 5.1 and Table 5.2 report the setting properties of W-MGC and P-MGC with their control groups (W0 and P0) respectively. Increasing the MGC content from 10% to 40% in the samples, increased the waiting time of the cements.

As reported in Section 4.4.1, the ambient temperature had an impact on waiting times of the samples.

Table 5.1 Waiting times of W0, W10, W20, W30 and W40 samples (The data presents mean value ± standard deviation (μ ±σ) for waiting time, $5 \leq n \leq 3$)

Sample Code	Ambient Temperature (°C)	Waiting Time Interval (min)
W0	23±1	4.3±0.8
W10	23.5±0.5	4.9±0.7
W20	23.5±0.5	6.2±0.8
W30	23.5±0.5	7.4±0.5
W40	22±0.5	8.8±0.6

Table 5.2 Waiting times of P0, P10, P20, P30 and P40 samples. The data presents mean value ± standard deviation (μ ±σ) for waiting time, $5 \leq n \leq 3$)

Sample Code	Ambient Temperature (°C)	Waiting Time Interval (min)
P0	23±1	2.1±0.4
P10	22±0.3	3.9±0.4
P20	22.5±0.6	4.5±0.2
P30	22.4±0.1	6.10±0.1
P40	20±0.1	9.6±0.3

Temperature profiles of P-MGC and W-MGC cement samples were recorded as described in Section 3.6.1. *Figure 5.2* presents temperature curves of P20 samples at 22.2-23°C (see Appendix C.1 for W-MGC and P-MGC samples). The temperature readings were taken for two cement bars at a time using four thermocouples, T1, T2, T3 and T4 (see Section 4.4.1). The pairs of cement bars prepared from each batch are coded A1-A2 (batch A), B1-B2 (batch B) and C1-C2 (batch C), see Figure 4.14. As seen in *Figure 5.2*, maximum polymerisation reaction temperatures varied between 26.08 and 29.4°C. This variation was due to improper filling of the sacrificial ends and caused lower temperature readings between and within the samples.

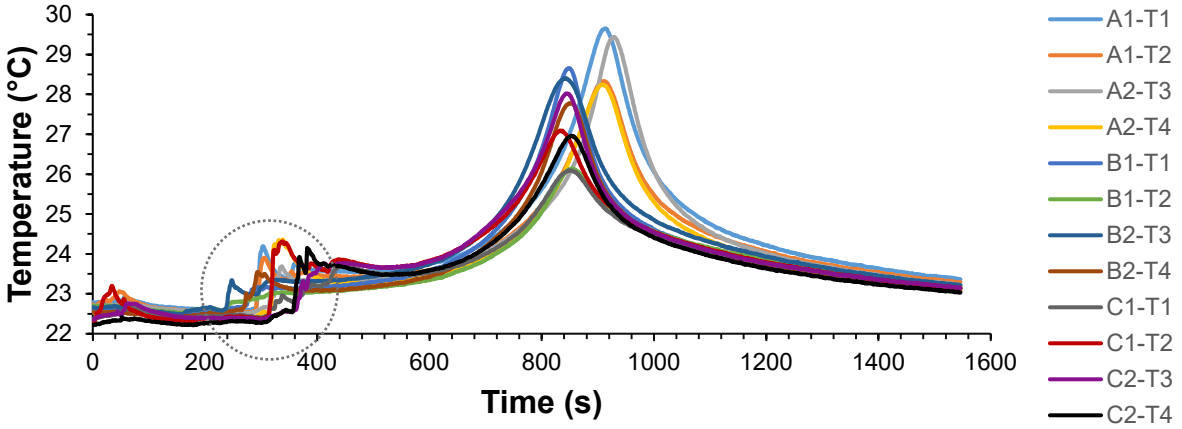

Figure 5.2 Polymerisation reaction temperature during the setting process of P20 samples at 22.2-23°C ambient temperature (The temperature fluctuations in the circled area are due to touching the thermocouples while placing the samples in the mould).

Since sacrificial ends showed variations, setting time and temperature could not be calculated. However, temperature readings of typical P0, P10, P20, P30 and P40 samples are shown in Figure 5.3. The stars on the curves indicate the corresponding setting times and temperatures (see Section 3.4.1). P0 samples had the highest setting temperature (27.8°C) and the shortest setting time (9 minutes). Increasing the MGC addition in the cements increased the setting time and slightly reduced the setting temperature, see Table 5.3.

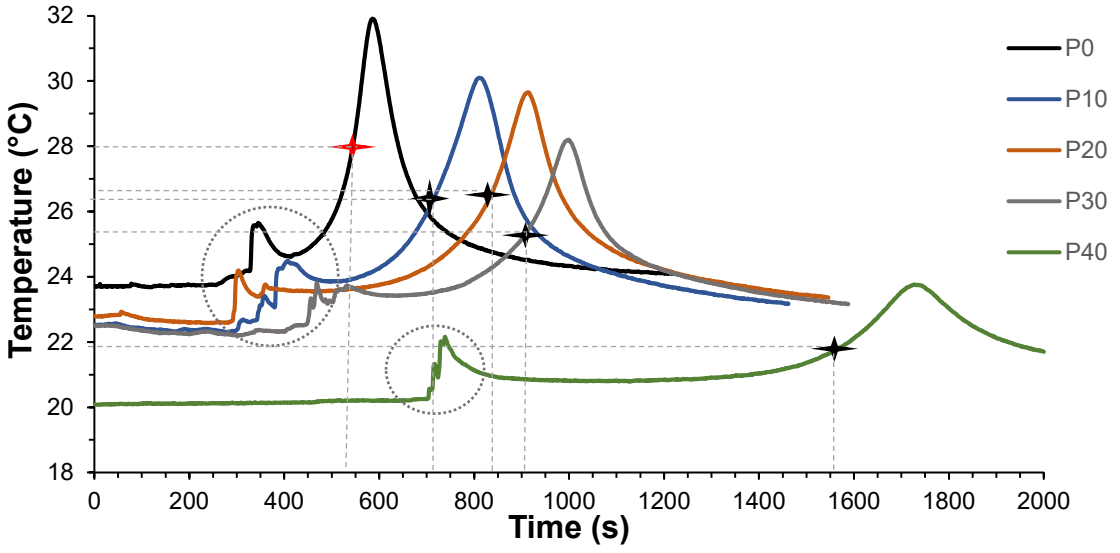

Figure 5.3 Temperature-time profiles of selected P0, P10, P20, P30 and P40 samples. The stars indicate setting temperature and time of the samples (see Figure 4.16). (The temperature fluctuations in the circled area are due to touching the thermocouples while placing the samples in the mould)

Table 5.3 Setting time and temperatures of P-MGC and P0 samples

Setting Properties	P0	P10	P20	P30	P40
Setting Time (min)	9.0	11.9	13.95	15.1	26.2
Setting Time (s)	540	710	837	906	1569
Setting Temperature (°C)	27.8	26.3	26.5	25.3	21.9

During cement sample preparation, it was observed that increasing MGC content from 10% to 40% increased waiting time. The increase of MGC amount in the cements reduced the viscosity of the cement. As the ratio of powder to liquid was kept at 2:1 (g/ml), increasing the amount of MGC powder in the cements resulted in the amount of PMMA powder being reduced. The ratio of powder to liquid was kept constant in order to compare the findings with a study performed by Bruno et al [163]. Moreover, powder accumulation in the cement was prevented by keeping the ratio constant since the total amount of powder increased by increasing MGC addition from 10% to 40%. It should be noted that densities of MGC and PMMA powder were different, therefore it did not mean the volumes were equal. The density of PMMA powder was 1.2/cm^3 (at 20°C, Wintercryl PMMA Cement SDS) and according to the density measurements using pycnometer (repeated three times), the density of MGC was 3.57±0.05 g/cm^3 (at 20°C). Based on the calculations, the volume ratios between MGC and PMMA are 4%, 8%, 14% and 22% (v/v %). Thus, the ratio between PMMA powder and MMA liquid reduced with the increase of MGC content. This led to longer waiting times and lower viscosity of the obtained cements. Bruno et al. [163] observed that increasing the magnetic glass ceramic amount from 10% to 20% (wt%) did not have a significant effect on the setting time of PMMA cements. However, Shin et al. [177] reported that decreasing viscosity of PMMA cement increased waiting time. Moreover, Kawashati et al. [60] confirmed that increasing magnetite particles from 40% to 60% (wt%) proportionally increased the setting time of PMMA cement since the magnetite particles may reduce the polymerisation reaction of MMA.

5.1.2 SEM Analysis of Magnetic Cements

The surface morphology and elemental composition of W-MGC and P-MGC samples were analysed using SEM. The magnetite crystals on the glass particles were still visible in magnetic cement samples, see Figure 5.4. SEM analyses showed that the particle sizes of MGC on the surface of the cements were relatively consistent between samples. SEM images of W-MGC and P-MGC cement samples and their corresponding EDS spectra of the samples are presented in Figure 5.5. MGC particles were uniformly distributed on the surface of all samples. They were mostly embedded into polymerised cement structure and their size was less than 50μm. Some of the glass particles are indicated with red circles on the images. As the amount of MGC particles increased from 10% to 40%, the peak of Fe in EDS spectra increased. Palacos powder contains ZrO_2 (zirconia) particles and these are indicated with red arrows on SEM images. The peaks of Zr in the EDS spectra images overlapped the peaks of P. ZrO_2 particles tended to agglomerate on the surface forming clusters with a size of 10-40μm.

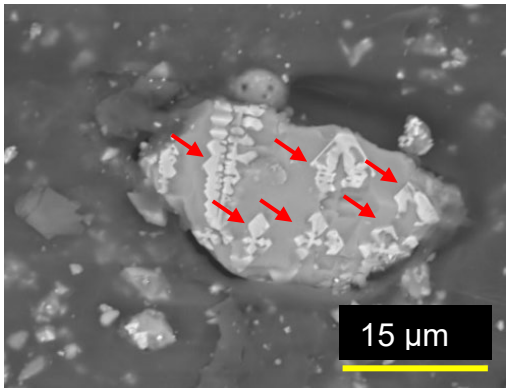

Figure 5.4 SEM image of W30 cement sample that had visible magnetite crystals on the glass residual (2000x magnification). Red arrows refer to magnetite crystals.

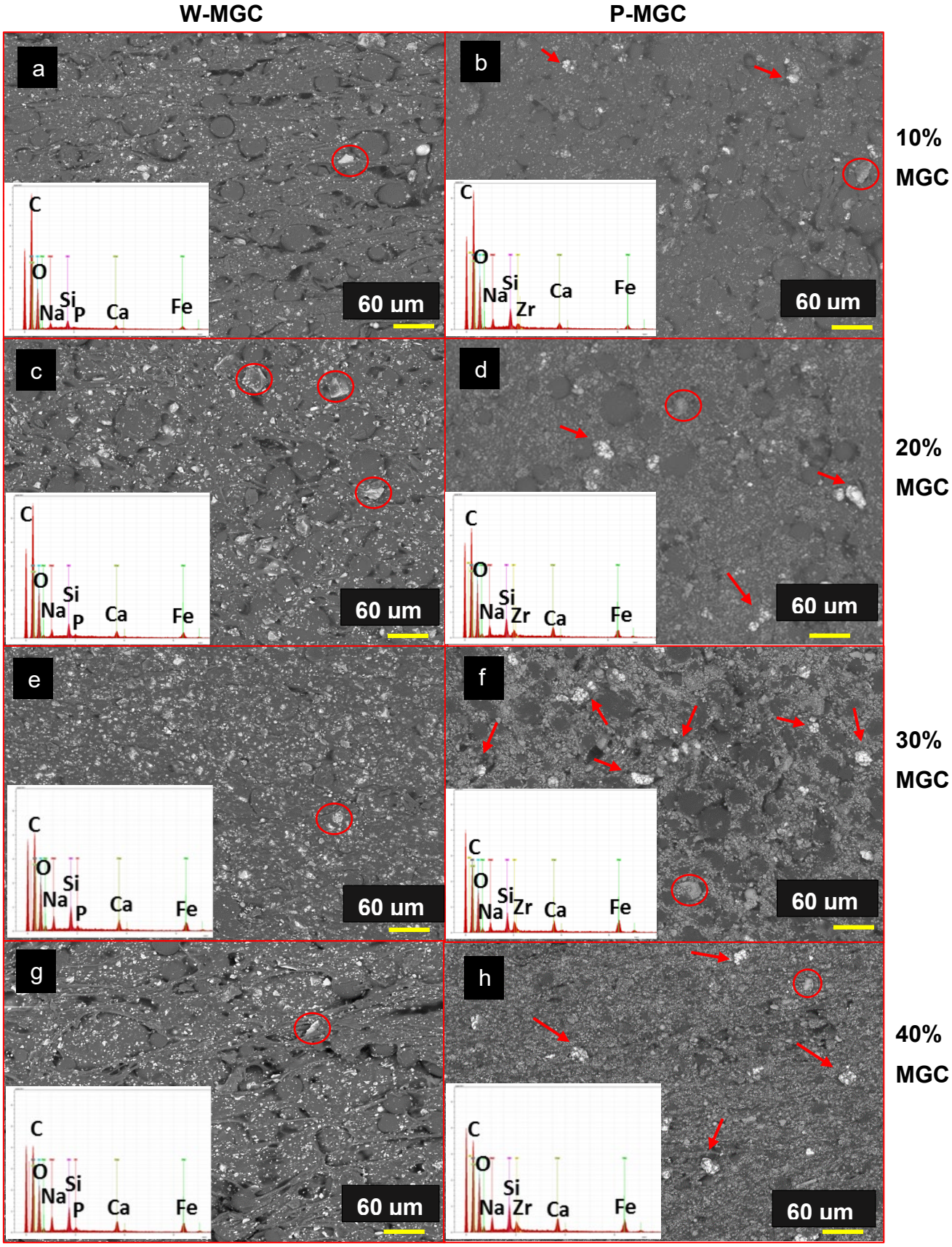

Figure 5.5 SEM images of MGC containing Palacos and Wintercryl cements (250x magnification) and corresponding EDS spectra a) W10 b) P10 c) W20 d) P20 e) W30 f) P30 g) W40 h) P40. Red arrows = ZrO2 particles in Palacos cement and red circles = the glass particles.

5.1.3 Four-point Bending Test

The influence of the MGC addition on the bending strength and bending modulus was analysed through four-point bending tests, see Section 3.6.2. All samples were tested after 24±2 hour. Figure 5.6 shows an image of W20 samples after the test. The fracture occurred towards the centre of the samples.

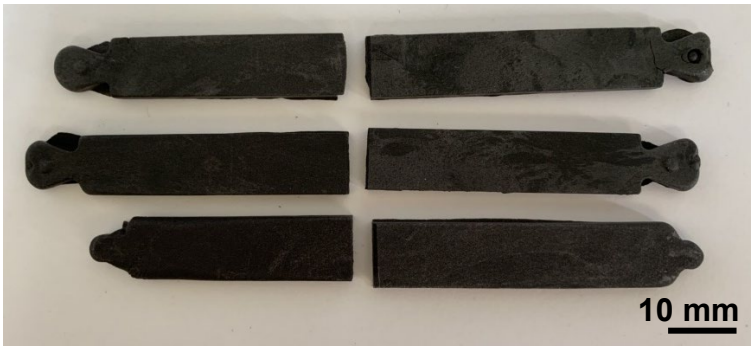

Figure 5.6 W-20 samples after four-point bending test

P-Bag and W-Bag cement samples, which were tested after 24±2 hours (day-1 time point), were used as control sample groups (P0 and W0). These samples were called W0 (0% MGC) and P0 (0% MGC) referring to plain Wintercryl and Palacos cement samples. As previously reported in Section 4.4.3, three out of six samples in W-Bag and one out of five samples of P-Bag point didn't fracture on day-1 time point. Also, one out of six samples from W20 did not fracture. The sample sizes of control groups and W-MGC and P-MGC for calculation of bending strength (B) and modulus (E) are summarised in Table 5.4.

Table 5.4 provides the sample sizes (n) of W-MGC and P-MGC samples along with their control groups for bending strength (B) and bending modulus (E) results.

	W0	W10	W20	W30	W40	P0	P10	P20	P30	P40
B	$n=3$	$n=6$	$n=5$	$n=6$	$n=6$	$n=4$	$n=6$	$n=6$	$n=6$	$n=6$
E	$n=6$	$n=6$	$n=6$	$n=6$	$n=6$	$n=5$	$n=6$	$n=6$	$n=6$	$n=6$

Figure 5.7 and Figure 5.8 present bending strength results of W-MGC and P-MGC samples as well as P0 and W0. W-MGC and P-MGC cement samples containing up to 30% MGC met the minimum requirement for the bending strength of standard ISO 5833:2002, 50 MPa. However, P40 and W40 did not meet the requirements since the mean values were lower than 50 MPa.

Increasing the MGC content in Palacos and Wintercryl cement samples gradually lowered the bending strength. Only W30 showed a slight increase compared to W20. The range of values for all magnetic cements were between 42.1 MPa and 64.4 MPa, see in Figure 5.7. The minimum value occurred for P40 and the maximum value occurred for W10 compared to the control samples. Moreover, the minimum bending strength values of W20 and P30 were below the requirement of the standard, which were 46 and 48 MPa respectively. The range of mean values of bending strength for magnetic cement samples was between 47.5 and 58.5 MPa (see Figure 5.8). The average values of W0 and P0 samples were 60.2 and 62 MPa respectively. One-way ANOVA followed by Tukey *post hoc* test showed that there was no significant difference ($p>0.05$) between P-MGC and W-MGC cements. W40, P40, P30 and P20 samples were significantly different ($p<0.05$) compared to the control samples.

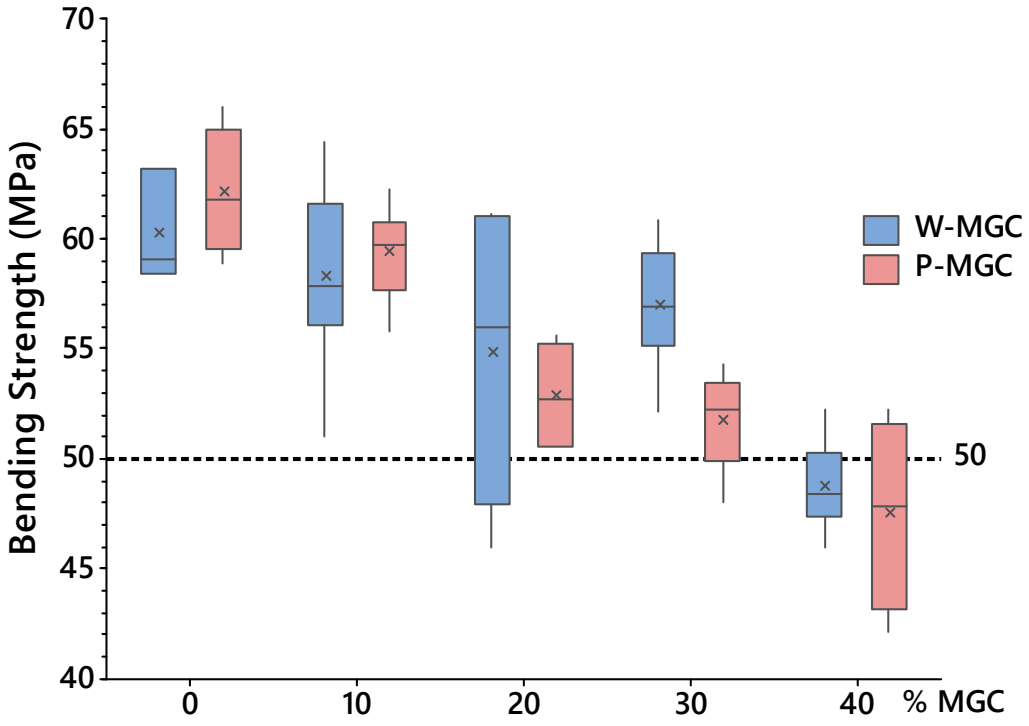

Figure 5.7 Data range of bending strength results of control samples (P0 and W0), W-MGC and P-MGC. The mean values of the samples are expressed with the X, and horizontal lines represent the median values.

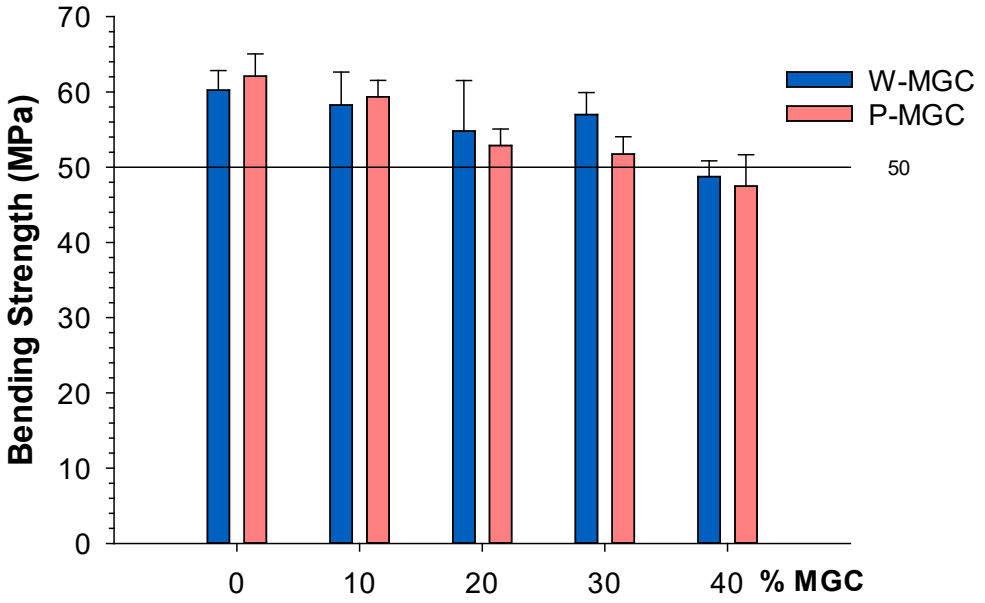

Figure 5.8 Bending strength results of control samples (P0 and W0), W-MGC and P-MGC samples. The data presents mean value ± standard deviation (μ ±σ). The line is minimum requirement of IS05833:2002 standard, 50MPa.

Bending modulus results of W-MGC, P-MGC and their control groups are presented in Figure 5.9 and Figure 5.10. All samples had higher bending modulus values than the standard requirement (1.8GPa). As the MGC addition increased in the samples, bending modulus values gradually increased. This increase was in a good agreement with the rule of mixing for composite materials [178]. The combination of two or more materials can result in having better properties compared to the individual materials. Whilst polymers show low elastic modulus and high ductility, glass-ceramics show high elastic modulus and high brittleness. Therefore, addition of MGC from 10% to 40% in PMMA cement gradually increased the bending modulus. The minimum value was obtained for W10 (2.3GPa) and the maximum value was obtained for W40 and P40 samples (4GPa) compared to control groups, Figure 5.9. The range of mean values for bending modulus for all magnetic cement samples varied between 2.7 and 3.8 GPa (Figure 5.10). The average values for W0 and P0 were 2.7 and 2.8 GPa respectively. One-way Anova followed by Tukey *post-hoc* analyses showed that there was no significant difference ($p>0.05$) between W-MGC and P-MGC samples. However, W40, P40, W30, P30 and P20 samples were significantly different ($p<0.001$) compared to their control samples.

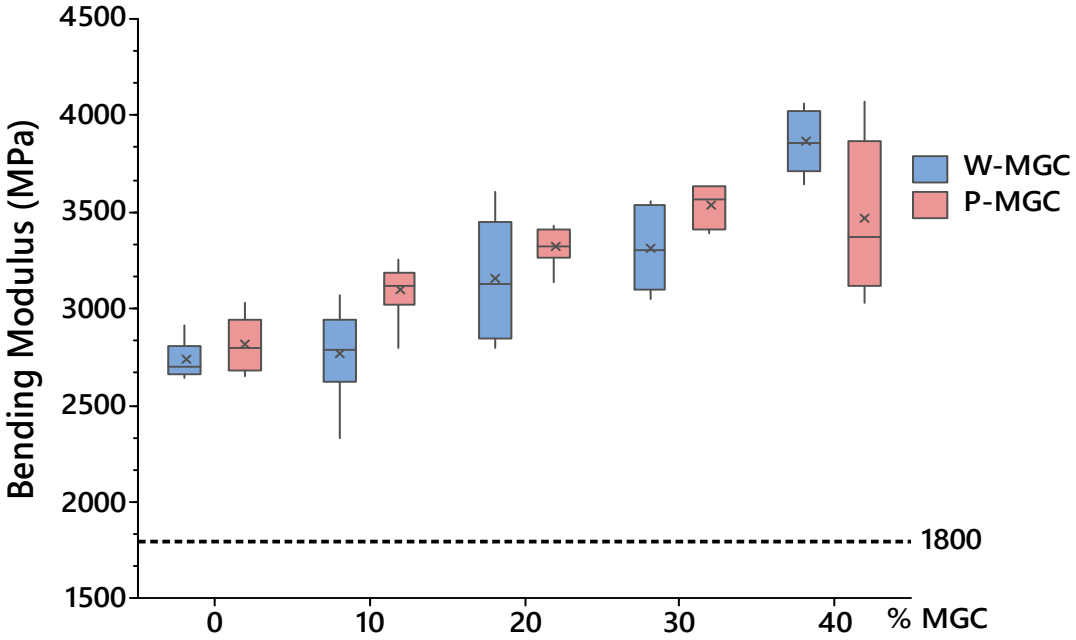

Figure 5.9 Data distribution of bending modulus results of control samples (P0 and W0), W-MGC and P-MGC. The mean values of the samples are expressed with the X, and horizontal lines represent the median values.

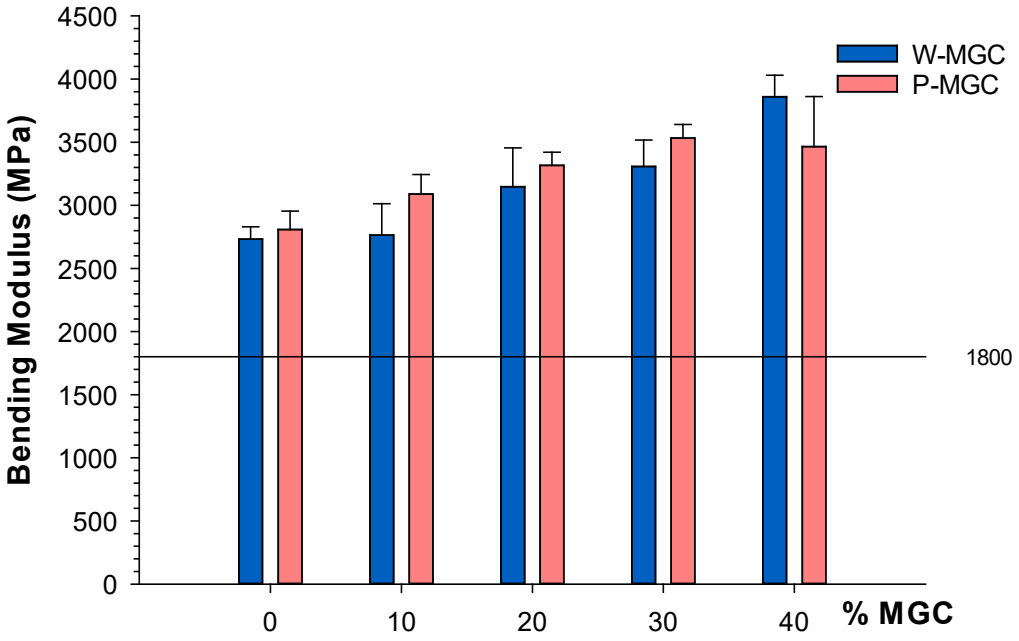

Figure 5.10 Bending modulus results of control samples (P0 and W0), P-MGC and W-MGC samples. The data presents mean value ± standard deviation (μ ±σ). The horizontal line represents the minimum requirement of IS05833:2002 standard: 1800MPa.

The typical stress-strain curves of W0, W-MGC, P0 and P-MGC samples are represented in Figure 5.11 and Figure 5.12. The stress-strain curves exhibited that with the addition of MGC to cement, the samples became more brittle. At the fracture point, W0 and P0, control samples, demonstrated higher stress values than magnetic cement samples, 60 and 62.3 MPa. W10 and P10 samples showed the maximum stress values at the fracture points, which were 58 and 60.5 MPa respectively, compared to other magnetic samples. W40 and P40 samples showed the minimum stress values at the fracture points, which were 49 MPa and 47 MPa. Increasing MGC content from 10% to 40% in the cement samples decreased the maximum strain (%) of the cement samples. Moreover, P-MGC samples had lower strain at the fracture points than W-MGC samples.

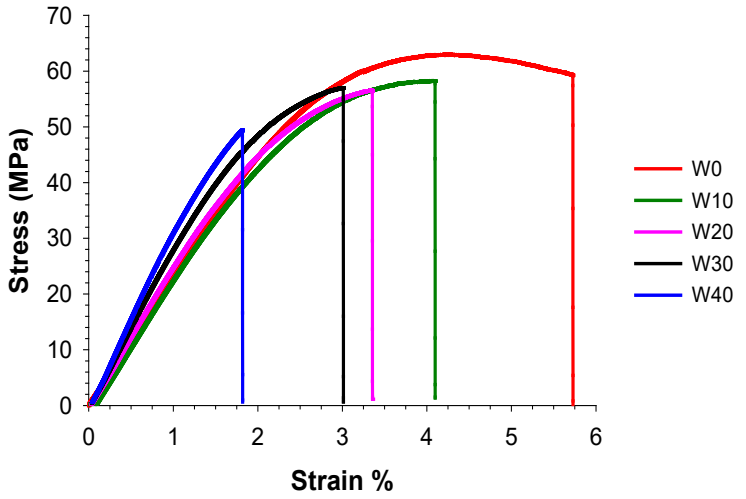

Figure 5.11 Stress-strain curves of W0 (control), W10, W20, W30 and W40 samples

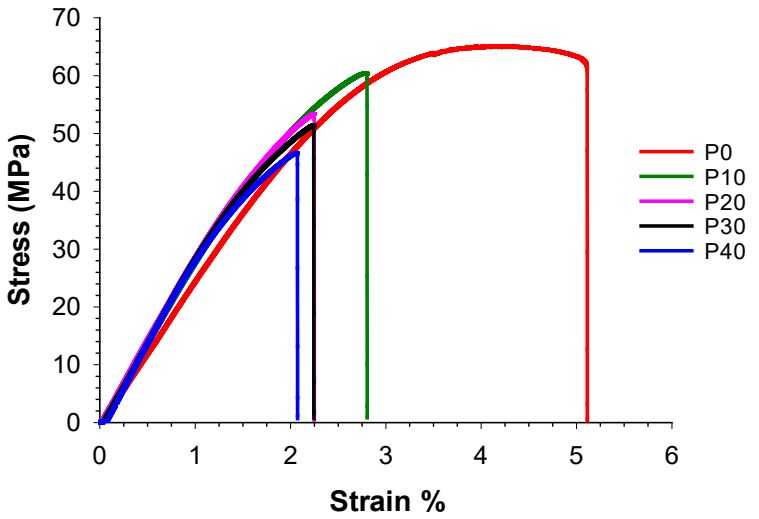

Figure 5.12 Stress-strain curves of P0 (control), P10, P20, P30 and P40 samples

Four-point bending results showed that increasing MGC in the cement decreased the bending strength and increased the bending modulus. These results are in a good agreement with several studies [163, 179]. It should be noted that compatibility of mechanical properties between contacted tissues and bone cement is crucial. The test results showed that bending strength of magnetic PMMA cement samples were within the range of cortical bone. Moreover, bending modulus of magnetic PMMA samples is similar to the cortical bone.

A study reported by Bruno et al. [163] showed that the addition of 20% (wt%) magnetic glass ceramic in PMMA cement did not meet the criteria of the standard since the bending strength results were lower than the requirement (50MPa).

In this study, the results showed that up to 30 % MGC addition in the cement samples met the standard criteria. The stress-strain curves also verified that the MGC addition caused a transition into a brittle-state. It should be noted that the ratio between PMMA powder and MMA liquid reduced with the addition of MGC particles and this may have contributed to a decrease in bending strength. Increasing the MGC content from 20% to 40% showed that P-MGC samples presented a slightly lower bending strength than W-MGC samples. The reason of this could be due to the presence of pre-mixed ZrO_2 (radiopacificer) particles in the composition of Palacos samples that could reduce the mechanical properties [174]. Moreover, there was no significant change in temperature and relative humidity during the four-point bending test (see Appendix C.2).

5.1.4 Compressive Strength Test

Compressive strength tests were used to assess the effect of MGC addition. All samples were tested after 24±2 hour. Compressive strength ($\sigma_{2\%}$) and maximum strength values (σ_{max}) were calculated as described in Section 4.4.4. Figure 5.13 shows a representative image of W40 samples after the test.

Figure 5.13 W40 samples after performing compressive strength test

P-Bag and W-Bag cement samples, which were tested after 24±2 hours (day-1 time point), were used as control sample groups. These samples were called W0 (0% MGC) and P0 (0% MGC) referring to plain Wintercryl and Palacos cement samples. One of the six samples from W10, W20 and P40 cements were discarded due to uneven surfaces as it would dramatically affect the test results. Table 5.5 provides sample sizes of W-MGC and P-MGC samples along with the control groups, W0 and P0.

Table 5.5 provides sample sizes (n) of W0, W-MGC, P0 and P-MGC samples for compressive strength test results

W0	W10	W20	W30	W40	P0	P10	P20	P30	P40
$n=6$	$n=5$	$n=5$	$n=6$	$n=6$	$n=5$	$n=6$	$n=6$	$n=6$	$n=5$

Compressive strength results of P-MGC and W-MGC are presented along with the control groups in Figure 5.14 and Figure 5.15. All samples met the minimum requirement of ISO 5833:2002 standard. The addition of MGC content up to 30 (wt%) had a negligible influence on compressive strength; however, with MGC content of 40%, there was a notable decrease for both types of cement. According to Figure 5.14, the highest compressive strength ($\sigma_{2\%}$) value of MGC containing samples was obtained for W10 (98.2 MPa) compared to the control samples. The minimum value was obtained for P40 (61 MPa). The range of mean values of compressive strength ($\sigma_{2\%}$) for magnetic cement samples varied between 72 and 86.2 MPa, Figure 5.15. The average compressive strength values for W0 and P0 were 86.9 and 80.4 MPa respectively. One-way ANOVA followed by Tukey *post hoc* test showed that there were no significant differences ($p>0.05$) between W-MGC and P-MGC and as well as within the groups ($p>0.05$).

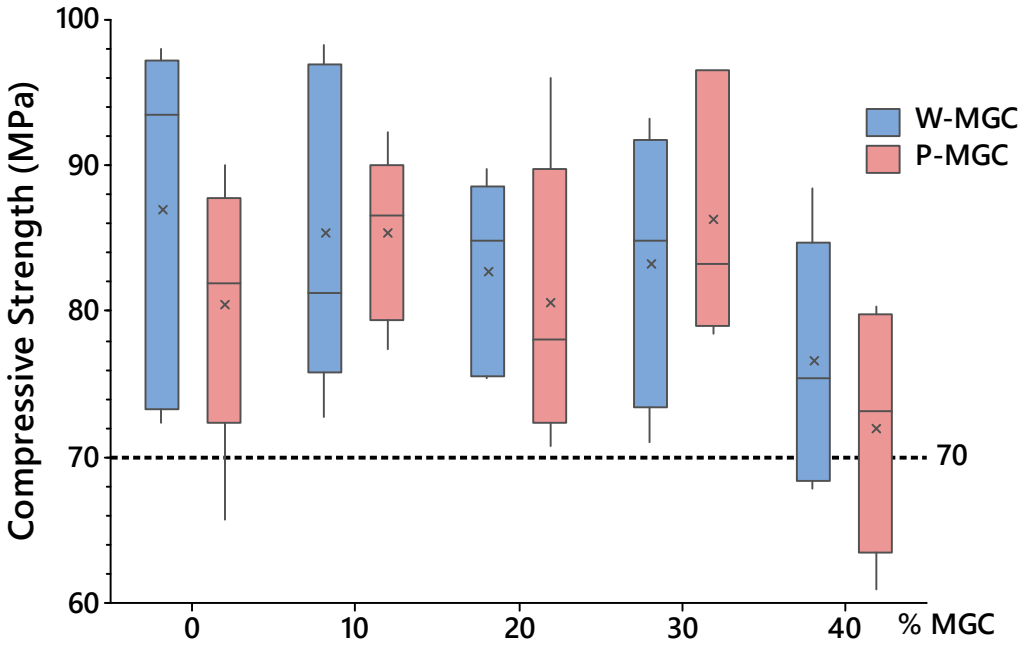

Figure 5.14 Data range representation of compressive strength results of P-MGC and W-MGC with the control groups. The mean values of the samples are expressed with the X, and horizontal lines represent the median values.

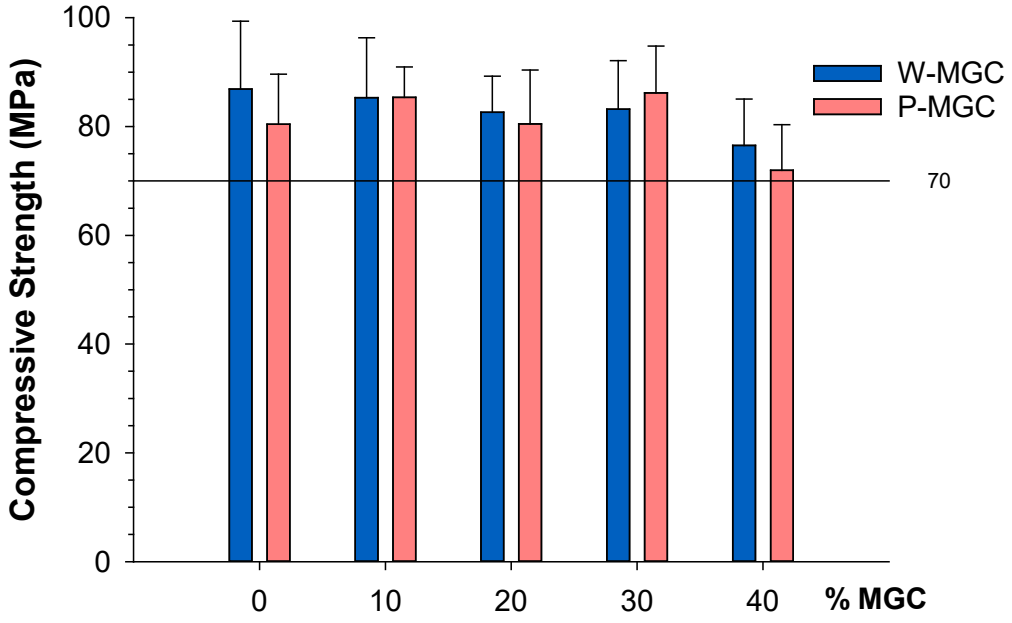

Figure 5.15 Compressive strength values of W-MGC and P-MMGC samples with the control groups. The data presents mean value ± standard deviation (μ ±σ). The line is minimum requirement of IS05833:2002 standard, 70MPa

The typical stress-strain curves of W-MGC, W0, P-MGC and P0 samples used to are shown in Figure 5.16 and Figure 5.17. As can be seen from the figures, with addition of MGC in the content, compressive stress decreased. The maximum stress values for magnetic cement samples were obtained for W10 and P10, compared to the control groups, which were 97 and 91 MPa. W40 and P40 samples had the minimum compressive stress values, which were 68 MPa and 74 MPa.

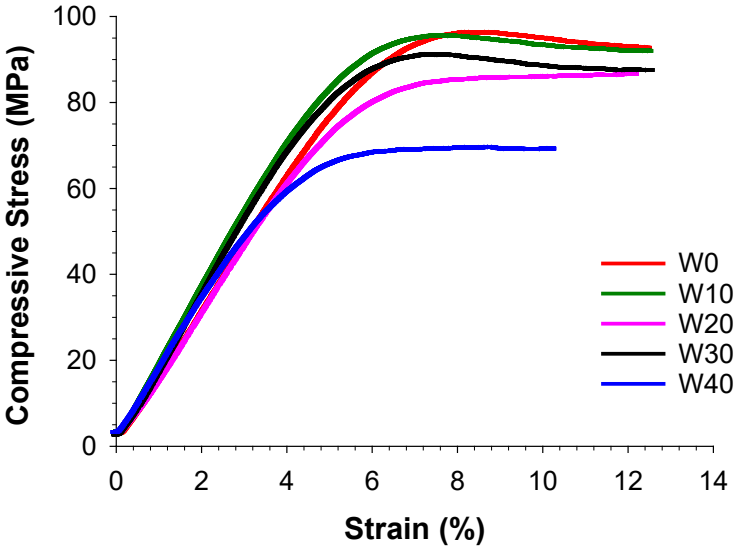

Figure 5.16 Stress-strain curves of selected W0, W10, W20, W30 and W40 samples

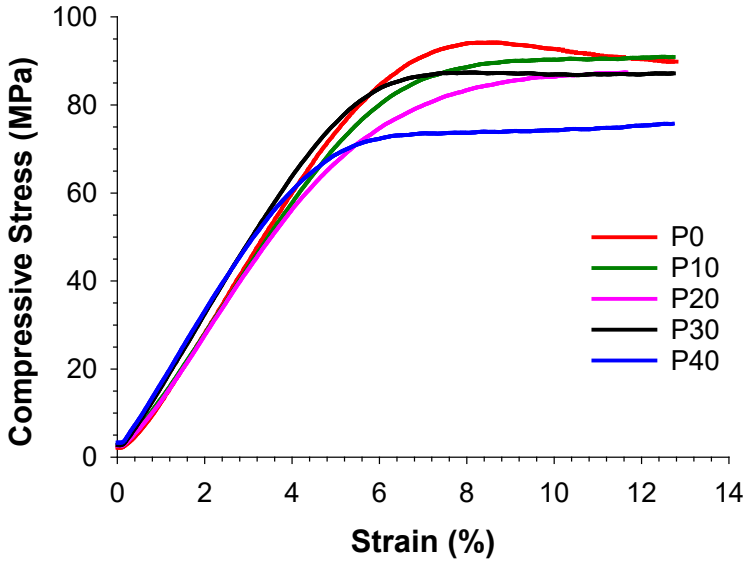

Figure 5.17 Stress-strain curves of selected P0, P10, P20, P30 and P40 samples

Maximum compressive strength (σ_{max}) values of W-MGC, P-MGC and their control samples are shown in Table 5.6. For all samples, maximum compressive strength of the samples was slightly higher than compressive strength ($\sigma_{2\%}$). The highest compressive strength was obtained for P10 and the lowest for P40.

Table 5.6 Compressive strength values of W-MGC and P-MGC samples (Data presents mean values and standard deviations)

	Compressive Strength (σ_{max}, MPa)	
Glass content	**W**	**P**
0%	86.2±11.0	83.1±7.9
10%	87.7±9.3	92.0±9.1
20%	86.3±3.1	87.3±9.8
30%	86.4±6.5	88.2±9.0
40%	80.0±7.2	76.7±4.0

Both maximum compressive strength (σ_{max}) and 2% compressive strength ($\sigma_{2\%}$) values of P-MGC and W-MGC samples met the minimum requirement of ISO 5833:2002 standard, which is in line with a considerable volume of studies [60, 163, 179]. Four-point bending and compressive strength results showed that up to 30% of MGC addition in PMMA cements met the requirements, despite of manual mixing. Increasing the MGC addition decreased PMMA powder content in the cement; therefore, the MGC particles may have acted as reinforcements in the structure and caused agglomerations. A study performed by Moloney et al. reported that the compressive strength decreased due to glass beads did not uniformly adhere to polymer matrix [180].

5.1.5 Vickers Hardness Test

The hardness of the P-MGC and W-MGC samples along with their control groups were tested using the Vickers Hardness test as described in Section 3.6.4. The results of W-MGC, P-MGC and the control groups (W0 and P0) for 18 data points ($n=6$, repeated three times ($r=3$)) are presented in Figure 5.18 and Figure 5.19. Two outliers were identified and presented in the data for Figure 5.18; however, these are not included in the data for Figure 5.19. After a notable increase in hardness with 10% MGC, further addition of MGC continued to increase hardness at a more gradual rate. These results are in a good agreement with several studies [181, 182]. In Figure 5.18, the maximum value was obtained for P40 (31.1 MPa) and the minimum value was obtained for W10 (21MPa) compared to the control groups. The range of mean values of Vickers hardness for magnetic cement samples varied between 22.2 and 28 MPa, Figure 5.19. The average values for W0 and P0 were 14.8 and 19.4 MPa respectively.

According to one-way Anova followed by Tukey *post-hoc* analyses, W-MGC and P-MGC samples were significantly different ($p<0.001$). The presence of ZrO_2 (zirconia oxide, radiopacifier) in Palacos cement can be shown as a reason of this significant difference. The analyses within the sample groups showed that there were significant differences between MGC (wt %) concentrations in all samples ($p<0.001$) with some exceptions; W20 and W30 were not significantly different ($p>0.005$) and similarly, no significant difference was found between P10 and P20 ($p>0.005$).

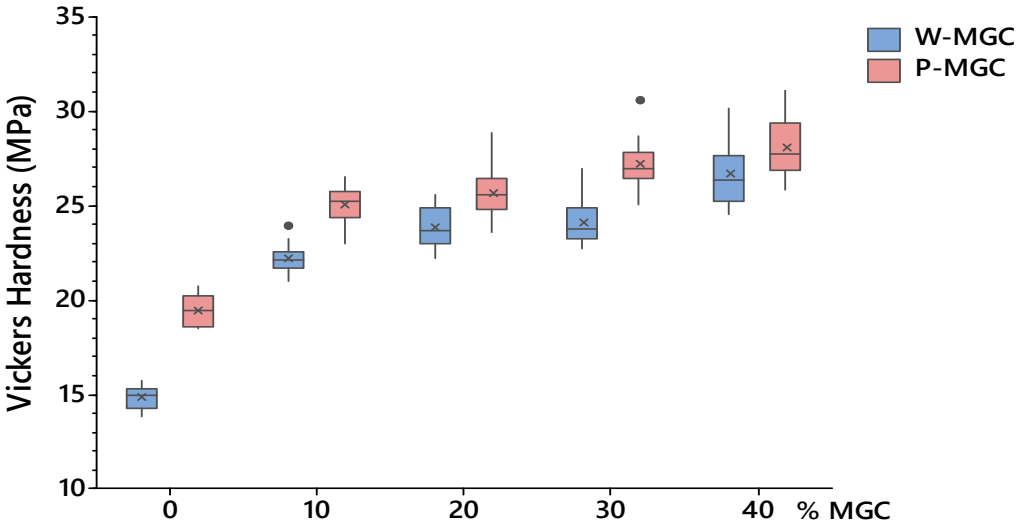

Figure 5.18 Data ranges of Vickers hardness test results of W0, P0, W-MGC and P-MGC samples with the outliers. The mean values of the samples are expressed with the X, and horizontal lines represent the median values, $n=6, r=3$.

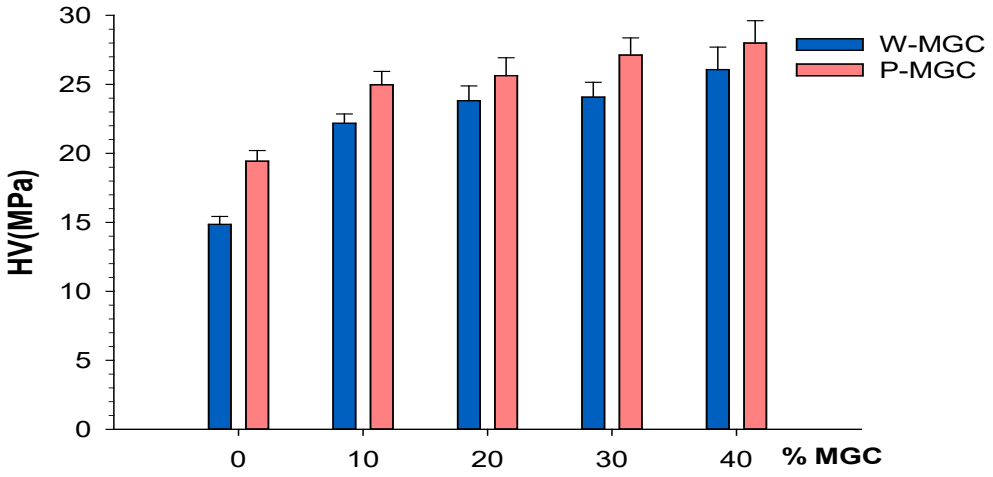

Figure 5.19 Vickers Hardness test results of W0, P0, W-MGC and P-MGC samples without the outliers. The data presents mean value ± standard deviation ($\mu \pm \sigma$), $n=6$, $r=3$.

5.1.6 Analysis of Water Absorption

Water absorption of W-MGC and P-MGC samples were measured and calculated following Archimedes method as described in Section 3.6.5. The results of W-MGC, P-MGC and the control samples are shown in Figure 5.20 and Figure 5.21. For magnetic cement samples, the minimum value was obtained for W10 (3.5%), and the maximum value was obtained for W40 (8.2%), Figure 5.20. Whilst the average water absorption (%) of the magnetic cements was in a range of 4.8-6.6%, it was between 4.7 and 7.2% for W0 and P0 respectively. For manually mixed PMMA bone cements, this range reflects the typical porosity (%) in the cement [183, 184]. The addition of MGC had opposing effects on the two cements; water absorption of W-MGC samples increased, whereas it decreased for Palacos cement samples up to 30% MGC addition. Several studies reported that the addition of particles/fillers in PMMA samples causes increments in porosity [163, 180, 182, 185]. The data range shows that water absorption may vary within the samples and this may be due to manual mixing, which may cause inhomogeneity. Regarding one-way Anova followed by Tukey *post-hoc* analyses, there was no significant difference between and within the sample groups ($p>0.05$).

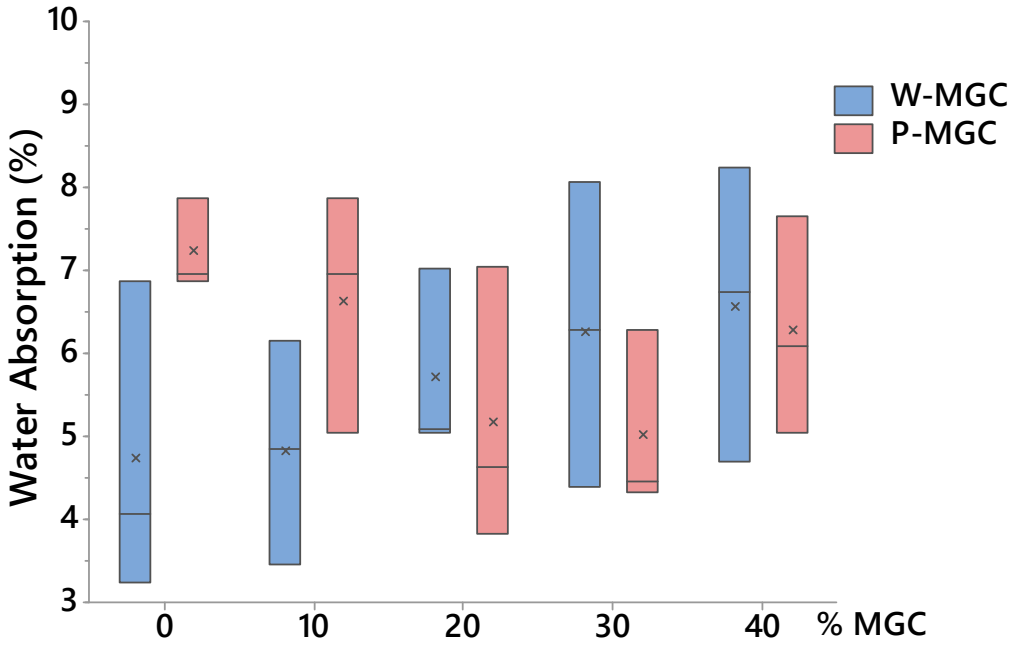

Figure 5.20 The data range of water absorption results of W0, P0, W-MGC and P-MGC samples. The mean values of the samples are expressed with the X, and horizontal lines represent the median values, $n=3$.

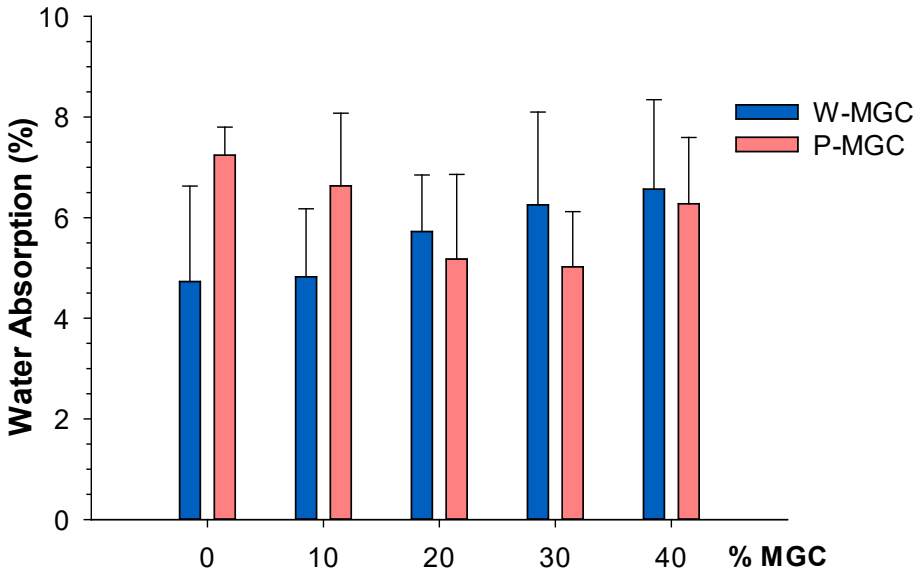

Figure 5.21 Water absorption results of P0, W0, W-MGC and P-MGC samples. The data presents mean value ± standard deviation (μ ±σ), n=3.

5.1.7 In vitro Bioactivity Characterisation

Bioactivity plays an important role in forming an interfacial bonding to the bone which enhances the bone regeneration as described in Section 2.6. In vitro, the SBF solution is used to mimic human body fluid to assess bone-like apatite formation on the surface of biomaterials. After immersion in SBF, initially, a silica layer is formed on the surface of the sample via ion exchange. This enhances precipitation of Ca^{+2} and P ions on the surface, which then leads to a nucleation and growth of apatite crystals [72]. According to the literature, iron ions may inhibit the release of Ca^{+2} from glass-ceramics due to Fe-O-P bonding, which may show resistance to hydration [186].

In this study, all samples were immersed in SBF solution for up to 6 months to observe the bioactivity of magnetic cements. The bioactivity analyses were performed as described in Section 3.6.7. SEM micrographs of W0, W10, W20, W30 and W40 at different time points are shown in Figure 5.22. As previously mentioned, PMMA cements are bioinert materials, therefore, there should not be any sign of bioactivity on the surface of plain PMMA cement samples. Although there was no sign of apatite formation in the first week, microcracks and apatite crystals on the silica gel layer started to form on the W10, W20, W30 and W40 samples after two weeks of immersion in SBF. However, the precipitation of apatite on the surface of the samples was found non-uniform.

Since apatite formation occurs on the glass ceramics the uniformity of apatite layer highly depends on the presence of glass-ceramics on the surface of the polymer matrix. A globular shape of precipitation was observed on W10 and W30 samples at week 2 but W20 and W40 samples had formation of a layer, which was attributed to a silica gel layer [187] formation on the surfaces. After 1 month of immersion in SBF solution, cauliflower-like precipitation of apatite was observed on all the samples and this in good agreement with the literature [61, 163, 188]. Whilst the cauliflower-like precipitation was maintained on the surface of W30, a large globular-like shape was observed on W40 at 2 months of immersion. W10 and W20 had only silica-rich layer formation on the surfaces. After 3 and 6 months of immersion, the growth silica-rich layer was observed on the surfaces of all samples. Overall, the formation of silica-gel layer and cauliflower-like precipitation of apatite indicate that magnetic cement has bioactive properties and it could enhance interfacial bonding to bone.

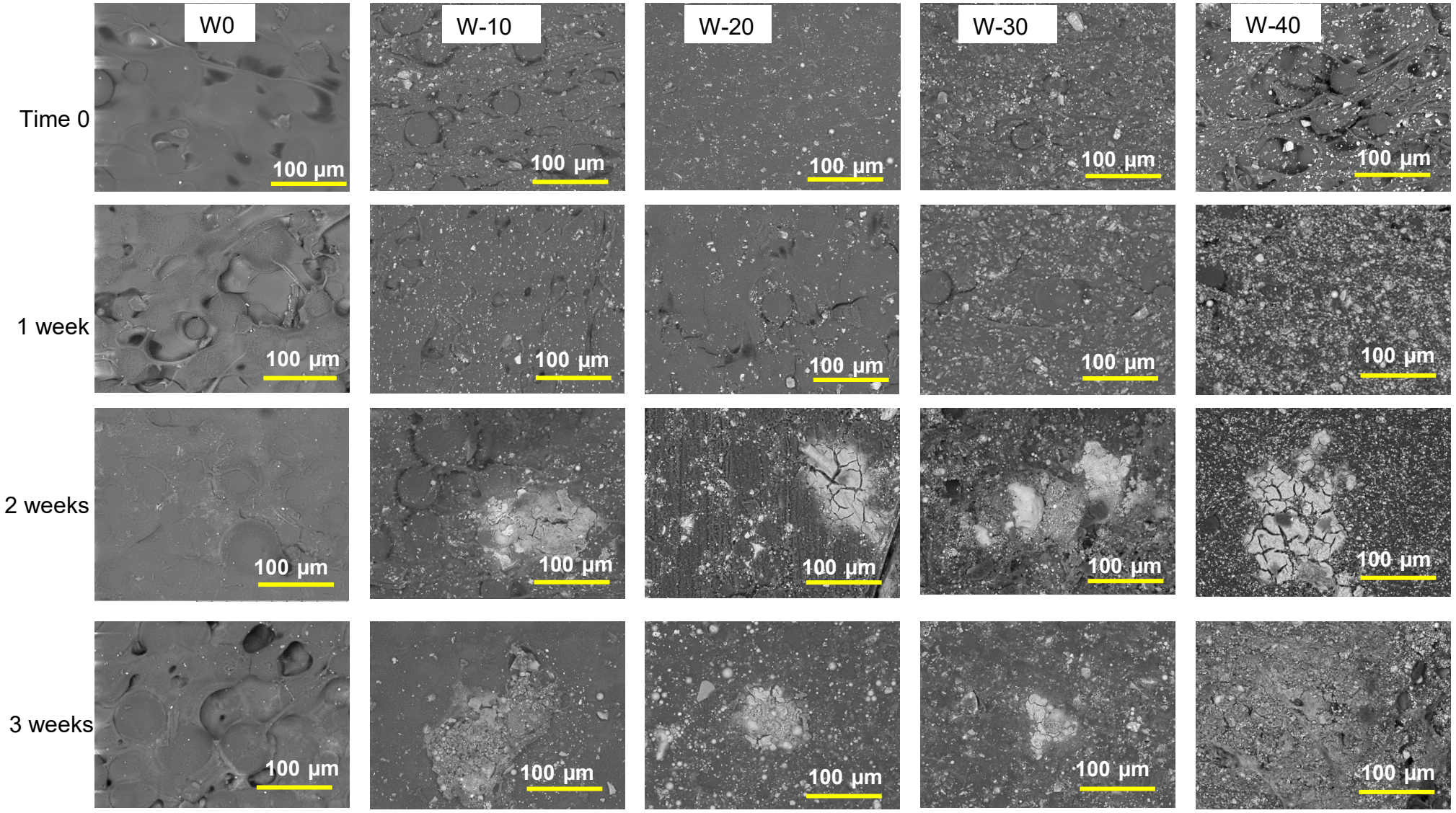
W0
W-10
W-20
W-30
W-40
Time 0
1 week
2 weeks
3 weeks
100 µm

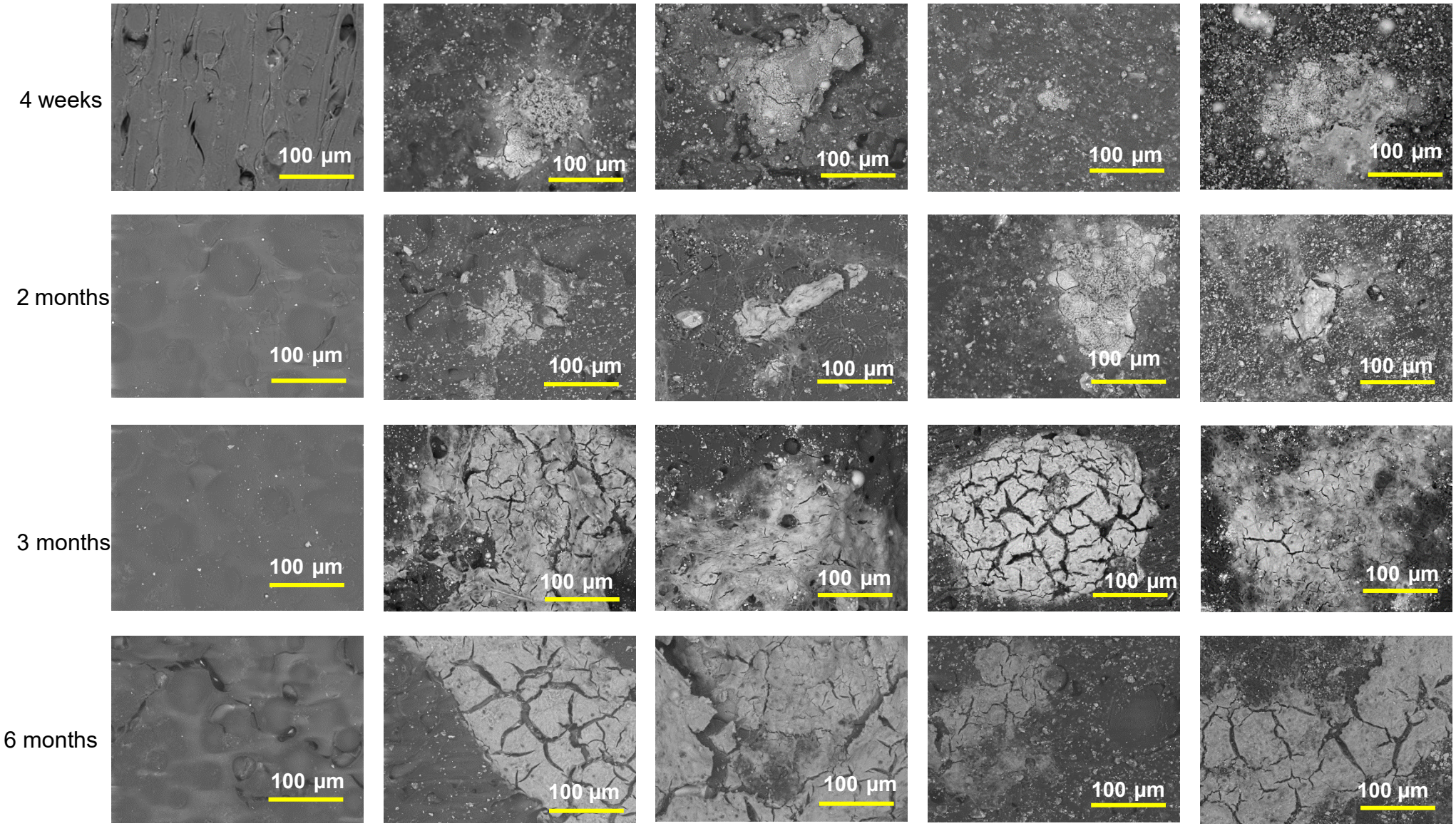

Figure 5.22 Morphology of W-MGC samples before (time 0) and after immersion in SBF solution up to 6 months (at 500x magnification)

The chemical composition of the samples before and after immersion in SBF was analysed using EDS. Figure 5.23 presents typical SEM images and corresponding EDS spectra of W0 and W10 samples before immersion in SBF and after 4 weeks and 6 months of immersion in SBF. The EDS analyses were performed in the circled areas. As W0 sample did not have any MGC addition it only showed elements of C and O. The EDS analyses on W10 showed that after the SBF immersion, precipitation of the peaks of P and Ca increased compared to the non-soaked samples.

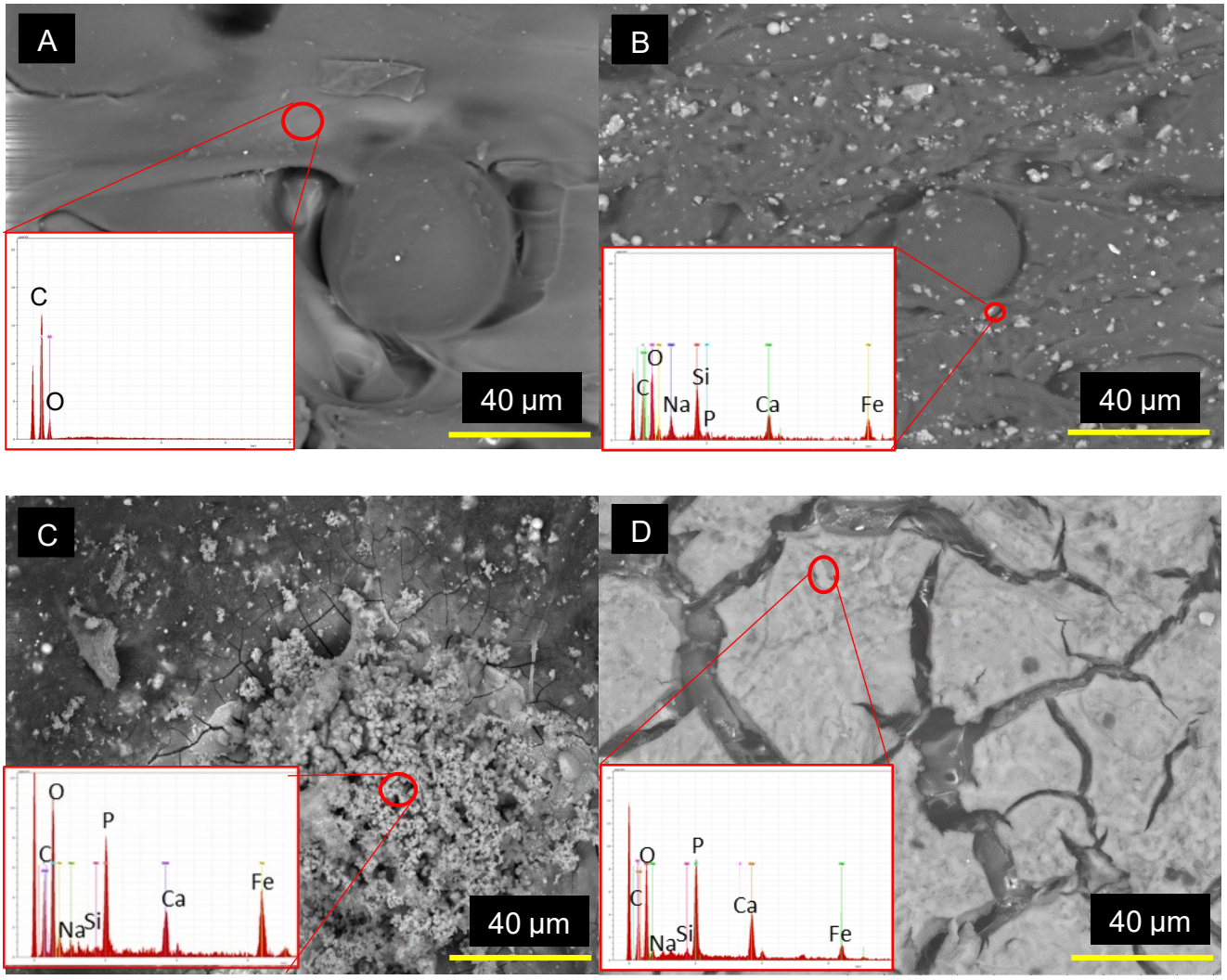

Figure 5.23 SEM micrographs (x1000 magnification) and EDS spectra of A) W0 at time 0 B) W10 at time 0 C) W10 after 1 months of immersion C) W10 after 6 months of immersion

5.1.8 Cytocompatibility Tests

Cell attachment and proliferation on the surface of magnetic cements were analysed using MTT and Alamar Blue assays. It should be noted that the sample side in contact with silicone mould surface was used for all experiments. According to the literature, PMMA cements are toxic due to the release of MMA monomer therefore, they have poor tissue compatibility [14, 189]. In contrast, bioactive glass-ceramics show good cell attachment and cell proliferation properties [72, 190, 191]. Verne et al. reported that cell viability and adhesion of osteosarcoma cells seeded on magnetic cement was considerably high [147].

5.1.8.1 MTT Assay

The analysis of cytocompatibility of W0 and W-MGC samples were investigated performing MTT assay as described in Section 3.6.8.2. For this assay, osteosarcoma (U2OS) cells were used. The samples were placed in two 12-well plates as described in Section 3.7.8.2 and Figure 3.18. W0-1 samples were placed in the first 12-well plate, which had W10 and W20 samples. W0-2 samples were placed in the second 12-well-plate, which had W30 and W40 samples. The sample sizes are provided in Table 5.7. Figure 5.24 and Figure 5.25 show viability (%) of U2OS cells seeded on the samples for up to 7 days, see Appendix D for the results without negative control. The average cell viability decreased from approximately 180% to 5%. On day 1, W40 samples showed relatively higher cell viability than W0 (1,2), W10, W20 and W30 samples. After 3 days of incubation, cell viability noticeably dropped in all samples, which continued to insignificant amounts in day-7. It was detected that on day-3 and day-7, W0-1 and W0-2 samples had relatively higher cell viability than W-MGC samples. Overall analyses showed that Wintercryl cement showed cytotoxic effects on the cells. Increasing the MGC content in cement samples did not increase the cell viability on the samples. However, these results were found inconclusive. This could be due to the complications that occurred during the test such as debris releases from the samples and cell contaminations. As the test was incomplete, statistical analyses were not performed and the data was not normally distributed ($p<0.05$) as well.

Table 5.7 Sample size (n) of W0 (1,2), W10, W20, W30 and W40 sample groups for MTT assay (W0(1,2)= control groups)

Samples	**W0-1**	**W10**	**W20**	**W30**	**W40**	**W0-2**
Sample size	$n=3$	$n=3$	$n=3$	$n=3$	$n=3$	$n=3$

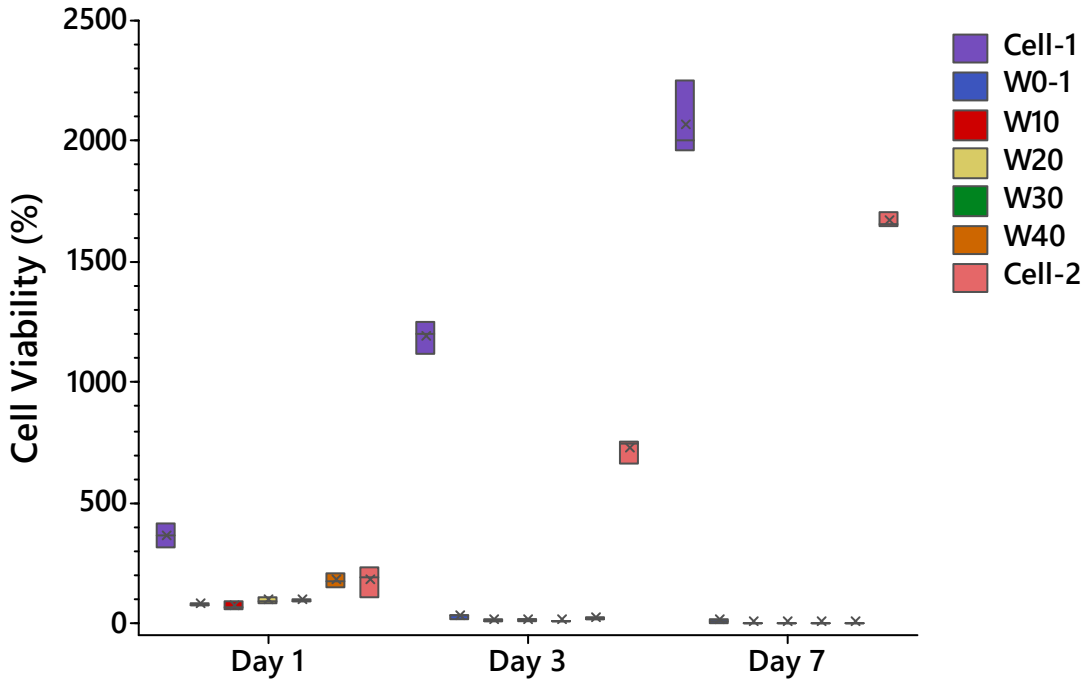

Figure 5.24 Data range of cell viability (%) of U2OS cells seeded on W0 and W-MGC samples along with negative control (cell1&2) for 1, 3 and 7 days. The mean values of the samples are expressed with the X, and horizontal lines represent the median values.

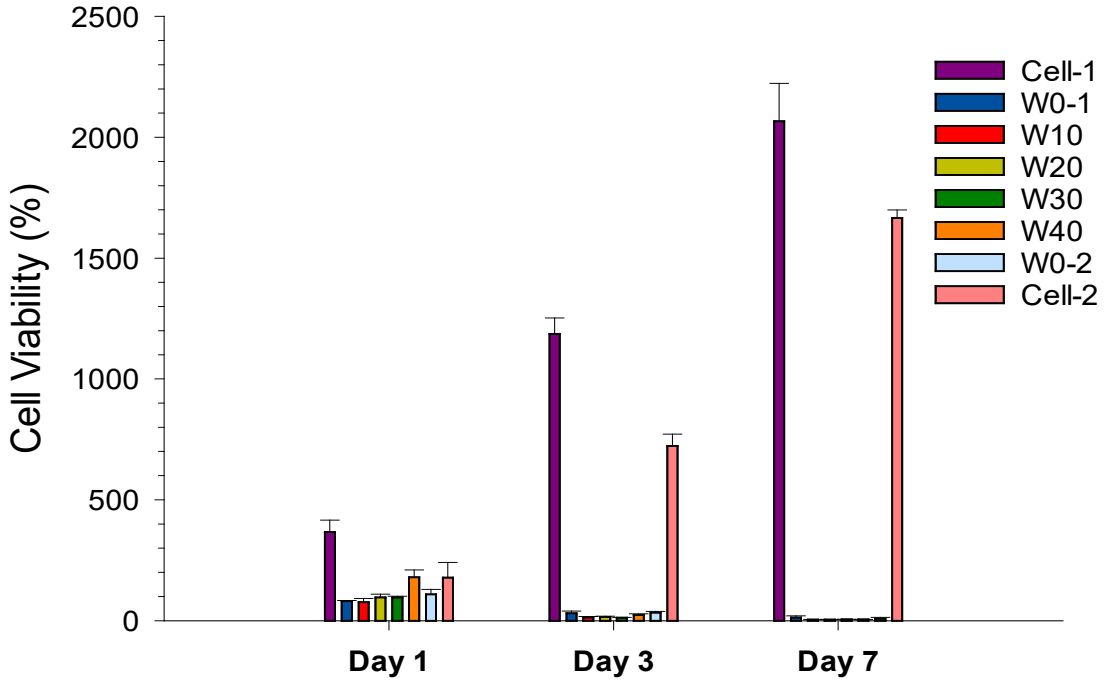

Figure 5.25 Cell viability of U2OS cells seeded on W0 and W-MGC samples along with negative control (cell1&2) for 1, 3 and 7 days. The data presents mean value ± standard deviation (μ ±σ).

5.1.8.2 Alamar Blue Assay

Alamar Blue assay was performed to assess the cell viability of two cell lines, U2OS and OBS, seeded on W-MGC, P-MGC and their control groups. The control samples were the plain cements P0 and W0. Negative control was the tissue culture. Initially five samples were used, and 4 aliquots were taken from each sample (20 data points for each group). However, some samples had cell contamination throughout the time-points and these samples were discarded. Sample size of the sample groups are provided in Table 5.8. Alamar Blue assay was repeated several times due to cell contaminations that occurred in the assigned incubator in laboratory.

Table 5.8 Sample size (n) of W-MGC and P-MGC along with the control groups

Cell Lines	Time Points	W0-1	W10	W20	W30	W40	W0-2
U2OS Cells	Day 1	*n=5*	*n=4*	*n=5*	*n=5*	*n=5*	*n=5*
	Day 3	*n=5*	*n=4*	*n=5*	*n=5*	*n=5*	*n=5*
	Day 7	*n=5*	*n=4*	*n=5*	*n=5*	*n=5*	*n=4*
	Day 10	*n=5*	*n=4*	*n=5*	*n=5*	*n=5*	*n=4*
	Day 14	*n=3*	*n=4*	*n=5*	*n=5*	*n=5*	*n=4*
OBS Cells	Day 1	*n=5*	*n=5*	*n=5*	*n=5*	*n=5*	*n=5*
	Day 3	*n=5*	*n=5*	*n=5*	*n=5*	*n=5*	*n=5*
	Day 7	*n=5*	*n=5*	*n=5*	*n=5*	*n=5*	*n=5*
	Day 10	*n=5*	*n=5*	*n=5*	*n=5*	*n=5*	*n=5*
	Day 14	*n=5*	*n=5*	*n=5*	*n=5*	*n=5*	*n=5*
Cell Lines	**Time Points**	**P0-1**	**P10**	**P20**	**P30**	**P40**	**P0-2**
U2OS Cells	Day 1	*n=4*	*n=5*	*n=5*	*n=5*	*n=5*	*n=5*
	Day 3	*n=4*	*n=5*	*n=5*	*n=5*	*n=5*	*n=5*
	Day 7	*n=3*	*n=5*	*n=5*	*n=5*	*n=5*	*n=5*
	Day 10	*n=3*	*n=5*	*n=5*	*n=5*	*n=5*	*n=5*
	Day 14	*n=2*	*n=5*	*n=5*	*n=5*	*n=5*	*n=5*
OBS Cells	Day 1	*n=5*	*n=5*	*n=5*	*n=5*	*n=5*	*n=5*
	Day 3	*n=5*	*n=5*	*n=5*	*n=5*	*n=5*	*n=5*
	Day 7	*n=5*	*n=5*	*n=5*	*n=5*	*n=5*	*n=5*
	Day 10	*n=5*	*n=5*	*n=5*	*n=5*	*n=5*	*n=5*
	Day 14	*n=5*	*n=5*	*n=5*	*n=5*	*n=5*	*n=5*

Cell viability (%) results of U2OS cells that were seeded on W0 and W-MGC samples along with the negative controls, cell-1 and cell-2, up to 14 days are shown in Figure 5.26 and Figure 5.27. The results without negative controls are presented in appendix D.2. A non-linear decrease of cell viability was observed in all samples with an increase of time. The highest cell viability was obtained in day-1 time point for W10 and W0 (~72%). The lowest cell viability was obtained in day-14 time point for W30 (8.7 %), Figure 5.26. Overall, the average cell viability decreased from 67% to 9%, Figure 5.27. There was an abrupt decrease of cell viability from day-1 to day-10. There were no statistically differences between day-10 and day-14. This major decrease implied that W0 and W-MGC samples did not enhance U2OS cell proliferation and attachment, and this may have indicated the cytotoxicity. Mann-Whitney analysis showed that that there was a significant difference ($p<0.001$) between time points; however, there was no significant difference ($p>0.05$) between the samples.

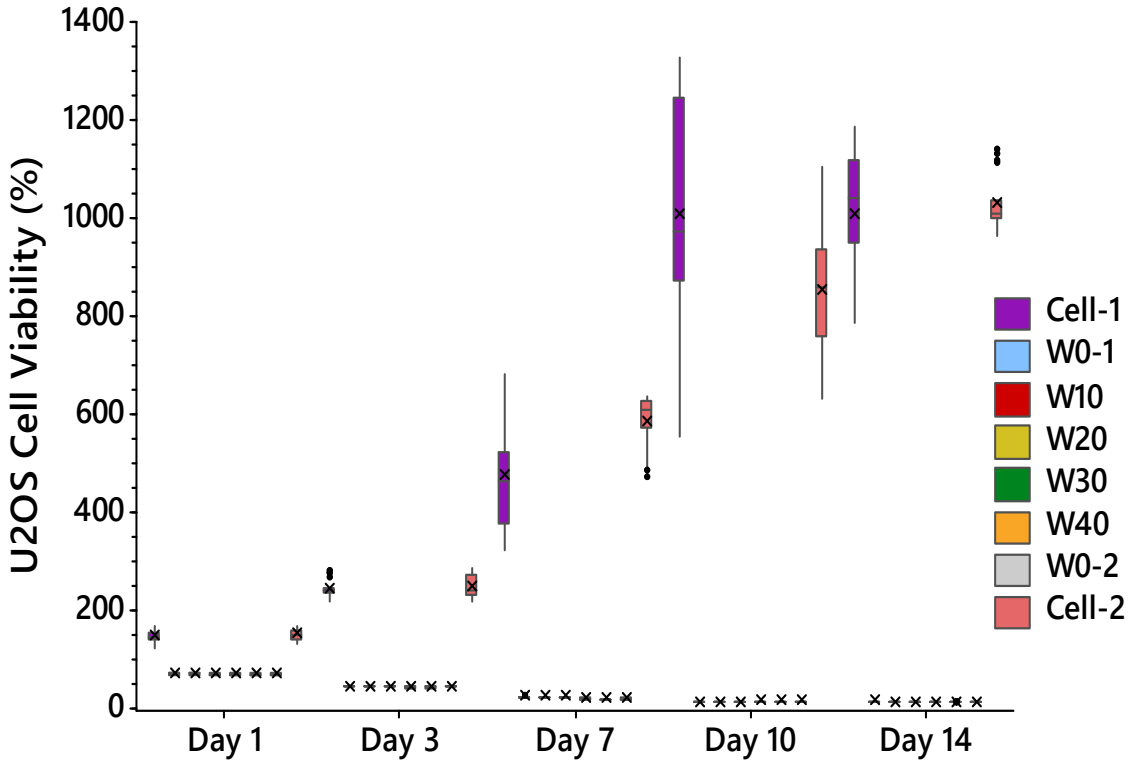

Figure 5.26 Data range of U2OS cell viability on W0-1(control sample in plate-1), W0-2 (control sample in plate 2) and W-MGC samples along with negative control (Cell-1&2) for 1, 3, 7, 10 and 14 days. The data includes outliers. The mean values of the samples are expressed with the X, and horizontal lines represent the median values.

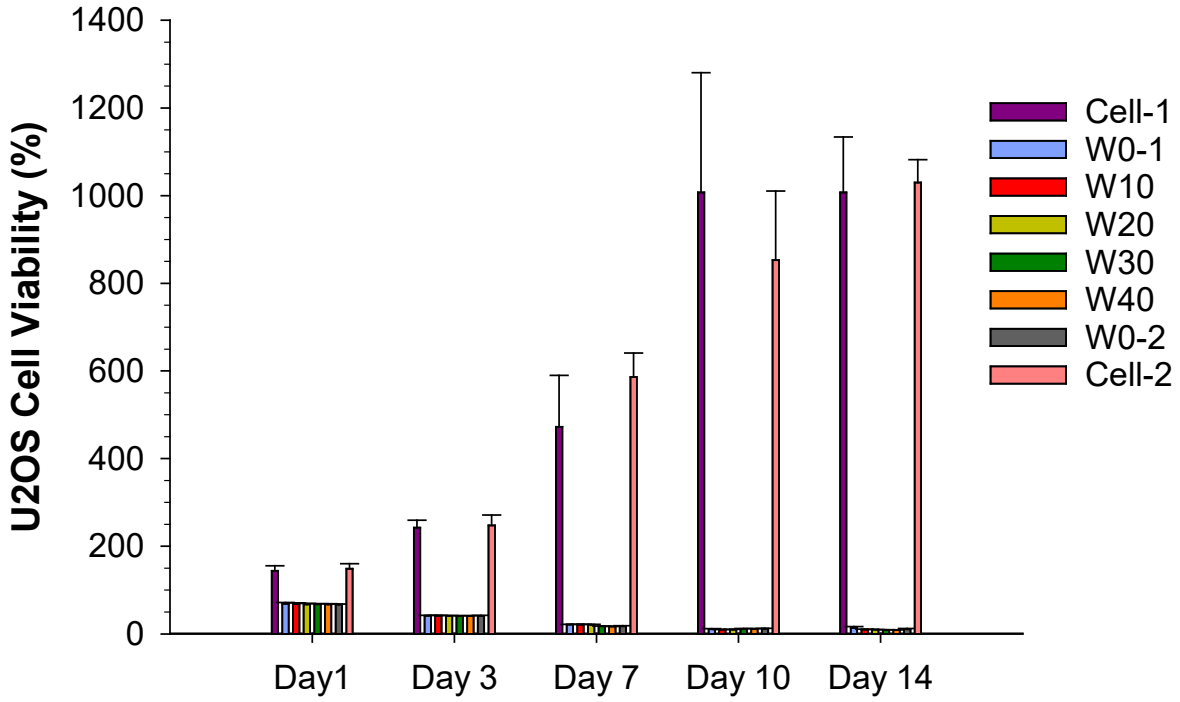

Figure 5.27 Percentage of cell viability of U2OS cells on W0-1(control sample in plate-1), W0-2 (control sample in plate-2) and W-MGC samples along with negative control (Cell-1&2) for 1, 3, 7, 10 and 14 days. The data do not include outliers. The data presents mean value ± standard deviation (μ ±σ).

Figure 5.28 and *Figure 5.29* present cell viability (%) results of U2OS cells, which were seeded on P0 and P-MGC samples along with the negative controls, cell-1 and cell-2 for up to 14 days. The results without negative controls are presented in appendix D.2. Similar to W0 and W-MGC samples, the cell viability sharply decreased from day-1 to day-14. In Figure 5.28, the highest cell viability was obtained for W0-1 on day-1 (73.2%) and the lowest cell viability was observed for P30 on day-14 time point (7.5%), Figure 5.28. Throughout the time period, the average cell viability decreased from 68% to 8%, Figure 5.29. This decrease suggested that P0 and P-MGC samples could have cytotoxic effects on U20S cells. Mann-Whitney analysis showed that that there was a significant difference ($p<0.001$) between time points; however, there was no significant difference ($p>0.05$) between the samples.

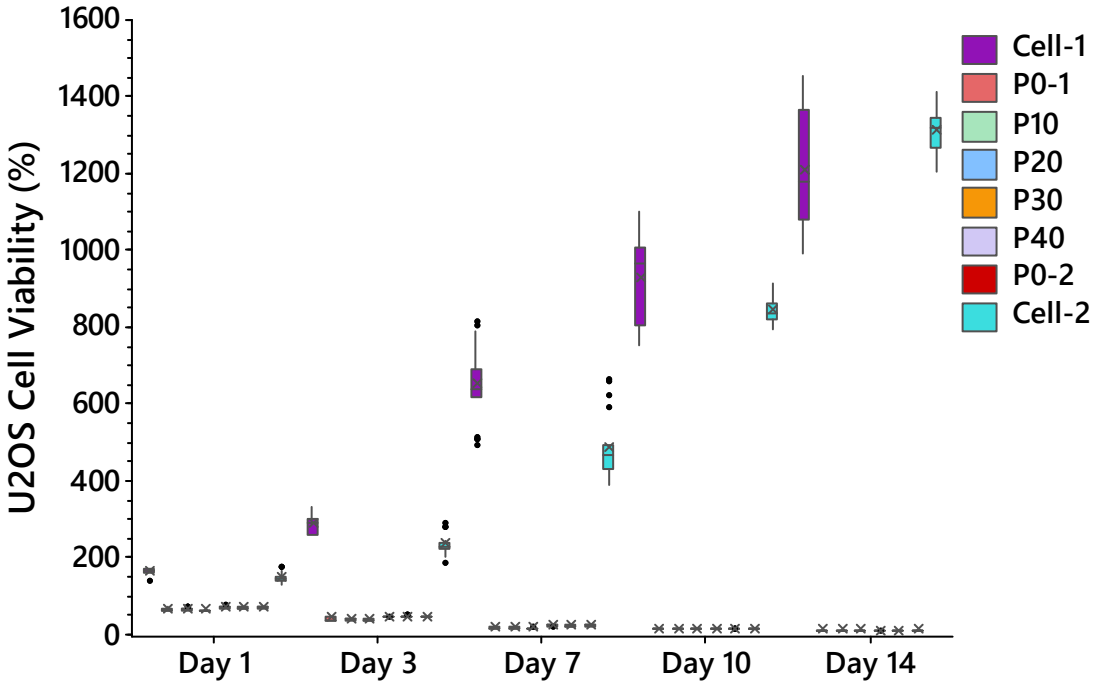

Figure 5.28 The data range of U2OS cell viability on P0-1 (control sample in plate-1), P0-2 (control sample in plate-2) and P-MGC samples along with negative control (Cell-1&2) for 1, 3, 7, 10 and 14 days. The data includes outliers. The mean values of the samples are expressed with the X, and horizontal lines represent the median values.

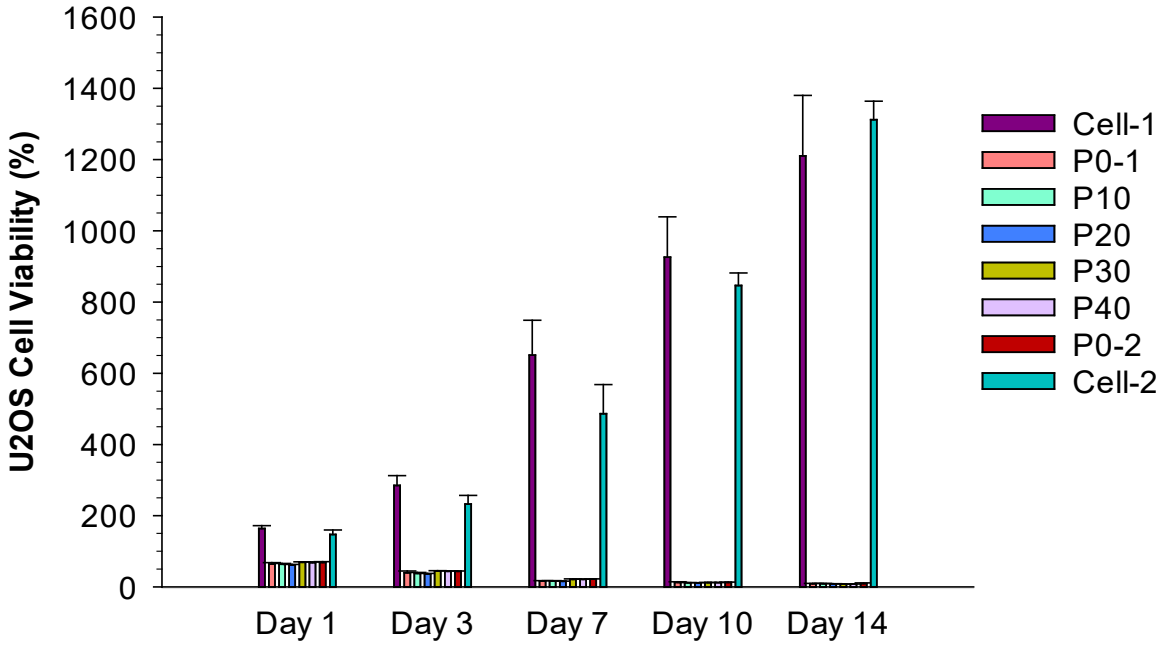

Figure 5.29 Percentage of cell viability of U2OS cells on P0-1 (control sample in plate-1), P0-2 (control sample in plate-2) and P-MGC samples along with negative control (Cell-1&2) for 1, 3, 7, 10 and 14 days. The data do not include outliers. The data presents mean value ± standard deviation (μ ±σ).

Cell viability (%) of OBS cells seeded on W0 and W-MGC samples along with the negative controls, cell-1 and cell-2 are plotted in Figure 5.30 and Figure 5.31. The results without negative controls are presented in appendix D.2. Despite U20S cells showing drastic reductions, OBS cells presented more gradual decreases over the 14-day time period. The aim of performing the test using two cell lines was to compare the effect of magnetic PMMA cements on both cancerous and healthy cells. The hypothesis was enhancing cell viability of OBS cells whilst decreasing the cell viability of U2OS cells. Although the cell viability of OBS cells did not increase gradually, this gradual decrease compared to U2OS cells was still favorable. In Figure 5.30, the highest cell viability was obtained for W0-2 on day-1 (105.5%) and the lowest was obtained for W20 on day-14 (50.6%). Although the percentage of average cell viability was still higher than 55% for all samples on day 14, the decrease still implied low cell proliferation and attachment as well as cytotoxicity effects of W0 and W-MGC samples on OBS cells. Mann-Whitney analysis showed that that there was a significant difference ($p<0.001$) between time points. The comparisons between the samples showed that there were significant differences ($p<0.001$) between the samples, with some exceptions. W10 sample was not significantly different ($p>0.05$) compared to W0-1 and W20 and also there was no significant difference ($p>0.05$) between W20, W30 and W40 samples.

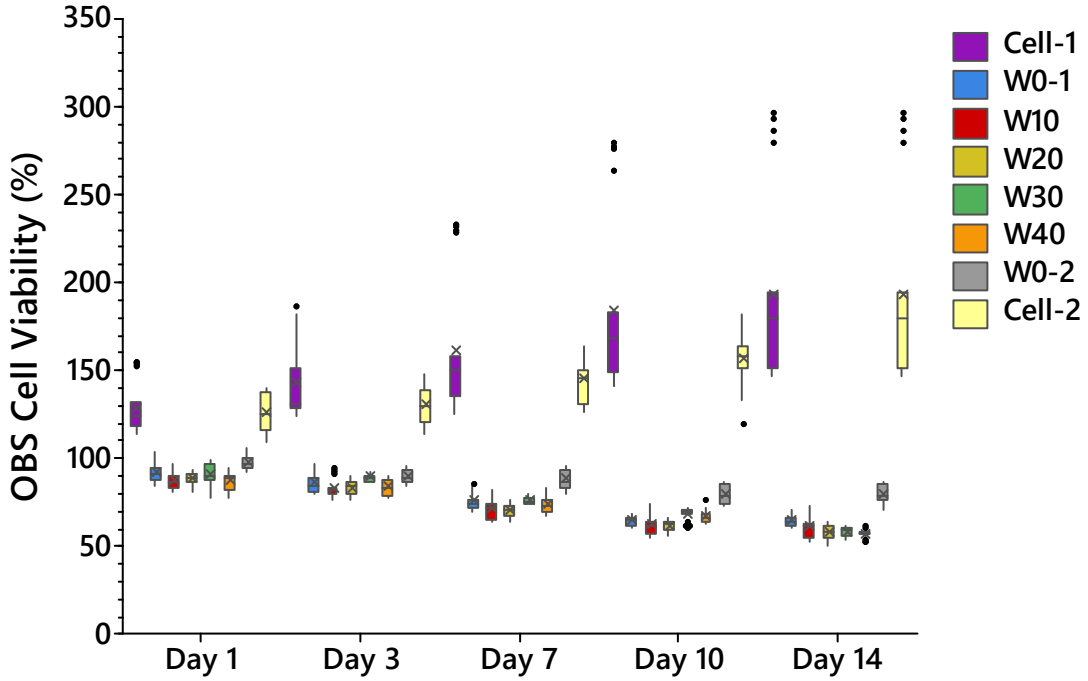

Figure 5.30 The data range of OBS cell viability W0-1(control sample in plate-1), W0-2 (control sample in plate 2) and W-MGC samples along with negative control (Cell-1&2) for 1, 3, 7, 10 and 14 days. The data includes outliers. The mean values of the samples are expressed with the X, and horizontal lines represent the median values.

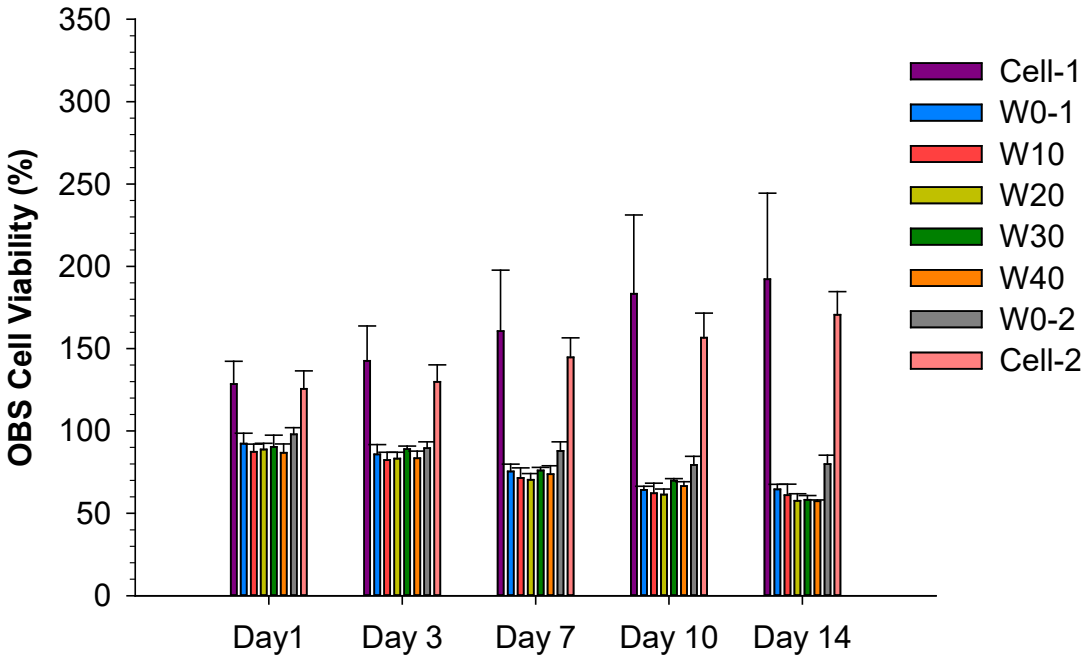

Figure 5.31 Percentage of cell viability of OBS cells on W0-1(control sample in plate-1), W0-2 (control sample in plate-2) and W-MGC samples along with negative control (Cell-1&2) for 1, 3, 7, 10 and 14 days. The data do not include outliers. The data presents mean value ± standard deviation (μ ±σ).

The cell viability of OBS cell results for P0 and P-MGC samples along with the negative controls, cell-1 and cell-2 are shown in Figure 5.32 and Figure 5.33. Similar to Wintercryl cements, OBS cells seeded on P0 and P-MGC samples exhibited a higher percentage of cell viability than U2OS cells over the time period. However, a gradual reduction of the cell viability was still observed. Whilst the highest cell viability was obtained for P0-1 and P10 samples (99%) on day-1 time point, the lowest value was obtained for P40 (52%) on day-14 time point, Figure 5.32. Throughout the time period, the average cell viability decreased from 90% to 55%, Figure 5.33. Although the samples showed more than 55% of cell viability, P0 and P-MGC samples may have been cytotoxic. Mann-Whitney analysis showed that there was a significant difference ($p<0.001$) between time points and the sample groups as well. However, there were some exceptions. There was no significant difference ($p>0.05$) between P10, P20 and P30. The comparison between P0-1 and P0-2 ($p>0.05$) showed that they were not significantly different as well.

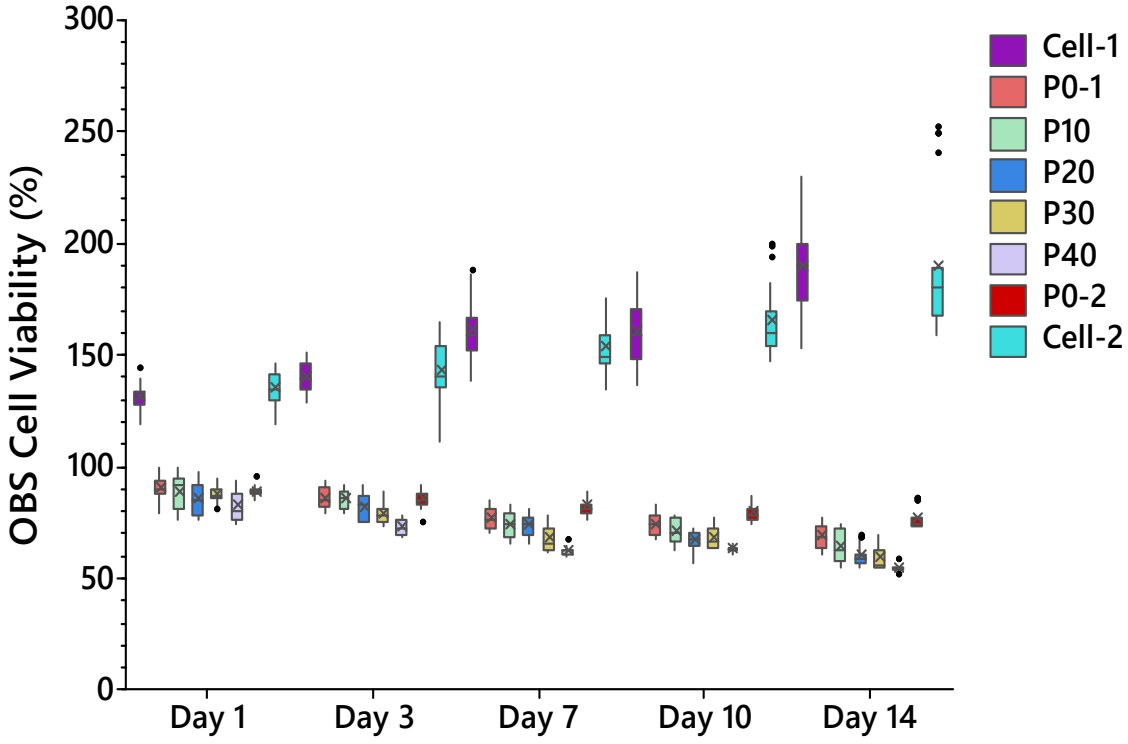

Figure 5.32 The data range of OBS cell viability (%) on P0-1 (control sample in plate-1), P0-2 (control sample in plate-2) and P-MGC samples along with negative control (Cell-1&2) for 1, 3, 7, 10 and 14 days. The data includes outliers. The mean values of the samples are expressed with the X, and horizontal lines represent the median values.

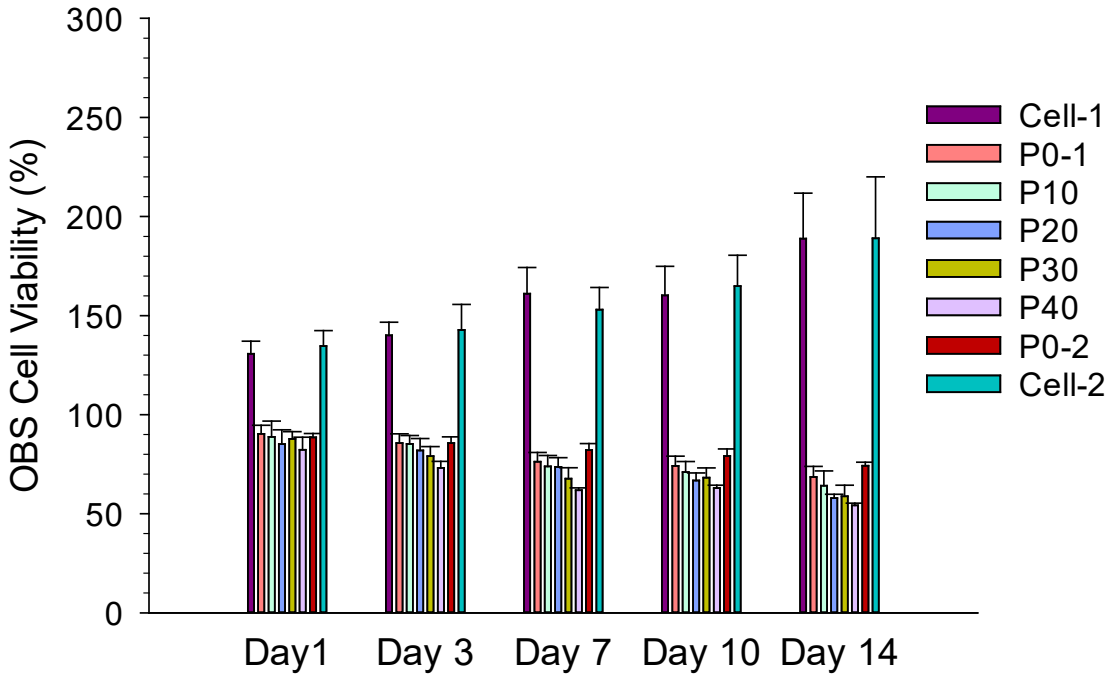

Figure 5.33 Percentage of cell viability of OBS cells on P0-1 (control sample in plate-1), P0-2 (control sample in plate-2) and P-MGC samples along with negative control (Cell-1&2) for 1, 3, 7, 10 and 14 days. The data do not include outliers. The data presents mean value ± standard deviation (μ ±σ).

It is important to note that two cell culture plates were used to hold the samples, as shown in Figure 3.20 in Chapter 3. This fact may have caused discrepancies in the results. The results showed that using two cell culture plates caused variations. It can clearly be seen in the difference between the control samples (W0-1 & W0-2, and P0-1 & P0-2) at each time point as they should have seen similar results. Considering the plates separately, a trend of cell viability reduction with increasing MGC could be seen in most tests. However, this trend did not continue from first plate containing MGC10 and MGC20 (wt%), to the second plate containing MGC30 and MGC40 (wt %) samples.

As can be seen that OBS cells had higher cell viability than U2OS cells on both Wintercryl and Palacos cements with and without MGC addition. Whilst the decrease in U2OS cell viability was sharp, OBS cell viability showed a gradual decrease. This indicated that OBS cells had higher cell proliferation than U2OS cells on the PMMA cement samples.

Cell attachment of OBS cells were found higher compared to U2OS cells for both cement types on day-1 time point. However, all samples showed poor cytocompatibility on U2OS and OBS cells throughout the time points. In addition to this, the reduction in cell viability was not in line with the literature [147]. Sharp edges of MGC may have destroyed the cells and inhibited their attachments on the surface. Moreover, as previously reported, increasing MGC (wt%) content caused a decrease in initiator concentration and this may have increased residual MMA in the test samples, which was toxic. Therefore, the addition of MGC from 10% to 40% MGC (wt%) addition in cement caused a further decrease in the cell viability. As previously reported, the sample side in contact with silicone mould surface was used for all work and this may have affected the results of MTT and Alamar Blue assays. Since silicone rubber is considered a hydrophobic material that has surface contact angle higher than 90° with low wettability [192]. Moreover, Rios et al., reported that silicone rubber has lower adhesion strength than PTFE. Thus, hydrophobicity of silicone rubber mould may have led to lower amount of MMA conversion into polymer holding the PMMA beads on the surface. In addition to that, surface properties can affect cell adhesion. It was reported that hydrophilic surfaces enhance cell adhesion due to their high wettability and low contact angle (<90°) properties [193]. This may have an influence on low cell viability on the surface of magnetic and plain PMMA cement samples.

Figure 5.34 shows the light microscope images of U2OS and OBS cells seeded in 24 well-plate, showing the growth of cells up to 14 days. As expected, U2OS cells showed a higher proliferation rate than OBS cells. U2OS cells reached confluency after day-3 in 24 well-plate whilst OBS cells showed confluency after day-7 time point. This fast growth of U2OS cells caused accumulation in the well.

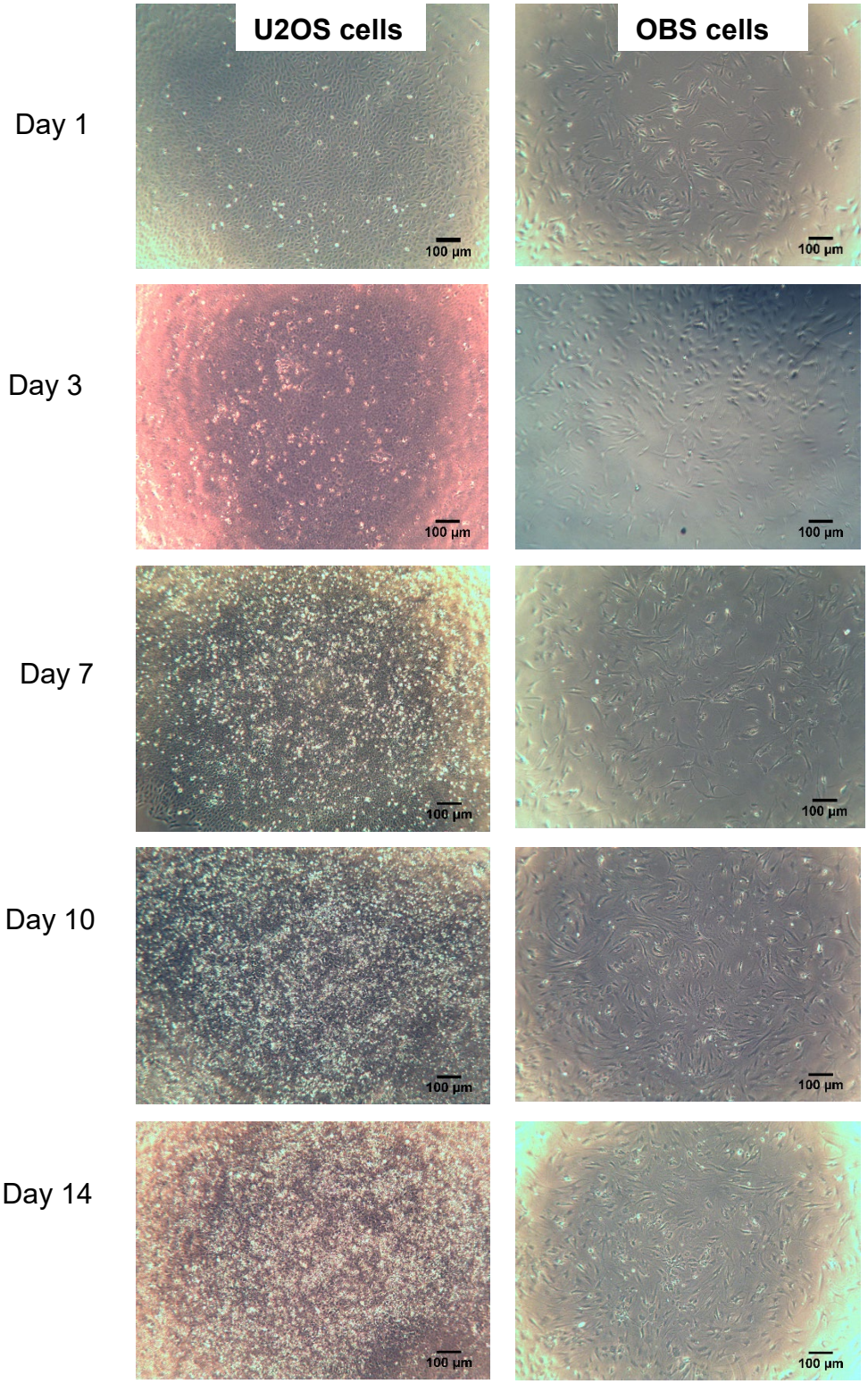

Figure 5.34 Light microscope images (4x magnification) of U2OS and OBS cells seeded in 24 well-plates up to 14 days. Colour variation is due to the microscope lightening- no cellular impact. Scale bars are 100 µm.

5.1.9 Fluorescence Imaging

In order to evaluate the cell attachment on W0, W10, W20, W30 and W40, as well as P0, P10, P20, P30, P40, fluorescence imaging was performed as described in Section 3.6.9. Representative fluorescence microscopy images of OBS and U2OS cells seeded on plain and MGC containing Wintercryl and Palacos® cement samples are shown in Figure 5.35. Blue colour (DAPI staining) represents the nucleus of the cells. Other than U2OS cells showing higher cell attachment than OBS cells, no correlation was found with cement type or the presence of MGC in the cements.

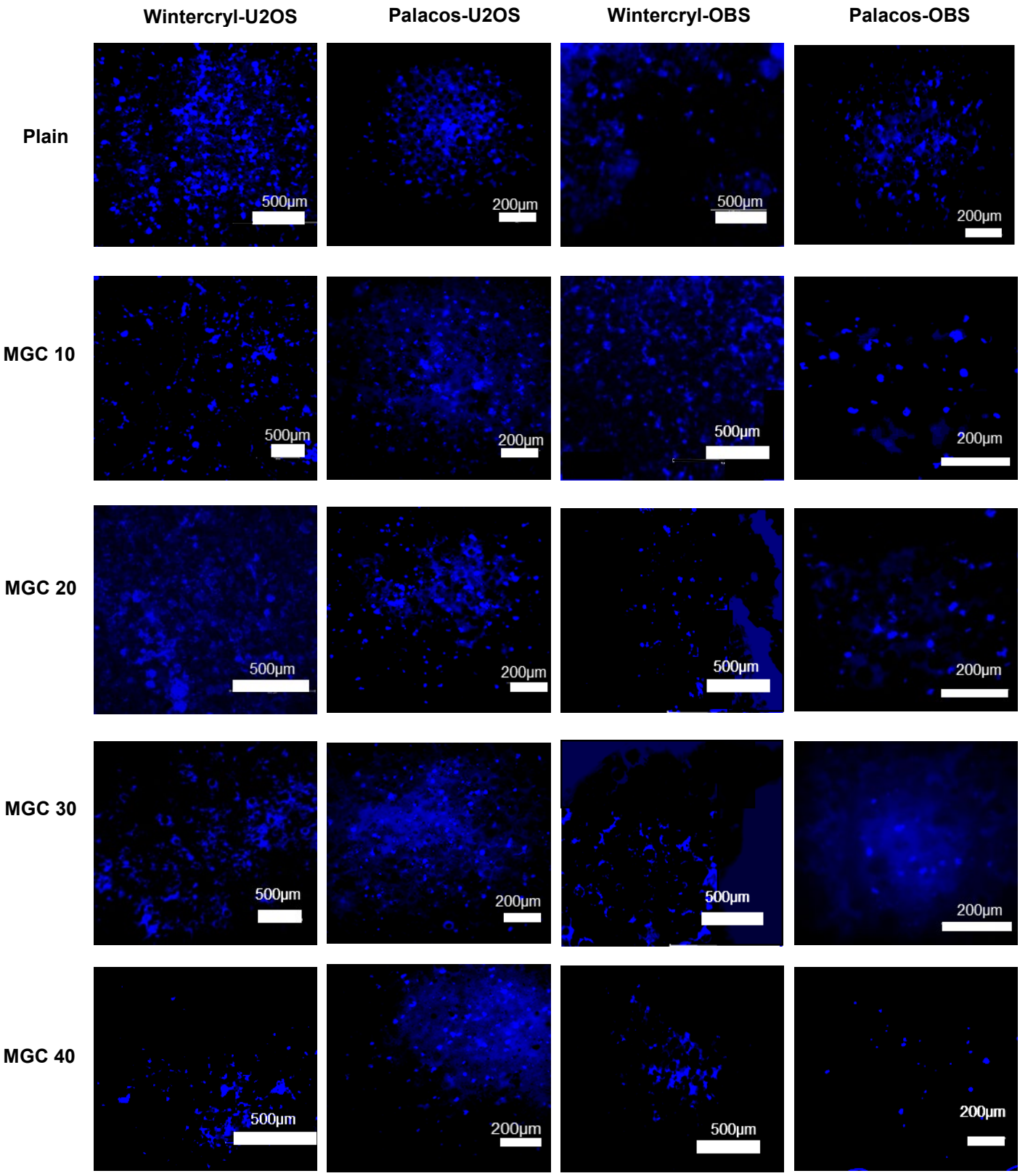

Figure 5.35 Representative fluorescence images of DAPI stained OBS and U2OS cells attached on the surface of plain (W0,P0) and MGC containing Wintercryl and Palacos cement samples (W-MGC and P-MGC samples). Magnification was changed to secure clean images.

5.1.10 Cell attachment SEM Imaging

Further cell attachment analyses on the surface of P0, P10, P20, P30 and P40 samples was performed as described in Section 3.6.10. Unfortunately, after the critical point drying process (CPD), the samples expanded. In the literature, the effects of CPD technique on PMMA cement was not reported; however, it is known that PMMA samples can absorb water, and this can cause swelling of PMMA samples [144]. Kazarian et al [194]., reported that liquid CO_2 may interact with polymers under high-pressure (~74 bars) and it may lead swelling.

SEM images of the samples were obtained not only to assess cell attachment, but also to understand how the cell culture media, cell fixation protocol and critical point drying could affect the samples. Figure 5.36, Figure 5.37, Figure 5.38, Figure 5.39 and Figure 5.40 show SEM images of P0, P10, P20, P30 and P40 samples respectively, at time 0 without cells (with and without CPD) and at 1 and 3-day time points of U2OS and OBS cells. Yellow arrows on the images indicate cell attachments. Detection of the cells on the surface were difficult as most of the cells may have been ruptured due to the expansion that occurred during the critical point drying process. Attachment of OBS cells on day-1 time point can be clearly seen on Figure 5.36, Figure 5.37, Figure 5.38 and Figure 5.39. The cells showed a flatten morphology and extended filopodias, which has been reported by several studies [195-197]. However, there was no correlation found between samples regarding the MGC addition due to rupture of cells and morphological changes in the samples, which was attributed to CPD process.

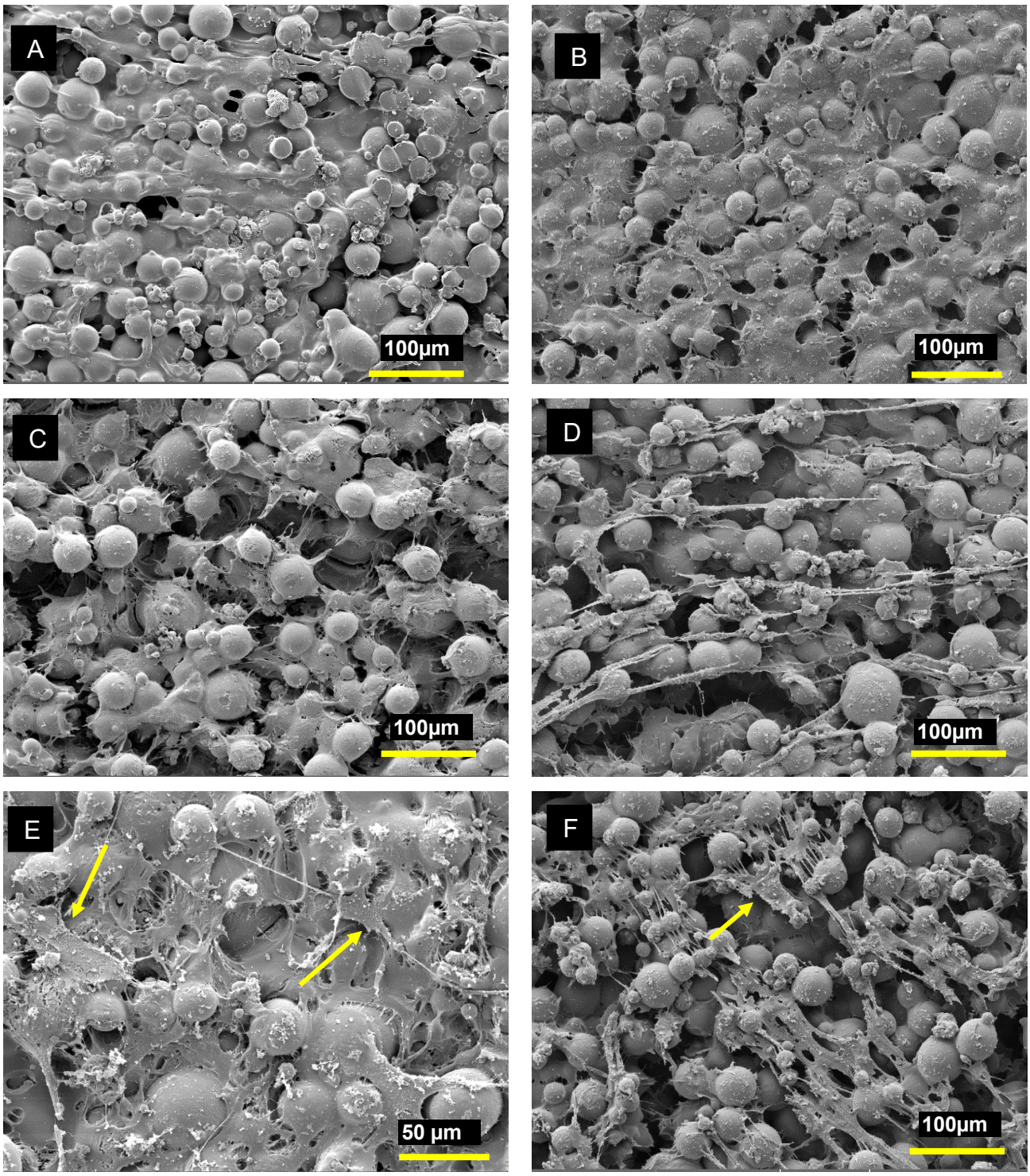

Figure 5.36 SEM images (500x magnification) of P0 samples A) before B) after treatment without cell seeding C) U2OS cells at 1-day time point D) U2OS cells at 3-day time point E)OBS cells at 1-day time point F) OBS cells at 3-day time point

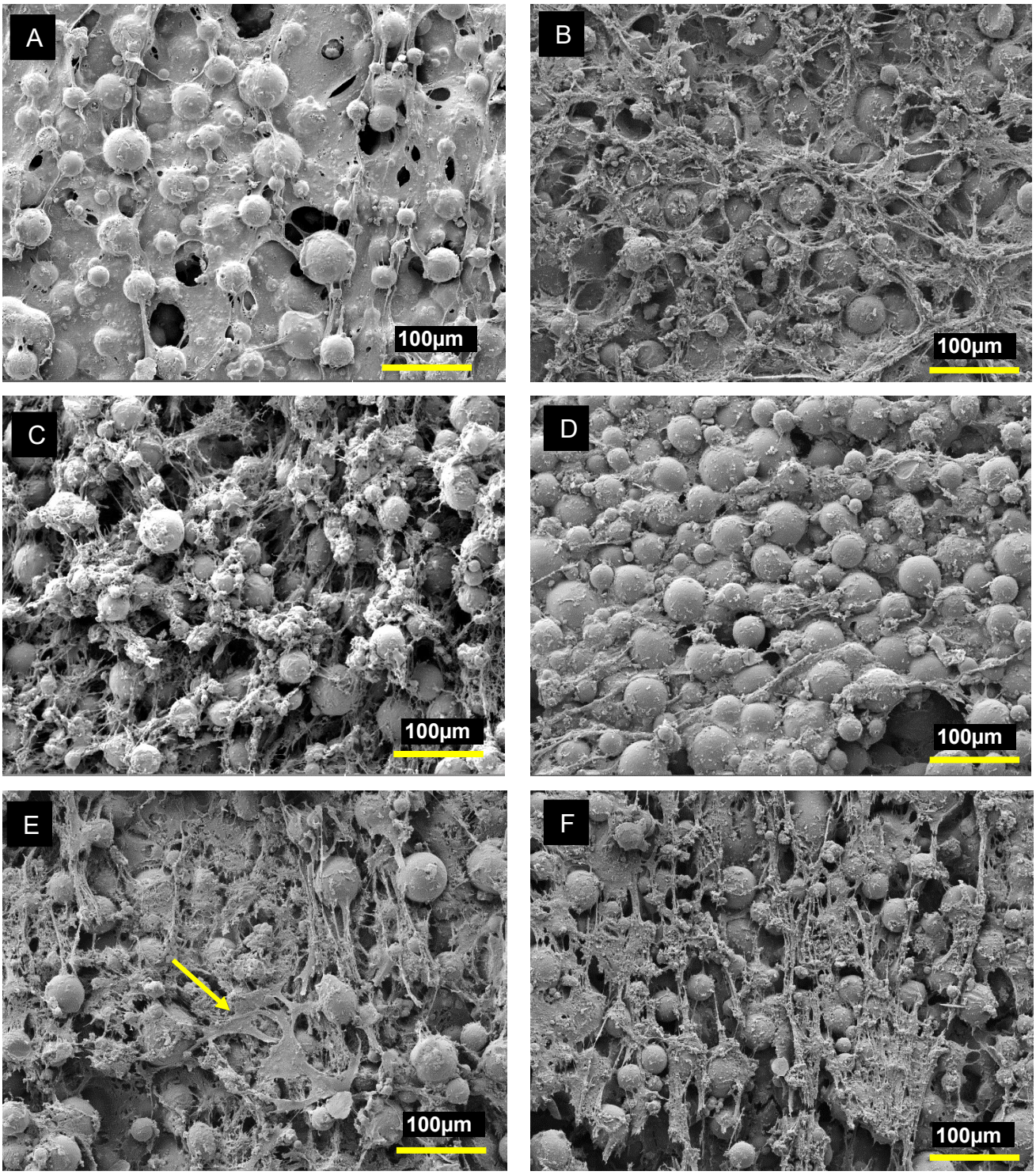

Figure 5.37 SEM images (500x magnification) of P10 samples A) before B) after treatment without cell seeding C) U2OS cells at 1-day time point D) U2OS cells at 3-day time point E)OBS cells at 1-day time point F) OBS cells at 3-day time point

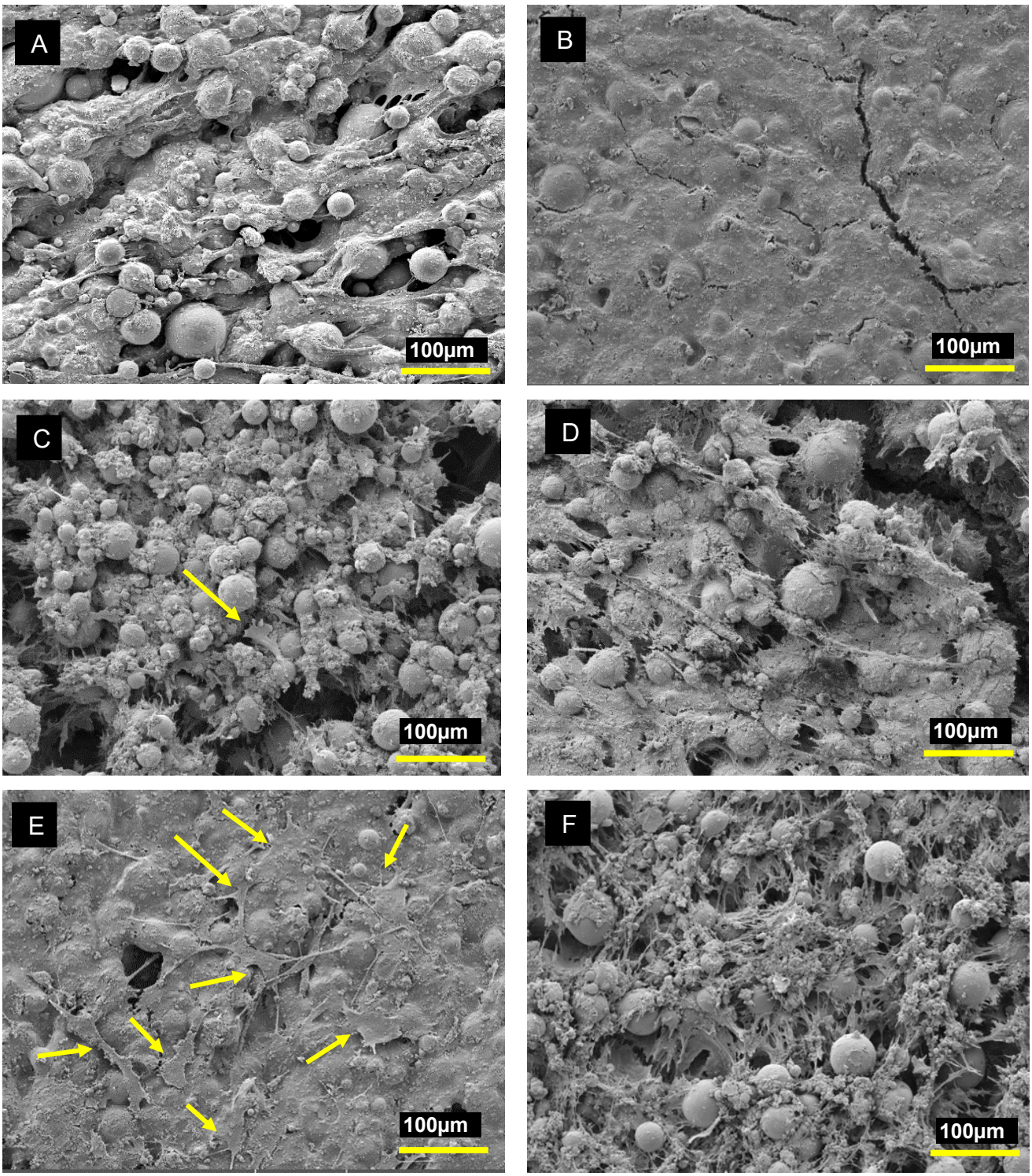

Figure 5.38 SEM images (500x magnification) of P20 samples A) before B) after treatment without cell seeding C) U2OS cells at 1-day time point D) U2OS cells at 3-day time point E)OBS cells at 1-day time point F) OBS cells at 3-day time point

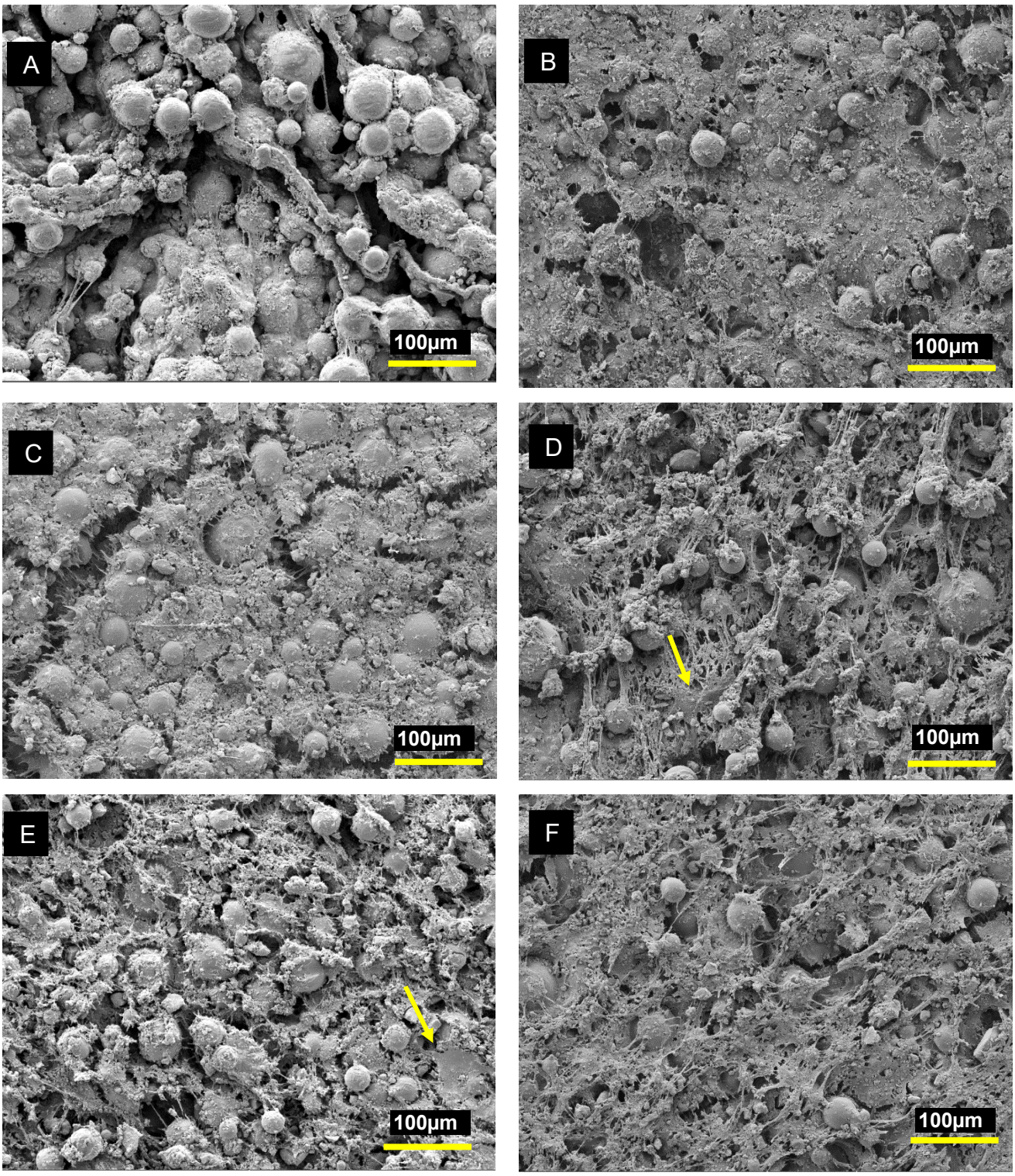

Figure 5.39 SEM images (500x magnification) of P30 samples A) before B) after treatment without cell seeding C) U2OS cells at 1-day time point D) U2OS cells at 3-day time point E)OBS cells at 1-day time point F) OBS cells at 3-day time point

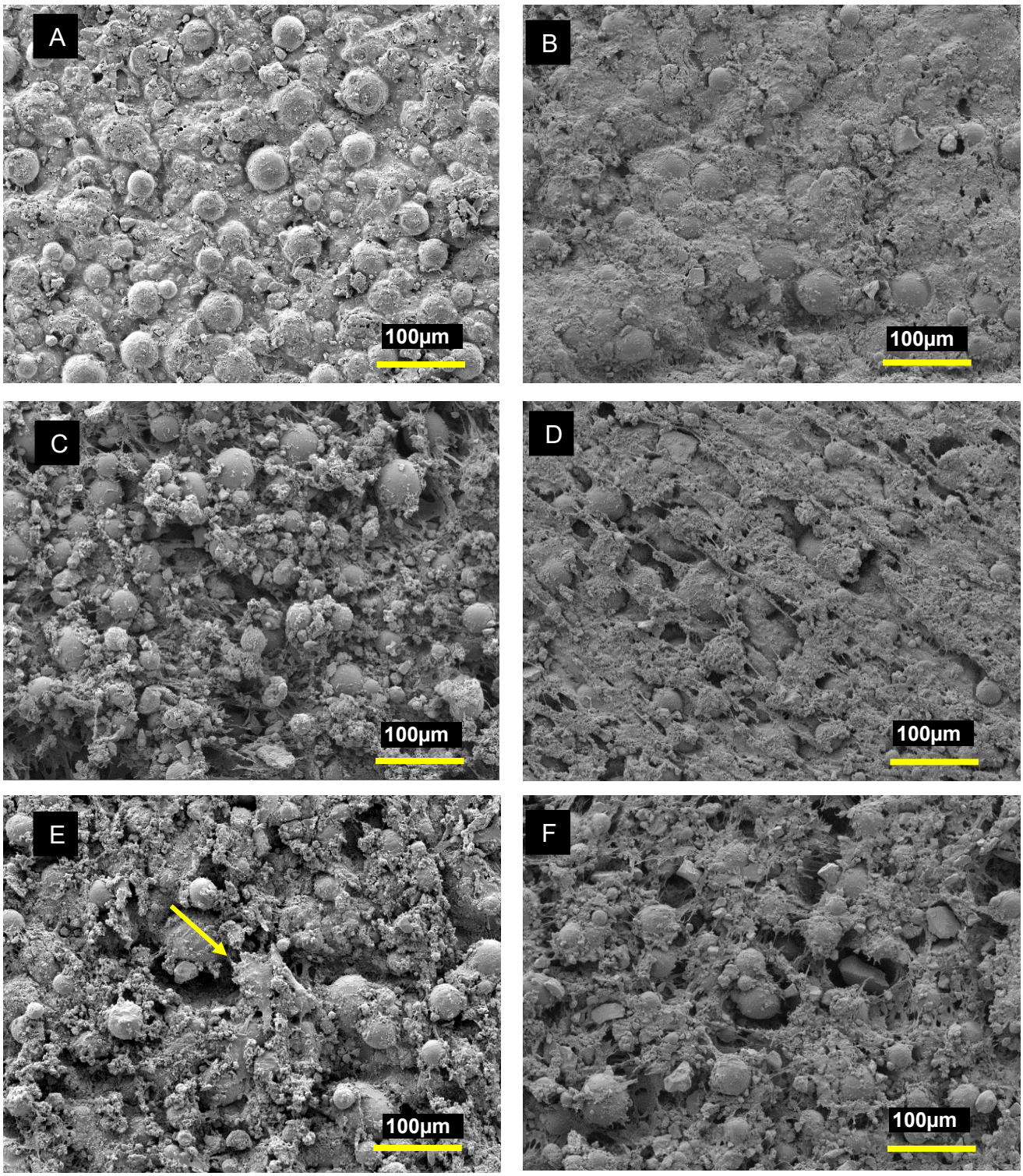

Figure 5.40 SEM images (500x magnification) of P40 samples A) before B) after treatment without cell seeding C) U2OS cells at 1-day time point D) U2OS cells at 3-day time point E)OBS cells at 1-day time point F) OBS cells at 3-day time point

5.1.11 Induction Heating

Successful heat generation of magnetic materials is crucial to destroy deep-seated bone cancer cells via hyperthermia treatment. The heat generation mostly depends on magnetic properties of the material and the parameters of the magnetic field (intensity and frequency). As reported in Section 2.3.2.1, the heat generation should be between 41-45°C to destroy the cells. However, the applied magnetic field should be also safe for patients and staff in operating rooms in hospitals and treatment centres.

Heat generation abilities of MGC containing samples (P-MGC and W-MGC), in comparison with the control groups, W0 and P0, were evaluated by performing a preliminary induction heating test. Kawashati et al. [60] reported that (see Section 2.8) increasing the magnetic material in cement samples exponentially increased the generated heat at a constant magnetic field.

In this study, the hypothesis was that increasing MGC content in the sample would reduce the energy needed to heat the sample to a targeted temperature range. Therefore, the induction current (A) was reduced as the MGC content increased in the samples (see Table 3.4). The reason for this was to control the heat generation in all the samples to reach a similar temperature range in 5 minutes. Then, the applied currents were reduced according to the MGC content in the sample, in order to maintain the generated heat for 5 minutes. The temperature readings were taken every 60 seconds. The sample sizes per group for heating (stage I) and holding (stage II) phases are shown in Table 5.9.

Table 5.9 Sample number per group for stage 1and stage 2

	W0	**W10**	**W20**	**W30**	**W40**	**P0**	**P10**	**P20**	**P30**	**P40**
Stage I	n=5	n=5	n=5	n=5	n=5	n=5	n=5	n=5	n=5	n=5
Stage II	n=2	n=5	n=5	n=5	n=5	n=1	n=5	n=5	n=5	n=5

Temperature profiles of control groups, W-MGC and P-MGC samples are presented in Figure 5.41 and Figure 5.42. W-MGC and P-MGC samples were successfully heated to a range of 55-60°C in 5 minutes (stage I). After the heating process, the temperatures were easily maintained ~1-4°C below the maximum temperature that they were heated to (stage II). All P-MGC and W-MGC samples followed a similar pattern as seen in Figure 5.41 and Figure 5.42.

It was assessed that as the MGC content increased in the cement lower induction current was needed since more energy could be absorbed by the sample for heat generation. Temperature differences (∆T °C) of W-MGC and P-MGC samples and their control samples (W0, P0) at stage I are presented in Table 5.10 and Table 5.11 respectively. It was expected that W0 and P0 would not generate any heat under the applied current; however, there was a slight increase in the temperatures, as seen in the figures below, which is due to convection and radiation from the coil. This effect will be further discussed in the following paragraphs.

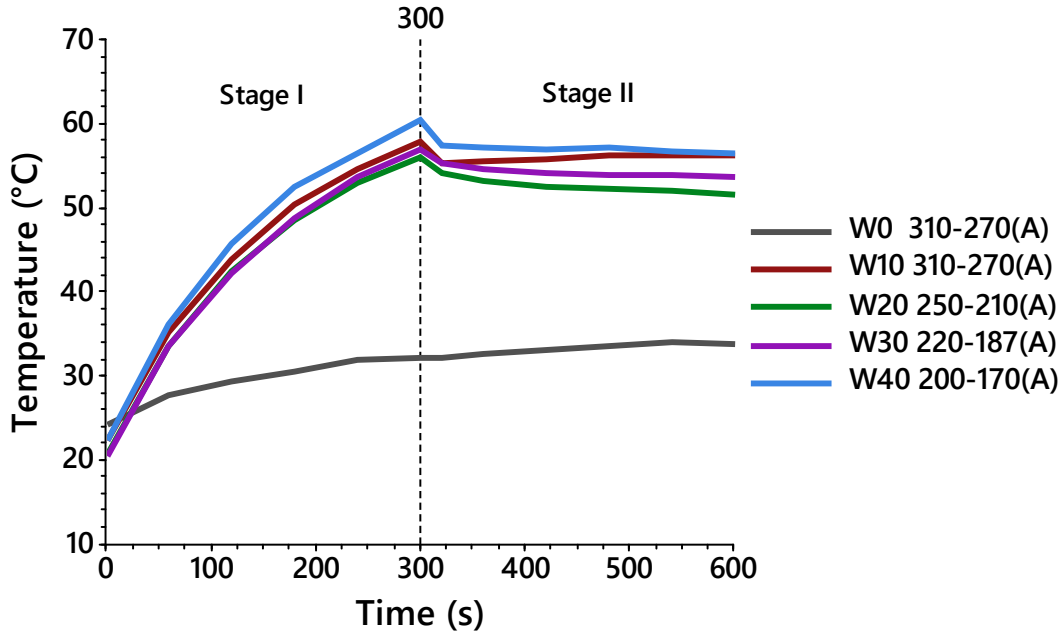

Figure 5.41 Temperature-time profiles of W0, W10, W20, W30 and W40 samples under the applied currents for 10 minutes. The temperature curves represent the average temperature readings in every 60 seconds collected from the samples. Stage I: heating phase and stage II: holding phase.

Table 5.10 Temperature differences of W-MGC and W0 samples at stage 1

∆T (°C)	**W0**	**W10**	**W20**	**W30**	**W40**
Stage I (°C)	8.1±0.2	35.4±2.9	35.5±1.4	36.5±1.3	38.0±1.5

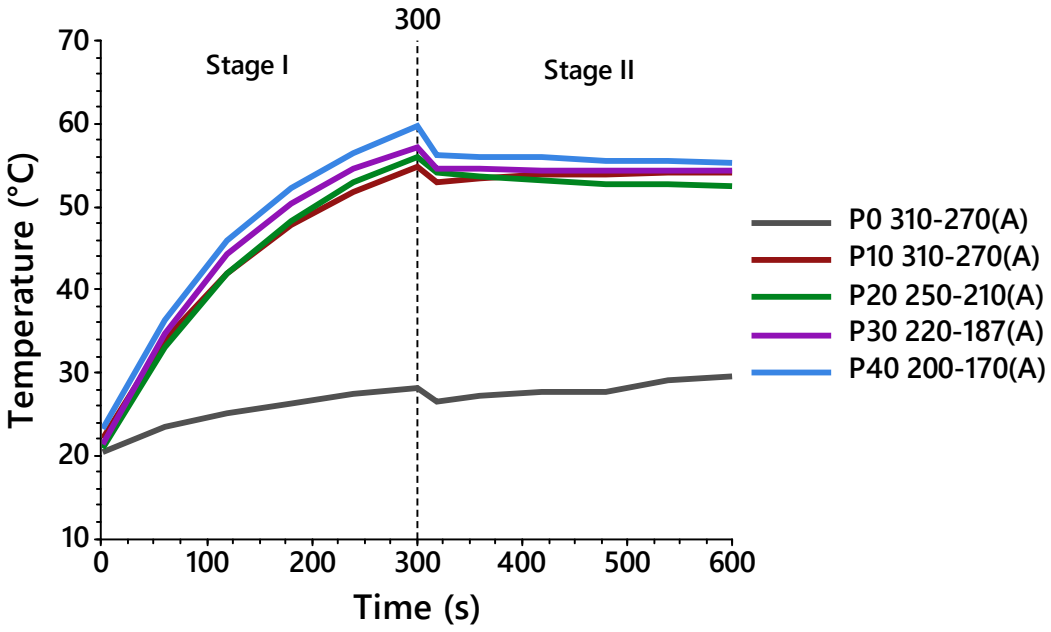

Figure 5.42 Temperature-time profiles of P0, P10, P20, P30 and P40 samples under the applied currents for 10 minutes. The temperature curves represent the average temperature readings in every 60 seconds collected from the samples. Stage I: heating phase and stage II: holding phase

Table 5.11 Temperature differences of P-MGC and P0 samples at stage 1

∆T (°C)	**P0**	**P10**	**P20**	**P30**	**P40**
Stage I (°C)	7.6±1.9	32.8±1.4	35.2±1.9	35.8±1.1	36.5±1.7

Table 5.12 shows the temperature readings of W0, P0, P-MGC and W-MGC samples at every 60 seconds throughout stage I and stage II. The initial temperatures (T_0) had a clear influence on the resulting maximum temperatures at the end of the heating phase, T_{300}. For instance, W20 and P20 samples had similar initial temperatures (T_0), which resulted in similar peak temperatures after 5 minutes of the heating process (T_{300}). Moreover, P30 was approximately 1°C higher than W30 at T_0, and this temperature difference was maintained throughout the heating stage. A similar trend was observed between P0 and W0 samples. In contrast, P10 and W10 samples did not exhibit the same behaviour. While the initial temperatures were similar; the temperature difference was approximately 3°C difference at T_{300}.

Table 5.12 Temperature recordings of the control samples, P-MGC and W-MGC samples in every 60 seconds throughout heating and holding stages. Data is presented as mean and ± standard deviations.

	T_0	T_{60}	T_{120}	T_{180}	T_{240}	T_{300}	T_{360}	T_{420}	T_{480}	T_{540}	T_{600}
P0	20.5±1.6	23.4±2.0	25.1±2.6	26.2±2.7	27.4±2.6	28.1±2.7	27.3	27.7	27.8	29	29.5
W0	24.1±0.4	27.6±1.4	29.3±1.0	30.5±1.0	31.8±0.9	32.3±0.6	31.8±0.9	32.4±0.9	32.7±1.3	32.2±1.1	32.8±1.3
P10	22.1±1.0	34±0.9	42±1.0	47.7±0.8	51.9±1.0	54.9±1.1	53.5±1.1	53.9±1.1	54.0±1.0	54.1±1.4	54.3±1.4
W10	22.4±0.8	35.1±1.3	44.1±1.8	50.4±2.4	54.7±2.5	57.8±3.0	55.5±1.9	55.8±1.9	56.4±2.1	56.4±2.1	56.2±1.9
P20	20.9±0.5	33.1±0.9	42.08±1.4	48.36±1.8	52.9±2.2	56.1±1.9	53.7±2	53.2±2.1	52.8±2.1	52.76±2.2	52.6±2.3
W20	20.6±0.7	33.6±0.9	42.6±0.8	48.6±0.9	52.9±1.0	56.0±1.3	53.2±01	52.6±0.8	52.2±1.1	52.0±1.1	51.7±1.3
P30	21.5±1.2	34.7±1.3	44.3±2.1	50.4±2.1	54.8±2.0	57.3±1.6	54.6±2.0	54.4±1.8	54.5±2.2	54.5±1.5	54.5±1.6
W30	20.4±1.2	33.4±0.5	42.3±0.6	48.9±1.1	53.8±0.9	56.9±1.2	54.6±1.1	54.1±0.8	54.0±0.9	54.0±0.8	53.6±1.1
P40	22.5±0.7	35.8±0.5	45.3±0.8	51.8±0.9	56.1±1.0	59.4±1.2	56.0±0.8	56.2±0.9	55.8±0.9	56.1±1.0	55.8±1.0
W40	22.2±0.9	36.1±1.0	45.7±1.3	52.6±1.4	56.6±0.9	60.4±1.5	57.2±1.0	56.9±1.0	57.2±1.2	56.7±1.2	56.6±1.0

It was found that the initial temperature of the coil had a more significant impact on the temperature increase in the sample compared to the other factors such as ambient temperatures and initial temperatures of the samples. This impact could be easily determined when the induction heating test was repeated on the same samples, sample 2 in group P10 (sample code: P10-2) and sample 1 in group W10 (sample code: W10-1).

Figure 5.43 demonstrates the temperature profiles of the sample P10-2, coil and ambient temperature for the first and second (repeated) tests. The temperature difference between the initial temperatures of P10-2A (sample 2 in group P10, A=first test) and P10-2B (sample number 2 in group P10, B=second test) was ~2°C. The initial temperature difference between coil-A (coil temperature at first test) and coil-B (coil temperature at second test), was approximately 10°C. Therefore, while P10-2A could reach 49°C, P10-2B reached 54°C at the end of stage 1. At the end of stage 2, the temperature differences between coil-A and coil-B were approximately 6°C, and the temperature difference between P10-2A and P10-2B was around 4°C.

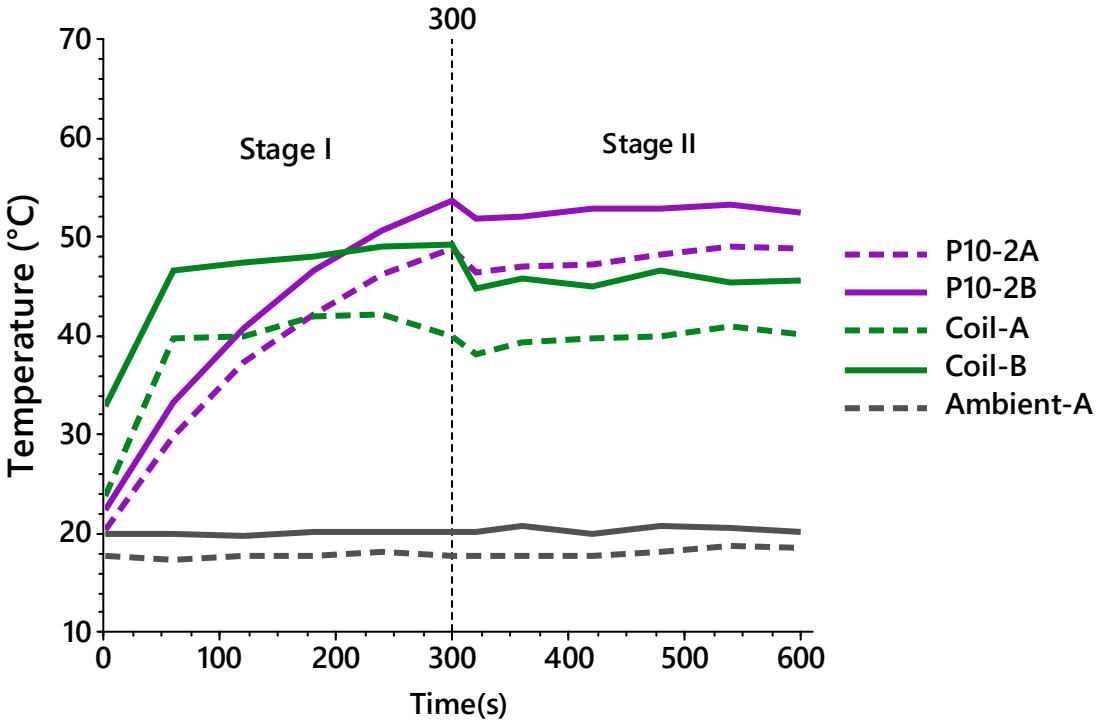

Figure 5.43 Temperature-time profile of the P10-2 sample, coil, acrylic holder and ambient temperature in the first and second tests. At stage I the current was 310A for 5 minutes, and at stage II the current was 270A for 5 minutes at a fixed frequency 290 kHz. The tests are coded as A, meaning first trial and B,, meaning the second trial.

Similar effects were observed on W10-1 when it was exposed to the magnetic field at different times (A and B), applying 310 A at 290 kHz, as seen in Figure 5.44. W10-1A (at first test) and coil-A had similar starting temperatures, 17°C and the sample reached 53 °C in five minutes. At the second (repeated) test, the starting temperature of coil-B was 31°C and the temperature of W10-1B raised from 23.3°C to 61°C in five minutes.

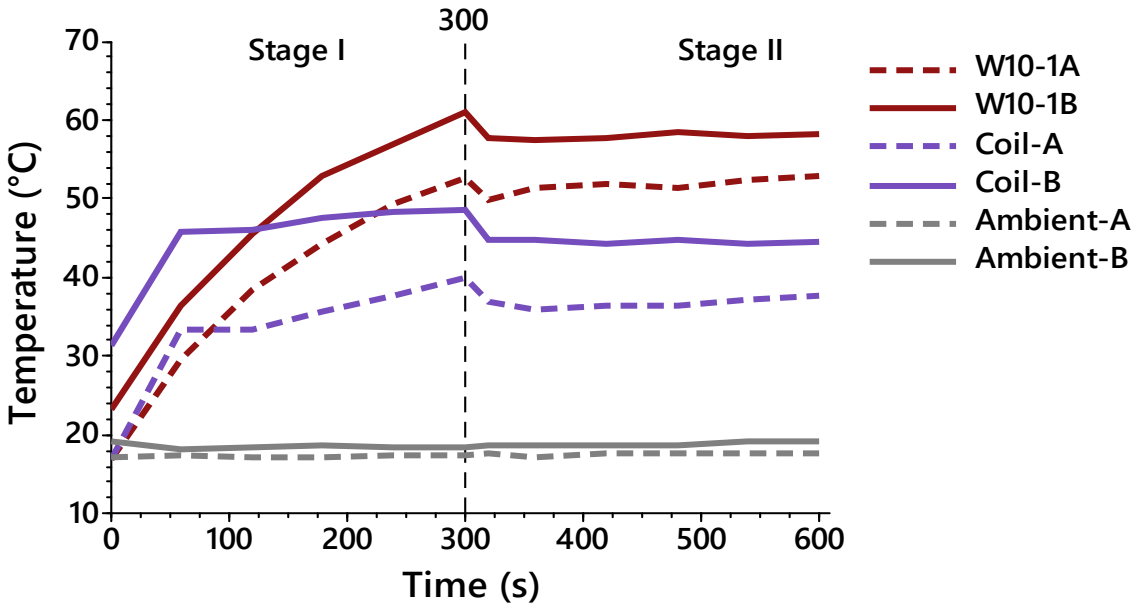

Figure 5.44 Temperature-time profile of the W10-1 sample, coil, acrylic and ambient in the first and second trials. At stage I the current was 310A for 5 minutes, and at stage II the current was 270A for 5 minutes at a fixed frequency 290 kHz. The tests are coded as A, meaning first trial and B, meaning the second trial.

Although the initial sample temperatures affected the heating stage to reach a target temperature, the coil temperature had a larger impact on the peak temperature as there was heat transfer (convection and radiation) from coil to the samples. As the coil temperature and ambient temperature could not be controlled, it caused variations in the final temperatures at the end of the heating stage as well as the holding stage. In order to maintain similar conditions for every test sample, the test should be performed in a more controlled environment to avoid any variations in the temperature changes. Despite these limitations and variations, W-MGC and P-MGC samples were successfully heated to above 50°C in five minutes and the temperatures were maintained for another 5 minutes, providing that W-MGC and P-MGC showed promising results for bone cancer treatment via magnetic hyperthermia.

As P0 and W0 lacked any MGC content, they were incapable of generating heat under a magnetic field. However, the temperature readings from the camera showed that temperatures of the plain cement increased approximately between 5 and 10°C when they were exposed to a magnetic field. Therefore, the temperature profiles of selected P0 and W0 samples were extensively evaluated with recordings of the coil, sample holder and the room temperatures. It should be noted that the sample holder was made of acrylic. Thus, temperature profile was expected to be similar to the PMMA based cement samples (P0 and W0).

Figure 5.45 presents the temperature curves of W0, coil, sample holder (made of acrylic) and ambient temperature during stage I (310 A and 290 kHz) and stage II (270 A and 290 kHz). The temperature of W0 increased by 8°C during stage I as the coil temperature increased by 15°C. The temperature profiles of the coil and W0 had a similar pattern, and during stage II, the temperature of the W0 raised and fell proportionally to the temperature of the coil. This influence was also observed on the acrylic holder.

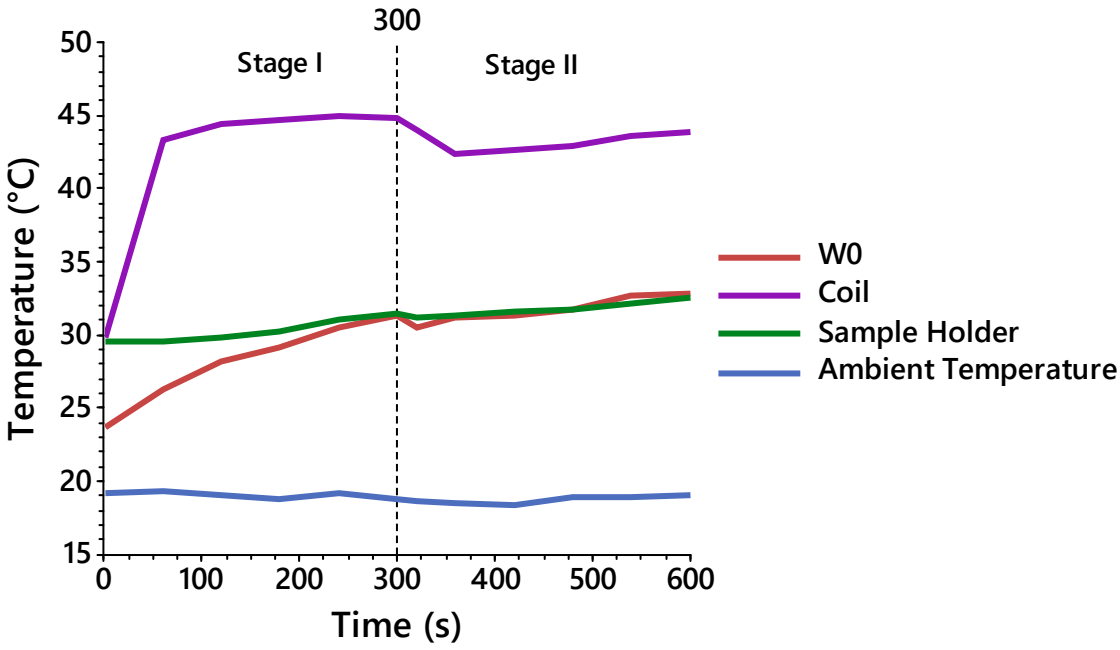

Figure 5.45 Temperature-time profile of selected W0, coil, sample holder and ambient temperature at during stage I and stage II. The data presents mean values.

Similarly, P0 samples showed similar behaviors under the applied magnetic field. Figure 5.46 presents the temperature curves of P0, coil, sample holder (made of acrylic) and ambient temperature during stage I (310 A and 290 kHz) and stage II (270 A and 290 kHz). The temperature of W0 increased by 6°C during stage I as the coil temperature increased by 20°C. The acrylic holder and P0 sample followed a similar trend for all stages due to convection and radiation heating from the coil.

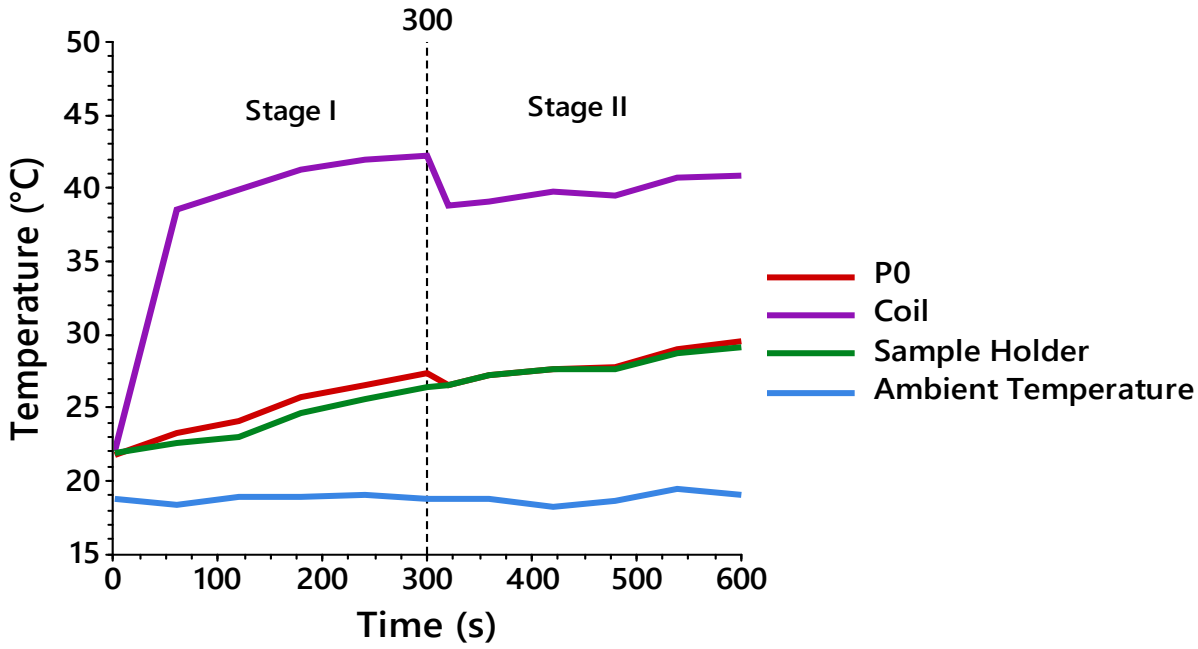

Figure 5.46 Temperature-time profile of selected P0, coil, sample holder and ambient temperature at during stage I and stage II. The data presents mean values.

Power to mass ratios of the samples was analysed to evaluate the generated power at 310 A and 290 kHz to heat the control (P0 and W0), W-MGC and P-MGC samples. The mean values and standard deviations of power to mass ratios of the samples are shown in Figure 5.47, and the data ranges of samples are presented in Figure 5.48. As the MGC content was increased from 10% to 40%, the applied current was reduced, and this resulted in lower power generation to heat the samples. For example, whilst the average power applied for P40 samples was 377 (W), it was increased to 974 (W) for P10 samples to reach a similar temperature range.

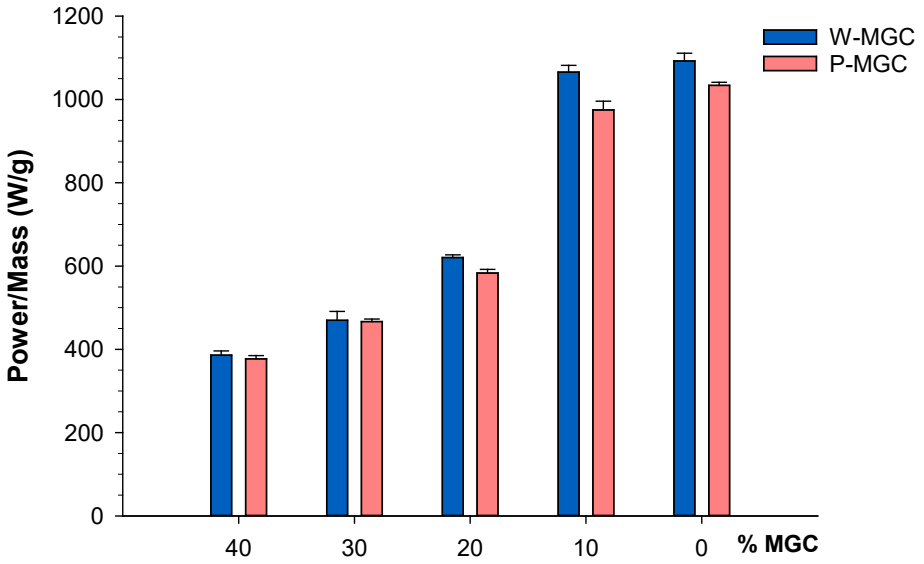

Figure 5.47 Power-to-mass ratios of control, W-MGC and P-MGC samples at 310A (stage 1). The data presents mean value ± standard deviation (μ ±σ).

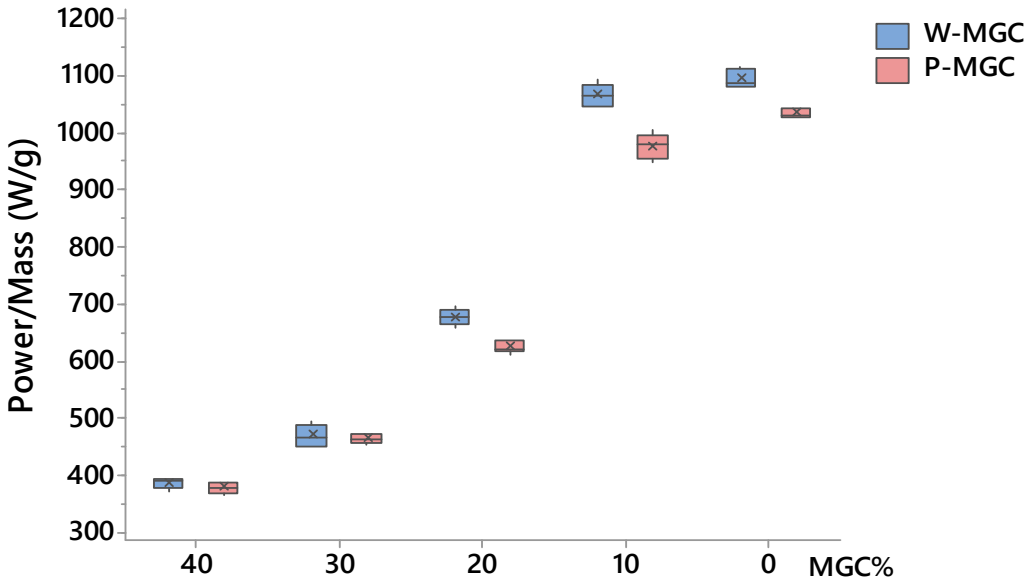

Figure 5.48 Data range of power-to-mass ratios of control, W-MGC and P-MGC samples at 310A (stage 1). The mean values of the samples are expressed with the X, and horizontal lines represent the median values.

In order to understand how much output energy was supplied to the coil in order to utilise heat generation in the samples per second the following equation 5-1 was used;

$$E = Pt \qquad \text{Equation 5-1}$$

Where *E* is the energy transferred to the coil (kJ), *P* is the generated power (kW), and *t* is the time period (s).

Figure 5.49 shows the average output energy transferred to the coil to heat W0 and W-MGC (Figure 5.49-a) and also P0 and P-MGC (Figure 5.49-b) samples. As the MGC content increased, the coil needed less energy input to heat the samples to above 50°C in five minutes and similarly to maintain the temperature.

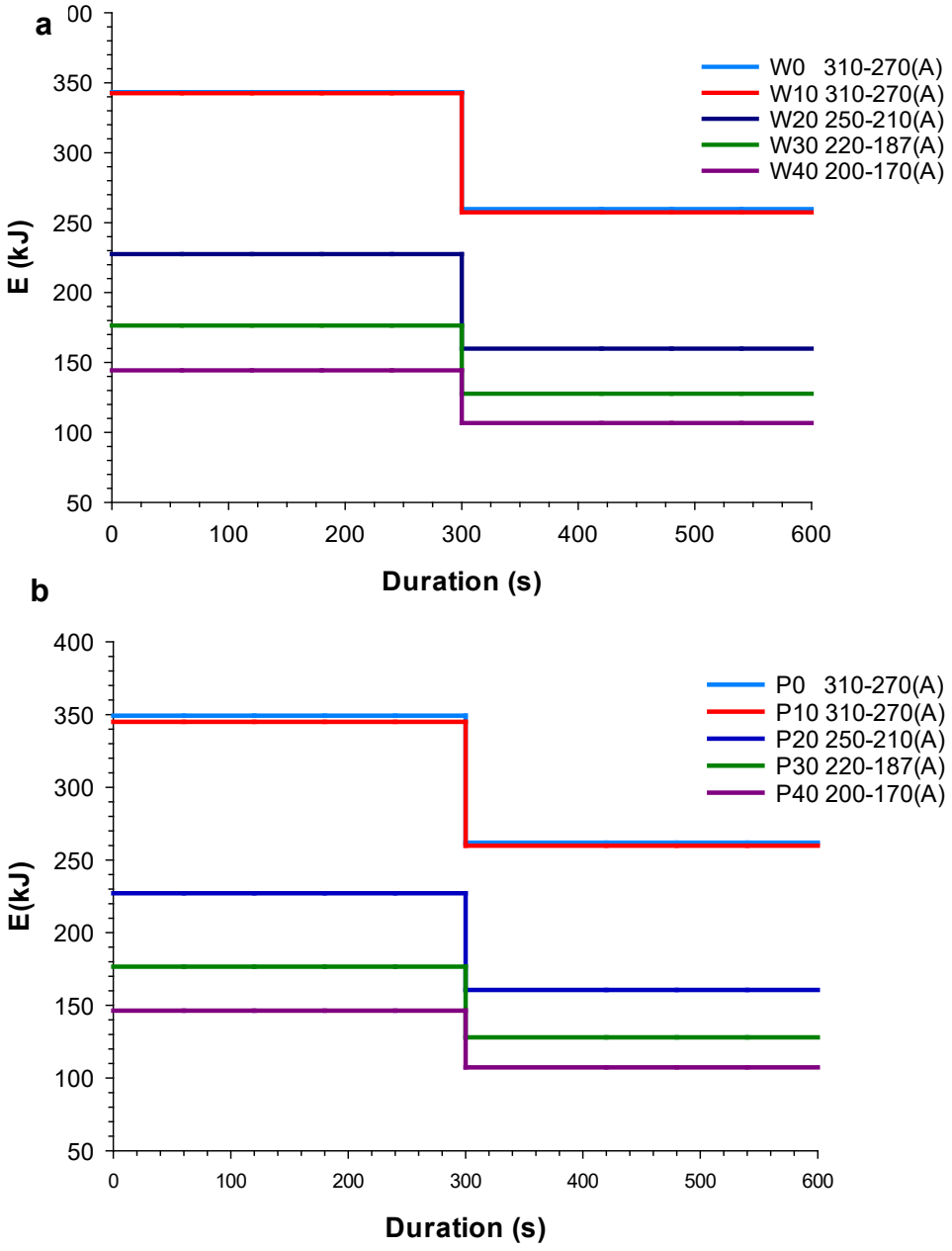

Figure 5.49 Estimated transferred energy to coil to generate and maintain the heat in a) W0 and W-MGC and b) P0 and P-MGC samples. The data represents the mean values.

Regarding the energy transferred to the coil (Q_{in}), it is not known exactly how much energy was transferred from the coil to samples, as some energy dissipated from the coil to the environment via radiation (Q_R) and convection (Q_c) and some of the coil energy was transferred to the sample, as shown in Figure 5.50. As previously discussed, the coil temperature has a small contribution to the increase of the sample temperature due to convection and radiation.

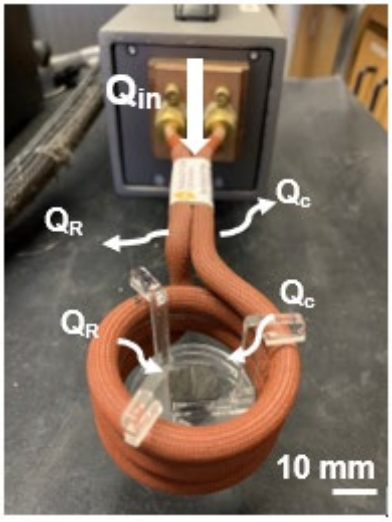

Figure 5.50 Representative image of heat transfer from the coil to sample

Regarding the assumptions above, it was necessary to understand how much heat was absorbed by the samples. Since the test was performed in air and the specific heat capacity of the W-MGC and P-MGC samples is unknown, the absorbed heat cannot be precisely calculated. The estimated heat absorption for the samples was calculated using the following equation;

$$Q = m_p c_p(\Delta T) + m_g c_g(\Delta T) \qquad \text{Equation 5-2}$$

Q= absorbed heat (kJ)

m_p= mass of PMMA in the sample (g)

m_g= mass of MGC in the sample (g)

c_p= specific heat capacity of PMMA (kJ/g°C)

c_g= specific heat capacity of MGC (kJ/g°C)

ΔT= difference between final and initial temperature (T_f-T_i) (°C)

In this calculation, specific heat capacities of PMMA and MGC are assumed to be 1.5 kJ/g°C and 0.9 kJ/g°C, respectively, based on EduPack 2018 software. The estimated heat absorptions in W-MGC and P-MGC and the control groups (W0 and P0) are shown in Figure 5.51. The calculations were done based on the average mass values and temperature changes of the samples, therefore, standard deviations could not be calculated. Whilst W40 and P40 could absorb approximately 60 kJ heat, W0 and P0 absorbed approximately 12 kJ. Heat absorption in the cement was directly related with MGC content in cement samples.

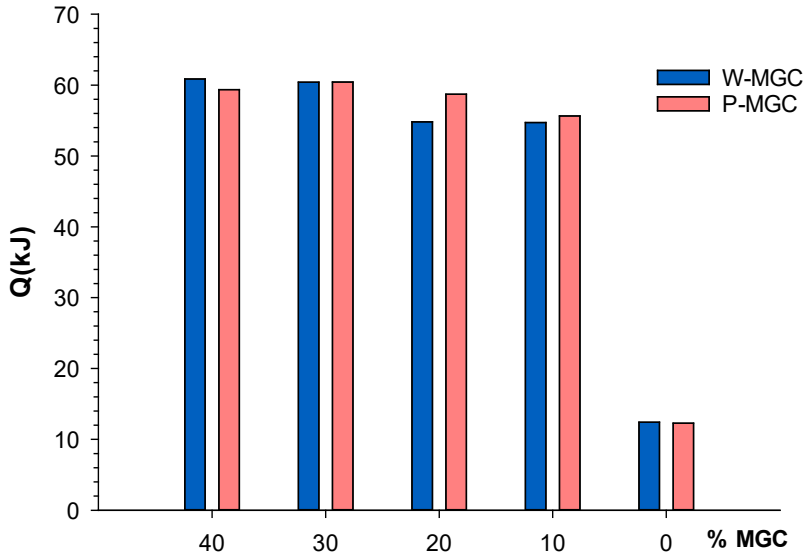

Figure 5.51 The estimated absorbed heat by control (W0, P0), W-MGC and P-MGC.

5.1.12 Summary of Results and Discussions

In this section, effects of MGC addition from 10% to 40% in Palacos and Wintercryl cement samples in handling, mechanical, microstructure, heat generation, bioactivity, cytocompatibility and heat generation properties were demonstrated with an array of experimental studies.

Time recordings of the cement preparations presented that increasing the MGC content in the cement delayed setting time with a longer waiting time. Due to the variations in setting temperature and time measurements, addition of MGC in the samples could not be compared. As reported previously, ISO5833:2002 could not be followed for setting time and temperature measurements because of limited Palacos cement kit and MGC. However, it was assumed that setting time also will be longer with the increase of MGC in PMMA cement based on a study performed by Kawashati et al [60].

A homogenous distribution of MGC particles embedded in the polymer matrix was observed using SEM imaging. EDS analysis showed a rise in Fe peak element in proportion to the increment of magnetic phase content in the cement samples. The microstructure analyses showed that PMMA beads were still visible on the surface of the cement. As previously reported (Section 4.4.2), this was due to partial polymerisation reaction between the powder and liquid components.

Bending strength of both Palacos and Wintercryl cements decreased with the addition of MGC content, while bending modulus increased. All compositions but 40% MGC fulfilled the 50MPa and 1.8GPa criteria of standard ISO 5833:2002 for the bending strength and bending modulus respectively. The average bending strength of all magnetic cement samples (W-MGC and P-MGC) varied between 47.5 and 58 MPa and bending modulus of all samples varied between 2.7 and 3.8 GPa. All W-MGC and P-MGC samples met the minimum requirement of this standard for compressive strength, which was 70MPa. However, a notable decrease was observed with the increase to 40% MGC. The average compressive strength of W-MGC and P-MGC samples were between 72 and 86 MPa. As it was expected, hardness of the cement samples increased with the increase of MGC in the PMMA cements, which was in a range of 22.2 and 28 MPa.

Porosities in PMMA cement had an adverse impact on the mechanical properties of the cement. However, porosity in bioactive PMMA cement could enhance their integration with soft and hard tissues [198-200]. In this study, it was found that addition of MGC from 10% to 40% increased water absorption of Wintercryl cement and a similar trend was observed in Palacos cement, with the exception of a decrease with 20% MGC addition. The range of average water absorption (%) for magnetic samples was between 4.8-6.6%. It was speculated that this increase in porosity as well as the brittleness of MGC particles might have an influence on the decrease of compressive strength in 40% MGC containing cement samples.

Due to the addition of MGC particles, PMMA cements became bioactive. The growth of apatite crystals on the cement samples was observed after 2 weeks of immersion in SBF solution.

Cytocompatibility tests showed that cell viabilities (%) of U2OS and OBS cell lines decreased over the time period. This trend was also true with increasing MGC content of cement samples. The average cell viability of U2OS cells on both Palacos and Wintercryl cement samples decreased approximately from 68% to 8%. This dramatic decrease in U2OS cells showed that these cells were not able to survive when PMMA cement was presented. The average cell viability of OBS cells were in a range of 98% and 55%. These decreases in cell viabilities were attributed to the increase of MMA ratio in proportion to MGC addition in the cement samples. MMA release may have been accelerated with the increase of porosity in the cement. Although PMMA cement was toxic, it did not have a catastrophic effect on the healthy cells. Although the decrease in U2OS cell viability was sharp, the decrease in OBS cell viability was more gradual. This was due to the toxicity of PMMA cement that U2OS cells could not survive in that environment However, the general decrease in cell viability was attributed to the decrease in initiator concentration in the magnetic cement samples due to the decrease in PMMA powder content, which may have led to increase in residual monomer in the cement samples. Moreover, silicone rubber mould had an influence on the surface of PMMA cement as previously reported (see Figure 4.20) and this may have caused low monomer conversion holding PMMA beads on the surface due to its hydrophobicity. Since the wettability of the surface decreased and contact angle increased the cell attachment may have been inhibited. It was reported that cells can attach on hydrophilic surfaces better than hydrophobic surfaces[193]. However, these results are found inconclusive and there was no pattern found in SEM and fluorescence images even though cell attachment was observed.

All magnetic PMMA cement samples were raised to above 50°C in five minutes at constant frequency of 290 kHz. The applied induction current was reduced with the increase of MGC addition in cement samples and this showed that less power was needed to generate similar heating response. However, a more controlled environment was needed to provide more efficient test results and data interpretation. Despite this, the samples were effectively heated in a range of 55 and 60°C and maintained at similar temperatures (between 53 and 57°C) lowering the induction current for all samples.

Magnetic hyperthermia has attracted many attentions, however little work is done for magnetic PMMA bone cement. Bioactive and magnetic properties are key points to provide interfacial bonding to bone and kill remnant cells. Magnetic glass-ceramic, which were reported in the literature, were lack of bioactive properties. However, MGCs developed by Bretcanu et al [61] and Kokubo et al [93]., showed bioactive properties.

In this study, magnetic glass-ceramics developed by Bretcanu et al [61]., were mixed with PMMA cements, Wintercryl and Palacos cements. All samples were prepared using silicone mould rather than PTFE mould. This mould provided consistent dimensions and there was no need for dry sanding or polishing, which could have affected mechanical properties. Moreover, this mould was used to monitor temperature of cement during polymerisation. However, there were variations due to not fully filling the sacrificial ends.

A study reported by Bruno et al. [163] showed that the addition of 20% (wt %) magnetic glass ceramic in PMMA cement did not meet the criteria of the standard, however, in this study, up to 30% MGC addition in Wintercryl and Palacos bone cements met ISO 5833:2002 standard. In addition to that, magnetic induction test was conducted in air and the test samples were in non-contact position. It was analysed that applied current and frequency were stable and easily controlled. In the literature, it was reported that magnetic induction test was always performed in water and applied current could not be stabilised and showed variations [163].There is no work in the literature that performed magnetic induction test in air for magnetic PMMA cement.

The magnetic PMMA cement samples can be used to fill the void after excision of cancer tissues. The volume of bone defect that PMMA cement can be applied is usually in a range of 1 mm^3 and 20 mm^3 [12]. However, it was reported that the layer of PMMA cement coating should not be thicker than 5 mm due to high exothermic reaction temperature since it may cause bone necrosis [14]. The exothermic reaction temperature can be dissipated by circulating blood around the implant and the surrounding tissue. After the surgery, magnetic hyperthermia treatment will be applied periodically. In order to determine duration and number of sessions of magnetic hyperthermia application *in vivo* tests should be performed using cancerous cells. Overall, MGC containing samples, with the exception of 40% addition, showed promising results in terms of bone regeneration and hyperthermic cancer therapies. In the next chapter, conclusions and future work will be presented.

6 Conclusions and Future Works

6.1 Conclusions

In the past few decades, PMMA cement has been widely used in medicine: orthopaedics, dental and vertebral applications have been the main areas where PMMA has been adopted due to its valuable mechanical properties. To expand its application and take advantage of its superior properties, it is important to gain a deeper understanding of the material and utilise innovative techniques for improvements. Moreover, little work has been done on magnetic glass ceramics containing PMMA cements regarding their characterisations. In this study, an array of experimental studies was performed to analyse the influence of magnetic glass-ceramic addition to PMMA cements for bone cancer treatment.

In this study, MGC glass-ceramics were added to commercial dental and orthopaedic PMMA cements in different amounts (10% to 40%) to investigate their mechanical properties, in vitro bioactivity, cytotoxicity and heat generation abilities. Plain PMMA cements were used as control: these samples were aged in open and closed air storage up to 180 days to examine their mechanical properties.

According to the main results in this study, the following conclusions can be drawn;

- Magnetic glass ceramics that belongs to the system Na_2O-CaO-SiO_2-P_2O_5 - Fe_2O_3-FeO were produced at 1550°C by a traditional melting and quenching technique. XRD results showed that a magnetite crystalline phase was successfully produced during quenching. Magnetite crystals were observed on the surface of the magnetic glass ceramics using SEM. MGC was not only mixed in PMMA cement to give bioactive and magnetic properties but also to provide better mechanical properties. Magnetic PMMA cement was produced following standard ISO 5833:2002 for testing mechanical properties. Addition of glass-ceramics could increase bending modulus of PMMA cement to give a better match to bone according to rule of mixing. Moreover, due to its magnetic properties, magnetite phase plays an important role in heat generation during magnetic hyperthermia applications.

- Reliable and cost-effective fabrication method of silicone rubber mould were developed to produce PMMA bone cements with accurate dimensions for mechanical properties testing. This mould was found to be an alternative to the PTFE mould suggested by standards ASTM F451-16 and ISO 5833:2002. More than 100 of PMMA samples could be produced and used without any post-processing requirements such as sizing, sanding and polishing. However, setting time and temperature measurements through sacrificial ends were not successful due to not fully filling the sacrificial ends. It was acknowledged that the polymerisation started at the centre of the cement. However, the samples would be tested under four-point bending test and therefore, thermocouples could not be placed in the centre of the sample.
- All aged samples met the minimum criteria of ISO 5833:2002 for bending strength (50 MPa), bending modulus (1.8 GPa) and compressive strength (70 MPa). Bending strength and bending modulus of samples showed a non-linear increase. This increase indicated that setting reaction of PMMA cement continued over the 180 days period. Compressive strength of all samples showed variations, but a notable increase was observed for Palacos® samples throughout ageing process. It was known that the addition of radiopacifier, zirconium oxide (ZrO_2), might alter the mechanical properties of cements. However, in this study, while Palacos cement showed higher Vickers hardness, flexural and compressive strength compared to Wintercryl cement, there was no significant difference between Wintercryl and Palacos® cements, even if Wintercryl cement did not have addition of radiopacifier.

- SEM images showed that plain PMMA cements had porous surfaces and some of the PMMA beads could be distinguished on the surface, which caused inhomogeneity in the structure.

- Addition of MGC from 10% to 40% (wt%) reduced viscosity of cements and increased the waiting time of the cement. It should be noted that increase in MGC addition lowered the ratio between PMMA powder and liquid and this increased the waiting time of cement. Furthermore, ambient temperatures below 22-23°C also increased the waiting time.

- SEM images showed that MGC particles were well dispersed in the polymer matrix. As the amount of MGC particles increased from 10% to 40%, the peak of Fe in EDS spectra increased.

- The cement samples with the addition of MGC from 10% to 30% met the minimum requirement of standard ISO 5833:2002 for bending modulus (1.8 GPa). For magnetic cement samples, the average bending modulus values was between 2.7 and 3.8 GPa. Bending strength of the cement samples decreased with the addition of MGC from 10% to 40% in PMMA cement and P40 and W40 samples did not meet the requirement of this standard for bending strength (50 MPa). The average bending strength was between 47.5 and 58.5 MPa. Although there was a sharp decrease in compressive strength of 40% MGC containing PMMA samples, all magnetic cement samples met the minimum requirement of standard ISO 5833:2002 (70 MPa). The average compressive strength was between 72 and 86.2 MPa. There was no significant difference between W-MGC and P-MGC cement samples.

- Vickers hardness of cement samples significantly increased with the increase of MGC addition in the cements. The average Vickers hardness of all magnetic cement samples varied between 22.2 and 28 MPa.

- Water absorption in Wintercryl cement samples increased with the addition of MGC powder in the structure. MGC containing Palacos cement samples showed variations. The average water absorption (%) of magnetic cements was in a range of 4.8-6.6%

- In vitro bioactivity characterisation demonstrated that formation of apatite crystals started after two weeks of immersion in SBF solution, providing the bioactivity properties of magnetic cements.

- Despite the inconclusive cytocompatibility tests, a decrease in cell viability was observed with the increase of MGC addition in cements. However, the reduction in U2OS cells were significantly higher than OBS cells. OBS cells could be distinguished from the background under SEM but U2OS cells could not be distinguished.
- Preliminary induction heating tests in free air were performed in two stages for all samples. Induction current was reduced with the increase of MGC from 10% to 40% in PMMA cement samples at a constant frequency, 290 kHz. In stage I, P-MGC and W-MGC samples were successfully heated within a range of 55-60°C. In stage II, induction current was reduced to maintain temperature in the cement samples for five minutes. The temperature recordings showed that the temperatures were successfully maintained 1-4°C below the maximum temperature that they were heated to in stage I. These results demonstrated that with the increase of MGC content in PMMA cement the required energy for heat generation and temperature maintenance decreased due to higher energy absorption.

Overall, this study contributed to build an extensive knowledge of PMMA cements and its combination with MGC. According to the main findings in this study, up to 30% MGC addition showed promising results to be successfully used in bone cancer treatment via magnetic hyperthermia.

6.2 Future Work

This PhD research contributed to extend knowledge on the addition of MGC in commercial PMMA cements, which showed promising results to be used in bone cancer treatment. Moreover, a new mould design was suggested and this, could be a better alternative to PTFE moulds. Nevertheless, there are more characterisation techniques need to be performed to have a better understanding of PMMA cement and magnetic PMMA cement. The suggestions are listed below;

- Determining setting time of magnetic Palacos cement:
  In this study, it was aimed to calculate setting time of magnetic cement. According to standard ISO 5833:2002, 25 grams of cement was needed, and this test should have been repeated 2 or 4 times for evaluation of setting time and temperature. This amount of Palacos cement and magnetic glass-ceramics were not available so this test was not performed.

- Assessment of ageing and storage conditions of plain and magnetic PMMA cement:

  Mechanical tests of ageing PMMA cement in dry conditions were carried out and it was seen that the mechanical properties showed changes over time. However, magnetic cements were not exposed to ageing conditions and they were always tested 24±2 hours after polymerisation. In order to determine the ageing behavior of magnetic cements, it is necessary to perform tests at the similar time-point. In addition to dry ageing, wet ageing test could take place in an aqueous solution which can replicate human body conditions such as PBS (phosphate buffer solution) or SBF (simulated body fluid).

- In vitro induction heating test:

  Heat generation of magnetic PMMA cement was evaluated and it was observed that all samples can be heated to above 50°C in five minutes. The test should also be carried out for OBS and U2OS cells seeded on magnetic PMMA cement to observe if there is any behavioral difference between the cells. Also induction test can be carried out in a 37°C wet environment using an implanted magnetic bone cement in animal bone.

- Observation of cell attachment on magnetic PMMA cement:

  Since the observation of cell attachments on magnetic PMMA cement was inconclusive in this study, cell staining can be more efficient using phalloidin, vinculin and paxillin.

- Anticancer drug binding:

  The magnetic PMMA cements can be linked with anticancer drugs, such as cisplatinum or doxorubicin. X-ray photoelectron spectroscopy (XPS) can be performed to analyse the presence of anticancer drugs. The drug-release variation in aqueous solutions can be determined for different pH, temperature and time points.

Appendix A- Magnetic Glass Ceramics

A.1 X-Ray Diffraction Analysis

XRD patterns obtained from eight batches of MGC powder and the reference materials, are presented in Figure A.0.1. The detector was set to scan over a range of 2θ angles from 10° to 70°, at a step size of 0.05°, 1s per step.

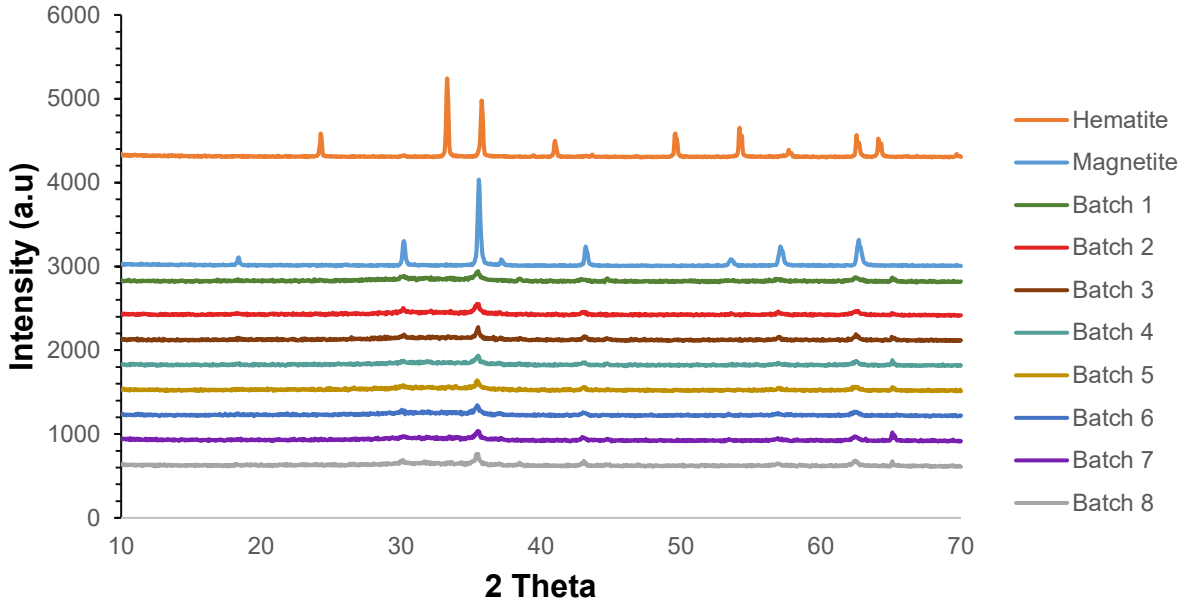

Figure A.1 XRD pattern of 8 batches of MGC, magnetite and hematite powders

A.2 Differential Thermal Analysis

DTA curves of 6 batches of MGC powder are presented in Figure A.0.2.

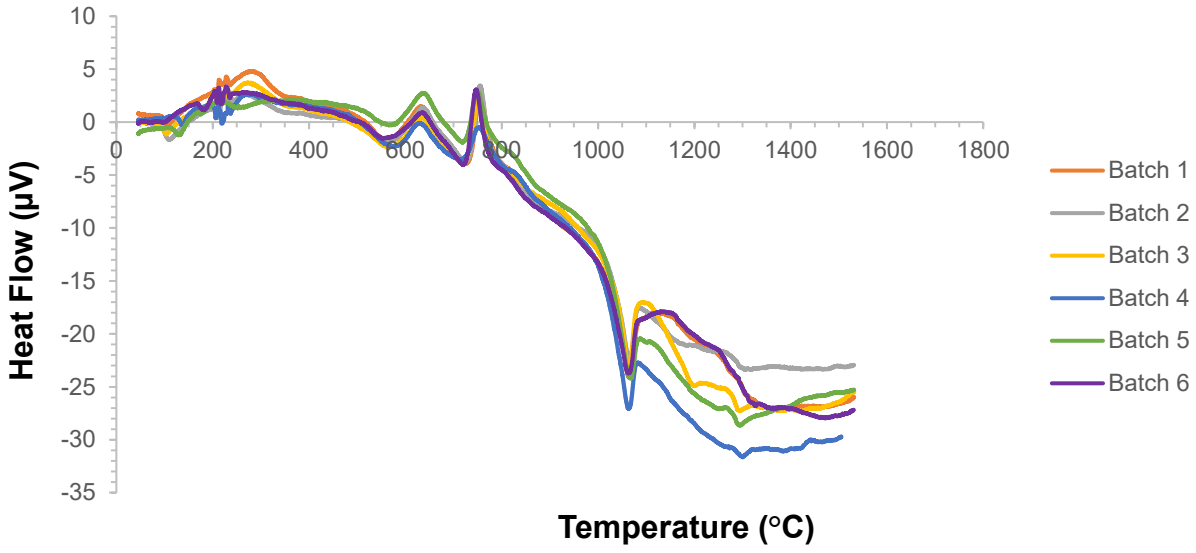

Figure A.2 DTA curves obtained for 6 batches of MGC at 20 C/min

Appendix B- PMMA Cement

B.1 Polymerisation reaction temperature during the setting process of Palacos cement

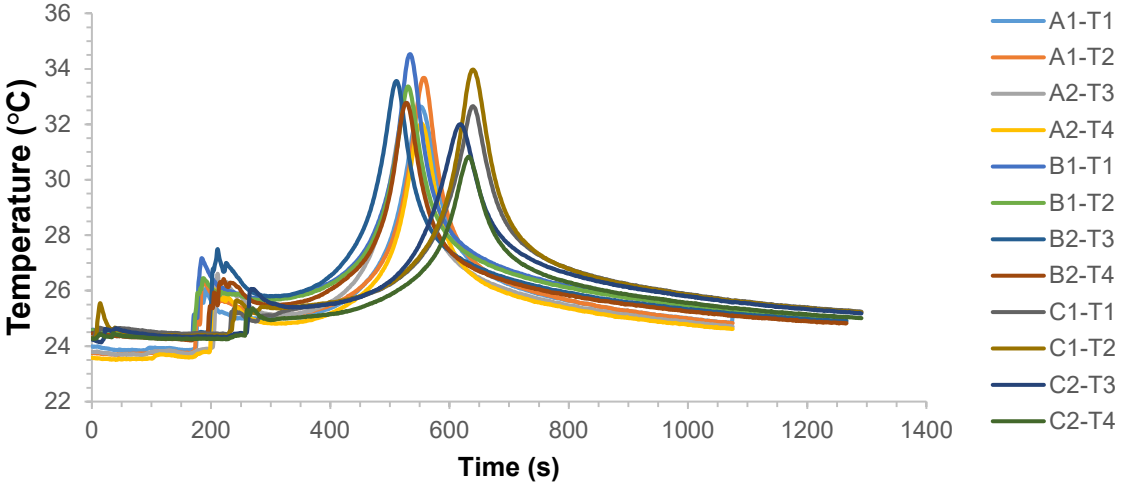

Figure B.1 Temperature-time profiles of A, B and C of Palacos cement samples

B.2 Humidity and temperature of four-point test environment

Table B. 1 Humidity and temperature recordings of test environment during four-point bending test

Samples (W0 and P0)	**Temperature (°C)**	**Relative Humidity (rh%)**
Day 1, 2, 3	24.5±0.5	47.2 ±1.1
Day 7, 14, 21	22.2±1.4	50.3±1.8
Day 28, 60 and 180	25.0±1.3	45.6±3.7

Appendix C- Magnetic PMMA Cement

C.1 Polymerisation reaction temperature during the setting process of W-MGC and P-MGC cement samples

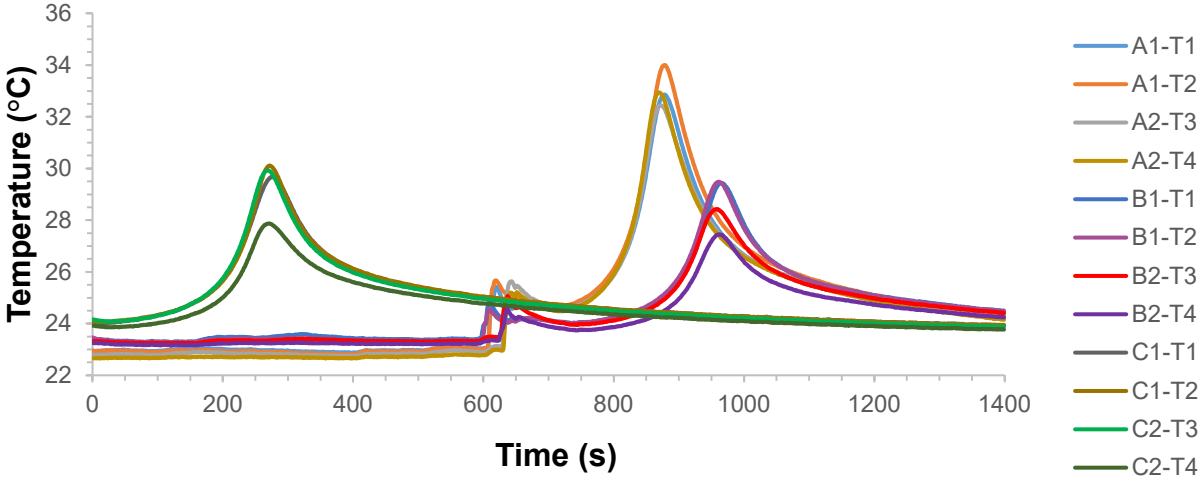

Figure C. 1 Temperature-time profiles of A, B and C of W10 cement samples

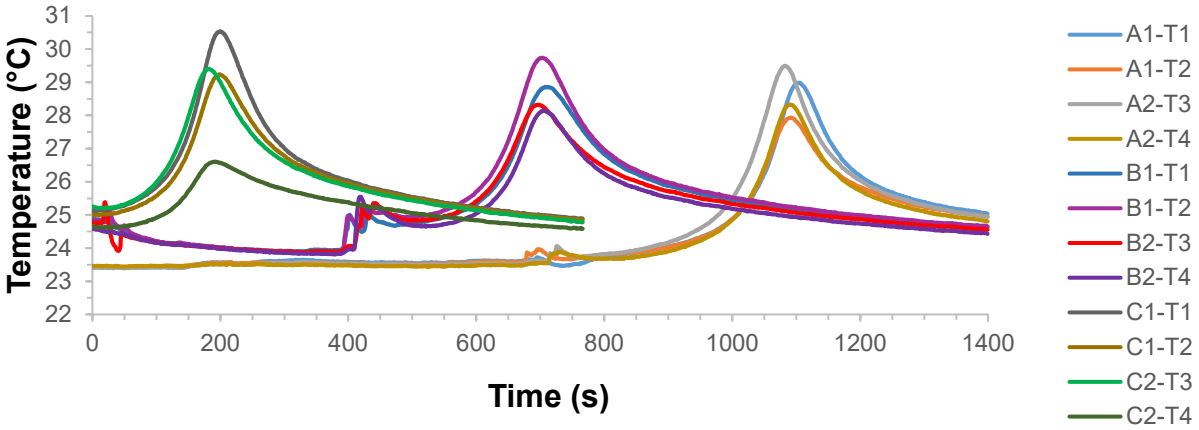

Figure C. 2 Temperature-time profiles of A, B and C of W20 cement samples

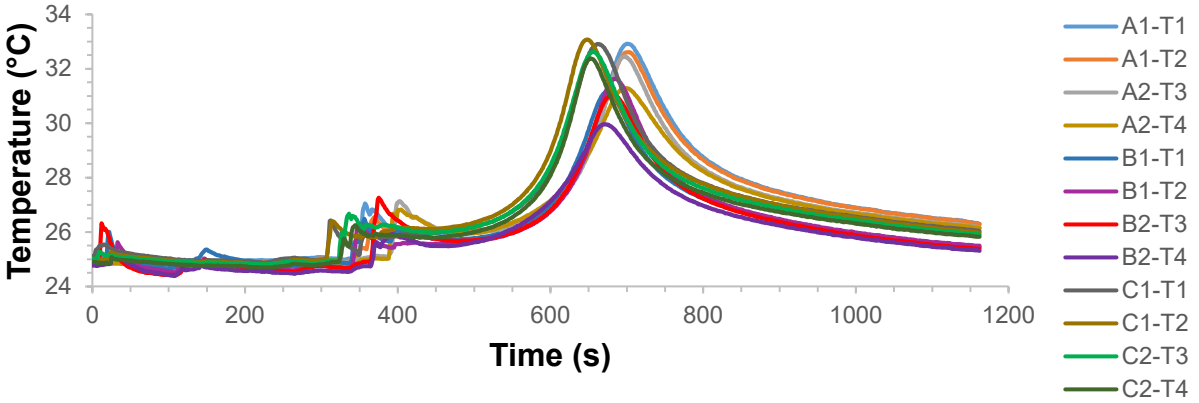

Figure C.3 Temperature-time profiles of A, B and C of W30 cement samples

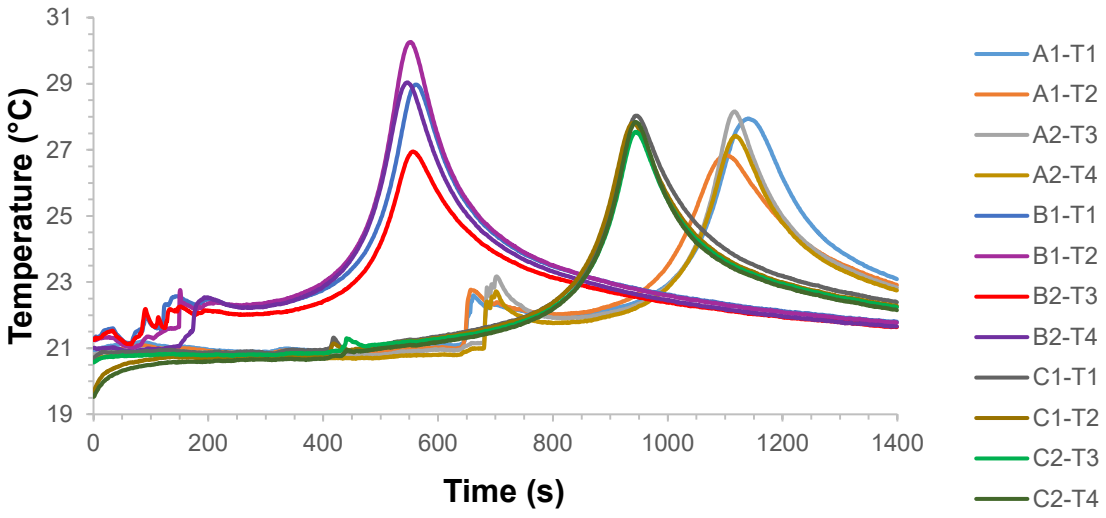

Figure C..4 Temperature-time profiles of A, B and C of W40 cement samples P10

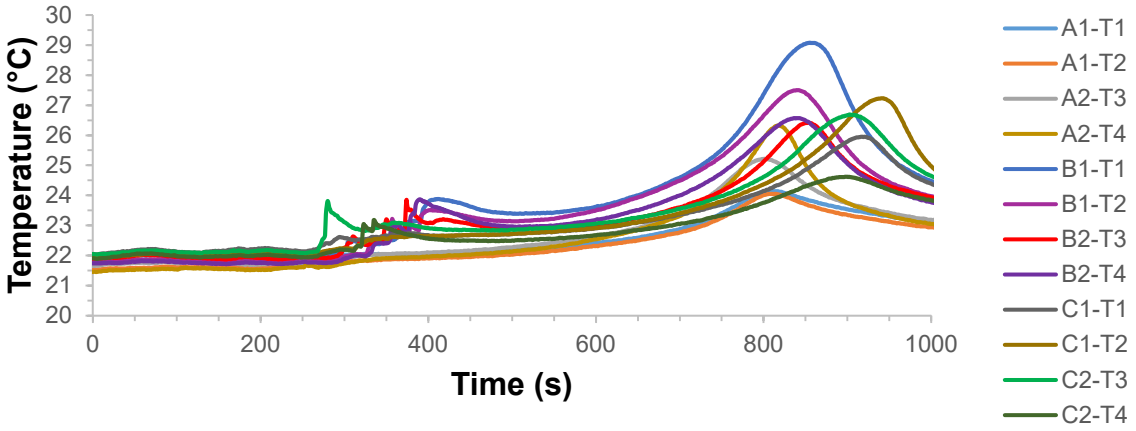

Figure C.5 Temperature-time profiles of A, B and C of P10 cement samples

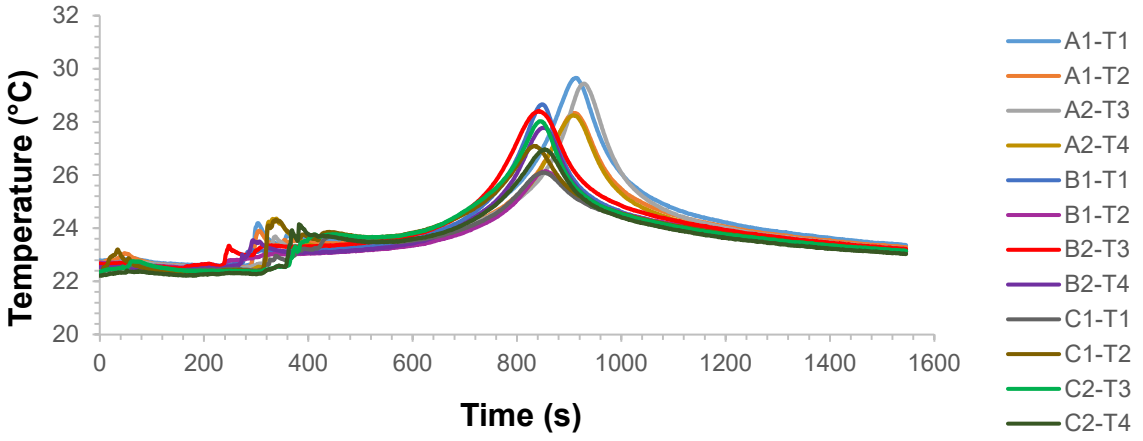

Figure C.6 Temperature-time profiles of A, B and C of P20 cement samples

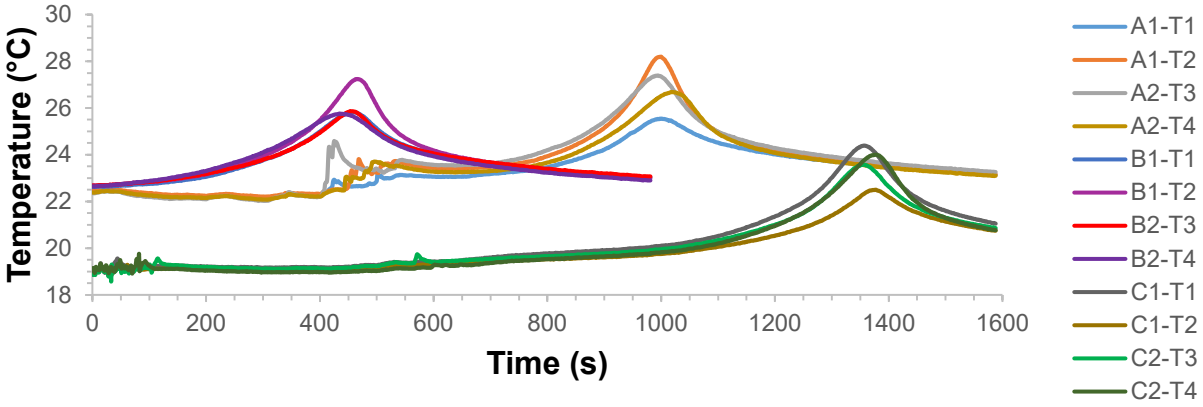

Figure C.7 Temperature-time profiles of A, B and C of P30 cement samples

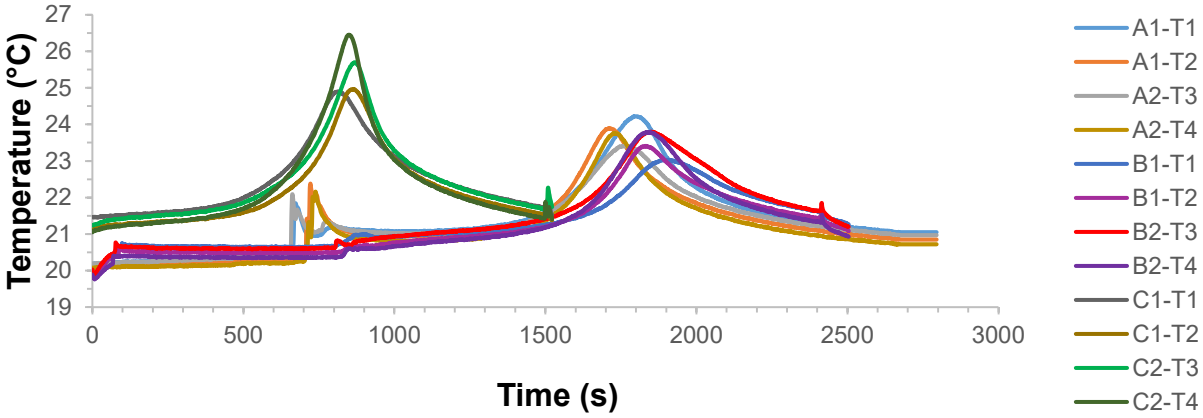

Figure C.8 Temperature-time profiles of A, B and C of P40 cement samples

C.2 Humidity and temperature of four-point test environment

Table C.1 Humidity and temperature recordings of test environment during four-point bending test

Samples (W-MGC& P-MGC)	Temperature (°C)	Relative Humidity (rh%)
10% and 20%	25.04± 0.2	38.6±0.5
30% and 40%	25.3±0.1	38.3± 0.4

Appendix D- Cytocompatibility Test

D.1 MTT Assay

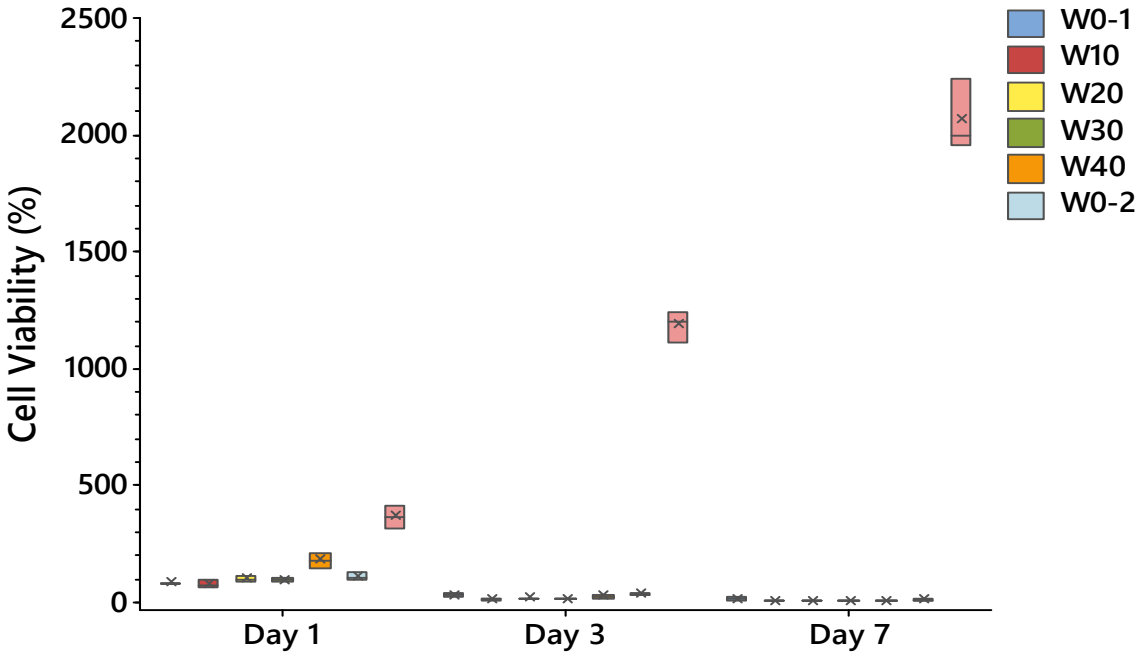

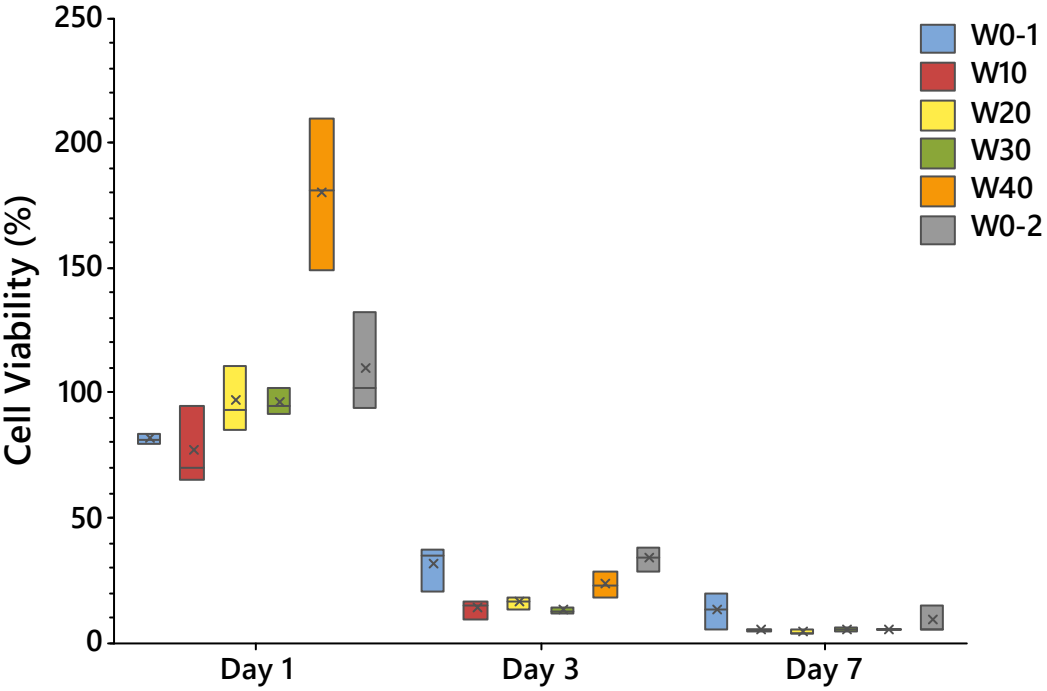

Figure D.1 Data range of cell viability (%) of U2OS cells seeded on W0 and W-MGC samples for 1, 3 and 7 days. The mean values of the samples are expressed with the X, and horizontal lines represent the median values.

D.2 Alamar Blue Asssay

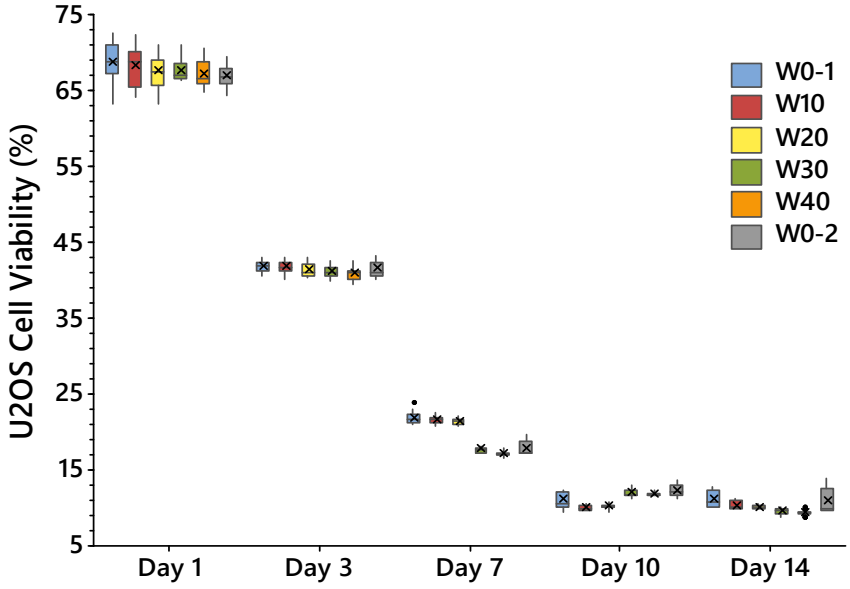

Figure D.2 Data range of U2OS cell viability on W0-1(control sample in plate-1), W0-2 (control sample in plate 2) and W-MGC samples for 1, 3, 7, 10 and 14 days. The data includes outliers. The mean values of the samples are expressed with the X, and horizontal lines represent the median values.

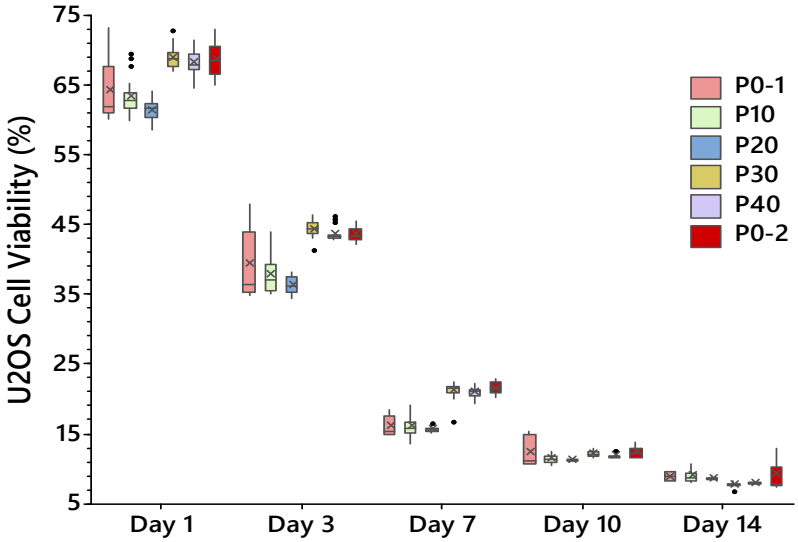

Figure D.3 The data range of U2OS cell viability on P0-1 (control sample in plate-1), P0-2 (control sample in plate-2) and P-MGC samples for 1, 3, 7, 10 and 14 days. The data includes outliers. The mean values of the samples are expressed with the X, and horizontal lines represent the median values.

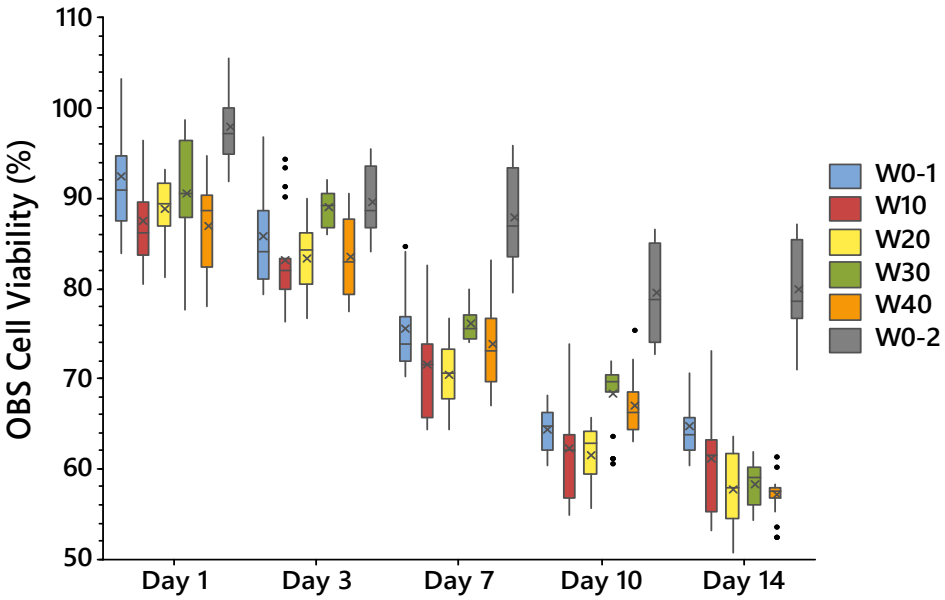

Figure D.4 The data range of OBS cell viability W0-1(control sample in plate-1), W0-2 (control sample in plate 2) and W-MGC samples for 1, 3, 7, 10 and 14 days. The data includes outliers. The mean values of the samples are expressed with the X, and horizontal lines represent the median values.

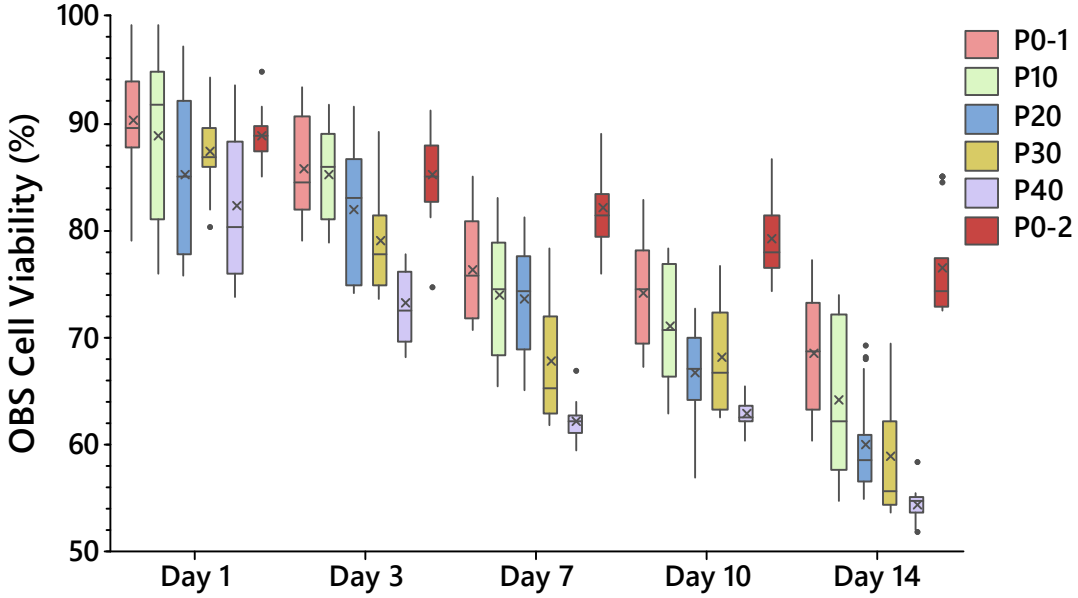

Figure D.5 The data range of OBS cell viability (%) on P0-1 (control sample in plate-1), P0-2 (control sample in plate-2) and P-MGC samples for 1, 3, 7, 10 and 14 days. The data includes outliers. The mean values of the samples are expressed with the X, and horizontal lines represent the median values.

7 References

1. Society, A.C. Cancer statistics center. 2018 [cited 2019 03.04.2019]; Available from: https://cancerstatisticscenter.cancer.org/?_ga=2.180852967.1359564434.1554322865-2103888015.1554322865#!/.
2. Service, N.H. Bone Cancer Overview. 2018 [cited 2019 03.04.2019]; Available from: https://www.nhs.uk/conditions/bone-cancer/.
3. Institute, N.C. Primary Bone Cancer. 2018 [cited 2019 04.04.2019]; Available from: https://www.cancer.gov/types/bone/bone-fact-sheet.
4. Takegami, K., et al., New ferromagnetic bone cement for local hyperthermia. Journal of biomedical materials research, 1998. 43(2): p. 210-214.
5. Pattrick, R.A.D., et al., Nanoscience: volume 1: nanostructures through chemistry. 2013, RSC Publishing, London.
6. Bretcanu, O., et al., The influence of crystallised Fe 3 O 4 on the magnetic properties of coprecipitation-derived ferrimagnetic glass–ceramics. Acta biomaterialia, 2005. 1(4): p. 421-429.
7. Matsumine, A., et al., Novel hyperthermia for metastatic bone tumors with magnetic materials by generating an alternating electromagnetic field. Clin Exp Metastasis, 2007. 24(3): p. 191-200.
8. Registry, N.J., 15th Annual Report 2018 2018, NJR Service Centre.
9. Webb, J.C.J. and R.F. Spencer, The role of polymethylmethacrylate bone cement in modern orthopaedic surgery. Journal of Bone & Joint Surgery, British Volume, 2007. 89(7): p. 851-857.
10. Kang, H.G. and S.H. Kang, Minimal Invasive Surgery of Metastatic Bone Tumor. Tumor Metastasis, 2016: p. 127.
11. Schemitsch, E.H., Size matters: defining critical in bone defect size! Journal of orthopaedic trauma, 2017. 31: p. S20-S22.
12. Rankin, D.K., Size of bone defects for PMMA cement application. 2019.
13. Aurégan, J.-C. and T. Bégué, Induced membrane for treatment of critical sized bone defect: a review of experimental and clinical experiences. International orthopaedics, 2014. 38(9): p. 1971-1978.
14. Vaishya, R., M. Chauhan, and A. Vaish, Bone cement. Journal of Clinical Orthopaedics and Trauma, 2013. 4(4): p. 157-163.
15. Stürup, J., et al., Effects of polymerization heat and monomers from acrylic cement on canine bone. Acta Orthopaedica Scandinavica, 2009. 65(1): p. 20-23.
16. Matsumine, A., et al., A novel hyperthermia treatment for bone metastases using magnetic materials. Int J Clin Oncol, 2011. 16(2): p. 101-8.
17. Leventouri, T., et al., Structure, microstructure, and magnetism in ferrimagnetic bioceramics. Biomaterials, 2005. 26(24): p. 4924-4931.
18. Ratner, B.D., et al., Biomaterials science: an introduction to materials in medicine. 2004: Academic press.
19. Habash, R.W., et al., Thermal therapy, part 2: hyperthermia techniques. Critical Reviews™ in Biomedical Engineering, 2006. 34(6).
20. Sardari, D. and N. Verga, Cancer treatment with hyperthermia, in Current Cancer Treatment-Novel Beyond Conventional Approaches. 2011, IntechOpen.
21. Oryan, A., S. Monazzah, and A. Bigham-Sadegh, Bone injury and fracture healing biology. Biomedical and environmental sciences, 2015. 28(1): p. 57-71.
22. Mohamed, A.M., An overview of bone cells and their regulating factors of differentiation. The Malaysian journal of medical sciences: MJMS, 2008. 15(1): p. 4.

23. Marques, C., et al., Multifunctional materials for bone cancer treatment. Int J Nanomedicine, 2014. 9: p. 2713-25.
24. Khurana, J.S., Bone pathology. 2009: Springer Science & Business Media.
25. Doblare, M., J.M. Garcia, and M.J. Gomez, Modelling bone tissue fracture and healing: a review. Engineering Fracture Mechanics, 2004. 71(13-14): p. 1809-1840.
26. Body, A. Structure of Long Bone 2018 [cited 2019 05.05.2019]; Available from: http://anatomybodysystem.com/hand-bone-diagram-unlabeled/hand-bone-diagram-unlabeled-long-bone-diagram-unlabled-block-and-schematic-diagrams-%E2%80%A2/.
27. Hofmann, S. and M. Garcia-Fuentes, Bioactive scaffolds for the controlled formation of complex skeletal tissues, in Regenerative Medicine and Tissue Engineering-Cells and Biomaterials. 2011, IntechOpen.
28. Kindblom, L.G., Bone tumors: epidemiology, classification, pathology, in Imaging of bone tumors and tumor-like lesions. 2009, Springer. p. 1-15.
29. Wu, J.S., Bone tumors a practical guide to imaging, ed. M. Hochman. 2012, New York

London: New York

London : Springer.
30. Suva, L.J., R.J. Griffin, and I. Makhoul, Mechanisms of bone metastases of breast cancer. Endocrine-related cancer, 2009. 16(3): p. 703-713.
31. O'Leary, U., Bone metastasis: secondary illness, primary concern. Nursing times, 2001. 97(41): p. 32.
32. Ma, J. and A. Jemal, Breast cancer statistics, in Breast Cancer Metastasis and Drug Resistance. 2013, Springer. p. 1-18.
33. Chowdhry, M., K. Hayward, and L. Jeys, Primary malignant tumours of the bone. Surgery (Oxford), 2009. 27(2): p. 80-85.
34. David, M.P., D.K. Joseph, and M.B. McCarville, Pediatric Malignancies: Pathology and Imaging. 2015 ed, ed. D.M. Parham, J.D. Khoury, and M.B. McCarville. 2015, New York, NY: New York, NY: Springer New York.
35. Balamuth, N.J. and R.B. Womer, Ewing's sarcoma. The lancet oncology, 2010. 11(2): p. 184-192.
36. Bolling, T., J. Hardes, and U. Dirksen, Management of bone tumours in paediatric oncology. Clin Oncol (R Coll Radiol), 2013. 25(1): p. 19-26.
37. MacDuff, E. and R. Reid, Bone tumour pathology. Surgery (Oxford), 2009. 27(2): p. 55-62.
38. Bahk, Y.-W., Combined scintigraphic and radiographic diagnosis of bone and joint diseases: including gamma correction interpretation. 2012: Springer Science & Business Media.
39. Sarcoma Stem Cells: Do We Know What We Are Looking for? Sarcoma, 2012. 2012: p. 8.
40. inform, N. Osteosarcoma. 2017 [cited 2019 08.04.2019]; Available from: https://www.nhsinform.scot/illnesses-and-conditions/cancer/cancer-types-in-children/osteosarcoma.
41. Huvos, A.G., Chondrosarcoma and its variants. Journal of Orthopaedic Science, 1996. 1(1): p. 90-97.
42. Szendröi, M., Giant-Cell Tumour of Bone. The Journal of Bone and Joint Surgery. British volume, 2004. 86-B(1): p. 5-12.
43. Alaqaili, S.I., et al., Malignant Sarcomatous Transformation of Benign Giant Cell Tumor of Bone after Treatment with Denosumab Therapy: A Literature Review of Reported Cases. Cureus, 2018. 10(12).

44. Longhi, A., et al., Primary bone osteosarcoma in the pediatric age: state of the art. Cancer Treat Rev, 2006. 32(6): p. 423-36.
45. American Cancer Society, I. Treating Bone Cancer. 2019 Available from: https://www.cancer.org/cancer/bone-cancer/treating.html.
46. Mercadante, S., Malignant bone pain: pathophysiology and treatment. Pain, 1997. 69(1-2): p. 1-18.
47. Group, I.M.R.T.C.W., Intensity-modulated radiotherapy: current status and issues of interest. International Journal of Radiation Oncology* Biology* Physics, 2001. 51(4): p. 880-914.
48. Levin, W., et al., Proton beam therapy. British journal of Cancer, 2005. 93(8): p. 849.
49. Gerber, D.E. and T.A. Chan, Recent advances in radiation therapy. Am Fam Physician, 2008. 78(11): p. 1254-1262.
50. Sawyers, C., Targeted cancer therapy. Nature, 2004. 432(7015): p. 294.
51. American Cancer Society, I. Targeted Therapy for Bone Cancer. 2018 [cited 2019 04.04.2019]; Available from: https://www.cancer.org/cancer/bone-cancer/treating/targeted-therapy.html.
52. Organization, W.H., WHO handbook for reporting results of cancer treatment. 1979.
53. Chicheł, A., et al., Hyperthermia–description of a method and a review of clinical applications. Reports of Practical Oncology & Radiotherapy, 2007. 12(5): p. 267-275.
54. Abdel-Hameed, S.A.M., M.A. Marzouk, and M.M. Farag, Effect of P 2 O 5 and MnO 2 on crystallization of magnetic glass ceramics. Journal of advanced research, 2014. 5(5): p. 543-550.
55. Ortega, D. and Q.A. Pankhurst, Magnetic hyperthermia. Nanoscience, 2013. 1(60): p. e88.
56. Wust, P., et al., Hyperthermia in combined treatment of cancer. The lancet oncology, 2002. 3(8): p. 487-497.
57. Issels, R.D., Hyperthermia adds to chemotherapy. European journal of cancer, 2008. 44(17): p. 2546-2554.
58. Kampinga, H. and E. Dikomey, Hyperthermic radiosensitization: mode of action and clinical relevance. International journal of radiation biology, 2001. 77(4): p. 399-408.
59. Lemmo, W. hyperthermia; An overview. 2013; Available from: http://www.lemmo.com/hyperthermia/hyperthermia-background/.
60. Kawashita, M., K. Kawamura, and Z. Li, PMMA-based bone cements containing magnetite particles for the hyperthermia of cancer. Acta Biomater, 2010. 6(8): p. 3187-92.
61. Bretcanu, O., et al., Synthesis and characterization of coprecipitation-derived ferrimagnetic glass-ceramic. Journal of Materials Science, 2006. 41(4): p. 1029-1037.
62. Ebisawa, Y., et al., Bioactivity of ferrimagnetic glass-ceramics in the system FeO□Fe 2 O 3□CaO□SiO 2. Biomaterials, 1997. 18(19): p. 1277-1284.
63. Libretexts, C. Hard and soft magnets. Available from: https://chem.libretexts.org/Bookshelves/Inorganic_Chemistry/Book%3A_Inorganic_Chemistry_(Wikibook)/Chapter_06%3A_Metals_and_Alloys_-_Structure%2C_Bonding%2C_Electronic_and_Magnetic_Properties/6.8%3A_Hard_and_soft_magnets.
64. Kingery, W.D., Ceramic Processes and Products, in Introduction to ceramics. 1976. p. 3-20.

65. Callister, W.D. and D.G. Rethwisch, Materials science and engineering: an introduction. Vol. 7. 2007: John Wiley & Sons New York.
66. James, P., Glass ceramics: new compositions and uses. Journal of Non-Crystalline Solids, 1995. 181(1-2): p. 1-15.
67. Rawlings, R., J. Wu, and A. Boccaccini, Glass-ceramics: their production from wastes—a review. Journal of Materials Science, 2006. 41(3): p. 733-761.
68. Pengpat, K., Ferroelectric glass-ceramics. 2001, University of Warwick.
69. Uhlmann, D., H.K. Bowen, and W. Kingery, Structure of Glass, in Introduction to Ceramics, D. Uhlmann, H.K. Bowen, and W. Kingery, Editors. 1976, New York: John Wiley & Sons Inc.
70. Shelby, J., Introduction to Glass Science and Technology, Royal Society of Chemistry. Cambridge CB4 0WF, UK, 2005.
71. Park, J., Development of A Glass-Ceramic For Biomedical Applications, in Natural and Applied Science. 2008, Middle East Technical University.
72. Hench, L.L., Bioceramics: from concept to clinic. Journal of the american ceramic society, 1991. 74(7): p. 1487-1510.
73. KARLSSON, K.H., The bioactivity of glasses, in High-performance glasses, M.C.a.J.M. PARKER, Editor. 1992, Blackie Academic & Professional.
74. Farooq, I., et al., Bioactive glass: a material for the future. World J Dent, 2012. 3(2): p. 199-201.
75. De Aza, P., et al., Bioactive glasses and glass-ceramics. BOLETIN-SOCIEDAD ESPANOLA DE CERAMICA Y VIDRIO, 2007. 46(2): p. 45.
76. LUTIŠANOVÁ, G., M.T. Palou, and J. Kozankova, Mechanism of bioactivity of LS2-FA glass-ceramics in SBF and DMEM medium. Ceramics–Silikáty, 2012. 56(3): p. 229-237.
77. Bohner, M. and J. Lemaitre, Can bioactivity be tested in vitro with SBF solution? Biomaterials, 2009. 30(12): p. 2175-2179.
78. HASHMI, M.U., Structural and In-Vitro Characterization of Bioactive Glass Ceramics with Different CaO/MgO Ratios. 2004, GC University Lahore, Pakistan.
79. Hench, L.L., Opening paper 2015-some comments on bioglass: four eras of discovery and development. Biomedical glasses, 2015. 1(1).
80. Kelly, J.R., I. Nishimura, and S.D. Campbell, Ceramics in dentistry: historical roots and current perspectives. The Journal of prosthetic dentistry, 1996. 75(1): p. 18-32.
81. Holand, W. and W. Vogel, Machineable and phosphate glass-ceramics. ADVANCED SERIES IN CERAMICS, 1993. 1: p. 125-138.
82. Dubok, V.A., Bioceramics—yesterday, today, tomorrow. Powder Metallurgy and Metal Ceramics, 2000. 39(7-8): p. 381-394.
83. Baino, F., S. Hamzehlou, and S. Kargozar, Bioactive Glasses: Where Are We and Where Are We Going? Journal of functional biomaterials, 2018. 9(1): p. 25.
84. Park, J., Glass-Ceramics, in Bioceramics: Properties, Characterizations, and Applications. 2008, Springer New York: New York, NY. p. 162-176.
85. Fiume, E., et al., Bioactive glasses: From parent 45S5 composition to scaffold-assisted tissue-healing therapies. Journal of functional biomaterials, 2018. 9(1): p. 24.
86. Höland, W., M. Frank, and V. Rheinberger, Surface crystallization of leucite in glasses. Journal of non-crystalline solids, 1995. 180(2-3): p. 292-307.
87. Abdel-Hameed, S.A.M., M.A. Marzouk, and R.L. Elwan, In vitro evaluation of some types of ferrimagnetic glass ceramics. International journal of biomaterials, 2014. 2014.
88. Farooq I, I.Z., Farooq U, Leghari A, Ali H, Bioactive glass for future

Multifunctional materials for bone cancer. World J Orthop, 2012. 3: p. 199-201.
89. Ebisawa, Y., et al., Bioactivity of Fe2O3-containing CaO-SiO2 glasses: in vitro evaluation. Journal of Materials Science: Materials in Medicine, 1993. 4(3): p. 225-232.
90. Singh, R.K., Investigations on Selected Bioactive Glasses and Glass-Ceramics Containing Iron Oxide. 2009.
91. Kaur, G., et al., Mechanical properties of bioactive glasses, ceramics, glass-ceramics and composites: State-of-the-art review and future challenges. Materials Science and Engineering: C, 2019: p. 109895.
92. Thompson, I. and L. Hench, Mechanical properties of bioactive glasses, glass-ceramics and composites. Proceedings of the Institution of Mechanical Engineers, Part H: Journal of Engineering in Medicine, 1998. 212(2): p. 127-136.
93. Kokubo, T., Bioactive glass ceramics: properties and applications. Biomaterials, 1991. 12(2): p. 155-163.
94. Wang, M.-C., et al., Crystallization and magnetic properties of a 10Li 2 O–9MnO 2–16Fe 2 O 3–25CaO–5P 2 O 5–35SiO 2 glass. Materials Chemistry and Physics, 2013. 140(1): p. 16-23.
95. Li, G., et al., A novel method to enhance magnetic property of bioactive glass-ceramics for hyperthermia. Ceramics International, 2019. 45(4): p. 4945-4956.
96. Merriam-Webster, I. Merriam-Webster Since 1828. 2018; Available from: https://www.merriam-webster.com/dictionary/cement.
97. Cama, G., Calcium Phosphate Cements for Bone Regeneration in Biomaterials for Bone Regeneration: Novel Techniques and Applications, P. Dubruel and S. Van Vlierberghe, Editors. 2014, Elsevier.
98. Nottrott, M., Acrylic bone cements: influence of time and environment on physical properties. Acta Orthopaedica, 2010. 81(sup341): p. 1-27.
99. Kühn, K.-D., S. Breusch, and H. Malchau, Properties of Bone Cement: What is Bone Cement? 2005: Springer Medizin Verlag Berlin.
100. Seyyed Hosseinzadeh, H.R., et al., The Acrylic Bone Cement in Arthroplasty. 2013.
101. Arora, M., et al., Polymethylmethacrylate bone cements and additives: A review of the literature. World J Orthop, 2013. 4(2): p. 67-74.
102. Ginebra, M.-P., T. Traykova, and J.A. Planell, Calcium phosphate cements as bone drug delivery systems: a review. Journal of Controlled Release, 2006. 113(2): p. 102-110.
103. Spierings, P.T.J., Testing and Performance of Bone Cements, in The Well-Cemented Total Hip Arthroplasty. 2005, Springer. p. 67-78.
104. Kühn, K.-D., Bone cements: up-to-date comparison of physical and chemical properties of commercial materials. 2012: Springer Science & Business Media.
105. He, Z., et al., Bone cements for percutaneous vertebroplasty and balloon kyphoplasty: Current status and future developments. Journal of Orthopaedic Translation, 2015. 3(1): p. 1-11.
106. Company, E.C., Hydroquinone. 2009.
107. Chaudhry, S. and D. Dunlop, Bone cement in arthroplasty. Orthopaedics and Trauma, 2012. 26(6): p. 391-396.
108. Ayre, W.N., Novel approaches to the development of PMMA bone cement. 2013, Cardiff University.
109. GmbH, H.M. Palacos R high viscosity bone cement. 2018 [cited 2019 12.04.2019]; Available from: https://www.heraeus.com/media/media/hme/doc_hme/products_hme/palacos_bone_cement/r_rg_mv_mvg_lv_lvg/ifu/PALACOS_R_IFU.pdf.

110. GmbH, H.M. Palacos Mv Medium Viscosity Bone Cement. 2017 [cited 2019 12.04.2019]; Available from: https://www.heraeus.com/media/media/hme/doc_hme/products_hme/palacos_bone_cement/r_rg_mv_mvg_lv_lvg/ifu/PALACOS_MV_IFU.pdf.
111. GmbH, H.M. PalacosLV low viscosity bone cement 2018 [cited 2019 12.04.2019]; Available from: https://www.heraeus.com/media/media/hme/doc_hme/products_hme/palacos_bone_cement/r_rg_mv_mvg_lv_lvg/ifu/PALACOS_LV_IFU.pdf.
112. Nottrott, M., Acrylic bone cements: influence of time and environment on physical properties. Acta Orthop Suppl, 2010. 81(341): p. 1-27.
113. Sanchez, M.A., et al. Thermal Curing and Strength of PMMA Bone Cement. in ASME 2003 Heat Transfer Summer Conference. 2003.
114. Dunne, N., Bone cement fixation: Acrylic cements, in Joint Replacement Technology. 2008, Elsevier. p. 212-251.
115. Samad, H.A. and M. Jaafar, Effect of polymethyl methacrylate (PMMA) powder to liquid monomer (P/L) ratio and powder molecular weight on the properties of PMMA cement. Polymer-Plastics Technology and Engineering, 2009. 48(5): p. 554-560.
116. Tong, Y. and B.M. Culbertson, Effect of the poly (methyl methacrylate) molecular weight on the mechanical properties BisGMA/TEGDMA semi-interpenetrating polymer networks. Journal of MACROMOLECULAR SCIENCE—PURE AND APPLIED CHEMISTRY, 1998. 35(9): p. 1433-1443.
117. Ong, K.L., S. Lovald, and J. Black, Orthopaedic biomaterials in research and practice. 2014: CRC Press.
118. Standards, B., Implants for surgery —

Acrylic resin cements BRITISH STANDARD, ISO 5833, 2002.
119. Koh, B.T.H., et al., Effect of storage temperature and equilibration time on polymethyl methacrylate (PMMA) bone cement polymerization in joint replacement surgery. Journal of orthopaedic surgery and research, 2015. 10(1): p. 178.
120. Kuehn, K.-D., W. Ege, and U. Gopp, Acrylic bone cements: composition and properties. Orthopedic Clinics of North America, 2005. 36(1): p. 17-28.
121. Hagan, C.P., et al., Real time monitoring of the polymerisation of PMMA bone cement using Raman spectroscopy. J Mater Sci Mater Med, 2009. 20(12): p. 2427-31.
122. Havelin, L.I., et al., Prospective studies of hip prostheses and cements. A presentation of the Norwegian arthroplasty register, 1987. 1999: p. 15-19.
123. Orr, J.F. and N.J. Dunne, Measurement of Shrinkage Stresses in PMMA Bone Cement. Applied Mechanics and Materials, 2004. 1-2: p. 127-132.
124. Wang, J.-S., The Benefit of Vacuum Mixing, in The Well-Cemented Total Hip Arthroplasty. 2005, Springer. p. 107-112.
125. Gilbert, J.L., et al., A theoretical and experimental analysis of polymerization shrinkage of bone cement: a potential major source of porosity. Journal of Biomedical Materials Research, 2000. 52(1): p. 210-218.
126. Clements, J., et al., Optimisation of a two-liquid component pre-filled acrylic bone cement system: a design of experiments approach to optimise cement final properties. Journal of Materials Science: Materials in Medicine, 2014. 25(10): p. 2287-2296.
127. Orr, J.F. and N.J. Dunne. Measurement of shrinkage stresses in PMMA bone cement. in Applied Mechanics and Materials. 2004. Trans Tech Publ.

128. JF1, O., et al., The Effect Of Shrinkage On Stresses In A Mantle Of Curing Acrylic Bone Cement, in 7th World Biomaterials Congress. 2004.
129. Gergely, R.C.R., et al., Towards the optimization of the preparation procedures of PMMA bone cement. Journal of Orthopaedic Research, 2016. 34(6): p. 915-923.
130. Chaplin, R.P.S., et al., The mechanical properties of recovered PMMA bone cement: a preliminary study. Journal of Materials Science: Materials in Medicine, 2006. 17(12): p. 1433-1448.
131. Dunne, N.J., et al., The relationship between porosity and fatigue characteristics of bone cements. Biomaterials, 2003. 24(2): p. 239-245.
132. Lewis, G., Properties of acrylic bone cement: state of the art review. Journal of biomedical materials research, 1997. 38(2): p. 155-182.
133. Orr, J.F., N.J. Dunne, and J.C. Quinn, Shrinkage stresses in bone cement. Biomaterials, 2003. 24(17): p. 2933-2940.
134. Admnistration, U.S.F.a.D., Class II Special Controls Guidance Document: Polymethylmethacrylate (PMMA) Bone Cement - Guidance for Industry and FDA. 2002.
135. International, A., ASTM 451-16 Standard Specification for Acrylic Bone Cement. 2016, ASTM International.
136. Heraeus, COPAL G+C- Evidence Overview.
137. UK, A.R. The challenge of revision hip replacement surgery. 2013; Available from: http://www.arthritisresearchuk.org/arthritis-information/arthritis-today-magazine/159-winter-2013/the-challenge-of-revision-hip-replacement-surgery.aspx.
138. Service, N.H., Hip replacement. 2014.
139. Saleh, K.J., et al., Acrylic bone cement in total joint arthroplasty: A review. Journal of Orthopaedic Research, 2016. 34(5): p. 737-744.
140. Wooley, P. and E. Schwarz, Aseptic loosening. Gene therapy, 2004. 11(4): p. 402.
141. Boyd, D., et al., Comparison of an experimental bone cement with surgical Simplex P, Spineplex and Cortoss. J Mater Sci Mater Med, 2008. 19(4): p. 1745-52.
142. Harper, E.J., Bioactive bone cements. Proceedings of the Institution of Mechanical Engineers, Part H: Journal of Engineering in Medicine, 1998. 212(2): p. 113-120.
143. Hughes, K.F., M.D. Ries, and L.A. Pruitt, Structural degradation of acrylic bone cements due to in vivo and simulated aging. Journal of Biomedical Materials Research Part A: An Official Journal of The Society for Biomaterials, The Japanese Society for Biomaterials, and The Australian Society for Biomaterials and the Korean Society for Biomaterials, 2003. 65(2): p. 126-135.
144. Ayre, W.N., S.P. Denyer, and S.L. Evans, Ageing and moisture uptake in polymethyl methacrylate (PMMA) bone cements. journal of the mechanical behavior of biomedical materials, 2014. 32: p. 76-88.
145. Radev, B.R., et al., Potential for thermal damage to articular cartilage by PMMA reconstruction of a bone cavity following tumor excision: A finite element study. Journal of biomechanics, 2009. 42(8): p. 1120-1126.
146. Serrano, M.C., et al., In vitro positive biocompatibility evaluation of glass-glass ceramic thermoseeds for hyperthermic treatment of bone tumors. Tissue Engineering Part A, 2008. 14(5): p. 617-627.
147. Verné, E., et al., Composite bone cements loaded with a bioactive and ferrimagnetic glass-ceramic: Leaching, bioactivity and cytocompatibility. Materials Science and Engineering: C, 2015. 53: p. 95-103.

148. Miola, M., et al., Composite bone cements for hyperthermia: modeling and characterization of magnetic, calorimetric and in vitro heating properties. Ceramics International, 2017. 43(6): p. 4831-4840.
149. Corning, D. XIAMETER RTV-3110, 3112 and 3120 Bases. 2010; Available from: https://conservationsupportsystems.com/system/assets/techdocs/3110HowTo.pdf.
150. Kokubo, T. and H. Takadama, How useful is SBF in predicting in vivo bone bioactivity? Biomaterials, 2006. 27(15): p. 2907-15.
151. Miola, M., et al., Glass-ceramics for cancer treatment: so close, or yet so far? Acta biomaterialia, 2018.
152. Kim, J.-W. and H.-G. Lee, Thermal and carbothermic decomposition of Na 2 CO 3 and Li 2 CO 3. Metallurgical and materials transactions B, 2001. 32(1): p. 17-24.
153. Berbenni, V., et al., Solid state reaction study in the systems Li2CO3–FeC2O4· 2H2O and Li2CO3–Fe2 (C2O4) 3· 6H2O. Thermochimica acta, 2000. 346(1-2): p. 115-132.
154. Carles, V., et al., Study of thermal decomposition of FeC2O4· 2H2O under hydrogen. Thermochimica acta, 1999. 334(1-2): p. 107-113.
155. Hermanek, M., et al., Thermal behaviour of iron (II) oxalate dihydrate in the atmosphere of its conversion gases. Journal of Materials Chemistry, 2006. 16(13): p. 1273-1280.
156. Singh, N. and N. Singh, Formation of CaO from thermal decomposition of calcium carbonate in the presence of carboxylic acids. Journal of thermal analysis and calorimetry, 2007. 89(1): p. 159-162.
157. Hsu, C.-K., A study on thermal behavior of uncalcined Ca (H2PO4) 2· H2O and CaCO3 mixtures. Thermochimica acta, 2002. 392: p. 157-161.
158. Boccaccini, A.R., et al., Sintering, crystallisation and biodegradation behaviour of Bioglass®-derived glass–ceramics. Faraday discussions, 2007. 136: p. 27-44.
159. Bretcanu, O., et al., Magnetic properties of the ferrimagnetic glass-ceramics for hyperthermia. Journal of Magnetism and Magnetic Materials, 2006. 305(2): p. 529-533.
160. Karamanov, A., et al., Glass transformation range of iron rich glass and glass ceramics determined by different methods. Glass technology, 2001. 42(4-5): p. 126-129.
161. Goel, A., et al., Sintering behavior and devitrification kinetics of iron containing clinopyroxene based magnetic glass-ceramics. Solid State Ionics, 2011. 186(1): p. 59-68.
162. Bretcanu, O., et al., Sintering and crystallisation of 45S5 Bioglass® powder. Journal of the European Ceramic Society, 2009. 29(16): p. 3299-3306.
163. Bruno, M., et al., Composite bone cements loaded with a bioactive and ferrimagnetic glass-ceramic. Part I: Morphological, mechanical and calorimetric characterization. Journal of biomaterials applications, 2014. 29(2): p. 254-267.
164. Bretcanu, O., et al., Synthesis and characterization of coprecipitation-derived ferrimagnetic glass-ceramic. Journal of materials science, 2006. 41(4): p. 1029-1037.
165. Karakus, O., et al., Effects of reinforcing materials on durability of bone cement: in vitro experimental study. Journal of orthopaedic surgery and research, 2018. 13(1): p. 94.
166. Dunne, N., et al., In vitro study of the efficacy of acrylic bone cement loaded with supplementary amounts of gentamicin: effect on mechanical properties,

antibiotic release, and biofilm formation. Acta orthopaedica, 2007. 78(6): p. 774-785.
167. Qu, G.-X., et al., Mechanical Properties and Porosity of Acrylic Cement Bone Loaded with Alendronate Powder. International journal of medical sciences, 2018. 15(13): p. 1458.
168. ŞERBETÇİ, K., F. KORKUSUZ, and N. HASIRCI, Mechanical and thermal properties of hydroxyapatite-impregnated bone cement. Turkish Journal of Medical Sciences, 2000. 30(6): p. 543-549.
169. Khodakarami, J. and N. Nasrollahi, Thermal comfort in hospitals–A literature review. Renewable and Sustainable Energy Reviews, 2012. 16(6): p. 4071-4077.
170. Jiranek, W., Thermal manipulation of bone cement. Orthopedics, 2005. 28(8): p. S863-S866.
171. Pascual, B., et al., New aspects of the effect of size and size distribution on the setting parameters and mechanical properties of acrylic bone cements. Biomaterials, 1996. 17(5): p. 509-516.
172. Weber, S.C. and W.L. Bargar, A comparison of the mechanical properties of Simplex, Zimmer, and Zimmer low viscosity bone cements. Biomaterials, medical devices, and artificial organs, 1983. 11(1): p. 3-12.
173. Dunne, N., et al., Validation of the small-punch test as a technique for characterizing the mechanical properties of acrylic bone cement. Proceedings of the Institution of Mechanical Engineers, Part H: Journal of Engineering in Medicine, 2006. 220(1): p. 11-21.
174. Salih, S.I., J.K. Oleiwi, and Q.A. Hamad, Investigation of fatigue and compression strength for the PMMA reinforced by different system for denture applications. International Journal of Biomedical Materials Research, 2015. 3(1): p. 5-13.
175. Zidan, S., et al., Investigating the Mechanical Properties of ZrO2-Impregnated PMMA Nanocomposite for Denture-Based Applications. Materials, 2019. 12(8): p. 1344.
176. Ambrosio, L. and E. Tanner, Biomaterials for spinal surgery. 2012: Elsevier.
177. Yoon, J.-R., Y.-R. Ko, and Y.-S. Shin, Effect of shape on bone cement polymerization time in knee joint replacement surgery. Medicine, 2018. 97(17).
178. Campbell, F., Introduction to composite materials, in Structural composite materials. 2010. p. 1-29.
179. Hamizah, A., et al., Mechanical and thermal properties of polymethylmethacrylate bone cement composites incorporated with hydroxyapatite and glass-ceramic fillers. Journal of Applied Polymer Science, 2012. 125(S1): p. E661-E669.
180. Moloney, A., H. Kausch, and H. Stieger, The fracture of particulate-filled epoxide resins. Journal of Materials Science, 1983. 18(1): p. 208-216.
181. Hasratiningsih, Z., et al. Hardness evaluation of PMMA reinforced with two different calcinations temperatures of ZrO2-Al2O3-SiO2 filler system. in IOP Conference Series: Materials Science and Engineering. 2017. IOP Publishing.
182. Alhareb, A.O., H.M. Akil, and Z.A. Ahmad, Impact strength, fracture toughness and hardness improvement of PMMA denture base through addition of nitrile rubber/ceramic fillers. The Saudi Journal for Dental Research, 2017. 8(1-2): p. 26-34.
183. Gergely, R.C., et al., Towards the optimization of the preparation procedures of PMMA bone cement. Journal of Orthopaedic Research, 2016. 34(6): p. 915-923.

184. Linden, U. and J. Gillquist, Air inclusion in bone cement. Importance of the mixing technique. Clinical orthopaedics and related research, 1989(247): p. 148-151.
185. Gad, M.M., et al., PMMA denture base material enhancement: a review of fiber, filler, and nanofiller addition. International journal of nanomedicine, 2017. 12: p. 3801.
186. Neel, E.A., et al., Effect of iron on the surface, degradation and ion release properties of phosphate-based glass fibres. Acta Biomaterialia, 2005. 1(5): p. 553-563.
187. Fernandes, H.R., et al., Bioactive glasses and glass-ceramics for healthcare applications in bone regeneration and tissue engineering. Materials, 2018. 11(12): p. 2530.
188. Li, G., S. Feng, and D. Zhou, Magnetic bioactive glass ceramic in the system CaO–P 2 O 5–SiO 2–MgO–CaF 2–MnO 2–Fe 2 O 3 for hyperthermia treatment of bone tumor. Journal of Materials Science: Materials in Medicine, 2011. 22(10): p. 2197.
189. Ciapetti, G., et al., In vitro testing of the potential for orthopedic bone cements to cause apoptosis of osteoblast-like cells. Biomaterials, 2002. 23(2): p. 617-627.
190. Kontonasaki, E., et al., Attachment and proliferation of human periodontal ligament fibroblasts on bioactive glass modified ceramics. Journal of oral rehabilitation, 2007. 34(1): p. 57-67.
191. Montazerian, M. and E.D. Zanotto, Bioactive glass-ceramics: processing, properties and applications. Bioactive glasses: fundamentals, technology and applications. Royal Society of Chemistry, London, 2016: p. 27-60.
192. Rios, P., et al., The effect of polymer surface on the wetting and adhesion of liquid systems. Journal of adhesion science and technology, 2007. 21(3-4): p. 227-241.
193. Dowling, D.P., et al., Effect of surface wettability and topography on the adhesion of osteosarcoma cells on plasma-modified polystyrene. Journal of biomaterials applications, 2011. 26(3): p. 327-347.
194. Kazarian, S.G., et al., Specific intermolecular interaction of carbon dioxide with polymers. Journal of the American Chemical Society, 1996. 118(7): p. 1729-1736.
195. Chen, L., et al., Silicate bioceramic/PMMA composite bone cement with distinctive physicochemical and bioactive properties. Rsc Advances, 2015. 5(47): p. 37314-37322.
196. Ku, K.-L., et al., Incorporation of surface-modified hydroxyapatite into poly (methyl methacrylate) to improve biological activity and bone ingrowth. Royal Society Open Science, 2019. 6(5): p. 182060.
197. Jiang, H.-J., et al., Mechanical properties and cytocompatibility improvement of vertebroplasty PMMA bone cements by incorporating mineralized collagen. Materials, 2015. 8(5): p. 2616-2634.
198. Sa, Y., et al., Bone response to porous poly (methyl methacrylate) cement loaded with hydroxyapatite particles in a rabbit mandibular model. Tissue Engineering Part C: Methods, 2017. 23(5): p. 262-273.
199. He, Q., et al., Porous surface modified bioactive bone cement for enhanced bone bonding. PloS one, 2012. 7(8): p. e42525.
200. Cimatti, B., et al., Physical and mechanical characterization of a porous cement for metaphyseal bone repair. Acta ortopedica brasileira, 2015. 23(4): p. 197-201.